

**A STUDY OF HYDROPHOBIC INTERACTION
IN FINE PARTICLE COAGULATION**

by

Zhenghe Xu

Dissertation submitted to the Faculty of the
Virginia Polytechnic Institute and State University
in partial fulfillment of the requirements for the degree of
Doctor of Philosophy
in
Materials Engineering Science

APPROVED:



R.H. Yoon, Chairman



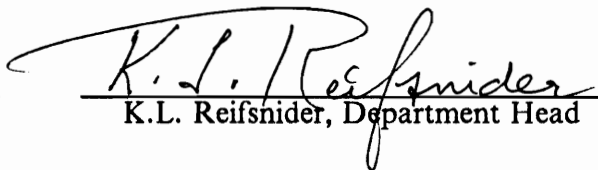
J.G. Dillard



G.T. Adel



G.H. Luttrell



K.L. Reifsnider, Department Head

April, 1990

Blacksburg, Virginia

A STUDY OF HYDROPHOBIC INTERACTION IN FINE PARTICLE COAGULATION

by

Zhenghe Xu

R.H. Yoon, Chairman

Materials Engineering Science

(ABSTRACT)

A stability theory for lyophobic colloids was put forth in the 1940's by Derjaguin, Landau, Verwey, and Overbeek. This theory, known as DLVO theory, has gone through the test of time and survived as a pillar of colloid science. In the present work, this theory has been used for describing the behavior of fine coal and silica particles in aqueous media. It has been found, however, that the classical DLVO theory is applicable only to weakly hydrophobic solids but not to very hydrophobic ones. The coagulation experiments conducted with very hydrophobic particles suggest that there exists a strong attractive force that has not been considered in the theory. This non-DLVO force has been estimated in the present work based on the data obtained from coagulation experiments.

Contributions from the non-DLVO force, which is referred to as hydrophobic interaction energy (V_H), have been related to the nondispersion component of work of adhesion of water on solids (W_a^{nd}). An expression for V_H , which is now a function of W_a^{nd} , has been added as a third term in the DLVO equation in order to better describe the stability of colloidal suspensions regardless of the hydrophobicity of the particles involved.

A population balance model for a system of isotropic turbulent flow has been developed. Both aggregate growth and breakage have been considered in the model and their rate constants have been derived from a phenomenological approach. Numerical procedures have been proposed for solving the coagulation kinetic equations. Computer simulations show that the model is fairly flexible and the results are in reasonable agreement with experiment.

ACKNOWLEDGEMENTS

First, and foremost, the utmost appreciation is expressed to my advisor, Dr. Roe-Hoan Yoon, for his guidance, inspiration and support throughout the course of this investigation. Special thanks are given to Dr. Gregory Adel and Dr. Gerald Luttrell for their continued interest and invaluable assistance, to the other committee members-Dr. John Dillard and Dr. Kenneth Reifsnider for their valuable time and constructive comments, and to Dr. Mark Davis for his helpful discussions on the numerical technique.

The financial support for this study from the U.S. department of Energy (Contract No. DE-AC22-86PC91221) and from the department of Mining and Minerals Engineering is sincerely appreciated.

Special appreciation is given to Dr. Jorge Yordan, Ricky Honaker, Mike Mankosa, John Looney and Richard Forrest for their many suggestions, support and friendship, and to Dr. Jerzy Mielczazski, Dr. Mehmet Celik, Dr. Woo-Zin Choi, Dr. Cesar Basilio, Dr. Dilo Paul, Michael Stallard, Joe Zachwieja, Courtney Young, Asa Weber, Eric Yan, and Hector Rojas for their helpful discussions, friendship and willing assistance. Gratitude is also expressed to the rest of my fellow graduate students in the department of Mining and Minerals Engineering and to all my friends for sharing with me my ups and downs, for their friendliness and continuous support.

Appreciation is also extended to Beth Howell, Wayne Slusser, Jerry Rose and Jim Overfelt for their technical assistance.

Finally, the most sincere appreciation is expressed to my wife, Chaoyi, for her outstanding support, understanding and love.

TABLE OF CONTENTS

CHAPTER 1 INTRODUCTION	1
1.1 Fine Particle Processing	1
1.2 Improvement of Fine Particle Processing	4
1.2.1 Design of New Flotation Reagents	4
1.2.2 Microbubble Column Flotation	5
1.2.3 Vacuum or Pressure Release Flotation	7
1.2.4 Selective Flocculation	8
1.2.5 Shear Flocculation	10
1.2.6 Carrier Flotation/Ultraflotation	11
1.2.7 Liquid Phase Agglomeration	12
1.2.8 Selective Coagulation	14
1.3 Scope of Research	15
1.4 References	17
CHAPTER 2 INTERPARTICLE FORCES	24
2.1 Introduction	24
2.2 Dispersion Forces	25
2.2.1 Dispersion Forces between Atoms or Molecules	25
2.2.2 Dispersion Forces between Two Macroscopic Objects I. Hamaker's Approach	31
2.2.3 Dispersion Forces between Two Macroscopic Objects II. Lifshitz's Approach	37

2.2.4	An Improved Approximation for A_{132} and A_{131}	42
2.2.5	Effect of Temperature and Surface Layer on Dispersion Forces	48
2.2.6	Implications from the Theories of Dispersion Forces	50
2.2.7	Experimental Measurement of Dispersion Forces	52
2.3	Electrical Double Layer Forces	58
2.3.1	Origins of Surface Charge	58
2.3.2	Surface Electrical Potential	63
2.3.3	Electrical Double Layer Theories	67
2.3.4	Electrostatic Interaction between Electrical Double Layers	80
2.3.5	Experimental Approach to Electrostatic Double Layer Interactions	100
2.4	Structural Forces	104
2.4.1	Classical DLVO Theory	104
2.4.2	Experimental Evidence of Non-DLVO Forces	108
2.4.3	The Structural Force Law	118
2.4.4	Statistical Mechanics Approach to Structural Forces	128
2.4.4	Proposed Mechanisms of Structural Forces	138
2.5	References	144
 CHAPTER 3 HYDROPHOBIC INTERACTION IN COAGULATION		161
3.1	Introduction	161
3.2	Experimental	162
3.2.1	Sample Preparation	162
3.2.2	Coagulation Tests	163
3.2.3	Contact Angle Measurements	164
3.2.4	Heat of Wetting and Heat of Displacement Measurements	164
3.2.5	Electrokinetic Studies	165
3.3	Experimental Results	165
3.3.1	Coagulation and Electrokinetic Studies	165

3.3.2	Characterizations of Surface Forces	171
3.4	Discussion	176
3.5	Summary and Conclusions	186
3.6	References	186
CHAPTER 4 A THEORY OF HYDROPHOBIC INTERACTION		190
4.1	Introduction	190
4.2	Experimental	191
4.3	Results and Discussion	193
4.3.1	Theoretical Analysis	193
4.3.2	Derivation of an Expression for V_H	197
4.4	Mechanism of Hydrophobic Interaction	209
4.5	Summary and Conclusions	215
4.6	References	216
CHAPTER 5 MODEL DEVELOPMENT FOR THE COAGULATION PROCESS		219
5.1	Introduction	219
5.2	Model for Aggregate Porosity	221
5.3	Model for Aggregate Growth	226
5.4	Model for Aggregate Breakage	233
5.6	Population Balance Model	245
5.7	Summary and Conclusions	248
5.8	References	249
CHAPTER 6 A SIMULATION OF THE COAGULATION PROCESS		253
6.1	Introduction	253
6.2	Numerical Procedures	254
6.3	A Typical Example of Simulation	258

6.4	Simulations with Varying Model Parameters	262
6.4.1	Effect of Model Parameter β on Coagulation Kinetics	262
6.4.2	Effect of Model Parameter k_1 on Coagulation Kinetics	267
6.4.3	Effect of Model Parameter k_3 on Coagulation Kinetics	270
6.4.4	Effect of Model Parameter A on Coagulation Kinetics	273
6.5	Simulations with Varying System Variables	276
6.5.1	Effect of Mixing Rate on Coagulation Kinetics	276
6.5.2	Effect of Zeta Potential on Coagulation Kinetics	287
6.5.3	Effect of Hamaker Constant on Coagulation Kinetics	292
6.5.4	Effect of Hydrophobic Interaction on Coagulation Kinetics	295
6.5.5	Effect of Interfacial Tension on Coagulation Kinetics	298
6.6	Aggregate Size Distribution Measurement and Discussion	303
6.6.1	Aggregate Size Distribution Measurement	303
6.6.2	Discussion	305
6.7	Summary and Conclusions	311
6.8	References	312
CHAPTER 7	SUMMARY AND CONCLUSIONS	313
CHAPTER 8	RECOMMENDATIONS FOR FUTURE RESEARCH	316
APPENDIX I	CALCULATION OF KINETIC ENERGY	319
APPENDIX II	PROGRAM FOR COAGULATION KINETIC SIMULATION	326
VITA		336

LIST OF FIGURES

Figure 2.1. Electrical Double Layer Structure and Distributions of Electrical Potential and Ion Species	66
Figure 2.2. Schematic Representation of Electrical Potential between Two Charged Surfaces	82
Figure 2.3. Schematic Illustration Showing the Extension of Flat Double Layer Interaction to Spherical One	96
Figure 2.4. A Profile of Potential Energy versus Separation between Particles as Calculated Using the Classical DLVO Theory	105
Figure 2.5. Schematic Illustration of Water Structure Confined between Two Surfaces	142
Figure 3.1. Coagulation and ζ -potential Measurements on Fresh and Oxidized (140 °C) Coal Samples as a Function of pH	166
Figure 3.2. Coagulation and ζ -potential Measurements on Coal Samples Oxidized at 170 and 200 °C as a Function of pH	168
Figure 3.3. Coagulation and ζ -potential Measurements on Silica Samples with and without Methylation as a Function of pH	170
Figure 3.4. Dispersion and Nondispersion Components of Work of Adhesion of Water on Coal as a Function of Oxidation Temperature	175
Figure 3.5. Heat of Wetting of Coal in Heptane and Heating of Heptane Displacement by Water as a Function of Oxidation Temperature	177
Figure 3.6. Interaction Energy Barrier as a Function of Surface Potential Calculated Using the Classical DLVO Theory	180
Figure 3.7. Hydrophobic Interaction Energy Plotted as a Function of Nondispersion Component of Work of Adhesion	183
Figure 4.1. Values of C and H_m as a Function of Decay Length (D_0) as Calculated Using Equations [4.9] and [4.12]	198

Figure 4.2. Potential Energy Profile as a Function of Separation Distance Calculated for Methylated Silica	199
Figure 4.3. Results of Coagulation and ζ -potential Measurements on Silica Samples Methylated at Various TMCS Concentrations	202
Figure 4.4. Hydrophobic Interaction Parameter (C) versus W_a^{nd} Plot for Methylated Silica and Oxidized Coal Samples	205
Figure 4.5. Hydrophobic Interaction Parameter (C) versus W_o Plot for Methylated Silica and Oxidized Coal Samples	207
Figure 4.6. Excess Free Energy per Water Molecule Confined in the Interlayer Region between Two Strongly Hydrophobic Solids	213
Figure 5.1. Schematic Representation of a Binary Aggregate Formation Model ..	223
Figure 5.2. Simulation Results of Porosity and Aggregate Size as a Function of Aggregate Number Using the Model of Figure 5.1.	225
Figure 5.3. Comparison of Collision Efficiency for Three Different Values of Model Parameter β	231
Figure 5.4. Variation of Binding Force as a Function of Aggregate Size for Three Different Values of Model Parameter k_1	236
Figure 5.5. Variation of Shear Force as a Function of Aggregate Size for Three Different Mixing Rates	238
Figure 5.6. Variation of Breakage Rate Constant as a Function of Aggregate Size for Different Values of Model Parameters k_1 and k_3	241
Figure 5.7. Variation of Breakage Rate Constant as a Function of Aggregate Size for Two Different Mixing Rates	242
Figure 6.1. Schematic Diagram of the Computer Program for Simulating Coagulation Kinetic Behaviors	259
Figure 6.2. Cumulative Aggregate Size Distributions of Fine Coal Particles at Various Coagulation Time	260
Figure 6.3. Changes of Mass Fraction of Primary Partiles and Aggregates in Different Size Ranges as a Function of Coagulation Time	263
Figure 6.4. Changes of Dimensionless Number Concentration as a Function of Coagulation Time for Different β Values	265
Figure 6.5. Equilibrium Cumulative Aggregate Size Distributions for Two Different β Values	266

Figure 6.6. Changes of Dimensionless Number Concentration as a Function of Coagulation Time for Different k_1 Values	268
Figure 6.7. Equilibrium Cumulative Aggregate Size Distributions for Different k_1 Values	269
Figure 6.8. Changes of Dimensionless Number Concentration as a Function of Coagulation Time for Different k_3 Values	271
Figure 6.9. Equilibrium Cumulative Aggregate Size Distributions for Different k_3 Values	272
Figure 6.10. Changes of Dimensionless Number Concentration as a Function of Coagulation Time for Different A Values	274
Figure 6.11. Equilibrium Cumulative Aggregate Size Distributions for Different A Values	275
Figure 6.12. Evolution of Mass Fraction of Primary Particles and Aggregates in Different Size Ranges under Mixing Rate of 800 rpm	277
Figure 6.13. Evolution of Mass Fraction of Primary Particles and Aggregates in Different Size Ranges under Mixing Rate of 500 rpm	279
Figure 6.14. Changes of Dimensionless Number Concentration as a Function of Coagulation Time for Mixing Rates of 800 and 1000 rpm	280
Figure 6.15. Changes of Dimensionless Number Concentration as a Function of Coagulation Time for Mixing Rates of 500 and 300 rpm	281
Figure 6.16. Comparison of Aggregation Rate Constants as a Function of Aggregate Size for Different Mixing Rates	283
Figure 6.17. Equilibrium Cumulative Aggregate Size Distributions as a Function of Coagulation Time for Three Different Mixing Rates	286
Figure 6.18. Changes of Dimensionless Number Concentration as a Function of Coagulation Time for Different Values of Zeta Potential	288
Figure 6.19. Equilibrium Cumulative Aggregate Size Distributions for Different Values of Zeta Potential	291
Figure 6.20. Changes of Dimensionless Number Concentration as a Function of Coagulation Time for Different Values of Hamaker Constant	293
Figure 6.21. Equilibrium Cumulative Aggregate Size Distributions for Different Values of Hamaker Constant	294
Figure 6.22. Changes of Dimensionless Number Concentration as a Function of Coagulation Time for Different Values of HI Parameter C	296

Figure 6.23. Equilibrium Cumulative Aggregate Size Distributions for Different Values of Hydrophobic Interaction Parameter C	299
Figure 6.24. Changes of Dimensionless Number Concentration as a Function of Coagulation Time for Different Values of γ_{rw}	301
Figure 6.25. Equilibrium Cumulative Aggregate Size Distributions for Different Values of γ_{rw}	302
Figure 6.26. Aggregate Size Distribution Measured from Three Independent Runs Using the Andreasen Pipette Technique	306
Figure 6.27. Aggregate Size Distribution of Elkhorn No. 3 Coal Formed in Three Different Suspension Conditions	307
Figure 6.28. A Comparison of Aggregate Size Distributions Obtained from Computer Simulation and Experimental Measurements at pH 8.4	310
Figure AI.1. Structure and Geometry of the Mixer Used in Coagulation Tests ..	320
Figure AI.2. Kinetic Energy as a Function of Mixing Rate for Coal Samples of Two Different Particle Sizes	325

LIST OF TABLES

Table 2.1. Hamaker Constant of Water and Fused Silica Calculated Using Eqs. [2.30] and [2.15]	42
Table 3.1. Critical pH and ζ -Potential Values Obtained Experimentally for Coagulation of Coal and Silica Samples	169
Table 3.2. Dispersion Component of Surface Free Energies of Coal and Silica Samples as Calculated from Methylene Iodide Contact Angles	172
Table 3.3. W_o^{nd} Values for Coal and Silica Samples Calculated from the Water Contact Angles	174
Table 3.4. Potential Energy Barriers at Critical pH of Coagulation and Hamaker Constants of Coal and Silica Samples	179
Table 4.1. Values of H_m and C as Calculated Using Equations [4.11] and [4.13] ..	200
Table 4.2. Values of W_o^{nd} of Water on Methylated Silica as Calculated Using Equation [4.1]	203
Table 4.3. Values of C Calculated Using Equations [4.11] and [4.13] and W_o^{nd} of Water on Oxidized Coal Samples	204
Table 6.1. Calculated Values of V_k , α , $\omega(a_1, a_1)$, $k(1, 1)$ and d_b at Various Mixing Rates.	282
Table 6.2. Calculated Values of V_{max} , α and $k(1, 1)$ for Three Different Values of Zeta Potential	289
Table 6.3. Calculated Values of V_{max} , α and $k(1, 1)$ for Three Different Values of Hydrophobic Interaction Parameter C	297

CHAPTER 1 INTRODUCTION

1.1 Fine Particle Processing

With the increasing demand for high quality coal as a substitute for fuel oil, it has become necessary to process fine coal, both from an economic and from an environmental point of view. In order to avoid wasting energy resources, the fine particle sizes of coal generated at the mine site need to be recovered. To meet environmental emission standards with regard to SO_2 content, the removal of pyritic sulfur from coal necessitates fine grinding for liberation and subsequent processing, since pyritic sulfur usually occurs in a finely disseminated form. This fact also dictates the need for fine coal processing.

It has been found that processing fine particles is extremely difficult due to the special properties of fines (1). The most pronounced changes accompanying decreased particle sizes are a significant increase in specific surface area along with a considerable decrease in the mass of the particles. This is particularly true for fine coal particles due to their low density and the high organic content of the coal matrix. Due to the very low mass of individual fine coal particles, conventional coal cleaning technology, such as hydrocyclones, dense medium cyclones, tabling, jigs, and heavy medium separators, fails when used to process fine particles either because of low separation efficiency or because

of the low throughput of the process. The high specific surface area and low mass of fine particles cause conventional flotation technology to become unsuccessful for upgrading fine coals because of the high reagent consumption and low flotation rate (2-3). Developing new technologies for fine particle processing has been a challenge to researchers in the mineral processing area for about 35 years (2).

In order to obtain effective and practical solutions to fine particle processing, it is important to understand the behavior of fines in the process. This behavior is most likely associated with the properties of the fines. It is obvious that fine particles are small in mass, which yields low inertia and low momentum. This fact regarding the nature of fines makes it very difficult to avoid entrainment of unwanted fine particles in the liquid medium reporting to the concentrate. As a result, the concentrate is degraded (4-6) if the entrained fines are gangue minerals.

It has been recognized that for the same minerals, fine particles have lower flotation rates because of their low inertia (2-3, 7-10). It is well known that fine particles tend to follow the streamline of liquid when they are moving in it because of this low level of inertia. Since the streamline deviates from the air bubble in the flotation pulp, fine particles will deviate from the air bubble along with the streamline, resulting in a low collision frequency and hence a low flotation rate. This gives rise to the problem of low recovery combined with poor concentrate grade common in fine particle processing.

As the particles decrease in size to the colloidal dimension, intermolecular forces become increasingly significant. As a result, slime coating causes another common problem in fine particle flotation chiefly due to the heterocoagulation between valuable mineral particles and gangue particles. Slime coating will not only reduce the selectivity of flotation, giving poor concentrate grade, but also reduce the flotation rate of valuable minerals because of the low flotability of coated gangue slimes, resulting in low recovery.

The significant increase in specific surface area of fine particles introduces some other problems for fine particle processing. Apparently, the larger specific surface area of fine particles requires a higher flotation reagent dosage to maintain the same adsorption density of the flotation reagent. Therefore, fine particle flotation requires high flotation reagent consumption. In other words, recovery will decrease significantly if a conventional flotation reagent package is used in fine particle flotation.

It should also be noted that the large specific surface area of fine particles increases their activity significantly due to the existence of a large amount of corners, edges and crystallographic imperfections (1). The high surface energy of fine particles causes the preferential adsorption of flotation reagents on them, consuming most of the flotation reagent existing in the pulp. As a consequence, the flotation reagent available for coarse particles becomes insufficient, giving poor surface hydrophobicity and sacrificing the recovery of coarse particles.

It is also not surprising to note that as the particle size decreases to colloidal dimensions, the differences in the surface properties of different kinds of fine mineral particles become less pronounced, causing nonspecific adsorption of the flotation reagent. Also associated with the decrease in the particle size is the increased dissolution of fine particles as predicted from the Kelvin equation. This will introduce a considerable amount of undesirable species into the pulp, causing unintentional activation and/or depression of minerals. In fine coal flotation, for instance, a considerable amount of organic species, such as humic acid, is expected to exist in the pulp due to the rapid oxidation of fine coal particles. These dissolved organic species will significantly affect the flotation behavior of coal, mineral matter, and pyritic sulfur (11-12). The difference between the flotabilities of these minerals is thus reduced, increasing the difficulty of removing mineral matter and sulfur from fine coal. Therefore, the selectivity of fine particle processing becomes a severe problem.

In order to solve the problems associated with fine particle processing, research and development activities have gathered unprecedented momentum since the 1960's. As a result, the number of new technologies has experienced a rapid growth. Some of the new technologies for improving fine particle processing are briefly discussed in the following section.

1.2 Improvement of Fine Particle Processing

1.2.1 Design of New Flotation Reagents

As discussed in the previous section, one of the most pronounced problems in fine particle processing is the high reagent consumption and the low selectivity of the process mainly due to the large specific surface area and the high specific surface energy of fine particles, respectively. In order to improve the selectivity of the flotation process by eliminating non-selective adsorption of flotation reagents, it is essential to design new flotation reagents which are capable of interacting with valuable mineral surfaces through specific chemical bonds. Efforts have been made to incorporate chelating functional groups into the hydrocarbon entities simply because these compounds have been known to provide a kind of metal specificity or selectivity (13-15).

Based on the type of coordinating atoms, three kinds of chelating reagents are useful in mineral processing, one using O/O atoms as bonding atoms and the other two using O/N and N/S atoms as bonding atoms, respectively. The first use of a chelating reagent in flotation may be attributed to Vivian (15) who floated cassiterite in an aqueous pulp containing acetic acid with cupferron, which is an O/O type chelating reagent. By introducing the hydroxamate group, another O/O type chelating functional group, into octanoate, octylhydroxamate has been produced for floating hematite ores

(16-17) and for removing impurities from clay minerals (18). Oxine, one of the important O/N type chelating reagents, has been used to float oxidized lead and zinc ores (19). Mercaptobenzothiazole and aminothiophenol, which are N/S type chelating collectors of different tail structures, have been tested on the Pb-Zn oxidized ores (14). The results have been interpreted on the basis of steric factors and the reactivity of the functional groups. More examples of the application of these three types of chelating reagents in mineral processing practice can be found, among others, in references 13 and 14.

The chelating type organic chemicals show potential application in fine particle processing because not only the selectivity but also the recovery can be improved. It is well known that chelating type collectors selectively adsorb onto mineral surfaces through chemical bonds, accompanying a significant free energy reduction. As a result, the residual concentration of the collector is lower. This not only reduces the reagent consumption but also eliminates the adsorption of collector on bubble surfaces, which contributes to better recovery of fine mineral particles. It is also recognized that the recovery of fine particles can be improved by neutralization of the surface charge on the mineral surface due to the ion exchange associated with collector adsorption. Since the chelating type organic chemicals are usually very expensive, they are practically useful only for processing precious metallic minerals.

1.2.2 Microbubble Column Flotation

In regard to the problems of fine particle processing associated with lower flotation rate mainly due to reduced collision frequency between fine particles and bubbles, column flotation appears to be a possible solution. Since counter current flow, with bubbles rising continuously through a downward flowing slurry, is utilized in the column, the probability of bubble/particle collision increases significantly, and the op-

portunity for the mineralized bubbles to be washed free of entrapped gangue particles increases considerably. However, the best results have been achieved by using micro-bubbles in the column flotation process as described by Yoon et al. (3, 20-21). It has been found (21) that decreasing the size of the flotation bubbles results in an increase in the bubble/particle collision frequency and, hence, the flotation rate constant, as indicated in Equation [1.1]:

$$P_c = A \left(\frac{R_p}{R_b} \right)^n , \quad [1.1]$$

where P_c is the bubble/particle collision frequency, R_p and R_b are the radii of particle and bubble, respectively, and A and n are the parameters whose values are determined by the hydrodynamics of the system. For a system with a large value of Reynolds number, n has the value of unity, while for a system with a small value of Reynolds number, n equals 2. Equation [1.1] suggests that the flotation of fine mineral particles is best accomplished by using small bubbles at low to mediate mixing conditions. Based on this concept, microbubble column flotation, in which a low turbulent flow condition is ensured, has been developed for the solution of fine particle processing problems. The column developed by Yoon et al. has been demonstrated with several different U.S. coals to be capable of producing ultraclean coal (< 0.8% ash) with high recoveries (22). The experimental results with other minerals also show the potential application of micro-bubble column flotation technology to fine particle processing of other minerals, such as clay.

The main advantage of using smaller bubbles has been found to be an increased recovery rate, which may be attributed to an improved bubble/particle collision frequency as bubble size decreases. It is also possible that by using microbubbles, the bubble/particle adhesion efficiency may be improved significantly because of the reduced

interaction energy barrier as predicted from the classical DLVO (Derjaguin- Landau- Verwey-Overbeek) theory. The increased adhesion efficiency will contribute to an increase in flotation rate and, hence, recovery. The selectivity of the process has been found to be improved by using microbubbles chiefly due to the quiescent flow conditions. Use of wash water in microbubble column flotation further improves the selectivity of the process by minimizing unwanted fine particles entrained in the froth phase.

1.2.3 Vacuum or Pressure Release Flotation

An alternative solution to the problem of lower bubble/particle collision frequency is to generate the bubbles directly on the valuable mineral surfaces. It is not difficult to understand that by preferential nucleation of gas bubbles on the hydrophobic surfaces, the bubble/particle collision step required in conventional flotation can be eliminated. It is noted that by creating a vacuum or releasing the pressure, the bubble will be generated in the slurry in which valuable mineral particles are rendered hydrophobic. Since the activation energy of nucleation of a vapor cavity on a hydrophobic surface is much lower than that on a hydrophilic surface, it is expected that the bubbles will selectively form on the hydrophobic mineral surfaces. The mineralization of bubbles in such a way not only eliminates the bubble/particle collision step but also reduces the entrapment of gangue particles.

The above discussion suggests that using the vacuum or pressure release technique seems to be an excellent idea for generating bubbles for the flotation of fine mineral particles. However, the application of this idea to the practice of mineral processing is rather limited, chiefly due to the difficulties associated with constructing the devices to generate a sufficient amount of bubbles for effective recovery of minerals and with

controlling the process. Further research is, therefore, required to utilize the vacuum or pressure release technology for recovering fine mineral particles.

1.2.4 *Selective Flocculation*

It is obvious that fine particle processing problems can be solved if one can selectively increase the apparent particle size of one or more components of a multi-component mixture prior to the separation process. After the selective enlargement of particle size, conventional separation technologies become more feasible. Based on this concept, a new unit operation called *selective flocculation* has been developed to process fine particles (1). In this operation, macromolecules, called *flocculants*, are used. Because of their long molecular chain lengths, a single macromolecule is capable of adsorbing on several fine particles simultaneously. As a result, these fine particles of one component in a mixture are bridged together, forming flocs of greater size.

It has been found that the success of selectively flocculating one component from a mixture depends on the selective interaction of macromolecules with the mineral surfaces of this component. In order to achieve high performance with selective flocculation, several efforts have been made to incorporate specific functional groups into polymer backbones. As a result, starch and cellulose xanthates have been prepared and have shown marked selectivity toward minerals such as pyrite (23-24), chalcopyrite (25), and chrysocolla (26). Evidence for the selectivity of flocculation has been demonstrated by using the polymer containing sulphhydryl groups which chelate heavy metal ions (26) and sulfide minerals (23-25). The polyacrylamide-based chelating polymers have been synthesized to selectively flocculate copper (26-27) and cassiterite (28) minerals.

In order to improve the efficiency of the selective flocculation process, attention has also been given to a subsequent stage for separating flocculated materials from the dispersed fine particles. Several methods have been suggested for selectively removing flocs. These include simple desliming by decantation (28-29), wet-screening (30), flotation (31-34) and magnetic separation (35). The desliming technique is the simplest, but suffers from severe entrainment problems and low throughput. The wet-screen technique requires flocs to be strong and dense to withstand the breakup due to erosion and splitting. This, in turn, may cause severe unintentional entrapment. The use of the floc flotation technique is attractive, but can be complicated because it requires an understanding of the interaction between flocculants and flotation reagents. Magnetic separation is a relatively simple method to separate flocs with magnetic properties from dispersed nonmagnetic fine particles. Good separation has been obtained using this method to separate titanomagnetite/ilmenite flocs from dispersed feldspar (35). It is obvious that this method is useful only for separating magnetic flocs from dispersed nonmagnetic particles. To use this separation method, at least one of the components to be flocculated should have magnetic properties. Otherwise, magnetic particles need to be added into the system as magnetic seeds, forming bulk flocs of desirable components and magnetic seeds. As a result, a subsequent unit operation is required to separate the given components of bulk flocs from the magnetic seeds.

Selective flocculation has been successfully used in the practice of mineral processing (36-38). A process of selective flocculation of finely-ground nonmagnetic taconite ore followed by selective desliming of dispersed silica and removal of the siliceous gangue by flotation has been developed for upgrading iron ores (36). Corn starch has been used as the flocculant in a commercial plant which went into operation at Tilden mine in 1974 (37). The selective flocculation-flotation technology has also been successfully applied to processing a sylvinitic ore on a commercial scale (38). Nonionic polyacrylamide has

been used to selectively flocculate potash from gangue minerals such as dolomite, hematite, quartz, kaolinite, illite, chlorite, and anhydrite.

1.2.5 *Shear Flocculation*

An alternative process for increasing apparent particle size prior to flotation, called *shear flocculation*, has been developed for fine particle processing (39). In this process, surfactants instead of macromolecules are added into a mixture to sensitize the surfaces of valuable fine particles by selective adsorption of the surfactants. Shear is then applied to bring the hydrophobized particles into close proximity over which hydrophobic association is possible. Due to favorable intermingling of the hydrophobic hydrocarbon chains of the surfactant coating, surfactant-coated particles are readily flocculated during a hydrodynamic encounter, releasing an association energy. The flocs formed as such are tough enough to withstand the turbulence encountered in flotation. High shear force is required in shear flocculation to overcome strong electrostatic repulsive forces because the reagent-coated particles are usually highly charged. Since the flocs formed in shear flocculation process are hydrophobic, it is suitable to recover them by flotation.

Systems investigated for selective shear flocculation include scheelite/garnet (40), scheelite ores (41-42), cassiterite/tourmaline (43), calcite/dolomite/magnesite (44), scheelite/fluorite (45), lead-zinc ore (46), malachite (47), and coal (48). As can be seen, selective shear flocculation can be applied to a wide range of minerals. However, the application of shear flocculation in mineral processing practice is rather limited due to the high reagent and energy consumptions of the process.

1.2.6 *Carrier Flotation/Ultraflotation*

It has been found that the aggregation between fine and coarse particles is more favorable than that between two fine particles (49-50). Based on this concept, a unit operation, called *carrier flotation* or *ultraflotation*, has been derived (49-52). In this operation, coarse particles are intentionally added into a colloidal suspension as carriers. The conditions are created so that the selective attachment of one component of fine particles to the surfaces of the carriers is favored by adding a suitable collector. The bulk aggregates formed under proper mixing conditions are then removed from the suspension by flotation. It can be seen that the basic principles involved in carrier flotation are similar to those in shear flocculation/flotation. However, the reagent and energy consumptions may be reduced substantially in carrier flotation as compared with those in shear flocculation, since the aggregation in the former process is more favorable and, hence, the shear condition becomes less critical.

Carrier flotation has been used for removal of colloidal impurities such as bacteria, silica, clays, metal oxides and humic acid from natural waste waters (1). It has also been used, on the commercial scale, in the purification of kaolin at Minerals and Chemicals Phillip's plant (53). Titaniferous impurities have been removed using 60-micron limestone particles as the carriers. However, wide application of carrier flotation in the mineral processing industry has been restricted due to the subsequent need for separation of the valuables from the carrier particles, which requires additional reagent consumption for "liberating" fines from carriers by selective dispersion (54). This second step may be eliminated if the coarse particles functioning as carriers, whether originally present in or intentionally added to the suspension, are of the same kind as the fine particles to be recovered (55-56).

1.2.7 Liquid Phase Agglomeration

Liquid phase agglomeration technology has been proven to be another effective way for converting fines to coarser sizes which can be processed in conventional systems (57). In liquid phase agglomeration, a minor amount of immiscible liquid is added into a finely divided solid suspension under appropriate agitation conditions. Due to the difference between the solid/water interfacial tensions of different solids, the preferential spreading of added liquid on the surfaces of one component causes the selective aggregation of fine particles of this component, leaving fine particles of the other components in dispersion. The immiscible liquid functions as a bridge between particles. Therefore, the inter-particle interactions are less important than the wetting behavior between the bridging liquid and the surfaces of the fine particles to be agglomerated. The increased aggregate size by liquid phase agglomeration makes it possible for one to use conventional separation technology, such as screening or conventional froth flotation, to separate the aggregates from the dispersed phase.

It is not difficult to understand that the success of liquid phase agglomeration as applied to fine particle processing relies on the favorable wetting of one component by the immiscible liquid phase. This is determined collectively by the relative magnitude of solid/water, solid/liquid and water/liquid interfacial tensions. The primary condition for the displacement of water by an immiscible liquid from the solid surface is given, as inferred from Young's equation, by:

$$\gamma_{wl} \leq \gamma_{sw} - \gamma_{sl} , \quad [1.2]$$

where γ_{wl} , γ_{sw} and γ_{sl} are the interfacial tensions of water/liquid, solid/water and solid/liquid interfaces, respectively. Apparently, any variables which affect one or more of the above interfacial tensions will influence the behavior of the agglomeration process.

Of these variables, the pretreatment of particles with traces of surfactant and the mixing intensity are of most interest. It has been found (58-59) that adding traces of long chain surfactant enhances the response of weakly hydrophobic materials to agglomeration. Therefore, it becomes possible to improve the selectivity of the process and to reduce the amount of oil required to obtain effective agglomeration by selectively sensitizing the surfaces of wanted minerals with the addition of traces of surfactant. It has also been found that very strong agitation emulsifies the liquid while very weak agitation results in an inadequate mixing and thus, poor efficiency.

The process of liquid phase agglomeration by competitive wetting with immiscible liquids forms a family of aggregate structures, depending on the levels of immiscible liquids existing in the suspension (57). At low levels of bridging liquids, pendular bridges are most probable, forming unconsolidated two-dimensional aggregates. As the liquid level increases above the funicular region, three-dimensional aggregates of open structure are expected. Finally, in the capillary wetting region, spheric compact pellets are formed with all the voids being filled with the oil. In this last case, the process is called spherical agglomeration.

Although liquid phase agglomeration technologies have been applied to a number of systems (59-61), such as upgrading barium sulfate, iron ore, and tin ore, the largest proportion of the applications is to coal cleaning technology (57-58, 62-65). The natural hydrophobicity of coal particles gives a low solid/liquid interfacial tension but a high solid/water interfacial tension. As a result, the wetting condition as given by Equation [1.2] can easily be satisfied for a variety of fuel oils. Also, it is not necessary to have a subsequent stage for separating the fuel oil from the recovered agglomerates because the coal/oil mixture is acceptable for most utilizations where the clean liquid fuels are used (66). These two reasons make the oil agglomeration technology almost unique to coal cleaning. Oil agglomeration technology has been adopted successfully

by the coal cleaning industry (64-65) and in waste water treatment practice (67). Despite the ability to recover an excellent product of fine particle coal, the high cost of oil used at these high levels is a continuing impediment to oil agglomeration technology as a common practice in coal cleaning industry. Current researchers are focusing on the incorporation of other technologies, such as shear flocculation and froth flotation, into the liquid phase agglomeration. This incorporation allows the agglomeration to be conducted at ever-decreasing oil levels. It is hopeful that with combined technologies, liquid phase agglomeration will become an attractive technology in coal cleaning practice.

1.2.8 Selective Coagulation

It has been found theoretically (68) that by carefully controlling the chemistry of the suspension, it is possible to coagulate finely divided particles. Unlike other techniques in which the fine particles are aggregated together through "bridges" of added chemicals, the aggregation in coagulation is achieved by controlling the net interparticle forces, mostly through adjusting the chemistry of the suspension. With low surface potentials, < 15 mV in magnitude, the lyphobic particles are readily coagulated (69). Because of the direct contact between particles, coagulation forms more compact aggregates, leading to macroscopic separation (70). Due to these features, coagulation has been widely used as an effective means for removal of colloidal particles in water treatment practice (71-72).

For the purpose of separating one component from another in a mixture, selective coagulation is required where conditions must be chosen so that two components carry the same sign of surface charge but a large difference in the surface potentials, one preferably having a low value, while the other retaining a relatively high value. As an application of this technology to mineral processing, weakly hydrophobic titanium par-

ticles have been selectively coagulated and separated by sedimentation from kaolin slurry (73). Following theoretical studies based on the classical DLVO theory (68), selective coagulation has also been conducted using quartz-hematite and quartz-rutile suspensions (74-75).

Recently, a selective hydrophobic coagulation process has been developed at Virginia Tech for treating ultrafine coal (76). This technology has been proven to be capable of producing superclean and ultraclean coals while maintaining high coal recovery. According to the results obtained from laboratory-scale tests, selective hydrophobic coagulation appears to be a more promising process for fine coal cleaning. The main advantage of this process is that it makes full use of the natural hydrophobicity of coal particles without adding any coagulant except *pH* regulators, resulting in no additional water pollution problems. The selective coagulation of fine coal particles is obtained at a high *pH* value of the slurry, about *pH* 9.0, where mineral matter is highly dispersed due to the presence of strong electrostatic repulsive forces. The coagulation of fine coal particles is possible at such a high *pH* value probably because the strong repulsive electrostatic force is overcome by an anomalous attractive hydrophobic force between strongly hydrophobic coal particles, whose role in coagulation is to be exploited. The selective hydrophobic coagulation process shows potential application in coal cleaning practice because of its low operation cost, high deashing efficiency, and simple process control.

1.3 Scope of Research

The unique advantages of selective hydrophobic coagulation applied to fine coal cleaning as discussed previously make this technology very attractive in coal cleaning practice. In order to have a better understanding of the principles involved in fine par-

ticle coal coagulation, fundamental studies of hydrophobic interaction in fine coal coagulation are the primary objectives of the present work. The specific goals of this research include:

1. to study the role of hydrophobic interaction in the coagulation of strongly hydrophobic fine particles suspended in aqueous solutions;
2. to correlate the coagulation behavior to the surface hydrophobicity of fine particles;
3. to establish an approach for quantitatively evaluating hydrophobic interaction energy as a function of surface hydrophobicity;
4. to develop aggregate growth and breakage rate models for describing coagulation kinetic behavior;
5. to simulate the coagulation kinetics and ultimate aggregate size distribution based on the population balance model.

Since interparticle forces play an important role in fine particle coagulation, it will be helpful to devote Chapter 2 to an overview on the types of surface forces involved in coagulation.

The coagulation and electrokinetic behavior of fine particle coal samples with different degrees of oxidation and silica samples with and without methylation are given in Chapter 3. The results of surface hydrophobicity characterizations with contact angle measurements and microcalorimeter measurements on the samples are also given in Chapter 3. Based on the experimental data, a method for back-calculating the magnitude of the hydrophobic interaction energy using the classical DLVO theory is proposed in this chapter.

Chapter 4 gives further evidence for hydrophobic interaction in coagulation by presenting results from experiments conducted using silica samples methylated to different degrees of surface hydrophobicity. Procedures are proposed in this chapter for esti-

mating the parameters used in describing hydrophobic interaction energy. An expression is derived in Chapter 4 to describe the hydrophobic interaction energy in terms of the surface hydrophobicity and the distance between two interacting particles.

In Chapter 5, the models for aggregate growth and breakup are developed from a theoretical point of view. By analysing aggregate growth and breakup events encountered in coagulation practice, four-parameter coagulation kinetic equations are derived based on the principles of population balance.

The numerical procedures are proposed in Chapter 6. Simulations are conducted using different values of model parameters and system variables, and the results are also presented in Chapter 6. A typical aggregate size distribution, obtained experimentally, is given in this chapter as a check on the validity of the models developed and the numerical procedures used.

Finally, the summary and conclusions and the future work are given in Chapters 7 and 8, respectively.

1.4 References

1. Fuerstenau, D.W., "Fine Particle Flotation," in *Fine Particle Processing*, ed. by Somasundaran, P., AIME, Inc., New York, 2, 669 (1980).
2. Warren, L.J., "Ultrafine Particles in Flotation," in *Principles of Mineral Flotation*, ed. by Jones, M.H. and Woodcock, J.T., The Australasian Institute of Mining and Metallurgy, Victoria, Australia, 185 (1985).
3. Yoon, R.H. and Luttrell, G.H., "The Effect of Bubble Size on Fine Coal Flotation," *Coal Preparation*, 2, 179 (1986).
4. Warren, L.J., "Determination of the Contributions of True Flotation and Entrainment in Batch Flotation Tests," *Int. J. Miner. Process.*, 14, 33 (1985).
5. Warren, L.J., "Entrainment of Particles into Flotation Froths," in *Frothing in Flotation (The Jan Leja Volume)*, ed. by Laskowski, J.S., Gordon and Breach Science Publishers, 123 (1989).

6. Waksmundzki, A., Necjaz-Bruzewica, J. and Planik, M., "Mechanism of Carryover of Gangue Slimes during Flotation of Sulfur Ore," *Trans. IMM*, 80, C249 (1971).
7. Trahar, W.J., "A Rational Interpretation of the Role of Particle Size in Flotation," *Int. J. Miner. Process.*, 8, 289 (1981).
8. Anfruns, J.S. and Kitchner, J.A., "Rate of Capture of Small Particles in Flotation," *Trans. IMM*, 86, C9 (1977).
9. Jameson, G.J., "Physical Aspects of Fine Particle Flotation," in *Principles of Mineral Flotation*, ed. by Jones, M.H. and Woodcock, J.T., The Australasian Institute of Mining and Metallurgy, Victoria, Australia, 215 (1985).
10. Derjaguin, B.V. and Dukhin, S.S., "Kinetic Theory of the Flotation of Fine Particles," *Mineral Processing: Developments in Mineral Processing (Proc. XIII Int. Miner. Processing Congr., Warsaw, Poland)*, ed. by Laskowski, J., Elsevier: Amsterdam; Polish Scientific Publishers, Warsaw, 2, 21 (1981).
11. Lai, R.W., Wen, W.W., and Okoh, J.M., "Effect of Humic Substances on the Flotation Response of Coal," *Coal Preparation*, 7, 69 (1989).
12. Firth, B.A. and Nicol, S.K., "The Influence of Humic Materials on the Flotation of Coal," *Int. J. Miner. Process.*, 8, 239 (1981).
13. Nagaraj, D.R., "The Chemistry and Application of Chelating or Complexing Agents in Minerals Separations," *Surfactant Sci. Ser. (Reagents in Mineral Technology)*, 27, 257 (1988).
14. Marabini, A., Cases, J. and Barbaro, M., "Chelating Reagent as Collectors and Their Adsorption Mechanism," in *Challenges in Mineral Processing*, ed. by Sastry, K.V.S. and Fuerstenau, M.C., Society Mining Engineers, Inc., Littleton, Colorado, 35 (1989).
15. Vician, A.C., *Min. Mag.*, 36, 348 (1927).
16. Fuerstenau, M.C., Harper, R.W. and Miller, J.W., "Hydroxamate Versus Fatty Acid Flotation of Iron Oxide," *Trans. AIME*, 247, 69 (1970).
17. Raghavan, S. and Fuerstenau, D.W., "On the Wettability and Flotation Concentration of Submicron Hematite Particles with Octylhydroxamate as Collector," *AIChE Symposium Ser. (Advances in Interfacial Phenomena of Particulate/Solution/Gas Systems; Applications to Flotation Research)*, 71, 59 (1975).
18. Yoon, R.H. and Hilderbrand, T.M., "Purification of Kaolin Clay by Froth Flotation Using Hydroxamate Collectors," *U. S. Patent*, PN 4629556, (1986).
19. Rinelli, G. and Marabini, A.M., "Flotation of Zinc and Lead Oxide-Sulfide Ores with Chelating Agents," in *Proc. X Inter. Miner. Processing Congr. (London)*, ed. by Jones, M.J., The Institute of Mining and Metallurgy, 493 (1974).

20. Yoon, R.H., Luttrell, G.H. and Adel, G.T., "Advances in Fine Particle Flotation," in *Challenges in Mineral Processing*, ed. by Sastry, K.V.S. and Fuerstenau, M.C., Society Mining Engineers, Inc., Littleton, Colorado, 487 (1989).
21. Yoon, R.H. and Luttrell, G.H., "The Effect of Bubble Size on Fine Particle Flotation," in *Frothing in Flotation (The Jan Leja Volume)*, ed. by Laskowski, J.S., Gordon and Breach Science Publishers, 101 (1989).
22. Yoon, R.H., Adel, G.T. and Luttrell, G.H., "Development of the Microbubble Column Flotation Process," in *Processing and Utilization of High Sulfur Coals II*, ed. by Chugh, Y.P. and Caudle, R.D., Elsevier Science Publishing Company Inc., New York, 533 (1987).
23. Attia, Y.A., "Cleaning and Desulfurization of Coal Suspensions by Selective Flocculation," in *Processing and Utilization of High Sulfur Coals*, ed. by Attia, Y.A., Elsevier Science Publishing Company Inc., New York, 267 (1985).
24. Sresty, C.C, Raja, A. and Somasundaran, P., "Selective Flocculation of Mineral Slimes Using Polymers," in *Recent Advances in Separation Science*, ed. by Li, N.N., Long, R.B., Stern, S.A., and Somasundaran, P., CRC Press, Inc., Boca Raton, Fla., 4, 93 (1978).
25. Baudet, G. and Morio, G., Rinaudo, M., and Nematollahi, H., "Synthesis and Characterization of Selective Flocculants Based on Xanthate Derivatives of Cellulose and Amylose," *Ind. Miner. Mineralurgie*, 1, 19 (1978).
26. Attia, Y.A. and Kitchener, J.A., "Development of Complexing Polymers for the Selective Flocculation of Copper Minerals," *Proc. XI Inter. Miner. Processing Congr.*, Cagliari, Italy, 1233 (1975).
27. Attia, Y.A., "Synthesis of PAMG Chelating Polymers for the Selective Flocculation of Copper Minerals," *Int. J. Miner. Process.*, 4, 191 (1977).
28. Clauss, C.R.E., Appleton, E.A. and Vink, J.J., "Selective Flocculation of Cassiterite in Mixtures with Quartz Using a Modified Polyacrylamide Flocculant," *Int. J. Miner. Process.*, 3, 27 (1976).
29. Lien, H.O. and Morrow, J.G., "Beneficiation of Lean Iron Ores Solely by Selective Flocculation and Desliming," *Can. Min. Metall. (CIM) Bull.*, 71, 109 (1978).
30. Yusa, M., "Mechanisms of Pelleting Flocculation," *Int. J. Miner. Process.*, 4, 293 (1977).
31. Villar, J.W. and Dawe, J.A., "The Tilden Mine - A New Processing Technique for Iron Ore," *Min. Congr. J.*, 61, 40 (1975).
32. Colombo, A.F., "Concentration of Iron Oxides by Selective Flocculation-Flotation," in *Advances in Mineral Processing*, ed. by Somasundaran, P., AIME, Inc., New York, 695 (1986).

33. Read, A.D. and Hollick, C.T., "Selective Flocculation Techniques for Recovery of Fine Particles," *Miner. Sci. Eng.*, 8, 202 (1976).
34. Koh, P.T.L. and Warren, L.J., "Flotation of Floccs of Ultrafine Scheelite," *Trans. IMM*, 86, C94 (1977).
35. Yoon, R.H., Xu, Z., Chen, J. and Chen, W., "Selective Flocculation of Titanomagnetite, Ilmenite and Feldspar Using Sulphonated Polyacrylamide," in *Flocculation in Biotechnology and Separation Systems*, ed. by Attia, Y.A., Elsevier Sci. Publishers, B.V., Amsterdam, 707 (1987).
36. Frommer, D.W. and Colombo, A.F., "Process for Improved Flotation of Iron Ores by Selective Flocculation," *U.S. Patent*, PN 3,393,780, (1966).
37. Colombo, A.F. and Frommer, D.W., "Cationic Flotation of Masabi Range Oxidized Taconite," in *Flotation*, ed. by Fuerstenau, M.C., AIME, Inc., New York, 2, 1285 (1976).
38. Banks, A.F., "Selective Flocculation- Flotation of Slimes from Sylvinitic Ores," in *Fine Particles Processing*, ed. by Somasundaran, P., AIME, Inc., New York, 2, 1104 (1980).
39. Warren, L.J., "Shear Flocculation," *Chem. Tech.*, 11, 180 (1981).
40. Jarrett, R.G. and Warren, L.J., "Shear Flocculation in Mixtures of Scheelite and Garnet," *Proc. Australas. IMM*, 262, 57 (1977).
41. Koh, P.T.L. and Warren, L.J., "Flotation of an Ultrafine Scheelite Ore and the Effect of Shear Flocculation," in *Mineral Processing: Developments in Mineral Processing (Proc. XIII Int. Miner. Processing Congr., Warsaw, Poland)*, ed. by Laskowski, J., Elsevier: Amsterdam; Polish Sci. Publishers, Warsaw, 2, 263 (1981).
42. Grasberg, M., "New Swedish Scheelite Flotation Process Results," *Wld. Min.*, 32, 54 (1979).
43. Warren, L.J., "Flocculation of Stirred Suspensions of Cassiterite, and Tourmaline," *Colloids Surfaces*, 5, 301 (1982).
44. Sadowski, Z., "Discussion of Papers," in *Mineral Processing: Developments in Mineral Processing (Proc. XIII Int. Miner. Processing Congr., Warsaw, Poland)*, ed. by Laskowski, J., Elsevier: Amsterdam; Polish Sci. Publishers, Warsaw, 2, 493 (1981).
45. Sivamohan, R., "Influence of Common Variables on the Shear Flocculation of and Oleate Adsorption/Abstractation by Very Fine Fluorite and Scheelite," in *Production and Processing of Fine Particles*, ed. by Plumpton, A.J., Can. IMM, 337 (1988).
46. Read, A.D. and Hollick, C.T., "Selective Flocculation Techniques for Recovery of Fine Particles," *Miner. Sci. Eng.*, 8, 202 (1976).

47. Rubio, J., "Conditioning Effects of Flotation of Finely Divided Non-sulphide Copper Ore," *Trans. IMM*, 86, C97 (1977).
48. Wojcik, W., "The Enrichment of Fine Particles of Coal by Aggregation, Part II. The Use of the Selective Aggregation Method," *Powder Technol.*, 26, 115 (1980).
49. Chia, Y.H. and Somasundaran, P., "A Theoretical Approach to Flocculation in Carrier Flotation for Beneficiation of Clay," *Colloids Surfaces*, 8, 187 (1983).
50. Fuerstenau, D.W., Li, C., and Hanson, J.S., "Shear Flocculation and Carrier Flotation of Fine Hematite," in *Production and Processing of Fine Particles*, ed. by Plumpton, A.J., Can. IMM, 329 (1988).
51. Cassell, E.A., Matijevic, E., Mangravite, F.J., Buzzell, T.M., and Blabac, S.B., "Removal of Colloidal Pollutants by Microflotation," *AIChE J.*, 17, 1486 (1971).
52. Jenkins, D., Scherfig, J. and Eckhoff, D.W., "Application of Adsorptive Bubble Separation Techniques to Waste Water Treatment," in *Adsorptive Bubble Separation Techniques*, ed. by Lemlich, R., Academic Press, New York, 219 (1972).
53. "Ultraflotation Gets First Commercial Try," *Chem. Eng. News*, 39 (Oct. 16), 52 (1961).
54. Collins, D.N. and Read, A.D., "The Treatment of Slimes," *Miner. Sci. Eng.*, 3, 19 (1971).
55. Waksmundzki, A., Neczaj-Bruzewica J. and Planik, M., "Mechanism of Carryover of Gangue Slimes During Flotation of Sulfur Ore," *Trans. IMM*, 80, C249 (1971).
56. Greene, E.W. and Duke, J.B., "Selective Froth Flotation of Ultrafine Mineral or Slimes," *Trans. SME/AIME*, 223, 389 (1962).
57. Capes, C.E., "Liquid Phase Agglomeration: Process Opportunities for Economic and Environmental Challenges," in *Challenges in Mineral Processing*, ed. by Sastry, K.V.S. and Fuerstenau, M.C., Society of Mining Engineers, Inc., Littleton, Colorado, 237 (1989).
58. Venkatadri, R., Markuszewski, R. and Wheelock, T.D., "Oil Agglomeration of Weakly Hydrophobic Coals and Coal/Pyrite Mixtures," *Energy & Fuels*, 2, 145 (1988).
59. Kawashima, Y. et al., "Spherical Agglomeration of Calcium Carbonate Dispersed in Aqueous Medium Containing Sodium Oleate," *Powder Technology*, 46, 61 (1986).
60. Smith, H.M. and Puddington, I.E., "Spherical Agglomeration of Barium Sulfate," *Can. J. Chem.*, 38, 1911 (1960).

61. McLead, W.D., King, D.E.C. and Morgan, W.A., "Concentration of Tin Ores by Selective Oil Agglomeration," *Paper Presented at Annual Meeting of AIME*, New York, (1966).
62. Capes, C.E., "Basic Research in Particle Technology and Some Novel Applications," *Can. J. Chem. Eng.*, 54, 3 (1976).
63. Nicol, S.K. and Brown, A., "An Experimental Appraisal of the beneficiation of Fine Coal by Selective Agglomeration," *Proc. Australas. IMM*, 262, 49 (1977).
64. Capes, C.E. and Jonasson, K.A., "Application of Oil-Water Wetting of Coals in Beneficiation," in *Surfactant Sci. Ser. (Interfacial Phenome. Coal Technol.)*, 32, 115 (1989).
65. Meadus, F.W., Paillard, G., Sirianni, A.F., and Puddington, I.E., "Fractionation of Coking Coals by Spherical Agglomeration Methods," *Can. Min. Metall. (CIM) Bull.*, 61, 736 (1968).
66. Capes, C.E., Coleman, R.D. and Thayer, W.L., "Treatment of Crude Petroleum/Water Emulsions by Agglomeration Methods Using Fine Coal," *Coal Preparation*, 1, 131 (1985)
67. Zuiderweg, F.J. and van Lookeren N. Compagne, "Pelletizing of Soot in Waste Water of Oil Gassification Plants - The Shell Pelletizing Separator," *Chem. Eng. (London)*, 220, CE223 (1968).
68. Pugh, R.J. and Kitchener, J.A., "Theory of Selective Coagulation in Mixed Colloidal Suspensions," *J. Colloid Interface Sci.*, 35, 656 (1971).
69. Usui, S. and Hachisu, S., "Interaction of Electrical Double Layers and Colloid Stability," in *Surfactant Sci. Ser. (Electrical Phenomena at Interfaces)*, 15, 47 (1984).
70. Sonntag, H. and Strenge, K., *Coagulation Kinetics and Structure Formation*, Plenum Press, New York, (1987).
71. Lawler, D.F., "Removing Particles in Water and Waste Water," *Environ. Sci. Technol.*, 20, 856 (1986).
72. Hall, E.S. and Packham, R.F., "Coagulation of Organic Color with Hydrolyzing Coagulants," *J. Water Works Assoc.*, 57, 1149 (1965).
73. Maynard, R.N., Millman, N. and Iannicelli, J., "Removing Titanium Dioxide Impurities from Kaolin," *Clays Clay Miner.*, 17, 59 (1969).
74. Pugh, R.J., "Selective Coagulation in Quartz-Hematite and Quartz-Rutile Suspensions," *Colloid Polym. Sci.*, 252, 400 (1974).
75. Pugh, R.J. and Kitchener, J.A., "Experimental Confirmation of Selective Coagulation in Mixed Colloidal Suspensions," *J. Colloid Interface Sci.*, 38, 656 (1972).

76. Honaker, R.Q., *Development of the Selective Shear Coagulation Process for Ultrafine Coal Cleaning*, M.S. Thesis, Department of Mining and Minerals Engineering, Virginia Polytechnic Institute and State University, (1988).

CHAPTER 2 INTERPARTICLE FORCES

2.1 Introduction

In Chapter 1, it has been discussed that selective hydrophobic coagulation of fine coal particles may become a promising technology in coal cleaning practice. Practical applications of coagulation/dispersion have also been found in many other fields, such as environmental engineering, chemical engineering, biochemical engineering, material engineering, and medical engineering, and in the food, paint and mineral industries. In some circumstances, such as in the paint, ceramics, and food industries, high stability of colloidal suspensions is required to ensure that the suspensions function properly. In others, such as in environmental engineering, the destabilization or coagulation is beneficial to the removal of colloidal particles for the purpose of water purification. In the mineral industry, the situation becomes more complicated. For the purpose of separating valuables from gangue minerals, the heterocoagulation of these components has to be avoided. Therefore, suspension conditions favorable for complete dispersion should be created to obtain an effective separation. For the purpose of effectively recovering fine particle valuables, however, particle enlargement by coagulation is desirable. As a result, selective coagulation/dispersion becomes crucial in the mineral industry. Due to

its importance in such diverse fields, the stability of colloidal suspensions has been studied extensively.

It is well known that as the particle size decreases to the colloidal size range, the surface forces between two particles dispersed in a medium become increasingly significant as opposed to the inertial force. As a result, the dispersion or coagulation of colloidal particles is mainly determined by the relative magnitude of various interparticle surface forces. At present, four distinct forces between colloidal particles in liquid have been recognized as playing an important role in controlling the dispersion/coagulation of colloidal particles (1-3). They are the attractive van der Waals and repulsive electrostatic "double-layer" forces, repulsive or attractive solvation forces, and repulsive steric forces between polymer-covered surfaces. The natures of these four forces are fairly well understood now. Since the first three of these forces are present in most colloidal suspensions, each of them will be discussed in detail in this chapter.

2.2 Dispersion Forces

2.2.1 Dispersion Forces between Atoms or Molecules

The existence of some long range forces between particles of colloidal dimensions can be inferred from observed coagulation phenomena. These long range forces are of the same nature as the attractive forces between neutral atoms. The existence of intermolecular forces was initially suggested by Clairault in 1743 (2). In an attempt to explain the observed capillary rising phenomenon of liquids in glass tubes, it has been suggested that the attraction between liquid and glass molecules is different from that between the molecules of each phase.

However, one of the most successful applications of the concept of intermolecular forces may be attributed to van der Waals. In order to explain the observed deviation of real gas behavior from the ideal gas law, van der Waals (4) considered the effect of intermolecular forces and arrived, in 1873, at his famous thermal equation of state for the nonideal behavior of real gases as given by Equation [2.1].

$$\left(P + \frac{a}{V^2}\right)(V - b) = RT , \quad [2.1]$$

where P represents pressure, V represents volume, R is the gas constant, T is absolute temperature, and a and b are two constants from which initial information about intermolecular forces can be obtained (5). In spite of the qualitative character of the argument used by van der Waals in his derivation, the great success of his equation of state in explaining experimental data on the properties of gases spurred thinking on the origin of molecular forces.

Collectively called van der Waals forces, these intermolecular forces consist of three components, including the induction (or Debye) force, the dipole orientation (or Keesom) force, and the dispersion (or London) force (2). Debye (6) proposed that the polarizability of molecules is the cause of intermolecular forces. He showed that a molecule with a permanent dipole moment polarizes a nearby neutral molecule. The interaction between the electric fields of these two different dipoles gives rise to an interaction force. The energy due to this interaction can be calculated using Equation [2.2] as derived by Debye in 1920 (6).

$$U_{Debye} = - \frac{(u_1^2 \alpha_2 + u_2^2 \alpha_1)}{d^6} , \quad [2.2]$$

where u_1 and u_2 are the permanent dipole moments of two interacting molecules, α_1 and α_2 are their polarizabilities, and d is the intermolecular distance.

In 1921, Keesom (7-8) suggested that two molecules with permanent dipole moments orient themselves in such a way as to attract each other. The interaction energy due to this orientation effect has been given by Keesom as

$$U_{\text{Keesom}} = -\frac{2u_1^2u_2^2}{3kTd^6} \quad kT > u_1u_2/d^3 \quad [2.3]$$

and
$$U_{\text{Keesom}} = -\frac{2u_1u_2}{d^3} \quad kT < u_1u_2/d^3, \quad [2.4]$$

where k is Boltzmann's constant. The second equation given above has been derived for the limiting case at low temperatures, in which a straight alignment of two dipoles has been assumed. The Debye theory and Keesom theory in combination have been used successfully to explain the interactions between polar molecules in a phenomenological way.

However, for neutral gas molecules such as H_2 , N_2 and CH_4 which possess no permanent dipole moments, the intermolecular forces deduced from van der Waals thermal equation are far greater than the force accounted for by the induction and orientation effects. The existence of attraction between a pair of neutral molecules, as shown by Wang (9) in 1927, is direct evidence for the third component of intermolecular forces. Forces of this type are referred to as dispersion forces since they are closely related to the optical dispersion of light in the visible and UV region of the spectrum. Of the three components of intermolecular forces, the dispersion forces make the most important contribution to the van der Waals force since they are always present and operate over a relatively long range, which makes them important in a host of phenomena, including coagulation, adhesion, polymer conformation, and physical adsorption.

The dispersion forces have been considered as a result of the charge fluctuations associated with the motion of electrons in their "orbitals". These charge fluctuations result in a time-dependent dipole moment. On one hand, the phase difference in the fluctuating dipoles leads to a mutual interaction. On the other hand, the time-dependent dipole generates an instantaneous electric field which polarizes any nearby neutral atom or molecule, inducing a dipole moment in it. As a result, a mutual instantaneous interaction is also generated. The time average of these interactions gives rise to a finite interaction force.

It is not difficult to realize that the dispersion forces are quantum mechanical in nature. Therefore, even though the dispersion forces have been recognized since 1873, theoretical treatment of this type of forces did not appear until 1927 when quantum mechanics was experiencing rapid development. An early theoretical analysis of dispersion forces was made using perturbation theory to solve the Schrödinger equation for two hydrogen atoms at a large separation distance (2). In this early treatment, the interaction between the electrons and protons of the two atoms was included and the overall interaction energy was found to be inversely proportional to the sixth power of interatomic distance.

Dispersion forces are sometimes referred to as London forces after London (10-11) who contributed much to the further understanding of this type of forces. Using rigorous quantum mechanical treatment, London found that the dispersion interaction energy between two atoms or molecules is given by (11-12):

$$U_{London} = -\frac{C}{d^6} , \quad [2.5]$$

where C is known as the London constant. The London constant can be expressed by Equation [2.6] for interactions between two dissimilar atoms or molecules in terms of the electronic polarizability of interacting atoms or molecules.

$$C_{12} = \frac{3}{2} \frac{\alpha_1 \alpha_2}{(4\pi\epsilon_0)^2} \frac{h\nu_1\nu_2}{\nu_1 + \nu_2} , \quad [2.6]$$

where ν represents the frequency of radiation associated with the ionization of atoms or molecules, with the subscript identifying the individual interacting atoms or molecules. ϵ_0 and h in Equation [2.6] are the permittivity of vacuum and the Planck constant, respectively. The London constant for two similar atoms or molecules, C_{11} , can be readily obtained from Equation [2.6] in which α_2 and ν_2 are set equal to α_1 and ν_1 , respectively.

It is interesting to note that the form of Equation [2.5], as given by London for calculating dispersion energy, has also been derived from a simplified electrostatic treatment by considering the interaction between two Bohr atoms (2, 5). This finding suggests that while the dispersion forces are quantum mechanical, the ensuing interaction is still electrostatic, a sort of quantum mechanical polarization force. From the nature of dispersion forces, it is not difficult to see that the interaction between molecules consisting of atoms of larger atomic number gives rise to larger dispersion forces. This is because, in general, the larger the atom, the further the outer shell electrons are away from the nucleus and, consequently, the greater the polarizability.

The calculation of dispersion interaction energy with London's theory may not be valid at either very small interatomic distances due to the overlap of their wave functions or at very large interatomic distances because of the electromagnetic retardation. The subsequent analysis on the subject of dispersion interaction has, therefore, been carried out by considering the retardation effect on the interaction energy when the

atom-atom separation exceeds the characteristic wavelength (λ) of radiation emitted due to the dipolar transitions (13).

It is evident that when two atoms are separated by an appreciable distance, the time taken for the electrostatic field at the first atom to reach the second and then return is comparable to the fluctuating period itself. As a result, the phase shift of the fluctuating dipoles will no longer differ from 180° . Consequently, the dispersion forces will decrease more rapidly than predicted by Equation [2.5]. In the limiting case of $d > \lambda$, the dispersion interaction energy has been found (13), by applying the fourth order perturbation theory to the interaction between atom and electric field, to be inversely proportional to the seventh instead of the sixth power of the interatomic distance. By extending London's theory, the retarded dispersion interaction energy has been obtained as:

$$U_{12} = -\frac{K_{12}}{d^7} \quad d > \max\left(\frac{\lambda_i}{2\pi}\right), \quad [2.7]$$

where λ_i 's are the characteristic absorption wavelengths of the atoms or molecules, and K_{12} is a constant called *retarded London constant*. K_{12} is given by:

$$K_{12} = \frac{23}{4\pi} hc\alpha_1\alpha_2, \quad [2.8]$$

in which c is the speed of light. Similarly, K_{11} can be calculated using Equation [2.8] by setting α_2 equal to α_1 .

In order to calculate the dispersion interaction energy in the presence of a third medium between two interacting atoms or molecules, a general microscopic theory of electric dipole dispersion forces, called the *susceptibility theory*, has been developed recently (14-16). According to this theory, the dispersion interaction energy is given by:

$$U = -\frac{3h}{\pi d^6} \int_0^\infty \frac{\alpha_1^*(i\xi)\alpha_2^*(i\xi)d\xi}{\epsilon_3^2(i\xi)} \quad \lambda > d \quad [2.9]$$

and
$$U = -\frac{23hc}{4\pi d^7} \frac{\alpha_1^*(0)\alpha_2^*(0)}{\epsilon_3^{5/2}(0)} \quad \lambda < d, \quad [2.10]$$

where $\epsilon_3(i\xi)$ is the dielectric constant of medium 3, $\alpha_1^*(i\xi)$ and $\alpha_2^*(i\xi)$ are the polarizabilities of atoms or molecules 1 and 2 in medium 3 as functions of imaginary frequency, $i\xi$, $\epsilon_3(0)$ is the static dielectric constant of medium 3, and $\alpha_1^*(0)$ and $\alpha_2^*(0)$ are the static polarizabilities of atoms or molecules 1 and 2 in medium 3, respectively. The polarizability in this case is often referred to as the excess or effective polarizability. Since the excess polarizability of an atom or a molecule depends, in a complicated way, on its interaction with the surrounding medium 3, theoretical analysis becomes rather complicated. The theories discussed so far are capable of explaining the origin of intermolecular forces and calculating the interaction energy between free atoms or molecules.

2.2.2 Dispersion Forces between Two Macroscopic Objects I. Hamaker's Approach

It seems natural to infer that the attractive forces between neutral atoms or molecules give rise to analogous forces between any two macroscopic bodies whose surfaces are separated by a small distance. The credit for the recognition that such a force would emerge from summing the London-van der Waals forces between pairs of atoms of interacting particles appears to be due to Kallmann and Willstratter (17) and to Bradley (18). Subsequently, the dispersion forces acting between colloidal objects were investigated theoretically for objects of different geometrical shapes by de Boer in 1936 (19) and by Hamaker in 1937 (20), among others.

Based on the microscopic treatment, Hamaker has considered spherical objects by assuming the pairwise additivity of interatomic dispersion energy, and demonstrated that although the range of atomic forces is of the order of atomic dimension, the sum

of the dispersion energies over the entire macroscopic objects yields an interaction existing over the range of the order of macroscopic dimension. It is a common practice to use Hamaker constant for evaluating the dispersion interaction between two macroscopic particles as given by (2):

$$A_{12} = \pi^2 N_1 N_2 C_{12} , \quad [2.11]$$

where N_1 and N_2 are the number of polarizable atoms per unit volume of objects 1 and 2, respectively, and the London constant, C_{12} , is as given by Equation [2.6]. An expression for calculating the combined Hamaker constant of two macroscopic particles interacting in the presence of a third medium has been derived using Hamaker's summation procedures as given (20) by:

$$A_{132} = A_{12} + A_{33} - A_{13} - A_{23} . \quad [2.12]$$

The dispersion interaction energy between two spherical particles of radii a_1 and a_2 is, then, given by (20-21):

$$\begin{aligned} V_A &= -\frac{A_{132}}{6} \left[\frac{2a_1 a_2}{Y} + \frac{2a_1 a_2}{Y + 4a_1 a_2} + \ln \frac{Y}{Y + 4a_1 a_2} \right] \\ &= -\frac{R}{6H} A_{132} , \end{aligned} \quad [2.13]$$

where H is the face-to-face distance between two interacting particles and Y is given by $H^2 + 2a_1 H + 2a_2 H$. The quantity R in Equation [2.13] refers to the reduced particle size as defined by:

$$R = \frac{a_1 a_2}{a_1 + a_2} . \quad [2.14]$$

As an approximation, the second equal sign in Equation [2.13] is valid for a small separation distance (H) while the first one covers a wide range of separations.

With a similar approach, an expression for calculating the dispersion component of surface free energy has been derived as a result of summing up the pair potentials of all the surface volume elements with all of the volume elements below the surface (10, 19). By using the potential as given by Equations [2.5] and [2.6] in combination for the interaction between elements, the above pair summation procedures yield:

$$\gamma_1^d = -\frac{\pi N_1^2 \alpha_1^2 I_1}{8r_{11}^2} , \quad [2.15]$$

in which r_{11} is the intermolecular distance and I_1 is the ionization potential which equals $h\nu_1$. Combining Equations [2.6], [2.11] and [2.15] to eliminate the polarizability, α_1 , and the ionization potential, I_1 , results in (22):

$$A_{11} = 6\pi r_{11}^2 \gamma_1^d . \quad [2.16]$$

Since the values of the polarizability or ionization potential are difficult to obtain experimentally to calculate the Hamaker constant using Equations [2.6] and [2.11], Equation [2.16] provides a convenient and useful means for calculating the Hamaker constant of single material in a vacuum using the value of γ_1^d which can be readily obtained from some simple procedures such as contact angle measurement or equilibrium spreading pressure measurement of the adsorbed film (22).

According to the Berthelot's principle (23) that the interaction constant between two particles of different materials equals the geometric mean of the interaction constants of individual materials, the London constant, C_{12} , between two different types of atoms or molecules can be written as:

$$C_{12} = \sqrt{C_{11}C_{22}} \quad . \quad [2.17]$$

By substituting Equation [2.17] into Equation [2.11], one readily obtains a common geometric mean law, i.e., Equation [2.18], for calculating the value of A_{ij} from the known values of A_{ii} and A_{jj} :

$$A_{ij} = \sqrt{A_{ii}A_{jj}} \quad . \quad [2.18]$$

Vold (24) has shown that the above geometric mean law holds fairly well as long as the ionization potentials of these two materials do not differ significantly, i.e., $v_i = v_j$. This argument can be readily illustrated by substituting Equation [2.6] for the cases of C_{ii} and C_{jj} into Equation [2.17] and comparing the resultant equation with Equation [2.6] for the case of C_{ij} . Substituting Equation [2.18] into Equation [2.12] yields Equation [2.19] for calculating the combined Hamaker constant of a system from the Hamaker constants of individual components in a vacuum:

$$A_{132} = (\sqrt{A_{111}} - \sqrt{A_{333}})(\sqrt{A_{222}} - \sqrt{A_{333}}) \quad . \quad [2.19]$$

It can be seen from the previous descriptions that like most simple theories, the Hamaker approach to dispersion interaction between two macroscopic objects has the virtue of ease of comprehension. As an approximation, it is customary to use Equation [2.18] for the calculation of A_{ij} and Equation [2.19] for the calculation of A_{132} or A_{131} from the known values of A_{ii} which can be obtained from Equation [2.16]. One of the successful applications of the Hamaker approach has been demonstrated by the calculation of the theoretical values of surface tensions of n-alkanes (25). Based on the idea that the work of separating two unit areas of material from contact to infinity equals twice the

surface tension, γ , Padday and Uffindell (25) have calculated the values of surface tension using the following relation:

$$W_{11} = 2\gamma_{11} = \frac{A_{11}}{12\pi r_{11}^2} \quad , \quad [2.20]$$

where r_{11} is the interatomic distance in the bulk. The calculated results have shown a remarkable agreement with experimentally measured values of surface tension, which suggests that the intermolecular forces of n-alkane are mainly of dispersion type. By using the same equation, Coakley and Tabor (26) have calculated the surface free energy of mica deposited with a multilayers of hydrocarbon film. The surface tension calculated as such is in a reasonable agreement with the experimentally measured surface tension of a hydrocarbon liquid. Clearly, the calculated value of surface tension depends critically on the assumed value of r_{ii} .

Due to the simplicity of this approach, the work of Hamaker has been used in subsequent estimates of the dispersion component of interparticle interactions which are fundamental in colloid science. However, it should be noted that the assumptions of simple pairwise additivity made in Hamaker's approach ignores the influence of neighboring atoms or molecules on the interaction between any pair of atoms.

It is obvious that the close packing of the atoms in a condensed object materially changes the properties of their electronic envelopes and, hence, their polarizabilities. It is also conceivable, by considering a simple three-atom system, that the instantaneous field of atom 1 will polarize atoms 2 and 3 simultaneously, and the induced dipole field of atom 3 will, in turn, act on atom 2. As a result, the field from atom 1 will also reach atom 2 by the reflection of atom 3 besides the direct interaction between the electric fields of atoms 1 and 2, which gives rise to an extra force term. The existence of multiple reflections of electric fields suggests that using the straightforward additivity approach

may lead to significant uncertainties in the values of dispersion forces between macroscopic objects.

Also ignored in Hamaker's approach is the retardation effect of electromagnetic wave propagation on the interaction energy. This may introduce substantial errors when calculating dispersion interaction energy using Equation [2.13] for a large inter-particle separation. In an attempt to take the retardation effect into account, the summation procedures become extremely difficult and the resultant Hamaker constant has been found to be a function of separation distance.

Nevertheless, as an approximation, Casimir and Polder (23) have adopted Hamaker's summation procedures in which Equation [2.7] has been used as an interelement potential to derive a simple expression for calculating the retarded dispersion energy as given by:

$$V_A = -\frac{2}{3} \frac{\pi B_{132}}{H^2} R , \quad [2.21]$$

where B_{132} is a constant termed the retarded Hamaker constant. B_{132} can theoretically be calculated from known values of B_{11} , B_{22} and B_{33} using similar procedures to that used in obtaining A_{132} from the known values of A_{11} , A_{22} and A_{33} . The constant B_{ij} is related to the constant K_{ij} by Equation [2.22]:

$$B_{ij} = \frac{\pi}{10} N_i N_j K_{ij} . \quad [2.22]$$

In order to extend Hamaker's approach, i.e., Equation [2.13], to the retarded region, Schenkel and Kitchener (27-28) have derived two simple expressions by applying the best fit approximation to their numerical integration, which are given by:

$$f_p = \frac{1}{1 + 1.77p} \quad \text{if } 0 < p < 0.57 \quad [2.23]$$

$$\text{and } f_p = \frac{2.45}{5p} - \frac{2.17}{15p^2} + \frac{0.59}{35p^3} \quad \text{if } 0.5 < p < \infty, \quad [2.24]$$

where $p = \pi H/\lambda$. By incorporating Equations [2.23] and [2.24] into Equation [2.13], dispersion interaction energy can be evaluated over a wide range of separation, including nonretarded and retarded regions. It is readily seen from Equation [2.24] that $f_p \propto H^{-1}$ for large values of H , which results in $V_A \propto H^{-2}$, a similar relation to that implied in Equation [2.21].

2.2.3 Dispersion Forces between Two Macroscopic Objects II. Lifshitz's Approach

In contrast to the microscopic approach, Lifshitz (29) has constructed a more accurate approach through a purely macroscopic framework. The problem associated with the use of direct additivity has been completely avoided in this macroscopic treatment of dispersion forces. Unlike the microscopic approach in which dispersion forces have been expressed in terms of microscopic properties of interacting objects, such as their polarizabilities, the atomic structure has been ignored and the interacting objects have been treated as continuous media in the macroscopic approach. The dispersion forces in this approach have been derived in terms of the macroscopic properties of interacting objects, such as their dielectric constants or refractive indices.

The interaction between macroscopic objects has been considered as the result of the fluctuational electromagnetic field in Lifshitz theory. It has been noted that this field is always present within any medium due to thermodynamic fluctuation, and it also extends outside the medium. In order to accommodate the temporal fluctuations of the fields, Lifshitz has adopted the fluctuation theory developed by Rytov (30). The electromagnetic fields have been calculated on the basis of the exact Maxwell's

equations. Therefore, the effects of retardation, caused by a finite velocity of propagation of electromagnetic fields, have been taken into account naturally in Lifshitz's approach. The Lifshitz theory, thus developed, has led to the Lifshitz-van der Waals constant $h\bar{\omega}$ which depends on the material only and is independent of the geometry of the interacting objects. Since the geometrical terms in both theories have been found to be identical, Hamaker's microscopic theory has been related to Lifshitz macroscopic theory by the relation of (31-33):

$$A_{132} = \frac{3h\bar{\omega}_{132}}{8\pi^2} . \quad [2.25]$$

Although the first general macroscopic theory of dispersion forces was derived by Lifshitz for two half spaces separated by a distance d in a vacuum, the theory has been extended to the interactions between two half spaces separated by a third medium using quantum field theory (34). According to Lifshitz (29) and Dzyaloshinskii et al. (34), the Lifshitz-van der Waals constant for two objects of materials 1 and 2 embedded in medium 3 is given by:

$$h\bar{\omega}_{132} = h \int_0^\infty \frac{\epsilon_1(i\xi) - \epsilon_3(i\xi)}{\epsilon_1(i\xi) + \epsilon_3(i\xi)} \frac{\epsilon_2(i\xi) - \epsilon_3(i\xi)}{\epsilon_2(i\xi) + \epsilon_3(i\xi)} d\xi , \quad [2.26]$$

where $\epsilon_j(i\xi)$ is the dielectric constant of material j along the imaginary frequency axis, $i\xi$. Recently, a similar expression has been derived through a different line of thinking by Kampen et al. (35), indicating the universality of the theory. The quantity of $\epsilon_j(i\xi)$ in Equation [2.26] can be determined from the Kramers-Kronig relation,

$$\epsilon_j(i\xi) = 1 + \frac{2}{\pi} \int_0^\infty \frac{\omega \epsilon''(\omega)}{\omega^2 + \xi^2} d\omega , \quad [2.27]$$

where $\varepsilon''(\omega)$ is the imaginary part of the complex dielectric constant. The value of $\varepsilon''(\omega)$ is always positive and determines the dissipation of the energy of the electromagnetic wave propagating in a body. It can be seen that the function $\varepsilon_j(i\xi)$ is a real quantity, monotonically decreasing from the value of ε_0 at $\xi = 0$ to 1 at $\xi = \infty$. The integration of Equation [2.26] can be carried out numerically with known values of $\varepsilon''(\omega)$ as obtained from the analysis of reflection measurements over a wide range of frequencies, from microwave through infrared to ultraviolet region. In principle, this approach gives a more accurate result in calculating the constant of dispersion interaction between two macroscopic objects.

The Lifshitz-van der Waals constant of two macroscopic objects of identical material imbedded in a medium can be readily obtained by replacing $\varepsilon_2(i\xi)$ with $\varepsilon_1(i\xi)$ in Equation [2.26]. Equation [2.26] holds for two objects interacting in a vacuum by replacing $\varepsilon_3(i\xi)$ with 1. According to Langbein (36), Equation [2.26] is independent of geometry and therefore is valid for objects of other shapes. It is obvious, however, that the application of the Lifshitz theory is restricted to those materials for which optical data are available. Since direct use of Equations [2.26] and [2.27] in combination is cumbersome and the reliable data are sparse, among other practical limitations, it is important to develop a relatively simple approach for practical purposes.

A commonly used procedure, which leads to a fairly accurate result with significantly increased simplicity, has been given by Gregory (37). In his approach, only the electronic transitions in the ultraviolet region have been considered. To relate the molar refraction of a material to its polarizability at angular frequency, ω , Lorentz-Lorentz equation has been used in the form of:

$$\frac{n^2 - 1}{n^2 + 2} \frac{M}{\rho} = \frac{4\pi}{3} N_0 \alpha(\omega) , \quad [2.28]$$

in which n is the refractive index of the substance, M is the molecular weight, ρ is the density, and N_0 is Avogadro's number. It has been shown that the quantity $\alpha(\omega)$ in Equation [2.28], which is a measure of overall oscillator strength at frequency ω , is given by:

$$\alpha(\omega) = \frac{e^2}{4\pi^2 m} \sum_j \frac{f_j}{\omega_j^2 - \omega^2} \quad , \quad [2.29]$$

where m is the mass of the electron and f_j is oscillator strength at frequency ω_j . It is obvious that Equation [2.29] is not valid at frequencies close to strong adsorption bands where an imaginary damping term has to be introduced and, hence, the refractive index takes a complex value. However, the damping terms are usually negligible on the imaginary axis and Equation [2.29] gives a good approximation for practical purposes. Substituting Equation [2.29] into Equation [2.28] results in:

$$\frac{n^2 - 1}{n^2 + 2} \frac{M}{\rho} = \frac{e^2 N_0}{3\pi m} \frac{s}{\omega_v^2 - \omega^2} \quad , \quad [2.30]$$

where ω_v is a characteristic frequency. The quantity s in Equation [2.30] has been regarded as the effective number of dispersion electrons, which equals $\sum f_j$, as can be deduced from Equations [2.29] and [2.30]. It has been implicitly assumed in the derivation of Equation [2.30] that the variation of the refractive index can be represented by an effective dispersion equation with only one dominating term being retained. It is convenient to rewrite Equation [2.30] as:

$$\frac{n^2 + 2}{n^2 - 1} = \frac{M}{\rho} \frac{3\pi m}{e^2 N_0} \frac{\omega_v^2}{s} - \frac{M}{\rho} \frac{3\pi m}{e^2 N_0} \frac{\omega^2}{s} \quad , \quad [2.31]$$

which suggests that a plot of $(n^2 + 2)/(n^2 - 1)$ vs ω^2 gives a straight line for a range of frequencies. The values of s and ω_v can, thus, be calculated from the slope S and intercept I using Equations [2.32] and [2.33], respectively:

$$s = -\frac{M}{\rho} \frac{3\pi m}{e^2 N_0} \frac{1}{S} \quad [2.32]$$

and $\omega_v = \sqrt{-I/S}$. [2.33]

Also obtained from the intercept is the limiting dielectric constant ϵ_0 of the material as given by:

$$\epsilon_0 = n_0^2 = \frac{I + 2}{I - 1} . \quad [2.34]$$

From these constants, the Hamaker constant of single material, A_{jj} , can be readily calculated using Equation [2.35] as derived by Gregory (37) and by Tabor and Winterton (38):

$$A_{jj} = \frac{27}{64} h\omega_v \left(\frac{\epsilon_0 - 1}{\epsilon_0 + 2} \right)^2 , \quad [2.35]$$

As an example, the values of Hamaker constants for liquid water and solid silica have been calculated using Equation [2.35] and the results are given in Table 2.1. The property constants of material that appeared in Equation [2.35] have been obtained from the published optical data (37, 39) using the procedures described previously. Also given in Table 2.1 are the values of Hamaker constant calculated using Equation [2.16].

It can be seen from Table 2.1 that the values obtained using these two different methods are in a remarkable agreement, indicating that Equation [2.16] gives a reasonable approximation for values of the Hamaker constant, A_{ii} , for a wide range of materi-

als. Since the use of Equation [2.16] only requires the value of dispersion component of surface free energy of materials which can be readily obtained from simple contact angle measurements, it is convenient to use this method for practical purposes. Due to its simplicity, this method has been widely used in practice (5, 22, 40-43).

Table 2.1. Hamaker Constant of Water and Fused Silica Calculated Using Eqs. [2.30] and [2.15]

Material	ω_v	n_0	γ^d	$A_{ii} (\times 10^{-20} J)$	
	($\times 10^{15} s^{-1}$)		(erg/cm^2)	Eq. [2.16]	Eq. [2.13]
H_2O	3.35	1.323	22	3.75	3.17
Fused Silica	3.69	1.65	76	13.8	10.9

2.2.4 An Improved Approximation for A_{132} and A_{131}

It has been shown that the combined Hamaker constant, A_{ij} , can be readily approximated using Equation [2.18] from known values of Hamaker constant of single materials. By comparing the calculated values of A_{ij} using Equation [2.26] from spectral data with that calculated using Equation [2.18], in which A_{ii} has been obtained using Equation [2.26] for a number of compounds, Bargeman et al. (44) have found that Equation [2.18] is valid with an accuracy of 99%, in conformance with the exact solution as given by Equation [2.26]. If the same combined law as given by Equation [2.17] is applied to the calculation of A_{132} or A_{131} using Equation [2.19], the calculated values have been found to differ substantially from that calculated using Equation [2.26] from the

same set of spectral data (33). Therefore, it becomes necessary to develop an improved method for estimating the value of A_{132} or A_{131} from known values of A_{11} , A_{22} and A_{33} while preserving the simplicity of approach.

An approximation has been proposed by Krup (44) for the function, $\varepsilon_j(i\xi)$, as given by:

$$\varepsilon_j(i\xi) = \frac{1 + c_j \exp(-b_j\xi)}{1 - c_j \exp(-b_j\xi)} \quad , \quad [2.36]$$

where c_j and b_j are adjustable parameters. Using Krup's approximation in Equation [2.26], Bargeman et al. (33) have derived two expressions as an approximation for calculating the values of A_{131} and A_{132} , respectively, from the known values of A_{11} , A_{22} and A_{33} . The arguments involved with a step-by-step derivation are given as follows.

By inserting Equation [2.36] into Equation [2.25], in which $h\bar{\omega}_{132}$ is replaced by Equation [2.26], for two macroscopic objects of the same material interacting through a vacuum, one readily obtains:

$$\begin{aligned} A_{11} &= \frac{3h}{8\pi^2} \int_0^\infty c_1^2 \exp(-2b_1\xi) d\xi \\ &= \frac{3h}{8\pi^2} \left(-\frac{c_1^2}{2b_1} \right) \exp(-2b_1\xi) \Big|_0^\infty = \frac{3hc_1^2}{16\pi^2 b_1} . \end{aligned} \quad [2.37]$$

Similarly, inserting Equation [2.36] into Equation [2.25] for the interaction of two macroscopic objects of different materials in a vacuum yields:

$$\begin{aligned}
A_{12} &= \frac{3h}{8\pi^2} \int_0^\infty c_1 \exp(-b_1\xi) c_2 \exp(-b_2\xi) d\xi \\
&= \frac{3h}{8\pi^2} \left(-\frac{c_1 c_2}{b_1 + b_2} \right) \exp[-(b_1 + b_2)\xi] \Big|_0^\infty = \frac{3hc_1 c_2}{8\pi^2(b_1 + b_2)} .
\end{aligned}
\tag{2.38}$$

It has been shown that the value of A_{12} as given by the geometric mean law of Equation [2.18] retains an accuracy above 99% as an approximation for the exact value as given by Equation [2.25]. Therefore, as an approximation, one can substitute Equation [2.37] for materials 1 and 2, respectively, into Equation [2.18] to find A_{12} as given by:

$$A_{12} = \sqrt{\left(\frac{3hc_1^2}{16\pi^2 b_1}\right)\left(\frac{3hc_2^2}{16\pi^2 b_2}\right)} = \frac{3hc_1 c_2}{16\pi^2} \sqrt{\frac{1}{b_1 b_2}} .
\tag{2.39}$$

By comparing Equation [2.38] with Equation [2.39], it is readily found that

$$b_1 + b_2 = 2\sqrt{b_1 b_2} .
\tag{2.40}$$

Equation [2.40] indicates that in general, the b_i value in Equation [2.36] can be assumed, as an approximation, to be the same for all the materials. The numerical value of b_i as given by Derjaguin et al. (45) for a number of materials has shown the validity of this assumption. With this assumption, the c_i value in Equation [2.36] can be expressed in terms of its Hamaker constant, A_{11} , and c_1^R and A_{11}^R of a reference material as:

$$c_1 = c_1^R \sqrt{\frac{A_{11}}{A_{11}^R}} ,
\tag{2.41}$$

which has been obtained from Equation [2.37] using the conditions given by Equation [2.40].

On the other hand, one can obtain, by inserting Equation [2.36] into Equation [2.25] in which $h\bar{\omega}_{132}$ is expressed by Equation [2.26] for the interaction of two macroscopic objects of different materials embedded in medium 3:

$$\begin{aligned}
 A_{132} &= \frac{3h}{8\pi^2} \int_0^\infty \frac{(c_1 - c_3)(c_2 - c_3) \exp(-2b\xi)}{[1 - c_1c_3 \exp(-2b\xi)][1 - c_2c_3 \exp(-2b\xi)]} d\xi \\
 &= \frac{3h}{8\pi^2} \frac{(c_1 - c_3)(c_2 - c_3)}{c_1c_3 - c_2c_3} \frac{1}{2b} \ln \frac{\exp(2b\xi) - c_1c_3}{\exp(2b\xi) - c_2c_3} \Big|_0^\infty \\
 &= \frac{3h}{16\pi^2b} \frac{(c_1 - c_3)(c_2 - c_3)}{c_1c_3 - c_2c_3} \ln \frac{1 - c_1c_3}{1 - c_2c_3},
 \end{aligned} \tag{2.42}$$

where b is a constant implicitly defined by Equation [2.36]. By inserting c_i , as implicitly expressed in Equation [2.37], into Equation [2.42], one can readily obtain:

$$A_{132} = \frac{(\sqrt{A_{11}} - \sqrt{A_{33}})(\sqrt{A_{22}} - \sqrt{A_{33}})}{c_1c_3 - c_2c_3} \ln \left(\frac{1 - c_2c_3}{1 - c_1c_3} \right). \tag{2.43}$$

Equation [2.43] provides a means to calculate the Hamaker constant, A_{132} , using known values of c_1 , c_2 , and c_3 . It is also possible to calculate the Hamaker constant A_{131} using Equation [2.42] at the limiting condition that $c_1 = c_2$. Since Equation [2.42] becomes indefinite by directly setting $c_1 = c_2$, l'Hospital's rule needs to be applied to this equation by letting $c_1 \rightarrow c_2$, which yields:

$$\begin{aligned}
 A_{131} &= \left(\frac{3h}{16\pi^2b} \right) \lim_{c_1 \rightarrow c_2} \left[\frac{(c_1 - c_3)(c_2 - c_3)}{(c_1c_3 - c_2c_3)} \ln \frac{1 - c_2c_3}{1 - c_1c_3} \right] \\
 &= \frac{3h}{16\pi^2b} \frac{(c_1 - c_3)^2}{1 - c_1c_3}.
 \end{aligned} \tag{2.44}$$

Similarly, Equation [2.44] can be rewritten in terms of A_{11} and A_{33} as:

$$A_{131} = \frac{(\sqrt{A_{11}} - \sqrt{A_{33}})^2}{1 - c_1 c_3} . \quad [2.45]$$

Following Dzyaloshinskii et al. (34), the value of c_j can be evaluated directly from Equation [2.36] by setting $\xi \rightarrow 0$, as given by:

$$\lim_{\xi \rightarrow 0} \varepsilon_j(i\xi) = \frac{1 + c_j}{1 - c_j} = \varepsilon_{0j} , \quad [2.46]$$

which, in turn, yields:

$$c_j = \frac{\varepsilon_{0j} - 1}{\varepsilon_{0j} + 1} . \quad [2.47]$$

Since the calculation of c_j using Equation [2.47] requires knowledge of the values of ε_{0j} , which are only readily accessible for the materials of apolar compounds, an alternative method which is semi-empirical in nature has been developed (33). For a reference system in which the values of A_{11}^R , A_{33}^R and A_{131}^R have been calculated using exact Lifshitz theory from optical data, it follows from Equation [2.45] that:

$$(c_1 c_3)^R = 1 - \frac{A_{11}^R + A_{33}^R - 2\sqrt{A_{11}^R A_{33}^R}}{A_{131}^R} , \quad [2.48]$$

where superscript R indicates that the quantity is referred to as reference. By choosing $Ag-H_2O-Ag$ as a reference system for which A_{11}^R , A_{33}^R , and A_{131}^R have been calculated (33), from optical data using Equations [2.25], [2.26], and [2.27] in combination, to be $39.6 \times 10^{-20} J$, $4.35 \times 10^{-20} J$, and $26.6 \times 10^{-20} J$, respectively, $(c_1 c_3)^R$ is found using Equation [2.48] to be 0.33. Following Equation [2.41], one readily obtains:

$$c_j c_k = (c_1 c_3)^R \sqrt{\frac{A_{jj} A_{kk}}{A_{11}^R A_{33}^R}} \quad [2.49]$$

Using the pertinent numerical data corresponding to the reference system of $Ag-H_2O-Ag$ in Equation [2.49] results in:

$$c_j c_k = 2.5 \times 10^{18} \sqrt{A_{jj} A_{kk}} \quad [2.50]$$

Replacing c_j and c_k in Equations [2.43] and [2.45] with Equation [2.50] yields two expressions as given by Equations [2.51] and [2.52] for calculating the values of A_{132} and A_{131} from the known values of A_{11} , A_{22} , and A_{33} .

$$A_{132} = \frac{(\sqrt{A_{11}} - \sqrt{A_{33}})(\sqrt{A_{22}} - \sqrt{A_{33}})}{2.5 \times 10^{18} \sqrt{A_{33}} (\sqrt{A_{11}} - \sqrt{A_{22}})} \ln \left[\frac{1 - 2.5 \times 10^{18} \sqrt{A_{22} A_{33}}}{1 - 2.5 \times 10^{18} \sqrt{A_{11} A_{33}}} \right] \quad [2.51]$$

and
$$A_{131} = \frac{(\sqrt{A_{11}} - \sqrt{A_{33}})^2}{1 - 2.5 \times 10^{18} \sqrt{A_{11} A_{33}}} \quad [2.52]$$

It should be remarked that the numerical value of 2.5×10^{18} in equations [2.51] and [2.52] has been introduced naturally as a result of choosing $Ag-H_2O-Ag$ as a reference system. However, the numerical calculations (33) have shown that the above approach leads to a similar value with different reference systems. The calculation using Equation [2.51] or [2.52] instead of Equation [2.19] has shown a better agreement with the exact results as obtained using the Lifshitz-Dzyaloshinskii approach, i.e., using Equations [2.25], [2.26], and [2.27] in combination. An improvement of a factor of approximately 10 in accuracy has been obtained. Since Equations [2.51] and [2.52] are easier to use and require less experimental data than Equation [2.25], they are preferred to both Equations [2.19] and [2.25] in practice for estimating the values of A_{131} and A_{132} from the known values of A_{11} , A_{22} , and A_{33} .

2.2.5 Effect of Temperature and Surface Layer on Dispersion Forces

It is also worth briefly mentioning that the temperature and the adsorption surface layer will influence the behavior of dispersion forces. It has been found (2, 46) that at finite temperatures, there is a temperature dependent or zero frequency contribution to the overall dispersion forces. The temperature-dependent contribution of the dispersion forces is usually only a small fraction of the overall dispersion forces for two objects interacting across a vacuum. However, when two similar objects interact across a third medium, the temperature-dependent contribution of the dispersion forces may become one of the major proportions. This is particularly true when the medium, such as water, is highly polar in nature and has a large value of static dielectric constant. It is well known that the dielectric behavior of many different materials is very similar over the UV frequency range. Therefore, the contribution from the UV range tends to cancel each other. This gives rise to the fact that the Hamaker constants do not differ significantly when calculated without taking temperature dependence into account. Since the dielectric behavior of different materials differs significantly over the low frequency range, the temperature-dependent contribution of the dispersion forces becomes substantial. Therefore, neglecting the temperature-dependent contribution in calculating the combined Hamaker constant may give a misleading result. It has been shown (47) that the temperature-dependent contribution is about half of the total value of the Hamaker constant for the interaction of two water phases separated by a hydrocarbon film.

The presence of a surface layer has been found to affect the dispersion forces significantly, in particular when the thickness of the surface layer is comparable to the interparticle distance of interest. By taking this effect into account, the general expression for calculating the exact dispersion forces becomes extremely complicated and

its application in practice is rather limited. It has been found that if there is a surface layer, the dispersion forces will no longer follow a simple power law. Israelachvili (48) has shown theoretically that in the presence of an adsorbed surface layer, the dispersion forces may be repulsive at a small interparticle separation and attractive at a larger interparticle separation which is still within the nonretarded region. As a result, the Hamaker constant is no longer a constant but a function of interparticle separations.

For practical purposes, however, it is usually possible to obtain a useful approximation from the analysis of special situations (36, 49). For example, if the thickness of a surface layer is greater than the interparticle distance, the characteristics of the surface layer will dominate the dispersion forces. In this case, the dispersion forces can be approximated by considering the interactions between two macroscopic objects of the same material as those of the surface layers separated by the medium. In the region where the interparticle distance is greater than the surface layer thickness, the bulk properties of the interacting particles dominate. Therefore, the effect of the presence of a surface layer may be neglected. As an approximation, the following equation has been commonly used in the literature (2, 50) for calculating the effective Hamaker constant of two particles of material 1 with a surface layer of material 2 embedded in a medium, 3:

$$A_{eff} = A_{232} - \frac{2A_{123}}{(1 + D/d)^2} + \frac{A_{121}}{(1 + 2D/d)^2} , \quad [2.53]$$

where D is the thickness of the surface layer. It can be seen from Equation [2.53] that A_{232} approximates A_{eff} when the thickness of the surface layers, D , is much greater than the interparticle distance, d , indicating that the surface layers dominate the dispersion forces between the particles at small separation distances.

2.2.6 Implications from the Theories of Dispersion Forces

A few important features of dispersion forces, which can be inferred from the above discussions, are worth pointing out. Equation [2.26] implies that the dispersion forces are always attractive for two macroscopic objects of the same material, regardless of the nature of the medium separating them. However, the dispersion forces between two objects of different materials separated by a third medium can be attractive or repulsive, depending on the relative magnitude of the dielectric constants of each phase. In most cases, the comparison can be made based on the magnitude of $\epsilon_j(i\xi)$ at a single wavelength, at which it gives the largest contribution to the integral of Equation [2.26]. The attractive force is expected if the dielectric constants of these two objects are either greater or less than that of the medium, otherwise the repulsive dispersion forces are obtained when the dielectric constant of the medium is greater than that of one object but less than that of the other object.

Although the acceptance of the concept of repulsive dispersion forces came far later than that of attractive dispersion forces (51-52), they have played an important role in many technologies and natural processes such as flotation, detergency, wetting, and spreading, where wetting films have been involved (53). In an asymmetric system of solid/water/air bubble, as encountered in flotation, where $\epsilon_1 > \epsilon_3 > \epsilon_2 (= 1)$, negative dispersion forces may largely hinder the air bubble from adhering to the solid, which is crucial for the success of the process. The repulsive dispersion forces have been experimentally deduced from the study of the coagulation behavior of PTFE and graphite aqueous suspensions (51), in which no mutual coagulation has been detected. For such a system, a negative Hamaker constant has been predicted, indicating that the PTFE and graphite particles repel each other, which explains the observed coagulation behavior. Negative Hamaker constants have been calculated for n-hexane and n-heptane films on

water in conformity with experimentally observed lense formation of these liquids on water (54-55). Other experimental evidence of repulsive dispersion forces has been given, among others, by Oss et al. (52).

The concept of repulsive dispersion forces has been proven to be useful in understanding the mechanisms of a few old separation technologies, such as those involved in hydrophobic chromatography and affinity chromatography (52). By using the concept of repulsive dispersion forces, a new method has been developed for measuring the surface tensions of particles, cells and polymers (56).

It is also interesting to note that nonretarded and retarded dispersion forces are not necessarily of the same sign. As can be seen from Equation [2.26], the function under the integral may change the sign if high-frequency contributions to $\epsilon_1(i\xi)$, $\epsilon_2(i\xi)$, and $\epsilon_3(i\xi)$ become progressively damped out with increasing interparticle distance, d . As a result, the overall integration may change sign at some value of d . Therefore, using the exact solution of dispersion forces, as given by Equation [2.26], becomes necessary when dealing with the interparticle forces over a wide range of separations. The application of the microscopic approach of dispersion forces to such systems may give misleading results because this theory does not predict the possibility of changing the sign of the dispersion forces as the interparticle distance changes.

Equation [2.26] can be used to predict the behavior of uncharged particle 1 at the interface of two immiscible dielectric liquids 2 and 3. It can be seen that if the dielectric constant of particle 1 is intermediate between that of liquids 2 and 3, the particle will be attracted toward the boundary from either side of the liquid phase and remain there upon reaching the boundary. However, if the dielectric constant of particle 1 is greater or less than that of liquids 2 and 3, the particle will be repelled from the boundary, staying in the liquid phase whose dielectric constant differs less significantly from that of the particle. In this case, if the particle is originally in the liquid phase, whose

dielectric constant differs most significantly from that of the particle, the particle will be attracted toward the boundary and will be repelled away from the boundary on the other side provided that the particle is allowed to cross the boundary. Qualitatively, it is more favorable for the particle to be driven toward the part of the system where the dielectric behavior is closest to its own, i.e., where it is least "visible". If the retardation effect, which may cause the dispersion forces to change sign from repulsive to attractive at a certain separation, is taken into account, the particle may approach this separation and remain there. These phenomena are of particular importance to mineralized froths in flotation systems and to solid-containing emulsion systems as well.

2.2.7 Experimental Measurement of Dispersion Forces

It is instructive to show some experimental approaches to studying the dispersion forces. The most satisfactory and commonly used approach would be the direct measurement of dispersion forces as a function of distance between macroscopic objects. The first attempts to measure the dispersion forces have been made by Derjaguin and Abrikossova (57-59) in Russia, using negative feedback in a balance. Similar measurements have been conducted by Kitchener and Prosser (60) in Britain and by Sparnaay (61) in Holland. In these early measurements, the force has been measured by the microbalance or the flexing of an elastic spring which is very susceptible, while the distance has been determined by the optical technique, i.e., measuring the diameter of the interface rings or the intensity of light reflected from the specimen. Due to the nature of these methods, the accuracy of measuring the distance was rather low, about 2 to 20 nm, while the sensitivity of the force measurement was insufficient, no better than 10^{-2} to 10^{-4} dyne. In addition, investigations in these early stages of surface force measurements have been restricted to the system of a silica plate and a lens interacting across a

vacuum or air since the knowledge about these samples is well established and the sample preparation is relatively simple.

Nevertheless, a number of important results have been obtained from these measurements. These early measurements have shown that the force of interaction between plane and lens is inversely proportional to the third power of the distance over the separation range of 0.1 to 0.5 μm , which agrees with what has been predicted from a theoretical treatment of retarded dispersion forces. However, the magnitude of dispersion forces measured as such is smaller than that calculated using Hamaker's theory. The discrepancy between these early theories of dispersion forces and experimental results stimulated the development of Lifshitz's macroscopic theory of dispersion forces (29). The prediction using the macroscopic approach proposed by Lifshitz has shown remarkable agreement with the measured force over the electromagnetic retardation region for the systems of silica interacting through a vacuum. However, the comparison between theoretical predictions and experimental results over the nonretardation region has not been feasible from these early investigations since the force measurements at such a small separation have been made difficult by the roughness of the sample surfaces.

In order to measure the dispersion forces between two opaque macroscopic objects, Derjaguin et al. (62) have designed a new set-up in which the distance between two interacting objects is pre-set by a negative feedback circuit. With this improved device, the dispersion forces between two gold spheres and between two quartz filaments interacting across air have been measured. The measured force is in satisfactory agreement with the theoretical predictions for both gold and quartz samples over the separation range of 10 to 100 nm. The values of the retarded Hamaker constant, B_{11} , obtained by fitting the experimental data to the theoretical expression of dispersion forces, are in good agreement with those obtained from Lifshitz theory using optical data.

Many other measurements of dispersion forces conducted during the 1950's and 1960's are of this type with small modifications on the methods of determining the distance or force to improve the accuracy of the measurement (63-66). These early measurements collectively show that over the retarded region, the measured force is in good agreement with that predicted from Lifshitz' theory. The Hamaker constants, B_{11} , obtained by fitting the experimental data into Equation [2.21], lie in the range of B_{11} as obtained from Lifshitz's calculations using optical data for the various systems investigated. However, as the separation decreases down to the nonretarded region, i.e., about 50 to 80 nm, the deviations between the experimental results and those predicted from the theory become substantial. This deviation has been mostly attributed to the effect of surface roughness on the experimental measurement.

In order to eliminate the effect of surface roughness on the measurement of surface force over the nonretarded region, muscovite mica has been used, for the first time, by Tabor and Winterton (38). The molecular smoothness of the mica surface allows the measurement to be conducted down to 5 nm with an accuracy of about 0.3 nm. In their measurements, the dispersion forces have been determined using the "jump method" as proposed initially by Overbeek and Sparnaay (67). Their experimental results clearly show a transition at a separation of 10 nm. When the separation is less than 10 nm, the measured force is inversely proportional to the second power of the separation distance, corresponding to nonretarded behavior. However, when the separation is greater than 10 nm, the measured force becomes inversely proportional to the third power of the separation distance, which shows the retarded behavior. It has also been found that the transition between nonretarded behavior and retarded behavior occurs fairly abruptly, within 10 nm. The values of two Hamaker constants, A_{11} and B_{11} , obtained by fitting the experimental data into Equations [2.13] and [2.21], corresponding to nonretarded and

retarded regions, respectively, are equal to the values calculated from Lifshitz theory using optical data.

It has been realized that the "jump method" for determining the force becomes less accurate when the separation distance is greater than 20 nm due to the increased influence of vibration as the rigidity of the spring decreases. In an attempt to improve the accuracy of the force measurement over a wide range of separations, Israelachvili and Tabor (49) have developed a new apparatus in which a new resonance method has been used. With this apparatus, the force measurement can be conducted down to a separation of 1.5 nm with a distance resolution of 0.1 nm. (68). Recently, this new apparatus has been commercialized by Anutech Pty. Ltd., Australia. In this surface force apparatus, a double-cantilever spring has been used by which the stiffness of the spring can be changed during experiments by simply adjusting the spring length through the change of the attachment point. With this apparatus, the dispersion forces between two mica surfaces coated with monolayers of stearic acid by the Langmuir-Boldgett method have been measured. The thickness of this adsorption layer has been estimated to be 2.5 nm. The experimental results show that the influence of surface monolayers begins only at a separation distance less than 3 nm, which is comparable with the thickness of the adsorption surface layer. The Hamaker constant, obtained by fitting the data for the separations greater than 5 nm, is the same as that of bulk mica, as calculated from Lifshitz theory using optical data. However, the data fitting for separations less than 3 nm yields an effective Hamaker constant of 1×10^{-12} erg, compared to the Hamaker constant of 0.9×10^{-12} erg as obtained again from Lifshitz theory for the material of surface monolayers. This finding suggests that the interaction at a smaller separation appears to be dominated by the properties of the surface monolayer. These results support the previous discussions as to the theory of dispersion forces in the presence of a surface adsorption monolayer.

The above discussions clearly show that with the advent of this apparatus, we are now at a stage where accurate surface force measurement can be conducted down to a close proximity of 0.15 nm. Although the measurement can only be conducted for the mica system, important information concerning other materials can be obtained by depositing the material of interest onto the mica surface and measuring the dispersion forces over a separation range smaller than the thickness of this deposition layer. In this region, the surface layer dominates the measured force behavior, as discussed previously. Therefore, it is reasonable to infer that the observed force law reflects the dispersion interaction between the two macroscopic objects of this deposited material instead of the mica substrate itself.

It has been shown that almost all the force measurements of two macroscopic objects conducted in air or vacuum are in agreement with Lifshitz theory over the separation distance range of 1.5 to 1000 nm, which indicates indirectly that for the dispersion interactions in air or vacuum, the theory holds down to molecular contact (2, 69). However, an accurate measurement of dispersion forces conducted in liquids appears to be considerably complicated. This can be attributed to the simultaneous presence of other forces, such as electrostatic and solvation forces. The viscosity of a fluid may also complicate the measurements and the interpretation of the results obtained. Therefore, the dispersion forces can only be obtained by conducting a series of measurements under different solution conditions and then subtracting other known forces or extrapolating to the limit condition at which other forces are absent. Other factors, such as contamination of the surface by traces of impurities present in the liquid, may completely change the qualitative nature of the dispersion forces. For these reasons, a comparison between experimentally measured dispersion forces and those predicted from theory is less straightforward in a liquid medium than in air or a vacuum.

Recently, Marra (70) has measured dispersion forces between L- α -dipalmitoyl-phosphatidyl-choline (DPPC) bilayers and digalactosyl-diglyceride (DGDG) bilayers deposited on a monolayer of L- α -dipalmitoyl-phosphatidyl-ethanolamine (DPPE) which has been previously deposited on molecularly smooth mica. The measurements have been made in conductive water and 0.3 M NaCl aqueous solution using the apparatus developed by Israelachvili. The experimental results obtained using DGDG bilayers have shown that the dependence of dispersion forces on the bilayer separation follows the Hamaker equation. The Hamaker constant obtained from long range force measurements is in good agreement with that obtained from adhesion force measurements. The "screened" dispersion forces have been determined in 0.2 M NaCl aqueous solution. The Hamaker constant calculated from these latter measurements has been considered to be a pure dispersion component. Therefore, the difference between the Hamaker constant obtained in conductive water and that in 0.2 M NaCl solution has been naturally considered as the temperature dependent or zero frequency component of the total Hamaker constant. The value obtained agrees reasonably well with that calculated using the simplified Lifshitz theory (47) and indicates that the contribution of the temperature-dependent interaction is equally as important as that of dispersion interaction to the total van der Waals interaction between DGDG bilayers in pure water.

However, the Hamaker constant obtained from the long range force measurements has been found to be lower than that obtained from the adhesion force measurements when the force has been measured between DPPC bilayers. This finding suggests that independent measurements of long range attractive and short range adhesive forces are necessary for one to study dispersion interactions by excluding other interactions, such as electrostatic double layer and hydration interactions.

2.3 Electrical Double Layer Forces

According to the theory of dispersion forces discussed in the previous section of this chapter, small particles of the same material will always coagulate regardless of the solution conditions in which they are embedded since the dispersion forces are always attractive between similar particles in a medium. This is of course contrary to what usually happens in the nature. The observed dispersion of similar particles in a third medium indicates the existence of other repulsive forces which dominate the net interaction under these conditions. In most cases, the repulsive forces are due to the interaction of electrical double layers formed around each particle. Electrostatic interaction between charged surfaces plays an important role in a number of processes (71), such as homo- and hetero-coagulation, flocculation, nonspecific ion adsorption, ion exchange, electrode process rate, configuration of macromolecules, swelling of clay minerals, fibrous material wetting (dyeing and detergency), mineral flotation, electrocapillary emulsification, dispersion as in cosmetics, papermaking, painting, biological cell interactions, and so on. In order to have a better understanding of the electrical repulsive forces, it is helpful to consider first the origin of the surface charge and, hence, the cause of an electrical double layer.

2.3.1 *Origins of Surface Charge*

It is well known that most substances carry an electric charge when brought into contact with a polar medium such as electrolyte aqueous solutions. The existence of surface electric charge can be easily demonstrated by applying an external electrical field to quiescent fine particle suspensions. It is conceivable that the charged particles move in the external electrical field due to electrostatic forces. The nature of an electrode to-

ward which a particle moves determines the sign of the average surface charge carried by this particle. If a particle moves toward a positive electrode, this particle must carry a negative charge, and vice versa. The transport velocity, called *electrical mobility*, at a given electrical field strength determines the magnitude of the surface charge.

The origin of the interface charge is somewhat complex. In general, the interface can be charged through one or more of the charge mechanisms. The most commonly encountered charge mechanisms include unequal distribution of lattice-forming ions at the surface, dissociation of surface groups, preferential adsorption, and non-stoichiometric substitution of crystal ions. In some cases, the surface may also carry the charge by the orientation of dipoles at the interface, by the tempering of solids, or by surface polarization.

The surface charge of AgI particles in water is an example of a charge mechanism with unequal distribution of lattice-forming ions at the surface. In this particular case, the unequal distribution of lattice-forming ions on the interface is due to asymmetrical dissolution of the solid. Although the solid AgI particle is electrically neutral, when brought into pure water, it becomes negatively charged due to the existence of excess surface I^- . This may be attributed to the stronger hydration of Ag^+ than I^- , which results in a low activity of Ag^+ in the solution phase. By increasing the concentration of Ag^+ above $10^{-5.6}$ M, the AgI surface becomes positively charged because of the excess Ag^+ on the surface. Ag^+ and I^- are referred to as potential-determining ions, *pdi*, with respect to AgI suspensions. Most inorganic solids suspended in a third medium such as aqueous solutions, in which they have some solubility, are charged according to this charging mechanism. More examples include CaF_2 , $BaSO_4$, $PbSO_4$, $CaWO_4$, etc.

It is well known that natural silica particles are negatively charged in pure water, which can be attributed to the surface hydrolysis followed by the *pH* dependent dissociation of surface hydroxyl groups. When the silica matrix is broken in air, the

surface concentrations of SiO^- and Si^+ are the same for the requirement of electrical neutrality of a particle. When the fractured surface is brought into contact with water, these charged sites, called unsaturated sites, are readily hydrolyzed to form neutral surface species of $SiOH$, releasing either OH^- or H^+ . By adjusting the pH , i.e. changing H^+ and OH^- concentrations, the neutral surface species will dissociate, giving rise to a net surface charge. In this case, H^+ and OH^- are the potential-determining ions and the pH at which the surface is neutral is called the point of zero charge, pzc . Negative surface charge is created by an acidic dissociation of surface hydroxyl groups, which occurs when the pH is above the pzc , while positive surface charge results from proton addition to the surface as in the case of pH value below the pzc . For most oxides, the surface charge originates from this mechanism. It is well documented (72) that the surface charge of low-rank coal and oxidized high-rank coal comes from the hydrolysis of surface oxygen-containing groups followed by the dissociation of these weakly acidic species of hydration, such as phenolic OH and $COOH$ groups. The surface charge may also be created by direct dissociation of the surface groups. Surfaces containing the groups such as sulfates, carboxyl, hydroxyl, oxides, and/or sulfonates are readily charged when the free energy of the system favors their dissociation (73).

In some cases, the adsorption of specifically adsorbing ions, such as Ca^{2+} and Mg^{2+} , is responsible for the surface charge of a previously uncharged surface. The positive surface charge of lipid bilayer surfaces of zwitterionic head groups in the presence of Ca^{2+} is due to the adsorption of Ca^{2+} on $-COO^-$ sites vacated by H^+ or Na^+ (5). Obviously, the surface charge due to this mechanism requires the existence of specifically adsorbing ions in the aqueous solution. Therefore, this charge mechanism can be easily tested.

It is interesting to note that the adsorption of specifically adsorbing ions not only makes certain neutral surfaces charged, but also changes the sign of the surface charge

for some previously charged surfaces. It is well known, for example, that in the absence of specifically adsorbing ions, hematite acquires a negative surface charge by surface hydrolysis followed by dissociation of hydroxyl surface species provided that the pH of the solution is above its pzc . However, the presence of Ca^{2+} , which adsorbs specifically onto the negatively-charged hematite surface, renders negatively charged hematite positive as long as the concentration of Ca^{2+} is high enough. In this case, Ca^{2+} , H^+ , and OH^- are all potential-determining ions. The charge mechanism of some salt-type minerals, such as calcite and apatite, is a combination of surface hydrolysis followed by preferential dissolution and adsorption of specifically adsorbing ions since these ions are always present due to the relatively high solubilities of these minerals. The preferential adsorption of simple charged ions is, in some cases, responsible for surface charge. The surface charges at air/water and hydrocarbon/water interfaces in the presence of simple electrolytes have been attributed to the preferential adsorption of anions at these interfaces (74-76).

The surface charge of clay particles is an example of a charging mechanism of non-stoichiometric substitution of crystal ions. To illustrate this, let us take the charging process of mica as an example. Mica is a layer-structured mineral, in which about 25% Si^{4+} are substituted by Al^{3+} , resulting in a positive charge deficiency. The excess negative charge in a mineral matrix is compensated by the interstitial cations, such as K^+ or Na^+ , in order to keep the mineral electrically neutral. These interstitial ions are usually small in size, less bonded to the matrix and easy to move. When mica is placed in water, the interstitial ions within the surface regions transfer into water, leaving a negative charge on its basal planes, which is independent of pH (77). However, the hydrolysis of unsaturated bonds, such as broken Si-O and Al-O bonds on the edges, followed by the dissociation of hydrated species creates a pH -dependent surface charge. Therefore, H^+ and OH^- may also act as potential-determining ions. It is worth mentioning that the

surface charge density cannot be reduced to zero in such a system. Both the basal faces and the edges may still carry charges of different signs although the overall effect shows a point of zero charge. It is because of this interesting characteristic of surface charge that clay minerals show peculiar coagulation properties, forming a so-called *card-house structure* under appropriate solution conditions due to the face-to-edge attachment (78).

For hydrophobic surfaces, the surface may be charged by preferential orientation of dipoles at the water/hydrophobic interface (79-80). Surface charge mechanisms of this kind are mostly deduced from the low sensitivity of the surface charge to the solution conditions, such as pH and simple electrolyte concentration, as observed experimentally. Therefore, the details of this charge mechanism are not clear in most cases. The negative surface charge of high-rank coal in the neutral pH range may be considered due to the preferential orientation of dipoles under the influence of the electrical field of water (80). The surface may also be charged by the tempering of solids (81). It is noted that high temperatures are favorable for the formation of crystal defects. Since the free energy associated with the formation of defects at a surface is different from that at the interior of the crystal, it is expected that the concentration of defects varies from surface to bulk. As the crystal is cooled rapidly, the defect distribution is frozen in, giving rise to a certain amount of surface charge. The surface charge formed as such is less sensitive to the solution conditions in the absence of specific adsorbing ions.

The surface can also be charged through electrical polarization. This charge mechanism is not as common as the charge mechanisms discussed previously in the practice of colloid chemistry, but it provides an important means to study properties of charged surfaces since the surface charge density can be controlled easily without changing the solution chemistry. For example, the well-known electrocapillary curves have been generated by polarizing mercury/electrolyte aqueous interfaces with a different electrode potential, from which the Lippmann equation has been derived to explain

the experimentally observed phenomena. By using a mercury electrode polarized with varying potential, Usui et al. have studied attachment between mercury and glass foil (82), argon bubbles (83), and hydrogen bubbles (84) in aqueous solutions, from which the van der Waals and electrostatic interactions have been assessed, respectively. This sort of charge mechanism also plays an important role in the electrode rate process (85).

2.3.2 *Surface Electrical Potential*

As discussed previously, different surfaces may be charged by different charging mechanisms when brought into contact with aqueous solutions. Regardless of the charge mechanism, the final surface charge will be balanced by an atmosphere of equal amounts of charges opposite in sign to preserve the electrical neutrality. This atmosphere, called *electrical double layer*, is rich in counter ions which act as balance charges and extend into the solution. The thickness of the electrical double layer is determined solely by the conditions of the electrolyte solutions and is independent of the nature of the surface charge, as will be illustrated later. A simplified structure of electrical double layer is schematically shown in Figure 2.1. One of the important parameters describing electrical double layer is surface potential, ψ_0 . This is the electrical potential of the solid/water interface with respect to the bulk solution where the electrical potential is customarily considered to be zero. Apparently, the surface potential is determined by the surface concentration of potential-determining ions if the surface is charged by preferential dissolution, preferential dissociation and/or preferential adsorption. The magnitude of the surface potential can be readily obtained from the equilibrium condition of equal electrical chemical potentials of *pdi* in solid phase and in aqueous phase (53, 79, 86-88). Mathematically, it can be expressed as:

$$\mu_s(pdi) + ze\phi_s = \mu_a(pdi) + ze\phi_a , \quad [2.54]$$

where μ is the chemical potential of pdi , ϕ is the electrical potential of the bulk phase, z is the valence of pdi and the subscripts s and a refer to surface and aqueous phases, respectively. The chemical potential in Equation [2.54] is given by:

$$\mu_i = \mu_i^0(pdi) + kT \ln[a_i(pdi)] , \quad [2.55]$$

where $a_i(pdi)$ is the activity of pdi in phase i , and μ_i^0 is the reference chemical potential of pdi . It has been realized that the electrical potential of the bulk solid, ϕ , in Equation [2.54], can be expressed as (79):

$$\phi_s = \chi + \psi_0 , \quad [2.56]$$

where χ is the potential drop across the solid surface layer mainly due to the dipole orientation effect. By choosing the bulk aqueous phase as a reference, i.e., $\phi_a = 0$ in Equation [2.54], inserting Equations [2.55] and [2.56] into Equation [2.54] and rearranging the resultant equation yield:

$$\psi_0 = \frac{1}{ze} \left[\mu_a^0(pdi) - \mu_s^0(pdi) + kT \ln \frac{a_a(pdi)}{a_s(pdi)} \right] - \chi . \quad [2.57]$$

Assuming that the surface potential becomes zero at a certain pdi concentration called point of zero charge (pzc), Equation [2.57] can be rewritten as:

$$0 = \frac{1}{ze} \left[\mu_a^0(pdi) - \mu_s^0(pdi) + kT \ln \frac{a_a(pdi)_{pzc}}{a_s(pdi)_{pzc}} \right] - \chi . \quad [2.58]$$

By subtracting Equation [2.58] from Equation [2.57] to eliminate quantities χ , $\mu_a^0(pdi)$ and $\mu_s^0(pdi)$, one readily obtains:

$$\begin{aligned}\psi_0 &= \frac{kT}{ze} \ln \left[\frac{a_c(pdi)}{a_a(pdi)_{pzc}} \frac{a_s(pdi)_{pzc}}{a_s(pdi)} \right] \\ &= \frac{2.303kT}{ze} \left[pzc - p[pdi] - \log \frac{a_s(pdi)}{a_s(pdi)_{pzc}} \right].\end{aligned}\tag{2.59}$$

where $p[pdi]$ is the negative logarithm of the activity of pdi in solution and pzc is that at the point of zero charge. Since the quantities $a_c(pdi)$ and $a_s(pdi)_{pzc}$ are not available in most cases, the direct application of Equation [2.59] in practice is restricted. However, the solid surface contains, in general, a larger number of potential-determining ions even at its pzc . A few extra ions which adsorb onto the surface in order to establish the potential, ψ_0 , are not likely to affect the activity of those surface ions. It is, therefore, reasonable to assume that $a_c(pdi) = a_s(pdi)_{pzc}$ in Equation [2.59]. Under this assumption, Equation [2.59] becomes:

$$\psi_0 = \frac{kT}{ze} \ln \frac{a_a(pdi)}{a_a(pdi)_{pzc}} = \frac{2.303kT}{ze} (pzc - p[pdi]) .\tag{2.60}$$

Equation [2.60] provides a simple but important means to calculate the surface potential from the activity of pdi in solution and the known value of pzc which can be readily calculated theoretically and/or determined experimentally with great accuracy (89-91). However, for the systems in which only a few potential-determining ions are present on the surface at its pzc , the additional pdi required for establishing surface potential ψ_0 may change the activity of pdi substantially. The assumption that $a_c(pdi) = a_s(pdi)_{pzc}$ may not hold for these systems. Therefore, Equation [2.60] needs to be modified to obtain more accurate values of surface potential.

Hunter and Wright (92), Levine and Smith (93), and Yates et al. (94) have proposed a site-dissociation model from which a series of relationships between surface po-

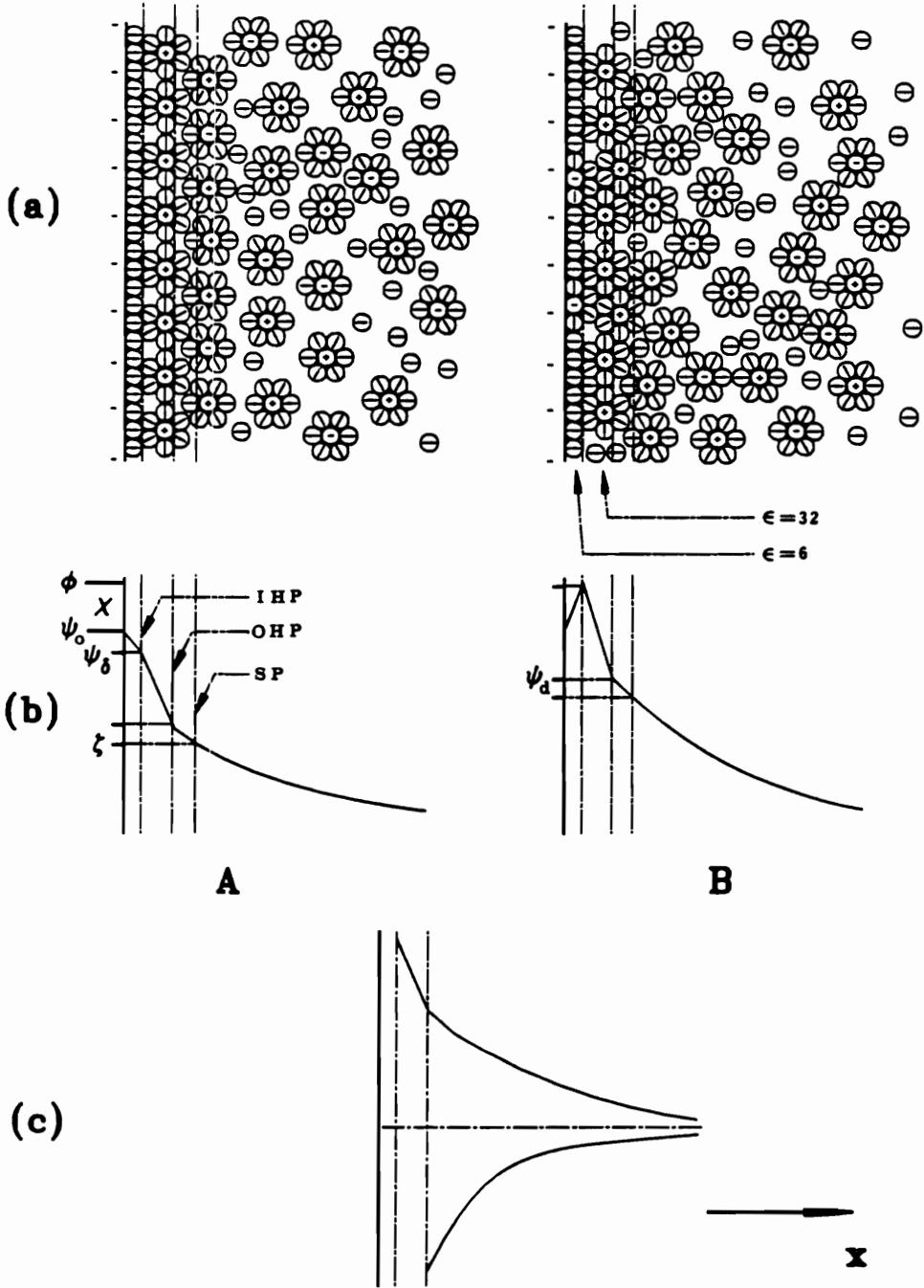


Figure 2.1. Electrical Double Layer Structure and Distributions of Electrical Potential and Ion Species

A. Without Specific Adsorbing Ions B. With Specific Adsorbing Ions
 a. Double Layer Structure b. Potential Distribution c. Ion Distribution

tential and pdi concentration have been derived for a number of different systems. Since the knowledge of the surface number density of functional groups, surface dissociation constant of these functional groups and the structure of resultant double layer are required in their models, the application of these relationships is rather limited in practice. Instead, Equation [2.60] has been used frequently.

2.3.3 Electrical Double Layer Theories

Under the influence of the electrical field of the charged surface, counter ions will be attracted toward the surface, forming a distribution of ions determined by the balance of the electrical forces of the surface charge and the diffusive forces induced by chemical potential gradient. These distributed ions and surface charges, together, form an electrical double layer. The simplest model for this double layer has been proposed by Perrin (95) as a molecular condenser, in which the counter ions are assumed to be distributed at a plane parallel to a solid surface for completely balancing the surface charges. According to this model, known as the Helmholtz-Perrin model, the basic electrostatic theory of capacitors has been used to derive an equation relating the potential of a double layer to the surface charge as given by (96):

$$dE = \frac{4\pi\delta}{\epsilon} dq_M , \quad [2.61]$$

where δ is the distance separating two electrical layers, ϵ is the dielectric constant of the material between the layers, and q_M is the charge density of each layer. Inserting this equation into the Lippmann equation and integrating the resultant equation yield:

$$\gamma_m + constant = -\frac{2\pi\delta}{\epsilon} q_M , \quad [2.62]$$

where γ_m represents the surface tension of liquid mercury. Equation [2.62] indicates that the surface tension reaches its maximum when the surface carries no net charge, i.e., at the *pzc*. This finding phenomenologically agrees with the experimentally observed electrocapillary phenomenon.

However, the asymmetry of electrocapillary curves and the dependence of capacity upon potential as observed experimentally cannot be predicted from the Helmholtz-Perrin model. This indicates that the Helmholtz-Perrin condenser model needs to be modified. The assumption that all counter ions are accumulated at one fixed plane has long been recognized as an inadequate representation of the actual situation. By considering that the counter ions are distributed in a liquid phase because of the competition of electrical forces with diffusive forces, a theory of diffuse double layer was first developed independently by Gouy (96) in 1910 and by Chapman (97) in 1913. In their treatment (98), a flat solid surface of infinite size with surface potential, ψ_0 , has been considered. The counter ions have been assumed to be point charges immersed in a continuous dielectric medium. By applying the fundamental law of electrostatics to a general relation between the electrostatic field strength and the electrical potential of one dimension, a general one-dimensional Poisson equation, which relates the charge density of the element to its potential, has been derived as given by:

$$\frac{d^2\psi}{dx^2} = -\frac{4\pi}{\epsilon} \rho , \quad [2.63]$$

where ρ is the volume density of charge and the coordinate system is shown in Figure 2.1 (c). During the derivation, the permittivity of liquid has been assumed to be independent of position, which is questionable since the electrical fields generated in the interfacial region may be high enough to modify solvent structure, as illustrated in Figure 2.1 (a).

To obtain a relation of volume charge density as a function of x , the driving force for the transportation of ions has been considered. At equilibrium, the electrical force exerted on the ions must be balanced by the diffusive force, i.e.,

$$\frac{d\mu_i}{dx} = -z_i e \frac{d\psi}{dx} , \quad [2.64]$$

where μ_i is the chemical potential and z_i is the valence of ions of type i . Inserting the chemical potential equation as given by Equation [2.55] into Equation [2.64] and integrating the resultant equation from a point in the solution, where $\psi = 0$ and $n_i = n_{i0}$, to an arbitrary position, x , lead to the well-known Boltzmann equation as given by:

$$n_i = n_{i0} \exp\left(-\frac{z_i e \psi}{kT}\right) . \quad [2.65]$$

Equation [2.65] determines the distribution of each type of ions in the double layer. As schematically shown in Figure 2.1 (c), the concentration of counter ions decreases while that of co-ions increases with distance away from the surface. Both of them reach their bulk concentration at a certain distance.

The charge density of a thin element, as shown in Equation [2.63], can then be expressed in terms of ion distribution as:

$$\rho = \sum_i n_i z_i e = \sum_i n_{i0} z_i e \exp\left(-\frac{z_i e \psi}{kT}\right) . \quad [2.66]$$

Inserting Equation [2.66] into Equation [2.63] to eliminate the volume charge density yields:

$$\frac{d^2\psi}{dx^2} = -\frac{4\pi}{\epsilon} \sum_i n_{i0} z_i e \exp\left(-\frac{z_i e \psi}{kT}\right) = \frac{8\pi z n_0 e}{\epsilon} \sinh\left(\frac{ze\psi}{kT}\right). \quad [2.67]$$

The second equal sign of Equation [2.67] has been obtained by expanding the exponential terms and retaining only the linear terms for the case of small electrical potential and one type of symmetric electrolytes in solution. Equation [2.67] is known as a complete one-dimensional Poisson-Boltzmann (*PB*) equation. Together with the boundary conditions defined by the mechanism of charge build-up at the interface, Equation [2.67] completely determines the potential distributions in the solution adjacent to the interface. Integrating this equation once gives:

$$\left(\frac{d\psi}{dx}\right)^2 = \frac{2kT}{\epsilon} \sum n_{i0} [\exp(-z_i e \psi / kT) - 1]. \quad [2.68]$$

The general analytical solution of Equation [2.68] is impossible to obtain. However, for a system where only one kind of symmetric electrolyte is present, Equation [2.68] has been solved analytically to give (89):

$$\psi = \frac{2kT}{ze} \ln \left[\frac{1 + \gamma \exp(-\kappa x)}{1 - \gamma \exp(-\kappa x)} \right], \quad [2.69]$$

where γ is defined by:

$$\gamma = \frac{\exp(-ze\psi_0/kT) - 1}{\exp(-ze\psi_0/kT) + 1}. \quad [2.70]$$

The quantity κ in Equation [2.69] is known as the Debye reciprocal thickness or screening length of the double layer, and given by:

$$\kappa = \left(\frac{8\pi e^2 n_0 z^2}{\epsilon kT} \right)^{1/2} = \left(\frac{8\pi c N_A e^2 z^2}{\epsilon kT} \right)^{1/2}, \quad [2.71]$$

where c is the concentration of electrolyte. In the derivation of Equation [2.69], the boundary conditions that $\psi = \psi_0$ at $x = 0$, and $\psi = 0$ and $(d\psi/dx) = 0$, at $x \rightarrow \infty$, have been used. In the case of $\kappa x > 1$, Equation [2.69] can be approximated by:

$$\psi = \frac{2kT}{ze} \ln[1 + 2\gamma \exp(-\kappa x)] = \frac{4kT}{ze} \gamma \exp(-\kappa x). \quad [2.72]$$

An analytical solution of the complete *PB* equation for the systems where asymmetric electrolytes are present can be obtained under the assumption of small potential everywhere in the double layer. By assuming that $z_i e \psi < kT$, known as the Debye-Hückel approximation, the exponential terms in Equation [2.68] can be expanded to a Maclaurin series. Retaining the linear terms of the expanded series in Equation [2.68] yields:

$$\frac{d^2\psi}{dx^2} = -\frac{4\pi}{\epsilon} \left(\sum z_i e n_{i0} - \sum z_i^2 e^2 n_{i0} \psi / kT \right). \quad [2.73]$$

The first term in the parentheses of the above equation must be zero to preserve the electroneutrality of the bulk electrolyte solution. Thus, Equation [2.73] can be simplified to:

$$\frac{d^2\psi}{dx^2} = \kappa^2 \psi, \quad [2.74]$$

where the quantity κ takes a more general form of:

$$\kappa = \left(\frac{4\pi e^2 \sum n_{i0} z_i^2}{\epsilon k T} \right)^{1/2} . \quad [2.75]$$

This simple form of Equation [2.74] is particularly useful when dealing with the problems of spherical shape because of the mathematical difficulty involved in the direct application of Equation [2.67]. Using the boundary conditions as given previously, Equation [2.74] can be readily integrated to give:

$$\psi = \psi_0 \exp(-\kappa x) . \quad [2.76]$$

Equations [2.71] and [2.75] show that increasing the electrolyte concentration causes an increase in κ , which in turn makes the potential fall off more rapidly with distance, as indicated in Equation [2.76]. This is a well-known double layer compression phenomenon.

From the potential functions, the surface charge density, σ , can be obtained by considering that this surface charge must be balanced by charge accumulation of counter ions in the double layer. Mathematically,

$$\sigma = - \int_0^{\infty} \rho dx . \quad [2.77]$$

Inserting the Poisson equation as given by Equation [2.63] into Equation [2.77] to eliminate the volume charge density of solution leads to:

$$\sigma = \epsilon \int_0^{\infty} \frac{d^2 \psi}{dx^2} dx = - \epsilon \left(\frac{d\psi}{dx} \right)_{x=0} . \quad [2.78]$$

A general equation relating the surface charge density to the surface potential can, then, be obtained by substituting Equation [2.68] into Equation [2.78] as given by:

$$\sigma = \left[2\epsilon kT \sum n_{i0} [\exp(-z_i e \psi_0 / kT) - 1] \right]^{1/2} . \quad [2.79]$$

With the assumption of small potentials, Equation [2.79] becomes:

$$\sigma = \frac{\epsilon \kappa}{4\pi} \psi_0 . \quad [2.80]$$

So far, the considerations have been restricted to flat interfaces by virtue of mathematical simplicity. The conclusions obtained are, however, applicable to curved surfaces, provided that the radius of curvature is large compared to the distance of interest. In general, the flat double layer model will be a good approximation for a spherical particle of radius a as long as $\kappa a > 10$ (99). Unfortunately, this will not always be the case to be investigated. It is, therefore, useful to discuss briefly curved double layers.

Theoretically, the procedures used in treating flat double layers can be adopted for the treatment of curved double layers. However, in a spherical coordinate system, an analytical solution to the general *PB* equation satisfying the boundary conditions of $\psi|_{r=a} = \psi_0$, $(d\psi/dr)|_{r=a} = -4\pi\sigma/\epsilon$, and $\psi(r)|_{r\rightarrow\infty} = 0$ has never been exhibited, although various numerical solutions have been given for a limited number of conditions (100). Because of the inconvenience of using these tables for general purposes, the Debye-Hückel approximation of small surface potential has been used to obtain an analytical solution to the *PB* equation in the spherical coordinate system (101). It remains doubtful whether the extension of the theory to the case of larger surface potential on spherical double layers, which is very difficult to deal with mathematically, is worth the

trouble (87). Nevertheless, a few different approaches based on Perturbation schemes (102-107) or the variational principle (108) have been applied to the treatment of spherical double layers (105), to extend the applicable range of the surface electrical potential equation by improving the accuracy of the approximation.

Perturbation schemes for solving the spherical *PB* equation are based on the replacement of the nonlinear term by its value in some solvable zeroth order approximation as a function of the independent variable. It appears that the solutions of high surface potential can be improved substantially by using a perturbation scheme in which only the solution of the planar *PB* equation needs to be used as a zeroth order solution (103). This approach can be easily extended to any high order solution by succeeding substitution of a lower order solution starting with a zeroth order solution. Electrostatic potential as a power series of κa has been involved in this early perturbation scheme. An alternative approach of the perturbation scheme is to attempt a solution of the linearized *PB* equation satisfying the given boundary conditions as a zeroth order approximation (101, 103). As a general rule, approximate theories starting with the planar result are restricted to the large κa regime, while those starting with a linearized solution are limited to the small κa regime (104). By realizing that for any sphere of radius a , a general perturbation solution should be simplified to the solution of the planar *PB* equation at a sufficiently small value of r , and to the solution of the linearized spherical *PB* equation over a sufficiently large value of r , White (104) has constructed a simple function which follows these two limiting forms and developed a novel perturbation scheme suitable for κa values from 1 to 15, where the Debye-Hückel linearized solution or the planar solution does not provide good approximations. Recently, Ohshima et al. (106) have proposed a different perturbation scheme in which the nonlinear term has been approximated by a function of the dependent variable. Approximate expressions

derived as such have been shown to be excellent approximations of the exact numerical values over a wide range of values of κa for all surface potentials studied (106-107).

Variational approach as applied to the electrostatic double layer theory provides an important means to find an accurate yet simple closed form for the electrostatic potential surrounding a spherical colloid particle. Brenner and Roberts (108) have proposed a potential function containing a single parameter which has been determined by a variational principle associated with the free energy. Specifically, an arbitrary function, with a variational parameter being included, has been constructed to be a surface potential function which has been used in calculating the free energy function of a spherical double layer. The arbitrary function has, then, been optimized by determining the value of the parameter which gives a minimal value of the free energy function. The optimized function has been considered as the best representation of potential function. It is obvious that many different functional forms need to be optimized in order to come up with a reasonable representation of the potential function. Because of the nature of this approach, it lacks the physical background and the clarity of a single function for the potential curve. Nevertheless, the expression derived by Brenner and Roberts does give an excellent approximation to the exact numerical solution of the *PB* equation of spherical electrical double layers.

A number of factors neglected in the previous theoretical treatments are important in determining the structure of a diffuse ion layer (53, 110), including image forces (111-112), finite volume of ions (112-115), dielectric saturation (114-115), and the hydration of ions. Using statistical theory, Martynov (111) has found that the effect of image forces becomes increasingly significant with the increase in the valence of electrolyte present in aqueous solution. A reduced error has been observed between the measured capacity of the electrical double layer and that predicted theoretically when image forces are taken into account in Gouy-Chapman theory.

It has been shown (79, 110, 116), by the calculation using the Boltzmann equation, that the surface concentration of counter ions is as high as 160 mole/liter for a 1:1 electrolyte in the concentration of 1×10^{-3} mole/liter at a surface potential of 300 *mV*. This anomalously high value, in view of the finite dimension of the ions, has been attributed to the assumption of an ion as a point charge which can approach the surface without any limit. The hydration of counter ions may compound this effect due to the existence of a hydration sheath. It is understandable that the hydration of counter ions will create a geometrical limitation which reduces the concentration of counter ions adjacent to the solid surface. In order to overcome these difficulties, several ion distributions in which a volume correction has been introduced have been used in the subsequent modifications of double layer theory (110, 117-119). These distributions have been derived using the method of local thermodynamic balance. A more rigorous approach of classical statistical mechanics (120) has shown that the linear *PB* theory holds fairly well at low electrolyte concentrations. It predicts, however, that the average space charge tends to alternate in sign due to an ionic ordering effect when electrolyte concentration is higher than 0.5 mole/liter. Under these conditions, the finite volume of ions results in the occurrence of a local lattice-like structure with alternative layers of positive and negative charges.

It has been assumed, in the Gouy-Chapman double layer theory, that the dielectric constant of the aqueous phase is the same everywhere. The actual situation is, however, that the dielectric constant decreases as the electrical field strength increases, which is known as dielectric saturation. Since the liquid adjacent to the charged surface is exposed to a substantial electrical field, the dielectric constant is much lower in this region than in bulk, as shown in Figure 2.1 (a), and the use of the dielectric constant at zero electrical field strength in *PB* equation will surely introduce some errors. The calculation (121) has shown that the predicted differential capacity of a diffuse double layer

is very sensitive to the functional form of dielectric saturation. However, the effect of dielectric saturation on the relation between the surface charge density and surface potential has been found to be less sensitive. On the other hand, the dielectric constant of an aqueous solution varies with electrolyte concentration (122). It becomes obvious that the accumulation of counter ions inside a double layer will have a significant effect on the dielectric constant and hence, the characteristics of the double layer. As expected, the effect of dielectric saturation has been found to be small at low surface charge density and low electrolyte concentration. Therefore, the dielectric saturation is unlikely to be important in experimental investigations of diffuse double layers if only pure water is involved. Of course, the complete picture of a double layer theory should take the dielectric saturation effect as a function of the position in the double layer into account since the electrical field strength decreases as the distance away from the charged surface increases. This will definitely introduce mathematical difficulty, and only the numerical solutions are possible.

Other factors such as ion polarization, the self-atmosphere effect of the counter ions, and electrostriction have also been found to be the possible reasons for the deviation of the Gouy-Chapman theory from the experimental results (110). It is expected that the polarization of the ion transferred from the bulk into the double layer region will contribute an extra energy term to the Boltzmann equation (118-119). When an ion gets into the double layer, the ionic atmosphere around it will be broken. Accompanied with this is an energy change which is not considered in the normal Boltzmann equation. It has been found (120) that this correction reduces the potential and becomes less important at high electrolyte concentration or in the region far away from the solid surface. When counter ions enter into the double layer, the electrical field of these ions is capable of wrenching solvent molecules to envelope the ions with a solvent sheath, and in turn to compress the solvent. Associated with this process is the additional work due to

electrostriction, which will affect the ion distribution and hence the double layer structure.

The above Gouy-Chapman double layer theory has been tested experimentally by measuring the impedance of an electrode system under a small a.c. signal to determine the differential capacitance or by measuring interfacial tension variations with electrode potential. In general, the differential capacitance calculated based on the Gouy-Chapman model has been found to be far greater than that experimentally measured (123). Also found is a disagreement between the interfacial tensions measured under various electrode potentials with that predicted from the theory (124). These discrepancies indicate that the original Gouy-Chapman theory is not satisfactory.

To alleviate the discrepancies between theory and practice, Stern (117) proposed a more elaborate model by combining Helmholtz-Perrin and Gouy-Chapman models. In this model, the space charges have been divided into two regions, a compact region next to the solid surface where adsorbed counter ions are allowed to interact specifically with the surface, and a diffuse region where remaining excess counter ions are distributed according to the Boltzmann distribution. The compact region can be considered to be a Helmholtz-Perrin condenser. Due to the geometrical restriction of hydrated ions or molecules, there is a charge-free thin layer defined by an inner Helmholtz plane as shown in Figure 2.1 (a) provided that there is no specific adsorption. Beyond this plane, the charge density decreases linearly as x increases until it reaches the boundary of a compact region and diffuse region. The slope of this decrease is determined by the adsorption density of counter ions which can be calculated from the Langmuir isotherm (125). Therefore, the surface potential appearing in the Gouy-Chapman equation is not equal to the wall potential but to the potential in the plane of closest approach of the counter ions to the wall. In the diffuse region, however, the Gouy-Chapman theory can be applied with some modifications. Instead of using the Boltzmann equation, Stern

(117) has constructed an ion distribution function in which the volume correction of ions has been introduced. For the compact region, the charge density has been derived from the adsorption density of specific adsorbing ions, which is given by the Stern-Grahame equation (88).

The contributions from Helmholtz-Perrin, Gouy-Chapman and Stern-Grahame form the basis of modern double layer theory. According to the Stern-Grahame model, the total condenser of a double layer is equivalent to two individual condensers in series, one representing the compact region and the other representing the diffuse region. The overall capacity of a double layer is, therefore, given by:

$$\frac{1}{C_{overall}} = \frac{1}{C_{inner}} + \frac{1}{C_{diffuse}} \quad . \quad [2.81]$$

Equation [2.81] indicates that introducing the compact layer virtually decreases the overall capacity of the interfacial region. Since the capacity of a diffuse region can be readily calculated using the Gouy-Chapman theory and the overall capacity can be measured experimentally for simple systems, the capacity of the compact region can, then, be evaluated from Equation [2.81]. Therefore, this relationship provides an important means for one to study the features of an electrical double layer and to test the validity of various theories.

The experimental results and calculations conducted for the systems of silver halide (126) and mercury (127) aqueous solutions of different electrolytes collectively show that at low potentials, a diffuse layer predominates and the Gouy-Chapman theory holds fairly well. Also found from these measurements and calculations is that the influence of co-ions is apparently negligible. It has been suggested that the Stern-Grahame model is important only when the specific adsorption of counter ions is involved. A number of other models have been developed on the basis of the Stern-

Grahame model for some particular systems as reviewed by Usui (99) and Hunter (86). Since the general form derived from the Stern-Grahame model is complicated and some quantities involved in this theory are inaccessible, the Gouy-Chapman theory with the Debye-Hückel approximation is commonly used in discussing the electrical double layer interactions as long as there exist no specific adsorbing ions in the aqueous phase.

2.3.4 Electrostatic Interaction between Electrical Double Layers

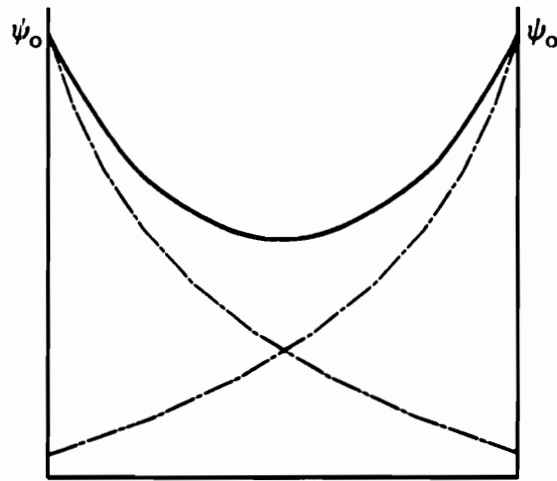
It is obvious that an electrostatic force will arise when two charged particles embedded in electrolyte solution are brought close to each other where partial double layers around each particle overlap. The magnitude of the force is determined collectively by the distribution of the space charge, the electrical potential between colloidal particles, the electrostatic boundary conditions at their surfaces, and the distance between two interacting particles. Qualitatively, with larger surface potential and lower ionic strength of solution, the interaction will be stronger and will extend over a longer range. Electrostatic double layer force becomes increasingly significant as the double layers around two interacting particles overlap more.

The electrostatic boundary conditions, i.e., charging mechanisms, are also an important parameter in determining the electrostatic potential energy of interaction. In general, two distinct boundary conditions are encountered (128-129). If electrochemical equilibrium between the surface and the bulk solution is maintained during the approach, such as the interactions between mineral oxides and insoluble inorganic salts, the electrical potential at the solid/liquid interface is assumed to be constant during the process of overlap of the double layers (130). Lack of adsorption equilibrium or shortage of potential-determining ions usually causes the surface charge density to be constant upon overlap of double layers (78). The electrostatic interactions between bubbles,

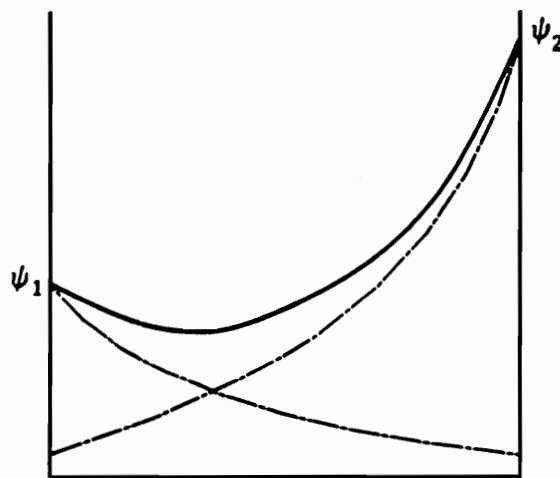
oil droplets in the presence of surfactant, and faces of clay particles are usually considered to be of constant surface charge density. Obviously, there are some systems in which one type of particles is of a constant surface potential and the other is of a constant surface charge density, during double layer interaction. Such systems include dispersions of clay particles; complex dispersions of clay and oxide, silicate or inorganic salt minerals; flotation systems involving air bubbles and oxide, silicate, or inorganic salt mineral particles in the presence of ionic surfactants; and oil flotation and industrial emulsion systems involving oil/aqueous emulsion and oxide, silicates, or inorganic salt mineral particles. In each of these systems, the interaction can be considered to be intermediate between constant surface potential and constant surface charge density, termed *mixed interaction model*. It has been found that interaction energy is independent of the choice of constant surface potential or constant surface charge density at large separations, but a stronger repulsion is predicted from the model of constant surface charge density than that predicted from the model of constant surface potential at small separations (131).

The electrostatic interaction potential has been formulated via either the force method or the free energy method (99). For the purpose of illustration, the interaction energy between electrical double layers of flat surfaces will be derived for a constant surface potential model using these two methods, respectively. The formula for the interaction of other geometric objects of different double layer boundary conditions can be obtained by either extending the solution of a flat double layer under constant surface potential conditions or by using similar procedures directly.

A typical electrical potential profile between two flat double layers of surface potential, ψ_0 , at a separation of $2d$ is schematically shown in Figure 2.2 (a). The dashed lines in Figure 2.2 (a) represent the potential profile of each plate without the influence of a second plate, which is given by Equation [2.76] corresponding to the Gouy-



(a)



(b)

Figure 2.2. Schematic Representation of Electrical Potential between Two Charged Surfaces

- a. Two Charged Surfaces of Same Potential
- b. Two Charged Surfaces of Different Electrical Potentials of Same Sign

Chapman double layer model with the Debye-Hückel approximation also involved, while the solid line is the summation of two single potential profiles. For convenience, a thin liquid element parallel to a solid surface is considered, on which two distinct forces are exerting, one due to the electrostatic force of a solid and the other due to the osmotic pressure of accumulation of ions in the diffuse layers. According to the electrostatic theory, the electrostatic force per unit volume, F_{el} , is given by the product of the charge density and the electrical field strength, i.e.,

$$F_{el} = \rho \frac{d\psi}{dx} . \quad [2.82]$$

The force acting on the volume element due to the osmotic pressure is given by:

$$F_{os} = \frac{dp}{dx} . \quad [2.83]$$

At equilibrium, these two forces must balance with each other, i.e.,

$$F_{os} + F_{el} = \frac{dp}{dx} + \rho \frac{d\psi}{dx} = 0 . \quad [2.84]$$

Inserting Equation [2.63] into Equation [2.84] to eliminate the volume charge density leads to:

$$\frac{dp}{dx} - \frac{\epsilon}{4\pi} \frac{d^2\psi}{dx^2} \frac{d\psi}{dx} = 0 . \quad [2.85]$$

By using the identity that

$$\frac{d^2\psi}{dx^2} \frac{d\psi}{dx} = \frac{1}{2} \frac{d}{dx} \left(\frac{d\psi}{dx} \right)^2 , \quad [2.86]$$

Equation [2.85] can be readily written as:

$$\frac{d}{dx} \left[p - \frac{\epsilon}{8\pi} \left(\frac{d\psi}{dx} \right)^2 \right] = 0 . \quad [2.87]$$

Equation [2.87] indicates that two influences of pressure and electrical field operating within the solution have a net effect that remains constant at any point between flat plates. This finding provide a convenient way to relate the interaction force of two flat double layers with the surface potential. To do this, a situation of two plates with the same surface potential, as shown in Figure 2.2, becomes helpful since ψ goes through a minimum at the middle between two plates where $(d\psi/dx) = 0$. Inserting Equation [2.66] for the case of z:z electrolyte into Equation [2.84] and integrating the resultant equation with respect to x from $x = \infty$, where $\psi = 0$ and $p = p_0$, to $x = d$, where $\psi = \psi_d$ and $p = p_d$, yield:

$$\int_{p_0}^{p_d} dp = \int_0^{\psi_d} -ze n_0 \left[\exp\left(-\frac{ze\psi}{kT} \right) - \exp\left(\frac{ze\psi}{kT} \right) \right] d\psi . \quad [2.88]$$

Equation [2.88] can be explicitly expressed as:

$$p_d - p_0 = 2kTn_0 \left[\cosh\left(\frac{ze\psi_d}{kT} \right) - 1 \right] = F_R , \quad [2.89]$$

where F_R represents the osmotic force per unit area due to the excess pressure ($p_d - p_0$) at $x = d$, with which the plates are driven close. This force can be reasonably assumed to be balanced by the electrostatic double layer force to maintain two flat double layers to equilibrate at a separation of $2d$.

In the case of weak interactions, Equation [2.72] can be used as the potential of each approaching surface, and the potential at the midpoint can be expressed, as an approximation, by:

$$\psi_d = \psi_1 + \psi_2 = 2 \left(\frac{4kT\gamma}{ze} \right) \exp(-\kappa d) . \quad [2.90]$$

According to this approximation, the electrostatic double layer force as given by Equation [2.89] can be simplified, by expanding $\cosh(ze\psi_d/kT)$ as a power series with only the leading term being retained, to:

$$F_R \simeq 64n_0kT\gamma^2 \exp(-2\kappa d) . \quad [2.91]$$

With the obtained expression of electrostatic double layer force, an interaction energy can be readily obtained since the energy simply equals the force times the distance through which it operates, as given by:

$$dV_R = -F_R d(2d) , \quad [2.92]$$

where a minus sign appears because the potential energy decreases with increasing separation distance. Inserting Equation [2.91] into Equation [2.92] and integrating the resultant equation from $2d = \infty$, where $V_R = 0$, to a given separation of $2d$ lead to:

$$V_R = \frac{64n_0kT\gamma^2}{\kappa} \exp(-2\kappa d) . \quad [2.93]$$

Alternatively, Equation [2.93] can be derived from the free energy change of a double layer formation. The free energy of a double layer per unit area formed at constant surface potential is customarily expressed as (99):

$$G_{dl} = G_{ch} + G_{el} = -\sigma\psi_0 + \int_0^\sigma \psi'_0 d\sigma' , \quad [2.94]$$

where ψ'_0 and σ' are surface potential and surface charge density, respectively, at each stage of establishing a double layer. G_{ch} in Equation [2.94] represents the chemical contribution of double layer formation free energy associated with the adsorption of potential-determining ions to acquire surface charge, while G_{el} represents the electrical contribution associated with the formation of a diffuse region due to the electrical work. In general, G_{dl} is negative because of the significant contribution of a chemical term ($G_{ch} = -\sigma\psi_0$), which is negative in sign, indicating that double layer formation is a spontaneous process. Integrating Equation [2.94] by parts yields:

$$G_{dl} = -\int_0^{\psi_0} \sigma' d\psi'_0 . \quad [2.95]$$

Under the assumption of small surface potential, Equation [2.80] can be inserted into Equation [2.95] to give:

$$G_{dl} = -\frac{1}{2} \sigma\psi_0 . \quad [2.96]$$

The potential energy of interaction between two flat double layers, V_R , equals the free energy change associated with bringing them from infinity to a separation of $H = 2d$, i.e.,

$$V_R = \Delta G_{dl} = 2G_{dl}^{2d} - 2G_{dl}^\infty . \quad [2.97]$$

By assuming that the surface potential remains constant when two plates approach closer, only the surface charge density at a plate separation of $2d$ needs to be known to calculate the potential energy using Equation [2.97]. In order to obtain surface charge density using Equation [2.78], the gradient of potential distribution between two flat surfaces immersed in an electrolyte solution as a function of separation distance, $2d$, needs to be known. Since the potential distribution between two flat double layers of the Gouy-Chapman type can still be described by a one-dimensional *PB* equation as given by Equation [2.67], the only difference from the case of single double layer has been found in the boundary conditions. For the convenience of the derivation, the substitutions of $y = ze\psi/kT$ and $\xi = \kappa x$ can be introduced into equation [2.67], where κ has been given by Equation [2.71] or [2.75]. As a result, Equation [2.67] for a system containing ions of one valency is simplified to:

$$\frac{d^2 y}{d\xi^2} = \sinh y , \quad [2.98]$$

with boundary conditions being transferred to be $y|_{x=d} = u = ze\psi_d/kT$ and $(dy/d\xi)|_{x=d} = 0$. After integrating Equation [2.98] once, one obtains:

$$\frac{dy}{d\xi} = -\sqrt{2 \cosh y - 2 \cosh u} . \quad [2.99]$$

Equation [2.99] can be rewritten in integral form as:

$$\int_v^u \frac{dy}{\sqrt{2(\cosh y - \cosh u)}} = -\int_0^{\kappa d} d\xi = -\kappa d , \quad [2.100]$$

where v is given by y at $x = 0$ as $v = ze\psi_0/kT$. At small values of v and u , expanding exponential terms and retaining the linear portions give an approximate substitution of:

$$2 \cosh v - 2 \cosh u = v^2 - u^2 = v^2 \left(1 - \frac{u^2}{v^2} \right). \quad [2.101]$$

Inserting Equation [2.101] into Equation [2.100] yields:

$$\begin{aligned} \kappa d &= \int_u^v \frac{dy}{\sqrt{2 \cosh y - 2 \cosh u}} \\ &= \int_u^v \frac{dy}{\sqrt{y^2 - u^2}} = \ln \left[\frac{v + \sqrt{v^2 - u^2}}{u} \right]. \end{aligned} \quad [2.102]$$

Rearranging Equation [2.102] to express v/u explicitly in terms of κd leads to (116, 132):

$$\frac{v}{u} = \cosh \kappa d. \quad [2.103]$$

By inserting equations [2.71], [2.101] and [2.103] into Equation [2.102] and transferring $dy/d\xi$ back to $d\psi/dx$, one readily obtains:

$$\left(\frac{d\psi}{dx} \right)_{x=0} = - \left(\frac{8\pi n k T}{\epsilon} \right)^{\frac{1}{2}} v \tanh \kappa d. \quad [2.104]$$

Thus, the surface charge density at a separation of $2d$ between two flat double layers can be obtained as:

$$\begin{aligned} \sigma &= - \frac{\epsilon}{4\pi} \left(\frac{d\psi}{dx} \right)_{x=0} = \frac{\epsilon \kappa k T}{4\pi z e} v \tanh \kappa d \\ &= \frac{\epsilon \kappa}{4\pi} \psi_0 \tanh \kappa d. \end{aligned} \quad [2.105]$$

Substituting σ in Equation [2.96] with Equation [2.105] leads to:

$$G_{dl}^{2d} = -\frac{\epsilon\kappa}{8\pi} \psi_0^2 \tanh \kappa d \quad [2.106]$$

and
$$G_{dl}^{\infty} = -\frac{\epsilon\kappa}{8\pi} \psi_0^2 . \quad [2.107]$$

Equation [2.107] in the above has been obtained from Equation [2.106] in which $\tanh \kappa d = 1$ as $2d \rightarrow \infty$. By inserting equations [2.106] and [2.107] into Equation [2.97], one obtains

$$\begin{aligned} V_R &= \frac{\epsilon\kappa}{4\pi} \psi_0^2 (1 - \tanh \kappa d) \\ &= \frac{2n_0 kT}{\kappa} z^2 (1 - \tanh \kappa d) . \end{aligned} \quad [2.108]$$

For the weak interaction, the approximate relationships of $1 - \tanh(\kappa d) = 2 \exp(-2\kappa d)$ and $v = 4\gamma$ can be used to obtain:

$$V_R = \frac{64n_0 kT}{\kappa} \gamma^2 \exp(-2\kappa d) , \quad [2.109]$$

which is identical to Equation [2.93]. This is the direct result of the circumstance that both force and free energy methods are based on a double layer theory involving the equilibrium between the electrical and osmotic forces acting on the ions in the solution (116, 132).

It is obvious that the electrostatic double layer interaction potential illustrated in the preceding derivation for two flat solid surfaces of infinite size, at constant surface potential of equal value, only accounts for very limited situations in practice. The assumption of weak interaction used in the derivation to obtain a simple analytical expression further restricts the direct applications of the solution. Nevertheless, the procedures used in the above derivations can be applied to more complicated systems, such as the interactions between two spheric or a spheric and a flat double layers under

different interaction models, constant surface potential model, constant surface charge density model, mixed interaction model, or regulation model.

The electrostatic interaction potential for two flat surfaces of infinite size with different constant surface potentials has been derived by Derjaguin (133-134) using the force method. The same system has been analyzed by Hogg et al. (135) using the Verwey-Overbeek method of calculating the free energy change associated with double layer overlap in which the Debye-Hückel approximation has been assumed. In this treatment, the *PB* equation has been solved by using the boundary conditions of $\psi = \psi_1$ at $x = 0$ and $\psi = \psi_2$ at $x = 2d$, where ψ_1 and ψ_2 are the surface potential of flat surfaces 1 and 2, respectively. The interaction potential derived as such is given by:

$$V_R = \frac{\epsilon\kappa}{8\pi} [2\psi_1\psi_2\text{cosech } 2\kappa d + (\psi_1^2 + \psi_2^2)(1 - \text{coth } 2\kappa d)] . \quad [2.110]$$

By letting $\psi_1 = \psi_2 = \psi_0$, Equation [2.110] can be readily simplified to Equation [2.109], which accounts for the interaction between two similar flat double layers.

It is understandable that the force of interaction between two similar double layers is always repulsive at any separation. According to the constant surface potential interaction model, however, the force of interaction between two dissimilar double layers of the same sign changes from a repulsion to an attraction after passing through the maximum, as analyzed theoretically by Usui (134). This phenomenon has been attributed to the sign reversal of the surface charge on a surface of low surface potential when the two plates approach closely. It has been found that the separation at which the maximum occurs depends upon the ratio of two potentials, while the value of the energy barrier is determined solely by the value of low surface potential. This is because at this location, the double layer with higher surface potential becomes the same as in the initial state, which results in the cancellation of the $G_{d_2}^{2d}$ and $G_{d_2}^{\infty}$ terms in the energy

change equation. Also found in this analysis is that the larger the ratio, the greater the distance of separation at which V_r shows a maximum.

The interaction energy on the basis of the constant surface charge density model has been derived by Frens and Overbeek (131, 136) for two similar flat double layers. In their derivation using the energy method, the charge density obtained by solving the one-dimensional *PB* equation using the Gouy-Chapman double layer model has been assumed to be a constant regardless of the separation between two interacting double layers. Since the interaction at a constant surface charge density is not accompanied by the adsorption of potential-determining ions, only the change associated with the electrostatic terms needs to be considered. Bell and Peterson (137) have analyzed the interactions between two dissimilar double layers using Derjaguin's force method. From their studies, it has been found that based on the model of constant surface charge density, the interaction between two dissimilar double layers of the same sign is always repulsive in contrast to the model of constant surface potential, which predicts an attractive interaction at a small separation. Surprisingly, the interaction between two double layers of surface electrical potentials different in magnitude and opposite in sign becomes repulsive when they approach in close proximity according to the model of constant surface charge density, in contrast to the model of constant surface potential, from which the interaction has been predicted to be always attractive.

Interactions between a double layer of constant surface potential and a double layer of constant surface charge density, known as the mixed interaction model, has been studied by Kar et al. (138). The linear one-dimensional *PB* equation of the Gouy-Chapman's electrical double layer model has been solved using the boundary conditions that $\psi = \psi_1$ at $x = 0$ and $(d\psi/dx) = 4\pi\sigma_2/\epsilon$ at $x = 2d$ in their study. Then, the energy approach developed by Verwey and Overbeek has been adopted to derive a relation for the potential energy of interaction. The comparison has been made by calculating the

potential energy at given surface potentials using theories corresponding to three different interaction models. It has been shown that the potential energy calculated using the theory of a mixed interaction model lies between those calculated using the theories of constant surface potential and constant surface charge density for all separation distances studied. Like the case of constant surface potential, the mixed interaction model shows a continuous readjustment of the charge density at the solid/aqueous interface of constant surface potential during the interaction. As a consequence, an electrostatic potential energy barrier and an attractive interaction region at small separation have been predicted from the mixed interaction model, even though the surface potentials are of the same sign but have different magnitudes.

The constant surface potential, constant surface charge density and mixed interaction models only represent idealized situations. The real conditions are much more complicated. Frens, Engel, and Overbeek (139) have analyzed the Brownian motion in colloidal dispersions and found that average collision time is about 10^{-7} sec. Within such a short period, the distorted double layers at each stage of approach are unlikely to be restored in order to maintain electrochemical equilibrium, which takes about 1 sec. This finding suggests that the constant surface potential model is unrealistic for describing the electrostatic double layer interactions between colloidal particles. According to the constant surface charge density model, however, the surface potential approaches infinity as the distance between two surfaces becomes very small (140), which is unrealistic also. These unrealities provided the impetus for developing a regulation model (141-143).

Using the concept of surface site dissociation equilibrium, Ninham and Parsegian (141) have derived a set of transcendental equations for self-consistent values of surface charge density and surface potential at all separations for any given set of bulk parameters. Since similar planar double layers of the Gouy-Chapman model with finite size

have been dealt with, the one-dimensional *PB* equation has been solved with two Gaussian boundary conditions of $(d\psi/dx)_{x=d} = 0$ and $(d\psi/dx)_{x=0} = -4\pi\sigma/\epsilon = 4\pi e\alpha/\epsilon S$, where α is the degree of dissociation and S is the surface area per ionizable group. From the potential distribution expressed explicitly in terms of elliptic functions, the electrostatic interaction force of double layers has been obtained using Verwey and Overbeek's approach (116).

Numerical solutions to the problem have shown that significant deviations from bulk electrolyte concentrations occur within a few multiples of $1/\kappa$. The surface concentration of divalent ions has been found to be practically the same as that of univalent ions even though the ratio of their bulk concentrations is as low as 0.025. As a consequence, the electrostatic force is reduced by more than 25%, presumably explaining the observed sensitivity of colloidal dispersions to the concentrations of divalent and trivalent ions. The surface *pdi* concentration has also been found to decrease as two double layers approach closer, indicating a decrease in surface charge density. This decrease is indirect evidence for the changes in surface potential as indicated in the Boltzmann distribution equation (Eq. [2.65]). This further suggests the importance of using the regulation model.

Chan et al. (142-143) have extended Ninham and Parsegian's method to a general amphoteric surface involving surface site equilibria. The equilibria have been assumed to be maintained by equal chemical potential of the *pdi* at any stage of interaction. Therefore, the regulation model is sometimes called the constant chemical potential model. From the numerical calculation, they have suggested that if the conditions limit the regulation of surface potential and surface charge density, both surface potential and surface charge density will change significantly during the interaction; otherwise, the conditions which are favorable for regulation will minimize the changes in surface potential and surface charge density during the interaction. They have ascribed the regu-

lation to a feedback phenomenon that as the double layers approach each other, the potential begins to rise, thereby decreasing the surface concentration of pdi . As a result, the surface dissociation occurs to maintain equilibrium so that the surface charge density decreases and, in turn, the surface potential decreases. The feedback mechanism works because of the buffer capacity of the surface, and regulation will minimize the surface potential changes at the expense of the surface charge. According to the regulation model, the surface charge reaches zero when two surfaces come in contact. They have also found that when the system can be regulated, the surface potential is kept remarkably constant during the approach compared with the interaction at constant surface charge density, and have suggested that the constant surface potential model is a case of perfect regulation, while the constant surface charge density model is a case of poor regulation.

The electrostatic interaction between two dissimilar flat double layers has also been investigated using the regulation model by Chan et al. (143). The boundary conditions of $(d\psi/dx)_{x=0} = -4\pi\sigma_1/\epsilon$ and $(d\psi/dx)_{x=2d} = 4\pi\sigma_2/\epsilon$ have been used in this case. The complex potential and, hence, the interaction behavior has been predicted from this model. Since the interaction potential of double layer overlap predicted from the regulation model always lies between those predicted from the constant surface potential and the constant surface charge density models, respectively, the interaction potential curve for two dissimilar double layers of the same sign may show multiple energy barriers or may not show any energy barrier, depending upon the regularity of the surface charge density, the surface potential and the solution conditions, according to the regulation model. A complete solution to this problem requires three types of elliptical functions for different separation ranges. The details of the arguments and the solutions can be found in the authors' original paper (143). The complexity of this approach materially restricts the application of this model to practical problems.

Theoretically, the interaction potential between two spherical double layers can be obtained using either the force method or the energy method in which approximate analytical solutions of the *PB* equation under proper boundary conditions are required (116). The solutions for the problem, however, are not in a simple analytical form and the application of this method is limited because of the complexity and mathematical difficulty. Instead, Derjaguin's approximate method (144) has been commonly used for practical purposes due to its simplicity and reasonable accuracy. This method is applicable as long as the range of the interaction is small compared with the radii of the interacting particles. Because the interaction between spherical double layers is encountered in practice for various areas of interest, the derivation of interaction potential using Derjaguin's method for two dissimilar spherical particles of different radii, as proposed by Hogg et al. (135), is given in the following as an example.

In this approach, the surfaces of the spheres are divided into a series of infinitesimally small ring elements with their centers on the axis of symmetry, as shown schematically in Figure 2.3. The interaction between double layers around two spheres may be considered to be made up of contributions from each pair of rings cut out of two spheres. Under the assumption of small separation, any pair of rings can be reasonably assumed to be parallel flat plates. According to the geometry shown in Figure 2.3, the contribution of interaction from each pair of rings is given by:

$$\delta V_R = 2\pi h(G_{d11}^H + G_{d22}^H - G_{d11}^\infty - G_{d22}^\infty)\delta h , \quad [2.111]$$

where H is the distance between two rings and h is the radius of each ring, with subscripts 1 and 2 representing the double layers around particles 1 and 2, respectively. It can be readily shown from Figure 2.3 that:

$$H - 2d = a_1 + a_2 - \sqrt{a_1^2 - h^2} - \sqrt{a_2^2 - h^2} . \quad [2.112]$$

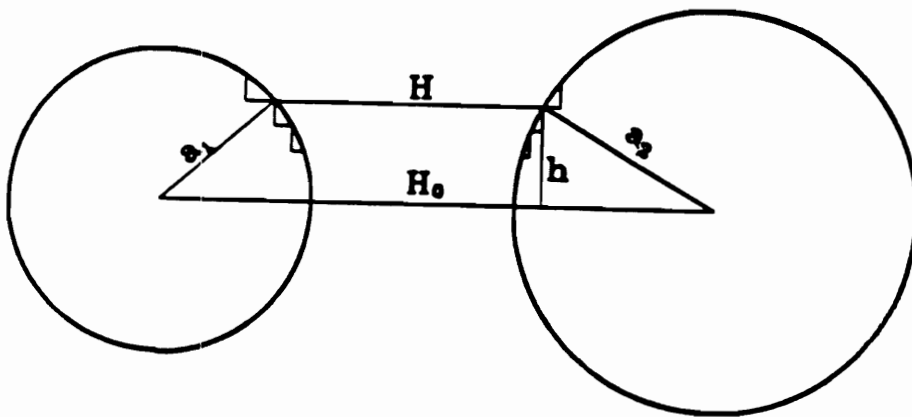


Figure 2.3. Schematic Illustration Showing the Extension of Flat Double Layer Interaction to Spherical One

Differentiating both sides of Equation [2.112] leads to:

$$dH = \left(\frac{1}{\sqrt{a_1^2 - h^2}} + \frac{1}{\sqrt{a_2^2 - h^2}} \right) h dh , \quad [2.113]$$

which, under the assumption of small separation, is simplified to:

$$h dh \approx \left(\frac{a_1 a_2}{a_1 + a_2} \right) dH . \quad [2.114]$$

Inserting Equation [2.114] into Equation [2.111] and summing up all pairs of rings yield an expression for calculating the total electrostatic potential between two double layers around two spheres, as given by:

$$V_R = \sum \delta V_R = \frac{2\pi a_1 a_2}{a_1 + a_2} \int_{2d}^{\infty} (G_{dl1}^H + G_{dl2}^H - G_{dl1}^{\infty} - G_{dl2}^{\infty}) dH . \quad [2.115]$$

The use of Equation [2.115] implicitly assumes that the interaction of each pair of rings is not influenced by the adjacent elements. This argument is equivalent to recognizing that the lines of force remain parallel to the axis connecting the centers of two spheres. In order to get a simple expression, the upper limit of integration is set to infinity although the highest value of the upper limit having any physical sense should be $(a_1 + a_2 - \sqrt{a_1^2 - a_2^2} + 2d)$. The error introduced from this assumption is under 1% since the pairs of rings making important contributions should be practically parallel and the contributions from the rings far from the axis are negligible.

Equation [2.115] is a general relation for calculating the electrostatic interaction potential between two double layers around two spheres from known functions of electrostatic interaction potential between two flat double layers of different interaction models. In the case of the constant surface potential interaction model, Equation [2.110]

can be inserted into Equation [2.115], and the resultant equation can be integrated to obtain (135):

$$V_R = \frac{\varepsilon a_1 a_2 (\psi_{01}^2 + \psi_{02}^2)}{4(a_1 + a_2)} \left[\frac{2\psi_{01}\psi_{02}}{(\psi_{01}^2 + \psi_{02}^2)} \ln\left(\frac{1 + \exp(-2\kappa d)}{1 - \exp(-2\kappa d)}\right) + \ln[1 - \exp(-4\kappa d)] \right]. \quad [2.116]$$

It has been suggested that Equation [2.116] is a good approximation for magnitudes of ψ_{01} and ψ_{02} less than 60 mV (135) and a product of κa greater than 10 (116), which are usually satisfied in systems of mineral dispersions. It is interesting to note that for two similar spheres of radius, a , and surface potential, ψ_0 , Equation [2.116] is reduced to:

$$V_R = \frac{\varepsilon a \psi_0^2}{2} \ln[1 + \exp(-2\kappa d)], \quad [2.117]$$

which is identical to that derived by Derjaguin (144). The expression for the electrostatic interaction potential between flat and spherical double layers can be readily obtained from Equation [2.116] by letting a_1 or $a_2 \rightarrow \infty$. The electrostatic interaction potential between two double layers around two spheres, or between one sphere and one plate, under a constant surface charge density model (145) or a mixed model (138) has been derived in a similar way by choosing proper functions for the interactions between flat double layers. However, there is no corresponding expression for the case of the regulation model because one cannot find a simple relation describing the interaction between flat double layers as required when using Derjaguin's integration procedures.

In recent studies, an improvement (109) has been made by including higher order terms in the Debye-Hückel linear approximation, which involves an increasingly com-

plicated mathematical treatment. The significant increase in the complexity of the mathematics, compared with the limited improvement that can be achieved, has brought researchers back to the use of a simple approximate expression.

It has been realized that the results predicted based on these electrostatic models are, at most, as good as the assumptions made in solving the *PB* equation to obtain potential distributions. Other than the imperfections inherent in the Gouy-Chapman theory as discussed earlier, two additional drawbacks are worthy of mention. One comes from the assumption that the distribution of ions in diffuse double layers is determined solely by their valency and not by their volume, shape, and polarizability. As a consequence, the theory is unable to discern among Li^+ , Na^+ , and K^+ . In other words, the theory is nonspecific. However, it has been found that the coagulation ability of these ions to As_2S_3 -sol increases in the order of Li^+ , Na^+ , and K^+ with the corresponding critical coagulation concentrations being 58, 51, and 49.5 *mM*, respectively (146).

The other drawback is due to the assumption that the surface charges on the particle and the space charges in the solution are smeared out. Israelachvili (5) has shown from a simplified model that near the surface, the effect of the discrete ion on the overall electrostatic interaction is substantial. Fortunately, the excess field induced by the discrete ion effect decays extremely rapidly with a decay length of $y/2\pi$, where y is the distance between discrete charges on the order of 2 nm. It is for this reason that the smeared-out approximation works so well in considering the electrostatic interaction between charged surfaces. A more rigorous treatment as to the discrete ion effect has been given by Levine and Bell (147-148). In their treatment, two types of discrete ion effects relating to the adsorbed counter ions have been considered, one being the entropy correlation due to the ion size and the other being the difference between the actual electrical potential at an adsorbed counter ion and the average potential on the adsorption plane. By taking this effect, known as the discreteness-of-charge effect, into

account, a new negative term proportional to the density of the adsorbed counter ion has been added to the adsorption energy. This theory predicts that the critical coagulation concentration increases as the electrical surface potential increases when it is small, but then reaches a maximum and decreases as the potential increases further. This phenomenon is particularly important in the presence of polyvalent coagulating ions and is a consequence of the maximum in the potential at the *OHP*. Therefore, this phenomenon will not be observed if the discrete ion effect is ignored. This treatment has led to the conclusion that the Schultz-Hardy rule must describe a range of ratios of coagulating concentrations dependent on the specific adsorption characteristics of the counter ions.

2.3.5 *Experimental Approach to Electrostatic Double Layer Interactions*

Surprisingly, the first evidence for the correctness of the double layer theory was found by Derjaguin and Kussakov (53) from equilibrium wetting film measurements in 1936 when the theory had not been developed yet. Following up Derjaguin and Kussakov's work, Read and Kitchener (149), among others (150-151), have measured the thickness of equilibrium wetting films of dilute aqueous solutions of *KCl*, *LiCl*, *BaCl₂*, and *LaCl₃* on polished silica. The film thickness was measured under a given hydrostatic pressure as a function of electrolyte concentration. The experimental results show that the film thickness decreases with increasing salt concentration and valence of the cation under constant hydrostatic pressure. The repulsive pressure between plates at various separation distances has been calculated using a numerical solution of the nonlinear *PB* equation for the interaction of flat double layers (152). The calculated thickness-concentration lines agree broadly with that measured experimentally, con-

firming that the fundamental origin of the phenomenon is the diffuse electrical double layer.

The variation of double layer repulsion with the distance between the monolayers formed within a ring of porous porcelain in the presence of sodium dodecyl or tetradecyl sulfate has been studied experimentally by Mysels and Jones (153) from film pressure and thickness measurements. It has been found that at low ionic strength and surface potentials, the pressure measured follows that predicted from the theory of constant surface potential model under the Debye-Hückel approximation. Barclay and Ottewill (154) have measured the pressure of an assembly of sodium montmorillonite plates as a function of the separation distance between the plates down to 1 nm. The results obtained in the presence of $10^{-4} M NaCl$ show that the measured force is greater than that predicted using either the constant surface potential or the constant surface charge density model at separation distances less than 15 nm. With separation distances greater than 15 nm, the measured force is less than predicted. The discrepancy has been attributed to the assumption of the Debye-Hückel approximation used in developing the theory of electrostatic double layer force, which gives an inaccurate screening length, κ^{-1} . It seems that the fit between the experimental results and theory can be improved by adjusting the value of the screening length. The repulsive force exerted by diffuse electrical double layers on a glass and a rubber surface as a function of their separation distance has been measured by Roberts and Tabor (155). In their work, the compression phenomenon of a double layer by indifferent electrolytes has been directly observed experimentally.

The validity of the theory of electrostatic repulsion has been verified by more accurate direct force measurements (68, 156-161). It has been found (68) that in the presence of supporting electrolytes over the concentration range from 10^{-4} to $10^{-1} M$, the measured double layer repulsive forces between two mica surfaces are well described

by non-linear (exact) solution of the *PB* equation for two double layers interacting at constant surface potential. The effective surface potentials have been found to be constant as the surfaces approach each other and as the concentration of the electrolyte changes. However, at electrolyte concentrations higher than 10^{-2} *M*, a higher value of screening length than that theoretically calculated needs to be used to fit the experimental results into the theory. The effect of ionic valence on the force law has also been studied in Israechvili and Adams' work (68). As expected, the measured double layer forces are reduced significantly in the presence of $Ca(NO_3)_2$ or $BaCl_2$ than those measured in the presence of KNO_3 of the same concentration. The agreement between theory and experimental results becomes poorer in the presence of higher valency ions. The screening length has been found to be much lower than predicted from the theory, even in dilute solutions, and interactions appear to be intermediate between constant surface charge density and constant surface potential (156). By fitting the experimental results into the theoretical curve, Israechvili found that the surface potential is smaller than that obtained in a 1:1 electrolyte solution of the same concentration, indicating the occurrence of specific adsorption of these ions on the surface. One of the striking findings from these measurements (156) is that the outer Helmholtz plane (*OHP*), as shown in Figure 2.1, may be as far as 2.5 nm beyond the solid surface, which implies the existence of a structured aqueous region. As the surfaces approach closer than 5 nm, these structure layers break down, giving rise to an anomalous repulsive force known as the hydration force. Beyond *OHP*, the diffuse double layer theory holds well and the behavior of 1:1 electrolytes is well described by the *PB* equation, although that of 2:1 electrolytes is not.

The electrostatic repulsive forces between crossed glass filaments interacting in *KCl* solution have been measured by Rabinovich et al. (158). In an electrolyte concentration range of 10^{-5} to 10^{-3} *M*, the measured forces over separation distances greater

than 5 nm, where the van der Waals forces are negligible, decrease exponentially as the distance increases, with a logarithmic decrement equal to the theoretically predicted screening length. However, the screening length has been found to be greater than that predicted theoretically when the electrolyte concentration is higher than 10^{-2} M. It is interesting to note that all of the forces measured lie between those predicted from the models of constant surface potential and constant surface charge density, suggesting that a proper regulation model may need to be used to obtain the best fit with the experimental results, in particular at small separation distances.

Recently, Ducker and Pashley (159) have measured the interaction forces between two mica surfaces embedded in aqueous solutions of different electrolytes. Their measurements show that the forces measured lie close to that predicted from the electrostatic interaction theory of constant surface charge density. To explain the measured force behavior, a mass action model (160), in which the size of the hydration sheath is considered, has been developed. By incorporating a mass action model into the *PB* equation, a regulation model (161) has been developed with the dissociation constant and the hydrated ion area being determined from the analysis of the electrical potential results. With this model, an excellent fit has been found between experimental results and theoretical predictions (159-161).

Experimental studies on the electrostatic interaction between two electrical double layers collectively show that the *PB* equation is a good representation of the electrical double layer. The constant surface potential model and constant surface charge density model represent two ideal conditions and the regulation model can be considered to represent the real situations. Nevertheless, the constant surface potential model and constant surface charge density model can be a good approximation under particular conditions. The direct surface force measurement provides a good means for studying and testing the electrical double layer theory.

2.4 Structural Forces

2.4.1 Classical DLVO Theory

It has long been considered that the stability of lyophobic colloid particles in aqueous media depends on the nature of the total interaction energy between interacting particles. By lyophobic particles, it is meant that these particles interact weakly with the molecules of the dispersion medium. On the basis of van der Waals attractive forces and electrostatic double layer repulsive forces, a stability theory called DLVO theory has been developed to explain quantitatively the stability of lyophobic colloids and the role of simple electrolytes in destabilization (132). This theory is nowadays almost generally accepted as the basis of colloidal stability because it is theoretically sound and appears to be in general agreement with many experimental facts.

According to the classical DLVO theory, the total interaction energy between two particles embedded in a third liquid medium consists of two components, i.e.,

$$V_T = V_A + V_R , \quad [2.118]$$

where V_A and V_R are the attractive van der Waals and repulsive electrostatic double layer interaction energies. In the classical DLVO theory, the dispersing liquid has been assumed to be a structureless medium defined solely by its bulk dielectric permittivity. As discussed in the preceding two sections, the van der Waals attractive interaction energy decays with H^{-1} , while the electrostatic double layer repulsive interaction energy decays with $\pm \ln[1 \pm \exp(-\kappa H)]$ for two similar spherical particles, where H represents the face-to-face separation between two interacting particles, with the plus sign corresponding to the interaction under constant surface potential and the minus sign corresponding to that under constant surface charge density. From these characters, it is

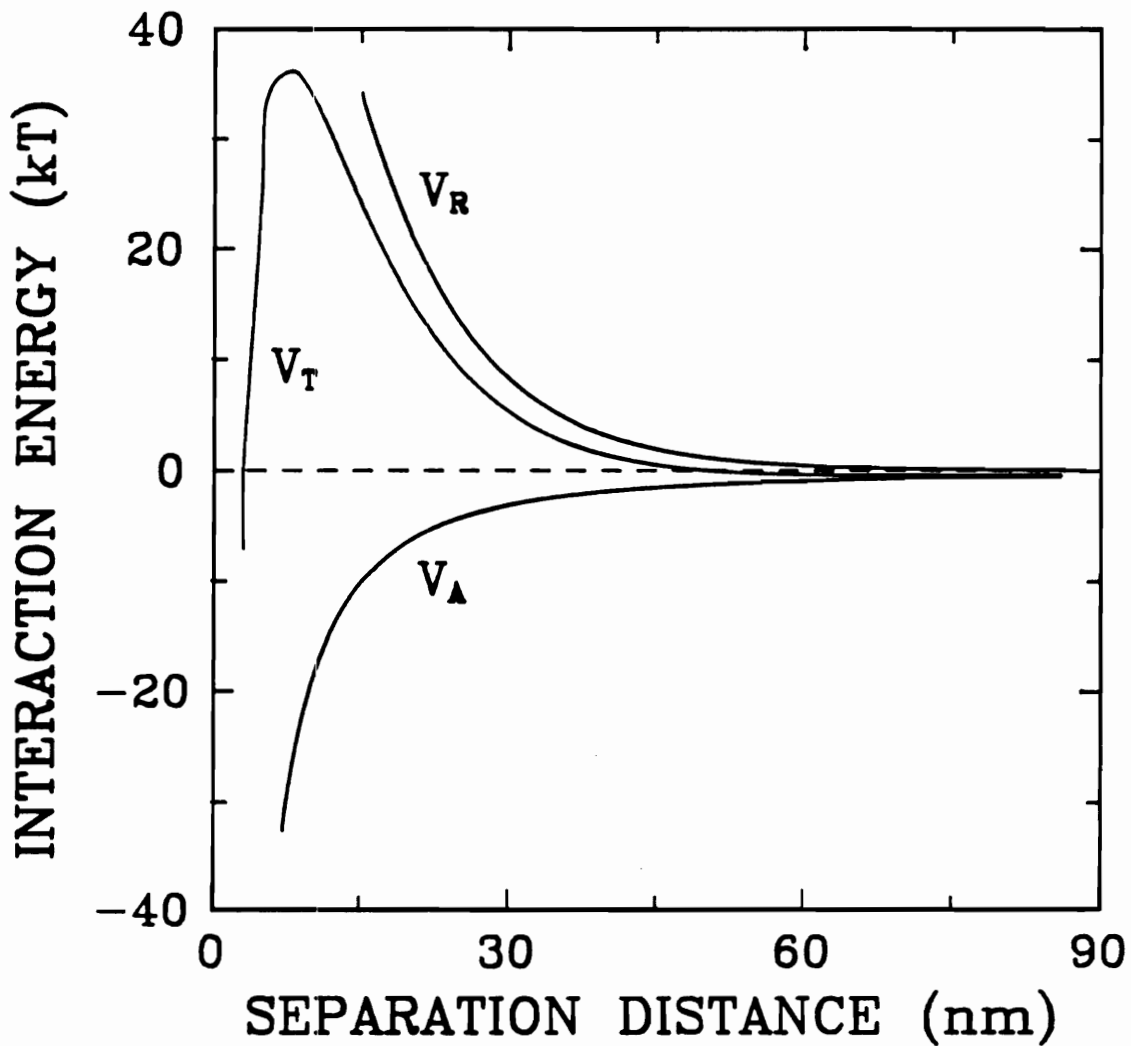


Figure 2.4. A Profile of Potential Energy versus Separation between Particles as Calculated Using the Classical DLVO Theory

Coal sample oxidized at 140 °C with $\psi_d = -5$ mV, $\kappa = 10$ nm and $A_{131} = 8.0 \times 10^{-2}$, corresponding to a critical coagulation condition of the sample

expected that at both large and very short distances of separation, the attractive energy exceeds the repulsive one. Therefore, the total interaction energy vs separation distance curve shows a minimum at a large separation, called the secondary minimum, and a maximum at an intermediate separation, as illustrated in Figure 2.4. By taking the Born repulsion into account, another minimum is expected at close proximity, which is not shown in Figure 2.4. The height of the maximum, called the energy barrier, has been customarily used as a criterion for the stability of lyophobic colloidal suspensions. If no barrier is present or the height of the barrier is negligible compared with the thermal energy, the net force of attraction will pull the particles toward each other and result in coagulation. The dispersion is, thus, considered to be unstable. However, if the height of the barrier is appreciable and the depth of the secondary minimum is small compared with the thermal energy, the particles will repel each other and the dispersion will be stable against coagulation. It is possible for particles to maintain at a separation distance where the secondary minimum is located if the depth of the minimum exceeds the thermal energy.

One of the successful applications of the classical DLVO theory is to explain the effect of supporting electrolyte concentrations on the stability of a colloidal dispersion as observed experimentally. It has been found experimentally (162-163) that the transition between dispersion and coagulation occurs at a certain value of supporting electrolyte concentration, termed the critical coagulation concentration (*ccc*), which is strongly dependent on the valence of the counter ions. Known as the Schulze-Hardy rule, the *ccc*'s of mono-, di- and trivalent coagulating ions have been found to be in the ratio of 1 to x to x^2 where x is about 1/30 to 1/40. This has been attributed to the fact that increasing the concentration and/or the charge number of the counter ions shortens the range of electric double layer repulsion, as reflected by a decrease in screening length. Therefore, the particles can approach each other very closely before repulsion is felt.

At such a close proximity, the significantly increased van der Waals forces materially decrease the height of the energy barrier. With a further decrease in screening length, the energy barrier will eventually disappear, resulting in coagulation. The strong influence of ionic valence, z , on the value of the Boltzmann term, $\exp(-ze\psi_0/kT)$, makes ccc sensitive to the valence of counter ions, as shown in Schulze-Hardy behavior. The ccc can, in principle, be found from the conditions of critical coagulation, as given by $V_T = (dV_T/dH) = 0$ (99, 164-165). From these two conditions, the ccc has been found to be inversely proportional to z^6 . However, at low surface potential approximations, solving the equations corresponding to critical coagulation condition leads to $ccc \propto z^{-2}$. It is interesting to note that the ratio of ccc 's for mono-, di- and trivalent ions, calculated from the classical DLVO theory, is in good agreement with that expected from the Schulze-Hardy rule. The ccc has been found to be rather sharp since a small change in supporting electrolyte concentration near its ccc easily changes the potential barrier by a few times kT (146).

Although coagulation is obviously a rate process with stability of the suspension being ascribed to virtually zero rate of coagulation, the classical DLVO theory focuses its attention more on the thermodynamics behind the rate process than on the rate processes themselves (129). The thermodynamics and kinetics of coagulation have been linked together by a stability ratio as proposed, by Fuchs (166). As pointed out in a monograph by Israelachvili and Adams (68), the DLVO theory has been extensively tested and viewed. Applications of this theory to aqueous dispersions have been confirmed by many experimental studies (167). An attempt to apply the classical DLVO theory to nonaqueous dispersions has been made by several investigators and it has been found that there are a number of systems in which experimental results can be explained by the theory (168-170). Recently, the theory has made inroads into biocolloidal phenomena (171) and successfully highlighted the forces involved in intercell and inter-

membrane interactions (172-173). Therefore, it is fair to say that the classical DLVO theory has withstood the test of time and endured as an unchanged pillar of colloid science (174). Most theoretical developments after the DLVO theory have served to improve and refine our understanding of the theory.

2.4.2 *Experimental Evidence of Non-DLVO Forces*

The success achieved by the classical DLVO theory based on the consideration of electrostatic double layer repulsion and van der Waals attraction only has detracted attention from the effects of liquid structure adjacent to the solid surfaces. (Experimental evidence of non-DLVO forces has been reported for a number of systems, including thin liquid layers confined between hydrophilic or strongly hydrophobic surfaces (175-177). These additional forces could be attractive or repulsive and their nature is more or less related to the structure of the liquid boundary layers. Therefore, this type of force may be called the structural component of surface forces, or solvation forces, which appear to be the commonly accepted terminology (175). Since solvation forces can be predicted by exact thermodynamic arguments (176), the focus should not be on their existence but, rather, on their form and magnitude and the way they are affected by the particle surfaces and the solvent. (An addition of simple electrolyte ions may weaken or enhance the solvation forces, depending upon how these ions affect the structure of the liquid.) It has been well documented that hydrophobic attraction is exhibited between the strongly hydrophobic surfaces, with the water advancing contact angle, θ_A , being greater than 64° , while hydrophilic repulsion becomes noticeable between hydrophilic surfaces with $\theta_A < 15^\circ$ (178). Therefore, the classical DLVO theory is applicable only to the systems in which the solid surfaces are partially wetted by the liquid phase.

Although the non-DLVO surface forces existing in a nonaqueous system are important in a number of areas (179), such as metal ore and coal particle extraction, water in oil microemulsions and surface forces in thin film lubrication, these applications are beyond the scope of the present work. A detailed review of the subject has been given by Christenson (175) and the present overview of non-DLVO forces is concentrated on aqueous systems.

The first recognition of this type of force may be attributed to Langmuir (180-181) who envisaged the measured repulsive force as being either electrostatic in origin or arising from a propagation of ordered water layers away from an interface, these essentially being due to short range forces passed on from molecule to molecule. At almost the same time, Derjaguin and Zorin (182) experimentally obtained the isotherms of the structural component of the so-called disjoining pressure. However, intensive investigations of the importance of structural forces did not start until after a fairly lengthy period of doubt as to their existence had been experienced (183). Derjaguin and Zorin's work was followed up by Pashley and Kitchener (184) who measured the polymolecular adsorption of water vapor on quartz. It was found from their studies that the range over which structural forces operate increases with the increased hydrophilicity of the solid substrate.

The additional non-DLVO forces have been found to play an important role in the stabilization of colloidal dispersions (185-187). When studying the stability of colloidal silica sols, Allen and Matijevic found (185) that the Schultz-Hardy rule is not applicable to silica sols and the stabilization of dispersions has been observed even at the pH value near their pzc where the classical DLVO theory predicts coagulation instead of dispersion due to van der Waals attraction predominating over the minimized electrostatic double layer repulsion. This remarkably high stability has been considered to originate from the water structure adjacent to the silica surface, which is not ac-

counted for in the classical DLVO theory. Similar behavior was observed by Depasse and Watillon (186) who studied the stability of amorphous colloidal silica and by Harding (187) who investigated the coagulation behavior of fumed silica. These studies showed that colloidal silica behaves as a lyophilic colloid under conditions where the silanolic surface is relatively undissociated, i.e., in acidic aqueous solutions. It was found (187) that although an untreated silica dispersion is stable over a pH range from 2.0 to 9.0, when the silica is methylated, converting the lyophilic surface to a lyophobic surface, a coagulated sediment appears at a suspension pH below 5. Since the measured electrical mobilities of treated and untreated silica samples are identical over a wide range of pH , the electrostatic repulsion for these two different samples is essentially the same. The different coagulation behavior for these two samples suggests that the additional repulsive forces operating between untreated silica particles is reduced by the sheltering of surface hydrophilic groups. The existence of additional repulsive interaction has also been inferred from the stability study of arachidic acid sols in which a stable dispersion has been observed even when colloids are of zero zeta potential (188).

From studying the stability of polyvinyl acetate colloidal dispersions of mono size as a function of temperature, Johnson et al. (189) found that the activation energy governing the coagulation process changes at higher temperatures for dispersions of larger sizes. This finding suggests that the additional energy barrier associated with water structure starts to break down at a higher temperature for larger particles, indicating that the magnitude and distance over which the repulsive potential due to water structure extends are greater for larger particles.

The existence of non-DLVO forces has also been demonstrated when studying the stability of air bubbles in aqueous solutions of various electrolyte concentrations (190). It has been found experimentally that air bubbles formed by passing gas through a fine sinter will coalesce to form larger bubbles as they ascend through a column of

water, and the addition of acids hardly affects the coalescence. However, the addition of simple electrolytes to a certain concentration prevents the bubbles from coalescing. The transition from coalescence to stabilization occurs within a narrow concentration range of electrolytes. Since this stabilization phenomenon of bubbles by simple electrolytes cannot be explained using the classical DLVO theory, it has been ascribed to the very strong repulsive force arising from the induced water structure of alkali or earth alkali metal ions adsorbed at an air/water interface (191). The concentration at which the transition occurs differs from one type of ions to another and may be collectively determined by their hydration degrees and adsorption densities.

The exponentially decaying repulsive forces have been obtained between lecithin bilayers from measuring the equilibrium osmotic pressure as a function of the lattice spacing detected by X-ray diffraction, as reported by LeNeveu et al. (192). Because they are independent of salt concentration, the measured forces are difficult to understand in terms of the classical DLVO theory. A similar behavior has been observed when measuring the swelling pressure of lamellar clay particles (193). However, the most straightforward evidence of non-DLVO forces stems from direct measurement of the total interaction forces between two macroscopic objects and subsequent comparison of the same forces calculated from the theory. Additional repulsive forces have been observed between hydrophilic surfaces embedded in aqueous solutions with face-to-face separations less than 10 times the molecular dimensions (158). The presence of hydrated ions on the solid/water interface has been found to enhance this additional repulsive force (118, 159, 194-196). This type of repulsive non-DLVO force has been recognized as a hydration force since it is measurable only when there exists a certain amount of hydrated ions on the solid surfaces. The repulsive hydration force has been considered as a result of the dehydration of hydrated cations during the approach of two surfaces.

The results reported by Rabinovich et al. (158) show that over a separation range less than 3 nm, the repulsive structural component of the interaction force between two glass filaments falls on one curve for all concentrations of simple electrolytes studied. The curve is of the exponential type with a decay length of 0.85 nm. At a separation greater than 3 nm, the structural component decreases as the electrolyte concentration increases, which has been ascribed to the destruction of the specific structure of boundary layer water under the influence of increasing concentration of electrolyte.

A similar result has been reported independently by Peschel et al. (197). In their measurements, the exponential decay length of additional non-DLVO forces has been found to be independent of simple electrolyte concentration but appears to increase in the order of $Li^+ < Na^+ < K^+$ in accordance with the lyotropic series (198). Their results suggest that the range of additional repulsive forces is controlled by both the structure of the bulk phase and the particular structure of the solid surface, including the pattern of adsorbed ions as proposed by Lyklema (199). A hydration layer of about 2.5 nm per surface can be inferred if the surface ordered water is considered to be formally composed of adsorbed and slightly immobilized clusters, each consisting of 240 water molecules (198). This layer thickness is in an excellent agreement with an experimentally observed separation range below which strong hydration forces are present.

More elegant force measurements have shown that this additional repulsive force oscillates around a mean profile which decays exponentially with the separation (1). The decay length is about 1.0 ± 0.2 nm (118, 183) and the amplitude of the oscillation decreases significantly as two surfaces are taken apart, with a periodicity being equal to the mean diameter of the liquid molecules. The nature of the exponential decay of repulsive non-DLVO forces has been ascribed to the hydration state of the surface hydrophilic groups or adsorbed cations, while the molecular origin of the oscillating forces may be attributed to the finite size of the solvent molecules (181). It has been found that the

maximum corresponds to a separation at which the lowest liquid density occurs within the gap, while the minimum corresponds to a separation at which the highest liquid density is retained within the gap. The decrease in oscillating amplitude with increasing separation indicates a more flexible or less layered structure of the liquid as it becomes more bulk-like. However, the oscillations can be smeared out if the liquid molecules are of irregular shape, which are unable to be packed into ordered layers, or when the surfaces are rough even at the simple molecular dimensions (200-201).

Systematic studies on the hydration forces (118, 159, 179, 194-196, 202) have been conducted by measuring the surface forces between mica surfaces in the presence of various types of electrolytes at different concentrations. The experimental results show that the strength of the repulsive non-DLVO forces depends on both the surface concentration of the hydrated ions and the hydration energy of the electrolytes, and is largely independent of ionic strength (156). For the surfaces on which no hydration species exists originally, a certain value of electrolyte concentration, termed the *threshold concentration*, is required to induce a substantial repulsive hydration force, which is specific for each type of cation. The value of the threshold concentration decreases as the free energy, associated with an ion exchange process between surface species and hydrated cations, decreases (194). In general, the threshold concentration is higher for divalent cations than for monovalent cations in the case of the mica/aqueous system. This is because the hydrated divalent cations are less tightly bound to the surfaces compared with hydrated monovalent cations. Consequently, when two surfaces approach each other, instead of dehydration of the hydrated divalent cations occurring on the surfaces, the cations are more readily removed from the surfaces, showing a less significant repulsive hydration force.

Other than repulsive hydration forces, attractive non-DLVO forces have been observed when measuring the interaction forces between two strongly hydrophobic sur-

faces (175, 177, 203). This attractive force is customarily termed *hydrophobic force* because its existence and behavior are closely related to the surface hydrophobicity. Since Pashley and Israelachvili published the direct evidence for the presence of a strong, long-range interaction between hydrophobic surfaces in 1981 (204-205), a great number of measurements of the force between various hydrophobic surfaces have been conducted (206-213). Systems investigated include methylated silica surfaces and mica surfaces deposited with a monolayer of cetyltrimethylammonium ions (*CTA*⁺), dihexadecyl-dimethylammonium acetate (*DHDAA*), dimethyldioctadecylammonium ion (*DDOA*⁺), *N*-(α -trimethylammonioacetyl)*O, O'*-bis(1*H, 1H, 2H, 2H, -perfluorodecyl*)*L*-glutamate chloride (*TMAAPFDG*), and *N*-methyl-*N*-(β -hydroxyethyl)-*N, N*-didodecylammonium bromide (*HEMDAB*). All the experiments collectively show that there exists an attractive non-DLVO force which decays exponentially as the distance separating the two interacting surfaces increases. This additional attraction is measurable to a separation of 90 nm (210, 213) and its strength exceeds the usual van der Waals forces by one to two orders of magnitude. The strength of the additional attraction increases with increasing surface hydrophobicity as determined by water contact angle (203). Early measurements with mica surfaces of less hydrophobicity showed that the measured attractive non-DLVO force can be reasonably described by an exponential function with only one decay length (205-207). However, in the case of more strongly hydrophobic surfaces, the measured attractive non-DLVO force shows a weaker tail. To fully describe the observed force behavior, an exponential function with two decay lengths needs to be used. One decay length is on the order of 1 to 3 nm for describing stronger, short range attractions and giving rise to the adhesion forces at zero separation, while the other is of greater value, varying significantly from one system to another, and describes essentially the weak tail behavior. Extrapolation of the exponential force law down to molecular contact predicts an adhesion force in good agreement with the measured ad-

hesion force and a solid/liquid interfacial tension consistent with that obtained from contact angle measurements (206, 208). The thickness of the monolayer has also been found not to affect the hydrophobic attraction dramatically (206), suggesting that the hydrophobic interaction does not require a thick hydrocarbon layer and the surface CH_2 and CH_3 groups are similarly hydrophobic.

It is interesting to note that the monolayer prepared with different methods may show different ranges over which attractive non-DLVO forces operate, with the deposition method giving the largest value (213). For example, the attractive non-DLVO force has been measured at a separation of 90 nm for mica deposited with a monolayer of *TMAAPFDG* in contrast to a reduced separation of 60 nm for mica adsorbed with a monolayer of *TMAAPFDG*. The reduction in the range of interaction has been attributed to an incomplete adsorption or additional adsorption of surfactant on the hydrophobic monolayer. A similar phenomenon has been observed for the mica surface covered with a monolayer of *CTA*⁺ (203). Only under optimal conditions may adsorbed monolayers give attractions of similar range. However, both types of surfaces exhibit the same interaction behavior at a separation shorter than 15 nm, where the measured adhesion force is the same.

Unlike the repulsive non-DLVO forces, the decay length claimed for attractive non-DLVO forces varies from 1 nm for mica with an adsorbed monolayer of *CTA*⁺ (204-205) to 15 nm for mica deposited with a monolayer of *TMAAPFDG* (210). Even though it appears that the decay length increases with the surface hydrophobicity, as indicated by a higher value of θ_A (178), a detailed survey shows a rather bewildering picture (175, 210). It has been found that the attraction is of a similar range and magnitude for mica surfaces deposited with a monolayer of *TMAAPFDG* and *DDOA*, respectively, although the advancing contact angles are quite different for these two types of monolayers, 113° and 93°, respectively (210). For the mica surface deposited with a

monolayer of *DHDAA*, a decay length of 1.4 nm (207) has been obtained as opposed to a longer decay length of 13 nm for the mica surface deposited with a monolayer of *DDOA*, although both types of surfaces give a similar advancing contact angle, as measured to be 94° and 93° , respectively. These results seem to indicate that there is no simple relation between surface hydrophobicity as measured by advancing contact angle and the range of hydrophobic attraction. But detailed analysis does show that the hydrophobic surfaces giving the most long-range attraction either are almost uncharged or carry only a very slight surface charge, giving negligible double layer repulsion. For surfaces prepared under similar conditions with $\theta_A > 90^\circ$, the range and the magnitude of the hydrophobic attraction are rather insensitive to the exact value of the contact angle.

Although it is believed that the net hydrophobic interaction is only marginally reduced with increasing electrolyte concentration (203), recent measurements (213) have shown that the simple electrolyte concentration affects the hydrophobic interaction significantly. Systematic investigations have demonstrated that as indifferent electrolyte concentration increases, the range of hydrophobic interaction decreases significantly while the preexponential factor increases substantially. For mica surfaces coated with a monolayer of *TMAAPFDG*, the decay length decreases from 16 nm to 1.5 nm and the preexponential factor increases from 2.2 *mN/m* to 60 *mN/m* continuously when the solution concentration of tetrapentylammonium bromide (*Pe₄NBr*) increases from 0 to 1×10^{-2} *M*. Similar behavior has been observed between *DDOA*⁺-covered mica surfaces embedded in different *KBr* solutions (208). However, over the short range regime, the hydrophobic interaction is much less sensitive to the electrolyte concentration as indicated by slight changes in the adhesion energy (213). The decreased range of hydrophobic interaction by increasing the electrolyte concentration has been attributed to the adsorption or exchange of ions onto hydrophobized surfaces, as indicated by an

increase in surface charge density. As a consequence, the surface hydrophobicity is reduced (213). However, it is questionable as to why reduced surface hydrophobicity shows a less pronounced effect on the hydrophobic interaction of shorter separation regime. It is possible that the presence of electrolyte ions between two hydrophobic surfaces will adjust and/or break the structure of a thin liquid layer and result in a less structured interlayer, giving rise to a reduced range of interaction. It remains unclear why the reduced surface hydrophobicity gives a higher value for the preexponential factor.

Since attractive hydrophobic forces and repulsive hydration forces arise from a changed state of water structure around hydrophobic and hydrophilic groups, it is not expected that these two types of forces are additive. Instead, it appears that when the local structure of water molecules is dominated by their interaction with the hydrophilic groups, the hydrophobic interaction is neutralized (206), a phenomenon having been experimentally proven. Investigations have shown that no hydrophobic attraction acts between surfaces composed of mixtures of hydrophobic and hydrophilic groups, such as the surfaces of ethylene oxide groups (214) or with adsorbed tetraalkylammonium ions (215). This indicates that a long-range hydrophobic attraction exists only between homogeneous hydrophobic areas larger than some critical size. Also interesting is that the non-DLVO force is less significant between a hydrophobic and a hydrophilic surfaces (216). The force measurement conducted between a negatively-charged hydrophilic mica surface and a positively-charged hydrophobic mica surface shows that attractive hydrophobic force is reduced significantly compared to that observed between two hydrophobic surfaces, if there is any (216). This agrees with what happens in flotation processes in which surface forces between two dissimilar surfaces play a crucial role. The air bubbles are believed to be inherently hydrophobic with an interfacial tension of 72 mJ/m^2 (203). Therefore, it is only when bubbles interact with hydrophobic mineral

particles that the hydrophobic attraction becomes dominant, resulting in hetero-aggregation and, hence, flotation. The hydrophobic interaction between air bubbles and hydrophilic particles is unlikely great enough to overcome repulsive dispersion and electrostatic double layer forces to form stable bubble/particle aggregates. Apparently, the hydrophobic attraction is the driving force for flotation and seems to be a most important factor in determining the selectivity of the flotation process.

2.4.3 The Structural Force Law

In the preceding section, it has been shown that the non-DLVO forces can be repulsive or attractive and the strength of these forces decreases exponentially as the interlayer thickness increases, regardless of the nature of them. In general, the interaction energy due to structural forces can be expressed by (205):

$$V_S(H) = R(K_1 D_{01} e^{-H/D_{01}} + K_2 D_{02} e^{-H/D_{02}}) , \quad [2.119]$$

where D_{01} and D_{02} are the two different decay lengths describing the decaying behavior of structural forces of short and long separation regimes, respectively, and K_1 and K_2 are the corresponding preexponential factors describing the magnitude of the forces. In some cases, such as most hydrophilic surfaces and relatively weak hydrophobic surfaces in aqueous solutions, one of the K_i value equals zero, indicating that the structural forces can be described properly by an exponential function with single decay length. The K_i values can be positive or negative but must be of the same sign. The positive K_i values indicate a repulsive structural force while, the negative values represent an attractive structural force. The value of K_1 corresponding to a shorter decay length can be approximated to be twice the solid-liquid interfacial energy (203) or evaluated from the measured adhesion energy (206). The magnitude of the K_i values has been found to be

related to the ordering state of liquid adjacent to the solid surfaces. The greater the value, the more ordered the liquid, and the stronger the structural forces. Therefore, the non-structural liquids or the liquids which exhibit no preferential ordering under the influence of surfaces will give zero K_i values. In these cases, the classical DLVO theory is perfectly applicable.

It is interesting to note that an experimentally observed force law of the exponential type has been derived from a variational mean-field theory based upon the idea that the interaction forces of this kind are mediated by structural changes in the thin water film separating the two surfaces (217-218). According to this theory, the value of the constant K_i is related to the ordering state of the dipole molecules of the liquid and the value of the constant D_0 to the corresponding correlation length.

In an early treatment proposed by Marcelja and Radic (217), the Landau expansion of free energy density function was expressed in terms of an order parameter $\eta(x)$ which has been defined by:

$$\eta(x) = \frac{1}{2} [3 \langle \cos^2 v(x) \rangle - 1] , \quad [2.120]$$

where $v(x)$ refers to the angle confined between the long axis of the molecule and the normal to the solid surface, while the angular brackets indicate that the quantity inside them is a statistical mean value. $\eta(x)$ is equal to zero for isotropic liquids or for surfaces without any ordering effect, which gives a zero structural component of free energy. In this particular case, the free energy density function inside a thin liquid layer, as given by Equation [2.121] (217), is identical to that of the bulk liquid:

$$g = g_0 + a\eta^2(x) + b\eta^3(x) + \dots + c[\partial\eta(x)/\partial x]^2 + \dots , \quad [2.121]$$

where g_0 is the free energy density of bulk liquid. For anisotropic liquids or surfaces of preferential ordering effect, $\eta(x)$ can be positive or negative, depending on the dipole orientation. The value of the order parameter can be obtained by minimizing the free energy density function under given boundary conditions, i.e., the values of the order parameter at two interacting solid/liquid interfaces, η_0s , which are accessible either from experimental measurements or from direct molecular simulation with assumed intermolecular potentials. For the hydrophilic surfaces, identical in the sense of order capability, $\eta(d) = -\eta(-d) = \eta_0$, where d is one half of the distance between two surfaces. This treatment results in a value of K proportional to η_0^2 . However, using a fixed value of surface order parameter at the surface as a free parameter makes this approach valid at large interfacial separations only. At small separations, using a fixed value of $\eta(\pm d)$ as a parameter becomes inadequate since it does not account for the mutual disturbance of the surface water structure caused by the approaching interfaces, leading to the non-physical singularity of the structural component of interaction free energy. As a consequence, the concept proposed by Marcelja and Radic has been extended by using the surface orienting field density instead of the surface order parameter (219). Since the orienting field density can be used down to small interfacial separations, the modified theory shows good agreement between both the microscopic and macroscopic experimental data and the theory, provided that the interfacial orienting fields are taken to be surface distributed.

As can be seen, this kind of theoretical approach involves only short-range contact forces which are propagated by structural and bonding effects. It does not require invoking any long-range forces, more or less evasive in nature, acting across the entire width of the liquid film. More recently, the mean-field theory has been recaptured in an attempt to modify this theory in order to also cover explicitly the case of the attractive structural force (218). Instead of using the order parameter $\eta(x)$, the parameter

$s(x)$ has been used to account for the local orientation of water molecules in this recent treatment. Although the quantity $s(x)$ has been considered as a relative increase of the average number of hydrogen bonds per water molecule in the film as compared with bulk water (218), it is more convenient to interpret it to be a measure of orientational order. The excess free energy per unit area due to the ordering of water molecules in a thin film can be expressed by:

$$G_{so}(2d) = g(s_0) + \int_{-d}^d \left[c_1 s(x) + c_2 [s(x)]^2 + \frac{1}{2} c_3 [ds(x)/dx]^2 \right] dx , \quad [2.122]$$

which is known as a mean-field gradient approximation. In Equation [2.122], $g(s_0)$ corresponds to the contributions of free energy arising from the orientation of contact between water molecules and surfaces. The function in the integral is a variation of Landau expansion (217, 220). Since $s(x)$ under the integral in Equation [2.122] is an unknown function, the problem can only be tackled by using the variational method. Therefore, the equilibrium condition requiring $G_{so}(2d)$ to be minimal leads to the Euler-Lagrange equation:

$$\frac{d^2 s(x)}{dx^2} - \frac{2c_2}{c_3} s(x) = \frac{c_1}{c_3} . \quad [2.123]$$

Equation [2.123] should be solved using the boundary condition of $s(d) = \pm s(-d) = s_0$, with a plus sign corresponding to the interaction between two hydrophobic surfaces and a minus sign, to that between two hydrophilic surfaces. The minus sign indicates that the mean orientation at the two hydrophilic surfaces is in opposite directions. The solution of Equation [2.123], satisfying the boundary conditions of hydrophobic surfaces, is:

$$s(x) = -\frac{c_1}{2c_2} + s_0 \frac{\cosh(bx)}{\cosh(bd)} , \quad [2.124]$$

in which $b = \sqrt{2c_2/c_3}$. Following that $s(x)$ goes to zero at $x = 0$ at a large value of surface separation, c_1 must be zero. To avoid oscillating behavior of $s(x)$, c_2 and c_3 must be of the same sign. From these arguments, Equation [2.124] is readily simplified to:

$$s(x) = s_0 \frac{\cosh(bx)}{\cosh(bd)} . \quad [2.125]$$

Inserting Equation [2.125] into Equation [2.122] and integrating the resulting equation yield:

$$G_{so}(2d) = g(s_0) + c_3 s_0^2 b \tanh(bd) . \quad [2.126]$$

In order to find the value of s_0 , it is necessary to define a function describing the contact free energy response to the excess number of hydrogen bonds of a water molecule s_0 . As a first approximation, a linear function has been used in Eriksson's work (218), as given by:

$$g(s_0) = -as_0 , \quad [2.127]$$

where a is a positive constant. This relation implies that the contact free energy decreases with an increase in the excess number of hydrogen bonds. It also requires $G_{so}(2d)$ to be minimal with respect to varying s_0 at equilibrium. This yields, by inserting the linear response of $g(s_0)$ to s_0 into Equation [2.126] and then differentiating the resultant equation, the following:

$$-a + 2c_3 s_0 b \tanh(bd) = 0 , \quad [2.128]$$

which in turn gives:

$$s_0 = \left(\frac{a}{2c_3b} \right) \coth(bd) . \quad [2.129]$$

Equation [2.129] indicates that as two interacting surfaces approach each other, the water molecules on each surface become more ordered, giving rise to a high level of contact excess free energy. Inserting Equation [2.129] into Equation [2.125] to eliminate s_0 results in:

$$s(x) = \left(\frac{a}{2c_3b} \right) \frac{\cosh(bx)}{\sinh(bd)} . \quad [2.130]$$

The use of Equation [2.130] with Equation [2.126] and successive substitutions of s_0 in Equation [2.127] with Equation [2.129] and $g(s_0)$ in Equation [2.126] with Equation [2.127] finally lead to the expression for the total free energy of hydrophobic attraction, as given by:

$$G_{sol}(2d) = - \left(\frac{a^2}{2c_3b} \right) \coth(bd) . \quad [2.131]$$

At infinitely large separations, Equation [2.131] reduces to:

$$G_{sol}(\infty) = - \left(\frac{a^2}{4c_3b} \right) . \quad [2.132]$$

Equation [2.132] implies that $a^2/8c_3b$ is the reduction of surface free energy between water and the hydrophobic surface caused by the imposed ordering effect of the surface. The interaction energy of structural forces as a function of separation distance, $2d$, is therefore obtained as:

$$V_S(2d) = G_{sol}(2d) - G_{sol}(\infty) = - \left(\frac{a^2}{4c_3b} \right) [\coth(bd) - 1] . \quad [2.133]$$

Since the value of the hyperbolic cotangent function is always greater than one when its argument is positive, Equation [2.133] predicts a negative value of V_S , which implies an attractive structural interaction between two hydrophobic surfaces. For sufficiently large values of d , Equation [2.133] can be approximated by:

$$V_S(2d) = - \left(\frac{a^2}{2c_3b} \right) e^{-2bd} , \quad [2.134]$$

which is identical to Equation [2.119] in the form of a single decay length, with D_0 being b^{-1} and K being $a^2/2c_3$.

Similarly, solving Equation [2.123] with boundary conditions corresponding to hydrophilic surfaces leads to:

$$s(x) = s_0 \frac{\sinh(bx)}{\sinh(bd)} . \quad [2.135]$$

Inserting this equation into Equation [2.122] and integrating it yield:

$$G_{sol}(d) = -as_0 + \frac{2c_2s_0^2}{b} \coth(bd) . \quad [2.136]$$

By minimizing $G_{sol}(2d)$ with respect to s_0 , s_0 in Equation [2.136] can be found to be:

$$s_0 = \frac{ab}{4c_2} \tanh(bd) . \quad [2.137]$$

Inserting Equation [2.137] into Equation [2.136] to eliminate s_0 gives:

$$G_{so}(2d) = -\frac{a^2}{4c_3b} \tanh(bd) , \quad [2.138]$$

and $G_{so}(\infty) = -\frac{a^2}{4c_3b} . \quad [2.139]$

Correspondingly, the structural component of the interaction potential between two hydrophilic surfaces becomes:

$$V_S(2d) = G_{so}(2d) - G_{so}(\infty) = -\frac{a^2}{4c_3b} [\tanh(bd) - 1] . \quad [2.140]$$

Because the value of the hyperbolic tangent function is always less than 1, Equation [2.140] gives a positive value of V_S for all positive values of d , which represents a repulsive structural component of interaction between two hydrophilic surfaces. Likewise, Equation [2.140] can be approximated for the case of sufficiently large surface separations by:

$$V_S(2d) = \frac{a^2}{4c_3b} e^{-2bd} , \quad [2.141]$$

which is, again, identical to Equation [2.119] in the form of a single exponential term, with K and D_0 being $a^2/2c_3$ and b^{-1} , respectively.

According to the nature of the hyperbolic tangent and cotangent functions, Equations [2.133] and [2.140] predict, respectively, a more rapid decay than do Equations [2.134] and [2.141] within a small separation regime, which is accounted for by a second exponential term with a shorter decay length in Equation [2.119]. It appears that a hyperbolic tangent or cotangent function, rather than an exponential function of two different decay lengths, can be used to describe the repulsive or attractive structural forces over a wide range of surface separations.

A comparison of the experimentally determined structural component of interaction energy with that predicted from the above phenomenological theory based on a mean-field gradient approximation (218) shows a remarkable agreement for surface separations greater than 5 nm. It also shows that an improved agreement with the experimental data can be obtained by including a quadratic term in the contact free energy contribution, supporting the fact that the structural component of surface forces is of a cooperative nature.

The corresponding constant in Equations [2.133] and [2.140] can be obtained by fitting experimental results to the theoretical curve. However, it is instructive to analyze the feature of the constants involved in this theory (218). Since the strength of the structural component of surface forces is determined by the constant $K (\propto a^2/\sqrt{c_2c_3})$, with larger value corresponding to stronger structural forces, the structural forces will be enhanced by a strong free energy response to s_0 , as indicated by a large value of a in Equation [2.127]. But the attenuated structural forces are expected for a system with a strong response to ordering as suggested by a large value of constant c_2 and/or with strong decoupling effects in the core of the film as indicated by an increased value of constant c_3 . As to the decay length, b^{-1} , determined by $\sqrt{c_3/c_2}$, a longer-ranged structural force will be originated for a system with a weak free energy response of liquid to increasing order parameter $s(x)$ as implied by a small value of constant c_2 and a strong tendency to avoid $s(x)$ -gradients as indicated by a large value of c_3 . According to this theory, thus, the decay length b^{-1} should be the same for all surfaces under identical solution conditions while the strength of structural forces should increase with the degree of hydrophobicity or hydrophilicity of the surfaces.

It is interesting to notice how this theory can be applied to practical problems. It has been documented (213) that the presence of simple electrolyte ions in solution results in increased strength of the structural forces but over a reduced range. It is well

known that the existence of these ions disturbs the water structure which causes c_3 to diminish but c_2 to remain unchanged. This behavior of ions will result in a decreased b^{-1} value but an increased K value, which in turn predicts a force behavior as observed in the experiments (213). Also the phenomenon that the hydrophobic surfaces prepared by surfactant deposition give stronger hydrophobic interaction than those prepared by surfactant adsorption (210) can be reasonably explained. It is believed that the surfaces prepared by surfactant deposition give a smooth and chemically homogeneous hydrophobic surface which promotes the formation of the first contact layer of water molecules, giving rise to a comparatively large value of the constant a and, hence, the constant K .

Apparently, the theory represents a distinct conceptual advance and captures the idea of propagation of force from molecule to molecule. Like many other theories, this theory bears some limitations. The Landau expansion as the basis of the theory is derived rigorously from statistical mechanics but holds strictly only for the limit of infinite correlation length. Therefore, extrapolating the Landau theory down to separations of molecular dimension may cause a misleading solution to the problem. Although the measured structural force oscillates at short surface separations, the theory predicts a monotonic force behavior, whether attractive or repulsive, corresponding to similar or dissimilar order at respective surfaces. This is a direct result of applying continuum theory to a separation distance of several molecular diameters where the discrete nature of liquids becomes important. As can be seen, the association of the order parameter with polarization is arbitrary and the boundary condition is not well defined in this theory. Nevertheless, the simplicity with its validity over a large surface separation regime makes this theory attractive.

2.4.4 Statistical Mechanics Approach to Structural Forces

The structural component of surface forces has been studied by using statistical mechanics. Two different types of methodologies have been adopted in these studies, including Monte Carlo simulation (221-226) and molecular dynamics simulation (227-229). Both methods presume a knowledge of potential energy function between molecules.

In the Monte Carlo method, a system of N molecules and/or particles interacting through some known potentials is assigned a set of arbitrarily chosen initial coordinates, and the total free energy of the ensemble corresponding to this initial configuration is calculated. The molecules and/or particles are then subjected to changes by successive random displacements and rotations to form a new configuration, and the corresponding system free energy is calculated. Based on the free energies of two corresponding configurations, the decision whether to accept or reject this new configuration is made in such a way as to ensure that the configuration space is sampled according to the equilibrium probability density appropriate to a chosen ensemble. The procedures of new configuration construction and decision making are repeated until the desired convergent criterion is satisfied. The ensemble average of a function of the molecule and/or particle coordinates, such as the potential energy and radial distribution, is then obtained as an unweighted average over the accepted set of configurations while sidestepping the evaluation of the partition function. Since a probabilistic element is an essential part of the Monte Carlo calculation, a tremendous amount of samples need to be taken, resulting in the consumption of great amounts of computational time, typically hours on large, modern machines.

The Monte Carlo method has been used in a canonical ensemble (NVT) by van Megen and Snook (221) to determine the structure of dense Lennard-Jones fluids and

the solvation forces between rigid Lennard-Jones solid surfaces separated by the fluids. In this treatment, the number of solvent molecules has been fixed at 216 and the solid has been assumed to be a closely-packed, face-centered cubic structure. The interaction between liquid molecules is described by the Lennard-Jones 12-6 potential while the interaction between a liquid molecule and a solid surface is represented by a summation of the interaction potential between the molecule and the lattice site over 100 continuous lattice planes. The solvation forces have been calculated using the Barker approach, as given by:

$$f_s(d) = A \left[\int_0^d F_s(x) \rho(x) dx - \int_0^\infty F_s(x) \rho(x) dx \right], \quad [2.142]$$

where A is the surface area considered in the simulation, $\rho(x)$ is the density of fluid, and $F_s(x)$ is the force between one liquid molecule and a solid surface, which can be obtained by differentiating the interaction potential with respect to x .

With these arguments, the solvation forces have been simulated as a function of surface separation distance d for different values of bulk fluid density. The results show that the force oscillates between attraction and repulsion and the range over which it is significant is about six molecules in diameter. Its strength is much stronger than that of van der Waals force and increases with increasing bulk density of the fluid. This behavior is similar to that experimentally observed when measuring the surface forces between mica surfaces interacting in an apolar simple liquid (230-231). Similar behavior of solvation forces has been obtained from the simulations conducted for a grand canonical ensemble in which V , T and μ are constant (232-233).

The solvation force between neutral surfaces in water has been studied by Luzar et al. (234) using the grand canonical Monte Carlo simulations. The system studied

contains up to 100 water-like particles between parallel smooth plates immersed in fluid. The intermolecular potential used in this study consists of hard sphere potential, dipole potential, and orientation-dependent sticky potential (234), while the fluid-wall interaction is assumed to be a hard core one. The solvation force in this simulation has been determined from the contact wall-fluid densities, as given by:

$$f_s = [\rho_{in}(c) - \rho_{out}(c)]kT , \quad [2.143]$$

which has been derived from thermodynamics. In Equation [2.143], $\rho_{in}(c)$ and $\rho_{out}(c)$ are the inside and outside wall-fluid contact number densities, respectively. It can be seen from Equation [2.143] that the interaction is attractive when $\rho_{in}(c) < \rho_{out}(c)$, and vice versa. Simple theoretical considerations (235) also suggest that a repulsive force will arise if the density of water between two surfaces increases as the surfaces approach each other, whereas an attractive interaction will arise if the density decreases, corresponding to a depletion of water between strongly hydrophobic surfaces. The simulation results show that parallel alignments of the water dipoles nearest to the interface are preferred, as indicated by a low value of order parameter $s(\theta)$. An oscillation of $\rho_{in}(c)$ with a period equal to the molecular diameter results in an oscillating solvation force. The simulation also predicts the evaporation of water in the squeeze limit, a phenomenon similar to cavitation formation as observed experimentally (212, 235-237).

Jonsson (238) has performed the Monte Carlo simulations in the canonical ensemble to study the structure of liquid water bounded by two parallel hard walls. The potential between the water molecules used in these simulations has been derived by Matsouka et al. (239) using a configurational method based on a configuration state function. The interaction between water molecule and wall is assumed to be infinitely repulsive if any atom of water molecules is outside the wall, otherwise zero. The number of water molecules simulated is 40, 80 or 150. A less strongly damped oscillatory be-

havior of density profile has been observed as compared with that observed by Snook and van Megen (222) who used different water/wall potential. The interesting finding from this study is that the number of hydrogen bonds is higher in a thin layer (2.2 Å) of water close to the wall than it is for bulk water. A relatively slow decay of the orientational order found in this investigation is an indication of a long-range effect of surface, which is consistent with an experimentally observed long range attraction between strongly hydrophobic surfaces embedded in water (210). A similar simulation on an extended system consisting of 216 water molecules between two structureless walls has been conducted by Christou et al. (240). A potential of the 9-3 form has been used to describe the interaction between each water molecule and a wall, while the potential describing the interaction between water molecules is the same as proposed by Rowlinson (241).

The water structure between two paraffin walls has been studied recently by Wallqvist and Berne (226) using Monte Carlo simulation. The interaction potentials between water and wall as proposed by Lee et al. (242) and between water molecules as developed by Watts et al. (243) have been used, and the results show that the water dipoles tend to orient approximately parallel to the surfaces with a slight preference of pointing slightly outward from the liquid. This is an indication of a rather ordered interface in such a way that the first layer of water molecules adjacent to the walls orient themselves to develop a maximum number of hydrogen bonds with water molecules of the next layer.

A more recent Monte Carlo simulation has been conducted by Il'in et al. to study the structure and average intermolecular interaction energy (U_f) of water molecules adjacent to a surface of varying surface hydrophilicities, as discussed in reference 178. In their investigation, the oxygen atom has been considered as a hydrophilic active center. The surface hydrophilicity is controlled by changing the number of active centers per

unit surface area, N . A strongly hydrophobic surface, such as paraffin, is characterized by a zero number of active centers, i.e., $N = 0$. The Rowlinson potential (241) has been used as the intermolecular interaction potential. The order parameter as defined by Equation [2.120] and the intermolecular interaction energy have been calculated as a function of N . The simulation results show that near a surface with $N = 0$, order parameter is minimal, representing a parallel orientation of dipoles of water molecules to the surface. An increase in N leads to a gradual increase in the order parameter. At $N = 16$, the order parameter reaches zero, corresponding to a structure similar to bulk water. A further increase of N results in a wall normal preference of orientation. It is interesting to note that the surface is water-like when $N = 16$, with the mean distance between the active centers on the surface being equal to that between bulk water molecules. When adjacent to a hydrophilic surface with $N > 16$, water molecules are strongly associated, as indicated by an increased magnitude of U_f , while they are weakly associated, as reflected by a reduced magnitude of U_f , when adjacent to a hydrophobic surface with $N < 16$. For the water molecules next to the surface with $N = 16$, U_f has been found to be the same as for bulk water molecules, representing a system in which the structural force is negligible. These simulation results indicate that an increase of N may give two different contributions to the potential of mean force between surfaces. For the surfaces with $N < 16$, the water in the thin layer is in a state of higher energy than the bulk water, representing an unfavorable state. Therefore, the exclusion of water during the approach of two very strong hydrophobic surfaces leads to a decrease in free energy, giving rise to an attractive contribution to the total interaction forces between the surfaces. On the contrary, a repulsive contribution is expected when two surfaces are hydrophilic with $N > 16$, since the free energy of water confined between them is in a state of lower energy, corresponding to a favorable state. These phenomena are the same as those experimentally observed non-DLVO forces.

On the other hand, in a conventional molecular dynamics simulation, a system of N molecules is confined in a cell of fixed volume. A set of velocities is assigned, usually drawn from a Maxwell-Boltzmann distribution appropriate to the temperature of interest and selected in such a way as to make the net linear momentum equal to zero. The subsequent trajectories of the particles are then calculated by integration of the differential equation of motion. The particles are assumed to interact through some prescribed force law and the motion of each particle is governed by the net force vector. Based on the principle of statistical mechanics, the mechanical properties of the system are obtained as a time average over the dynamical history of the system. Since the energy, volume, and number of particles are fixed, molecular dynamics operates in a microcanonical ensemble.

Marchesi (227) has performed molecular dynamics simulation on a system of 150 ST2 water molecules between two quasi-hard repulsive walls to study the structure of water molecules near hydrophobic surfaces. In his investigation, the interaction potential between ST2 water molecules is based on a rigid four-point-charge model as given by Stillinger and Rahman (244), while the interaction between water molecule and wall is described by a purely repulsive potential acting on both oxygen and hydrogen atoms. The simulation shows a strong repulsive behavior of water molecules by walls. The density profiles of the oxygen and hydrogen atoms are quite different from those obtained by Jonsson (238) who studied a similar system using Monte Carlo simulation. The discrepancies have been attributed to the use of different interaction potentials between water molecules since the density profiles have been found to be substantially unaffected by using different water-wall potentials. However, the angular probability distribution functions obtained from these two simulations are similar, showing a preference for water dipole orientation parallel to the walls. The water self-diffusion coefficient, which is defined as a function of the limiting slope of the molecular center of mass

mean-square displacement (244), has been found to be about half in the wall-normal direction than that in the wall-parallel direction for water molecules adjacent to the walls. The different diffusion behaviors have been attributed to the preferential orientation of water molecules, which leads to a smaller interaction energy in the wall-normal direction compared with those in wall-parallel directions.

Sonnenschein and Heinzinger (245) have extended Marchesi's simulation to a system including 216 ST2 water molecules confined between 12-6 Lennard-Jones walls. Besides the general agreement with those obtained by Marchesi (227), this investigation also shows that although significantly decreased, the preferential orientation of water dipoles parallel to the walls persists into the central region and thus indicates an orientational correlation extending beyond a distance of 10 Å. Molecular dynamics simulation using the *Boltzmann averaged* potential as the wall-water interaction potential has been conducted by Barabino et al. (228) on a system of 150 water molecules. The same potential for water-water interaction as used by Jonsson (238) in Monte Carlo simulation has been used. It has been found from their simulation that there are no substantial differences with respect to a simulation using a simple hard wall, and the water structure not very close to the wall is unchanged by the presence of a different potential. The results obtained lead to the conclusion that water properties near a wall are determined more by the changes in the geometric structure of water induced due to the presence of the wall rather than by the direct influence of the wall potential on the water molecules. Their simulation also predicts the effects of a given wall potential on water as a complex combination of the wall influence and the changes in water structure.

The structure of liquid water confined between two extended hydrophobic surfaces has been studied by Lee et al. (242) using molecular dynamics simulation. 216 ST2 water molecules have been included in this simulation and the water-wall interaction is described by a 9-3 type potential appropriate for a molecule interacting with the homo-

geneous solid surfaces. The coefficients of the 9-3 type potential have been chosen to represent the interaction of ST2 water with a material like paraffin. The simulation results show that the hydrophobic walls produce density oscillations propagated to the center of two walls, indicating that the water structure near either wall is possibly perturbed due to the presence of the opposite wall. Compared with the results obtained by using the simple Lennard-Jones liquid, the paraffin-like surface shows the lack of wetting by ST2 water as reflected from the small amplitude and a slight shift away from the wall of the first peak in the density profile. The presence of the wall reduces the number of hydrogen bonds per water molecule as getting close to the wall simply for geometrical reasons. However, the decrease is only about 25% instead of 50%, as expected if the bulk liquid structure continued up to the surface, indicating a structural rearrangement at the surface without changing the molecular packing. This is possible because the molecular electronic density is nearly spherical in liquid water (238). As to the orientation of the dipole moment of water molecules, a general agreement with other simulations, i.e., a wall-parallel preference, has been observed in the simulation. This orientation gives an avoidance of surface electrostatic polarization. The simulation leads to a structure of nearly planar layers of bounded molecules, which is a result of competition between packing forces and the tendency of maintaining a maximal number of hydrogen bonds. The orientational preference induced in the first layer propagates into the fluid, manifested in the form of successive layers of alternating water orientations.

Although the structure of water near hydrophobic surfaces has been extensively studied through molecular dynamics simulations, the study of the interfacial behavior of polar systems is still in its infancy. A molecular dynamics simulation of water between uncharged silicate surfaces has been conducted by Low et al. (246) to understand, on a molecular basis, the structural and dynamical properties of vicinal water. The system investigated consists of 256 ST2 water molecules located between two parallel planes

of uncharged oxygen atoms, each representing a surface of uncharged silicate mineral. Only the Lennard-Jones part of the ST2 potential is included in the interaction between water molecules and surface oxygens. Due to the nature of the water-wall interaction potential used in their simulation, the results obtained here are in general agreement with those obtained for water molecules confined between structureless walls. In addition, this simulation shows that the surfaces induce a substantial hindrance in the rotational motion of water molecules located as far as 10 Å from the surfaces.

A more representative simulation of water structure near a polar surface has been conducted by Kjellander and Marcelja (229). The ST2 water molecules are allowed to interact with a replica of a mica surface via electrostatic and Lennard-Jones potentials. A significant increase in the number density of water molecules in the vicinity of the surfaces (247) has been observed in their simulation. However, the number of hydrogen bonds has been found to decrease substantially in this region. The decrease is restricted to a thin layer, indicating clearly a short-range effect of surfaces in contrast to a long-range effect of strongly hydrophobic surfaces. This result is in good agreement with experimentally observed short-range repulsive hydration forces as opposed to long-range hydrophobic forces. The decrease in the number of hydrogen bonds in the vicinity of a polar surface has been ascribed to the orientation of water molecules in the electrical field of the discrete surface charges. In contrast to hydrophobic surfaces, the major force acting on water molecules near a polar surface is from an electrostatic field associated with discrete surface charges. The orientation of the molecules in this field takes precedence over the formation of a hydrogen bond network. For reasons of molecular geometry, it is impossible to align the water molecules according to the requirement of the surface electrical fields and at the same time form a normal hydrogen bond network. As a consequence, the open structure of bulk water is partially broken down. This agrees with an increase in the average density and in the number of neighbors for each

water molecule in this region, as observed in the simulation. It is clear that the approach of two hydrophilic surfaces makes the environment of the remaining water molecules even more restrictive, which may contribute to the hydration forces. Therefore, the repulsion is due to the entropy lost as the surfaces approach, there being fewer configurations which are able to satisfy the boundary conditions without breaking the bond network of the fluid phase (248). The repulsive hydration forces are also expected from the increased density of the liquid in the vicinity of the inward surfaces, as indicated in Equation [2.143].

Although the solvation forces and the structure of water near solid surfaces have been studied extensively by molecular simulations, the systems studied would never be a replica of an actual situation encountered in colloid science since it is only possible to investigate limited sizes of the system using these methods due to the tremendous amount of computation time required. The use of a cut-off radius when calculating the interaction may also impose significant uncertainty on the simulation results. Nevertheless, the molecular simulation does provide a useful starting point for further theoretical work. Molecular simulation will not only be able to generate the boundary conditions of the order parameter, which is essential for deriving the force law using the mean-field gradient theory, as discussed in the previous section, but can also provide some important information as to the oscillation behavior which may be crucial in determining the stability of colloidal dispersions. For example, if an oscillation generates a local repulsion greater than the activation energy of a system, each pair of particles will be equilibrated at this solvent separated state, even though the average potential profile predicted from phenomenological mean-field gradient theory shows a net attraction at all separations. Therefore, it is important to study the structural forces by using a molecular simulation approach and the mean-field gradient theory in combination, the former providing the boundary conditions required for the latter. A complete picture of the

structural force can be obtained by superimposing the oscillation component of the structural force due to the molecular packing limitation on the force law derived from the mean-field gradient theory.

2.4.4 Proposed Mechanisms of Structural Forces

Experimental studies have clearly shown the existence of non-DLVO forces and molecular simulations have illustrated the preferential orientation of water molecules near the surfaces. However, the nature of the perturbation has proven to be a difficult subject to study. To understand the origin of these non-DLVO forces, a number of mechanisms have been proposed.

The image-charge mechanism has been considered as a possible source of the repulsive non-DLVO force. This mechanism was first proposed by Jonsson and Wennerstrom (249) and improved by Kjellander (250). In this mechanism, the repulsive non-DLVO force has been considered as a result of a creation of image charge due to the dielectric discontinuity across the interface. The physical effect of the exclusion of some polarized water by an approaching surface is equivalent mathematically to the creation of image charges there. The interaction per primary charge site on the surface consists of two parts, one between a primary charge and its own images and the other between its images and other charge sites on the surfaces. Theoretically, the observed total non-DLVO force between two surfaces across a liquid of different dielectric constants is the summation of this type of forces over all possible pairs of image charges and charged sites on the surfaces. However, their treatment has led to the conclusion that the interaction is generally dominated, for large separation distances, by the interaction of primary charge sites with their own images (250). According to an image-charge model, the non-DLVO forces are essentially electrostatic in nature. Although this model

explains reasonably the repulsive non-DLVO forces between lecithin lamellae separated by water if suitable parameters are chosen, the general exponential force law as observed experimentally can only be fitted by using very special, unrealistic orientations and distributions of surface charge sites. The calculated force has been found to vary significantly or even to change the sign with the parameters chosen. A question may also arise when this mechanism is used to explain the absence of a monotonic non-DLVO force in some systems, such as mica plates interacting through pure water, as studied by Israelachvili and Adams (70), or mica plates interacting through isotropic liquids (251).

The polarization of water molecules near the surface by an electrical field of solids has been proposed as one of the possible mechanisms for repulsive non-DLVO forces (252-253). It has been found that the polarization normal to the surface will be conserved until a defect such as Bjerrum defects which are much more numerous than ionic defects, is encountered. Therefore, the polarization profile will be associated with a density profile of Bjerrum defects. Since the polarizations on the normal direction from both surfaces are opposite, a repulsive force is expected as a result of the competing demands on water polarization by the two surfaces, which increases as two such surfaces approach closer to each other. The problem becomes analogous to the Gouy-Chapman theory of double layer interaction, with the electrical field and ions being replaced by polarization and Bjerrum defects, respectively. The presence of electrolyte ions will significantly increase the density of the defects, resulting in a substantially decreased decay length as observed experimentally. By realizing that the polarization will vanish within the first few layers of liquid molecules adjacent to the surface if this surface induces the dipoles of liquid parallel to the surface, as in the case of a hydrophobic surface, it is difficult to account for the long-range attractive non-DLVO forces, as observed experimentally between two strongly hydrophobic surfaces, according to this mech-

anism. Therefore, the polarization mechanism can hardly be extended to account for generally observed non-DLVO forces, whether they are repulsive or attractive.

It has been suggested that the very long range attraction between strongly hydrophobic surfaces embedded in water could be due to the induced electrostatic fluctuations between neutral bodies (254), the same origin as the classical van der Waals forces. It is the anomalous electrostatic response of water molecules adjacent to strongly hydrophobic surfaces that gives rise to the remarkable attractions measurable at large separation distances when the surfaces are coupled via bulk water and electrolyte. The substantial density fluctuation is expected near hydrophobic surfaces since water molecules there are thermodynamically metastable, as reflected by the spontaneous cavitation upon the contact between surfaces. These density fluctuations may give an enhanced electrostatic response. The theoretical treatment leads to an attraction which decays exponentially as the distance between two surfaces increases. The decay length has been found to be one half of the Debye screening length as defined by Equation [2.75]. This finding is qualitatively consistent with the experimentally observed salt-dependence of decay length (213) and with the conclusion that the decay length is determined solely by the solution conditions, as drawn from the mean-field gradient approach. Since electrostatic fluctuation starts at one surface and induces a response at the other surface, which returns and then interacts with the original fluctuation, the distance travelled is actually twice the separation. This explains why this type of fluctuation force decays twice as fast as the usual mean-field double layer repulsion. However, the theory based on the electrostatic fluctuation mechanism predicts a force too weak to account for the experimentally observed hydrophobic attraction. This theory is also unable to explain the repulsive non-DLVO forces.

The most satisfactory explanation can be obtained by considering the origin of non-DLVO forces, attractive or repulsive, as the structuring of liquid molecules under

the influence of the surfaces. Due to the geometrical restriction, the hydrogen bond network existing in bulk water has to be broken. In order to minimize the loss of hydrogen bonds, only a limited number of configurations is possible, depending on the nature of the surfaces. The effect is exacerbated at smaller separations, resulting in a steep increase in the non-DLVO forces. However, it is important to distinguish the language of structure used here from that used in thermodynamics. In thermodynamics, the structure indicates a decrease in the degree of molecular freedom or the number of configurations of molecules, which results in an increase in free energy. According to thermodynamics, the removal of the structured water molecules from the vicinity of the surfaces to the less structured bulk phase will give a decreased free energy, corresponding to a more favorable state. Therefore, it becomes confusing that both hydrophobic and hydrophilic surfaces make water molecules more ordered in the vicinities of the surfaces, but hydrophobic surfaces induce the attractive hydrophobic force while hydrophilic surfaces induce the repulsive hydration force. Based on the thermodynamics, both cases will give an increased entropy when structured water is released from the interlayer region to the bulk, resulting in a negative component of the free energy change.]

In order to understand this phenomenon physically, Isearalachvili (1, 252) has presented a schematic diagram as replicated in Figure 2.5, demonstrating how the different orientations of water molecules near hydrophobic and hydrophilic surfaces could give attractive and repulsive structural forces, respectively. Figure 2.5 (a) shows a wall-parallel orientation of water molecules near two hydrophobic surfaces as found in molecular simulations. The structural change from bulk water to this type of orientation is entropically very unfavorable. During the approach of these two surfaces, the water molecules in this region are able to rearrange themselves due to their spherical geometry of electronic distribution. This rearrangement will give a configuration of cooperative alignment which also satisfies the required wall-parallel orientation as shown in Figure

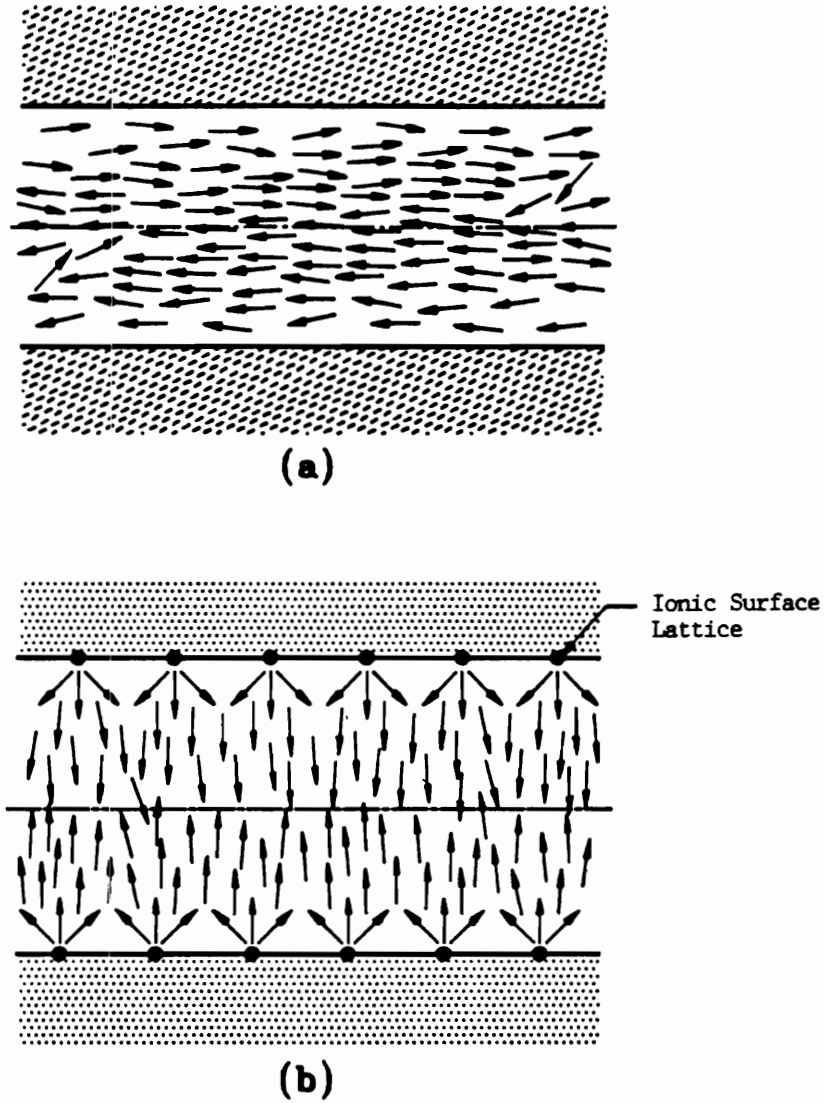


Figure 2.5. Schematic Illustration of Water Structure Confined between Two Surfaces

- a. A Parallel Orientation to the Strongly Hydrophobic Surfaces
- b. A Perpendicular Orientation to the hydrophilic Surfaces

2.5 (a), resulting in a net attractive solvation force. The water molecules around a charged hydrophilic surface, on the other hand, are of a wall-normal orientation as also recognized in the molecular simulation. When two hydrophilic surfaces approach each other, the water molecules are unable to adjust themselves due to the strong influence of the surface electrical field. As a consequence, antiparallel orientation of water molecules in the middle of the interlayer, as illustrated in Figure 2.5 (b), leads to repulsive solvation forces.]

It is clear that, experimentally, the structural forces represent everything that cannot be understood and, theoretically, they are everything that goes beyond the DLVO theory. Therefore, the issue is not properly formulated and controversial arguments are still under dispute. The structural component of surface forces can possibly be described quantitatively only through defining a quantity that reflects the statistically averaged ordering of liquid (253). This quantity, called the ordering parameter, is accessible through computer simulations, such as the Monte Carlo simulation or the molecular dynamics simulation. Combined with this quantity, the mean-field gradient theory is able to give a satisfactory explanation of non-DLVO forces, attractive and repulsive, as has been discussed in Section 2.5.3.

It is worth mentioning at the end of this chapter, that the materials presented in this review only reflect the limited knowledge and availability of material to the author. Surface forces are such a broad subject and involve such a wide range of areas that it is difficult, if not impossible, to cover every important detail in a review of limited size. A multidisciplinary knowledge is called for in order to have a better understanding and a more complete picture of this subject. The interest in the topic is still growing rapidly over a wide range of areas.

Since the importance of van der Waals attraction and electrostatic repulsion is well-known and the theory of these two interactions has been fairly well established, in

the subsequent two chapters, the focus will be on the role of the third interaction, in particular, the hydrophobic interaction. As far as the classical DLVO theory is concerned, only very brief descriptions are given in these two chapters simply because detailed information has been included in this review. For more details, it would be helpful to come back to this chapter.

2.5 References

1. Israelachvili, J.N. and McGuggan, P.M., "Forces between Surfaces in Liquids," *Science*, 241, 795 (1988).
2. Israelachvili, J.N. and Tabor, D., "van der Waals Forces: Theory and Experiment," in *Progress in Surface and Membrane Science*, ed. by Danielli, J.F., Rosenberg, M.D. and Cadenhead, D.A., Academic Press, New York, 7, 1 (1973).
3. Israechvili, J.N., Kott, S.J., Gee, M.L., and Witten, T.A., "Entropic Orientational Forces between Surfaces in Anisotropic Liquids," *Langmuir*, 5, 1111 (1989).
4. van der Waals, J.D., *Ph.D. Thesis*, University of Leiden, 1873.
5. Israelachvili, J.N., *Intermolecular and Surface Forces: With Applications to Colloidal and Biological Systems*, Academic Press Inc., London, 1985.
6. Debye, P., "van der Waals' Cohesion Forces," *Phys. Z.*, 21, 178 (1920).
7. Keesom, W.H., "Van der Waals Attractive Forces," *Phys. Z.*, 22, 129 (1921).
8. Keesom, W.H., "The van der Waals Attractive Forces," *Phys. Z.*, 22, 643 (1921).
9. Wang, S.C., "The Mutual Influence of the Two Atoms of Hydrogen," *Phys. Z.*, 28, 663 (1927).
10. London, F., "The General Theory of Molecular Forces," *Trans. Faraday Soc.*, 33, 8 (1937).
11. London, F., "Theory and Systematics of Molecular Forces," *Z. Phys.*, 63, 245 (1930).
12. London, F., "Properties and Applications of Molecular Forces," *Z. Phys. Chem.*, 11, 222 (1930).
13. Casimir, H.B.G. and Polder, D., "The Influence of Retardation on the London-van der Waals Forces," *Phys. Rev.*, 73, 360 (1948).

14. McLachlan, A.D., "Retarded Dispersion Forces between Molecules," *Proc. Roy. Soc.*, A271, 387 (1963).
15. McLachlan, A.D., "Retarded Dispersion Forces in Dielectrics at Finite Temperatures," *Proc. Roy. Soc.*, A274, 80 (1963).
16. McLachlan, A.D., "Effect of the Medium on Dispersion Forces in Liquids," *Discuss. Faraday Soc.*, 40, 239 (1965).
17. Kallmann, H. and Willstatter, M., "The Theory of the Structure of Colloidal Systems," *Naturwiss.*, 20, 952 (1932).
18. Bradley, R.S., "The Cohesive Force between Solid Surfaces and the Surface Energy of Solids," *Phil. Mag.*, 13, 853 (1932).
19. de Boer, J.H., "The Influence of van der Waals' Forces and Primary Bonds on Binding Energy, Strength and Orientation with Special Reference to Some Artificial Resins," *Trans. Faraday Soc.*, 32, 21 (1936).
20. Hamaker, H.C., "The London-van der Waals Attraction between Spherical Particles," *Physica*, 4, 1058 (1937).
21. Sonntag, H. and Strenge, K., *Coagulation Kinetics and Structure Formation*, Plenum Press, New York, (1987).
22. Fowkes, F.M., "Attractive Forces at Interfaces," *Ind. Eng. Chem.*, 56, 40 (1964).
23. Berthelot, D., "Sur Le Mélange des Gaz," *Compt. Rend. Acad. Sci.*, 126, 1703, 1857 (1898).
24. Vold, M., "The Effect of Adsorption on the van der Waals Interaction of Spherical Colloidal Particles," *J. Colloid Interface Sci.*, 16, 1 (1961).
25. Padday, J.F. and Uffindell, N.D., "The Calculation of Cohesive and Adhesive Energies from Intermolecular Forces at a Surface," *J. Phys. Chem.*, 72, 1407 (1968).
26. Coakley, and Tabor, D., "Attractive Surface Forces," in *Colloidal Dispersions*, ed. by Goodwin, J.W., Royal Soc. Chem., Burlington House, London, 23 (1982).
27. Schenkel, J.H. and Kitchener, J.A., "A Test of the Derjaguin-Verwey-Overbeek Theory with a Colloidal Suspension," *Trans. Faraday Soc.*, 56, 161 (1960).
28. Chia, Y.H. and Somasundaran, P., "A Theoretical Approach to Flocculation in Carrier Flotation for Beneficiation of Clay," *Colloids Surfaces*, 8, 187 (1983).
29. Lifshitz, E.M., "The Theory of Molecular Attractive Forces between Solids," *J. Exp. Theor. Phys.*, 29, 94 (1955).
30. Rytov, S.M., *Theory of Electric Fluctuations and Thermal Radiations*, Moscow Academy of Sciences Press, Moscow, (1953).

31. Visser, J., "On Hamaker Constants: A Comparison between Hamaker Constants and Lifshitz-van der Waals Constants," *Adv. Colloid Interface Sci.*, 3, 331 (1972).
32. van den Tempel, M., "Interaction Forces between Condensed Bodies in Contact," *Adv. Colloid Interface Sci.*, 3, 137 (1972).
33. Bargeman, D. and van voorst Vader, F., "Van der Waals Forces between Immersed Particles," *J. Electroanal. Chem.*, 37, 45 (1972).
34. Dzyaloshinskii, I.E., Lifshitz, E.M. and Pitaevskii, L.P., "General Theory of van der Waals Forces," *Adv. Phys.*, 10, 165 (1961).
35. van Kampen, N.G., Nijboer, B.R.A., and Schram, K., "On the Macroscopic Theory of van der Waals Forces," *Phys. Lett.*, 26A, 307 (1968).
36. Langbein, D., "Van der Waals Attraction between Macroscopic Bodies," *J. Adhes.*, 1, 237 (1969).
37. Gregory, J., "The Calculation of Hamaker Constants," *Adv. Colloid Interface Sci.*, 2, 369 (1969).
38. Tabor, D. and Winterton, R.H.S., "The Direct Measurement of Normal and Retarded van der Waals Forces," *Proc. Roy. Soc.*, A312, 435 (1969).
39. *CRC Handbook of Chemistry and Physics: 66th edition*, CRC Press, Inc., Boca Raton, Florida, E-369 (1985).
40. Fowkes, F.M. and Pugh, R.J., "Steric and Electrostatic Contributions to the Colloidal Properties of Nonaqueous Dispersions," in *Polymer Adsorption and Dispersion Stability*, ed. by Goddard, E.D. and Vincent, B., American Chemical Society, 331 (1984).
41. Hough, D.B. and White, L.R., "The Calculation of Hamaker Constants from Lifshitz Theory with Applications to Wetting Phenomena," *Adv. Colloid Interface Sci.*, 14, 3 (1980).
42. van Oss, C.J. and Good, R.J., "The 'Equilibrium Distance' between Two Bodies Immersed in a Liquid," *Colloids Surfaces*, 8, 373 (1984).
43. van Oss, C.J., Chaudhury, M.K. and Good, R.J., "Interfacial Lifshitz-van der Waals and Polar Interactions in Macroscopic Systems," *Chem. Revs.*, 88, 927 (1988).
44. Krupp, H., "Particle Adhesion: Theory and Experiment," *Adv. Colloid Interface Sci.*, 1, 111 (1967).
45. Derjaguin, B.V., Churaev, N.V., and Rabinovich, Ya.I., "The Modern State of the Macroscopic Theory of Molecular Forces and the Results of its Experimental Verification for Thin Interlayers," *Adv. Colloid Interface Sci.*, 28, 197 (1988).
46. Mahanty, J. and Ninham, B.W., *Dispersion Forces*, Academic Press, Inc., New York, 1976.

47. Parsegian, V.A., and Ninham, B.W., "Temperature-Dependent van der Waals Forces," *Biophys. J.*, 10, 664 (1970).
48. Israelachvili, J.N., "The Calculation of van der Waals Dispersion Forces between Macroscopic Bodies," *Proc. Roy. Soc.* A331, 39 (1972).
49. Israelachvili, J.N., and Tabor, D., "The Measurement of van der Waals Dispersion Forces in the Range 1.5 to 130 nm," *Proc. Roy. Soc.* a331, 19 (1972).
50. Ninham, B.W., and Parsegian, V.A., "Van der Waals Interactions in Multilayer Systems," *J. Chem. Phys.*, 53, 3398 (1970).
51. Visser, J., "The Concept of Negative Hamaker Coefficients: I. History and Present Status," *Adv. Colloid Interface Sci.*, 15, 157 (1981).
52. van Oss, C.J., Visser, J., Absolom, D.R., Omenyi, S.N., and Neumann A.W., "The Concept of Negative Hamaker Coefficient: II. Thermodynamics, Experimental, Evidence and Applications," *Adv. Colloid Interface Sci.*, 18, 133 (1983).
53. Derjaguin, B.V., Churaev, N.V. and Muller, V.M., *Surface Forces (English Translation Edition)*, Consultants Bureau, New York, 1987.
54. Kruglyakov, P.M., "Stability of Hydrocarbon Films on the Surface of Water," *Coll. J. USSR*, 36, 145 (1974).
55. Hough, D.B., and White, L.R., "The Calculation of Hamaker Constants from Lifshitz Theory with Applications to Wetting Phenomena," *Adv. Colloid Interface Sci.*, 14, 3 (1980).
56. van Oss, C.J., Gillman, C.F., and Neumann, A.W., *Phagocytic Engulfment and Cell Adhesiveness*, Marcel Dekker, New York, 1975.
57. Derjaguin, B.V., Titijevskaia, A.S., Abrikosova, I.I., and Malkina, A.D., "Investigations of the Forces of Interaction of Surfaces in Different Media and Their Application to the Problem of Colloid Stability," *Discuss. Faraday Soc.*, 18, 24 (1954).
58. Derjaguin, B.V., and Abrikosova, I.I., "Direct Measurements of Molecular Attraction of Solids," *Phys. Chem. Solids*, 5, 1 (1958).
59. Derjaguin, B.V., Abriikosova, I.I., and Lifshitz, E.M., "Direct Measurement of Molecular Attraction between Solids Separated by a Narrow Gap," *Quart. Rev. Chem. Soc.*, 10, 295 (1956).
60. Kitchener, J.A., and Prosser, A.P., "Direct Measurement of the Long-Range van der Waals Forces," *Proc. Roy. Soc.* A242, 403 (1957).
61. Sparnaay, M.J., "Measurements of Attractive Forces between Flat Olates," *Physica (Utrecht)*, 24, 751 (1958).

62. Derjaguin, B.V., Rabinovich, Ya.I., and Churaev, N.V., "Direct Measurement of Molecular Forces," *Nature*, 272, 313 (1978).
63. van Blokland, Pet.H.G.H. and Overbeek, J.Th.G., "Van der Waals Forces between Objects Covered with a Chromium Layer," *JCS Faraday Trans. I*, 74, 2637 (1978).
64. Hunklinger, S., Geisselmann, H., and Arnold, W., "Dynamic Method for Measuring the van der Waals Forces between Macroscopic Bodies," *Rev. Scient. Instrum.*, 43, 584 (1972).
65. Rouweler, G.C.J., and Overbeek, J.Th.G., "Dispersion Forces between Fused Silica Objects at Distances between 25 and 350 nm," *Trans. Faraday Soc.*, 67, 2117 (1971).
66. Black, W., de Jongh, J.G.V., Overbeek, J.Th.G., and Sparnaay, M.J., "Measurements of Retarded van der Waals' Forces," *Trans. Faraday Soc.*, 56, 1597 (1960).
67. Overbeek, J.Th.G., and Sparnaay, M.J., "Long-Range Attractive Forces between macroscopic Objects," *J. Colloid Sci.*, 7, 343 (1952).
68. Israelachvili, J.N. and Adams, G., "Measurement of Forces between Two Mica Surfaces in Aqueous Electrolyte Solutions in the Range 0-100 nm," *JCS Faraday Trans. I*, 74, 975 (1978).
69. Aveyard, R. and Saleem, S.M., "Interfacial Tensions at Alkane-Aqueous Electrolyte Interfaces," *JCS Faraday Trans. I*, 72, 1609 (1976).
70. Marra, J., "Direct Measurements of Attractive van der Waals and Adhesion Forces between Uncharged Lipid Bilayers in Aqueous Solutions," *J. Colloid Interface Sci.*, 109, 11 (1986).
71. James, R.O. and Parks, G.A., "Characterization of Aqueous Colloids by Their Electrical Double-Layer and Intrinsic Surface Chemical Properties," in *Surf. Colloid Sci.*, ed. by Matijevic, E., 12, 119 (1982).
72. Quast, K.B. and Readett, D.J., "The Surface Chemistry of Low-Rank Coals," *Adv. Colloid Interface Sci.*, 27, 169 (1987).
73. Labib, M.E., "The Origin of the Surface Charge on the Particles Suspended in Organic Liquids," *Colloids Surfaces*, 29, 293 (1988).
74. Frumkin, A.N., "Phase-Boundary Forces and Adsorption at the Interface Air: Solutions of Inorganic Salts," *Z. Phys. Chem.*, 109, 34 (1924).
75. Yoon, R.H. and Yordan, J.L., "Zeta-Potential Measurements on Microbubble Generated Using Various Surfactants," *J. Colloid Interface Sci.*, (1986).
76. Haydon, D.A., "Surface Charge of Cells and Some Other Small Particles as Indicated by Electrophoresis I. Zeta Potential-Surface Charge Relations," *Biochim. Biophys. Acta*, 50, 450 (1961).

77. deBruyn, P.L. and Agar, G.E., "Surface Chemistry of Flotation," in *Froth Flotation*, ed. by Fuerstenau, D.W., AIME Inc., New York, 91 (1962).
78. van Olphen, H., *An Introduction Clay Colloid Chemistry: For Clay Technologists, Geologists, and Soil Scientists*, Interscience Publishers, New York, 1963.
79. Hachisu, S., "Surface Electricity," in *Surfactant Sci. Ser. (Electrical Phenomena at Interfaces)*, 15, 3 (1984).
80. Jessop, R.R. and Stretton, J.L., "Electrokinetic Measurements on Coal and a Criterion for Its Hydrophobicity," *Fuel*, 69, 317 (1969).
81. Honing, E.P. and Hengst, J.H.Th., "The Point of Zero Charge and Solid-State Properties of Silver Bromide," *J Colloid Interface Sci.*, 31, 545 (1969).
82. Usui, S. and Yamasaki, T., "Adhesion of Mercury and Glass in Aqueous Solutions," *J. Colloid Interface Sci.*, 29, 629 (1969).
83. Usui, S., Sasaki, H., and Hasegawa, F., "Attachment between Mercury and Argon Bubbles in Aqueous KF Solutions," *Colloids Surfaces*, 18, 53 (1986).
84. Kaisheva, M., Usui, S., and Qi, D., "Interaction between a Stationary Mercury Electrode and a Hydrogen Bubble in an Aqueous Sodium Dodecyl Sulphate Solution," *Colloids Surfaces*, 29, 147 (1988).
85. Guyer, K.L., Barr, S.W., Cave, R.J., and Weaver, M.J., "Electrode Kinetics and Double-Layer Structure at Solid Electrodes," in *Proc. Third Symposium on Electrode Process.* ed. by Bruckenstein, S., Miller, B., McLntyze, J.D.E., and Yerger, E., The Electrochemical Society, Inc., Princeton, N.J., 390 (1980).
86. Hunter, R.J., *Zeta Potential in Colloid Science*, Academic Press, London, (1981).
87. Overbeek, J.Th.G., "Electrochemistry of the Double Layer," *Colloid Science*, ed. by Kruyt, H.R., Elsevier, Amsterdam, 1, 115 (1952).
88. Fuerstenau, D.W., "Mineral-Water Interfaces and Electrical Double Layer," in *Principles of Flotation*, ed. by King, R.P., South African IMM, Johannesburg, 17 (1982).
89. Parks, G.A., "The Isoelectric Points of Solid Oxides, Solid Hydroxides, and Aqueous Hydroxo Complex Systems," *Chem. Revs.* , 65, 177 (1965).
90. Yoon, R.H., Salman, T., and Donnay, G., "Predicting Points of Zero Charge of Oxides and Hydroxides," *J. Colloid Interface Sci.*, 70, 483 (1979).
91. James, R.O. and Parks, G.A., "Characterization of Aqueous Colloids by Their Electrical Double-Layer and Intrinsic Surface Chemical Properties," in *Surface and Colloid Science*, ed. by Matijevic, E., Plenum Press, New York, 12, 119 (1982).
92. Hunter, R.J. and Wright, H.J.L., "The Dependence of Electrokinetic Potential on Concentration of Electrolyte," *J. Colloid Interface Sci.*, 37, 564 (1971).

93. Levine, S. and Smith, A.L., "Theory of the Differential Capacity of the Oxide/Aqueous Electrolyte Interface," *Disc. Faraday Soc.*, 52, 290 (1971).
94. Yates, D.E., Levine, S., and Healy, T.W., "Site-Binding Model of the Electrical Double Layer at the Oxide/Water Interface," *JCS Faraday Trans. I*, 70, 1807 (1974).
95. Perrin, J., "Mecanisme de Lélectrisation de Contact et Solutions Colloïdales," *J. Chim. Phys.*, 2, 601 (1904).
96. Gouy, G., "Constitution of the Electric Charge at the Surface of an Electrolyte," *J. Phys.*, 9, 457 (1910).
97. Chapman, D.L., *Phil. Mag.*, 25, 475 (1913).
98. Shaw, D.J., *Introduction to Colloid and Surface Chemistry (Third Edition)*, Butterworth & Co Ltd, London, 1980.
99. Usui, S., "Electrical Double Layer," in *Surfactant Sci. Ser. (Electrical Phenomena at Interfaces)*, 15, 15 (1984).
100. Loeb, A.L., Overbeek, J.Th.G., and Wiersema, P.H., *The Electrical Double Layer Around a Spherical Colloidal Particle*, MIT Press, Cambridge, Mass., (1961).
101. Gronwall, T.H., La Mer, V.K., and Sandved, K., "The Influence of the So-called Higher Terms in the Debye-Hückel Theory of Solutions of Strong Electrolytes," *Phys. Z.*, 29, 358 (1928).
102. Dukhin, S.S. and Derjaguin, B.V., "Equilibrium Double Layer and Electrokinetic Phenomena," in *Surf. Colloid Sci.*, ed. by Matijevic, M., New York, 7, 49 (1974).
103. Abraham-Shhrauner, B., "Nonlinear Poisson-Boltzmann Potential for a Uniformly Charged Dielectric Sphere in an Electrolyte," *J. Colloid Interface Sci.*, 44, 79 (1973).
104. White, L.R., "Approximate Analytic Solution of the Poisson-Boltzmann Equation for a Spherical Colloidal Particle," *JCS Faraday Trans. II*, 73, 577 (1977).
105. Parlange, J.Y., "Note on the Poisson-Boltzmann Equation," *J. Chem. Phys.*, 57, 376 (1972).
106. Ohshima, H., Healy, T.W., and White, L.R., "Accurate Analytic Expressions for the Surface Charge Density/Surface Potential Relationship and Double-Layer Potential Distribution for a Spherical Colloidal Particle," *J. Colloid Interface Sci.*, 90, 17 (1982).
107. Bentz, J., "Electrostatic Potential around a Charged Sphere with Cation Binding," *J. Colloid Interface Sci.*, 80, 179 (1981).
108. Brenner, S.T. and Roberts, R.E., "A Variational Solution of the Poisson-Boltzmann Equation for a Spherical Colloidal Particle," *J. Phys. Chem.*, 77, 2367 (1973).

109. Ohshima, H., Healy, T.W., and White, L.R., "Improvement on the Hogg- Healy- Fuerstenau Formulas for the Interaction of Dissimilar Double Layers," *J. Colloid Interface Sci.*, 89, 484 (1982).
110. Haydon, D.A., "The Electrical Double layer and Electrokinetic Phenomena," in *Recent Progress in Surface Science*, ed. by Danielli, J.F., Pankhurst, K.G.A. and Riddiford, A.C., Academic Press, New York, 1, 94 (1964).
111. Martynov, G.A., "The Statistical Theory of the Double Electrical Layer: Part II," in *Research in Surface Forces*, Consultants Bureau, New York, 2, 84 (1966).
112. Sanfeld, A. and Defay, R., "Electric Repulsion between Two Diffuse Ionic Layers: Effect of Molar Volumes," *J. Chim. Phys.-Phys. Chim. Biol.*, 63, 577 (1966).
113. Martynov, G.A., "The Statistical Theory of the Double Electrical Layer: Part III," in *Research in Surface Forces*, Consultants Bureau, New York, 2, 94 (1966).
114. Frahm, J. and Dickman, S., "Numerical Calculation of Diffuse Double Layer Properties for Spherical Colloidal Particles by means of a Modified Nonlinearized Poisson-Boltzmann Equation" *J. Colloid Interface Sci.*, 70, 440 (1979).
115. Levine, S. and Bell, G.M., "Modified Poisson-Boltzmann Equation and Free Energy of Electrical Double Layers in Hydrophobic Colloids," *Discuss. Faraday Soc.*, 42, 69 (1966).
116. Verwey, E.J.W. and Overbeek, J.Th.G., *Theory of the Stability of Lyophobic Colloids*, Elsevier Publishing Company, Inc., New York, 1948.
117. Stern, O., "The Theory of Electrolytic Double-Layer," *Z. Elektrochem.*, 30, 508 (1924).
118. Pashley, R.M., "DLVO and Hydration Forces between Mica Surfaces in Li^+ , Na^+ , K^+ , and Cs^+ Electrolyte Solutions: A Correlation of Double-Layer and Hydration Forces with Surface Cation Exchange Process," *J. Colloid Interface Sci.*, 83, 531 (1981).
119. Ruckenstein, E. and Schiby, D., "Effect of Excluded Volume of the Hydrated Ions on Double-Layer Forces," *Langmuir*, 1, 612 (1985).
120. Stillinger, F.H. and Kirkwood, J.G., "Theory of the Diffuse Double Layer," *J. Chem. Phys.*, 33, 1282 (1960).
121. Grahame, D.C., "Effects of Dielectric Saturation on the Diffuse Double Layer and the Free Energy of Hydration of Ions," *J. Chem. Phys.*, 18, 903 (1950).
122. Hasted, J.B., Ritson, D.M. and Collie, C.H., "Dielectric Properties of Aqueous Ionic Solutions I.," *J. Chem. Phys.*, 16, 1 (1948).
123. Grahame, D.C., "The Electrical Double Layer and the Theory of Electrocapillarity," *Chem. Revs.*, 41, 441 (1947).

124. Frumkin, A.N., "The Theory of Electro-Capillarity," *Phil. Mag.*, 40, 375 (1920).
125. Parsons, R., "Equilibrium Properties of Electrified Interphases," in *Morden Aspects of Electrochemistry*, ed. by Bockris, J.O.M. and Conway, B.E., Butterworths, London, 1, 103 (1954).
126. Lyklema, J. and Overbeek, J.Th.G., "Electrochemistry of Silver Iodide. The Capacity of the Double Layer at the Silver Iodide-Water Interface," *J. Colloid Interface Sci.*, 16, 575 (1961).
127. Grahame, D.C., "The Role of the Cation in the Electrical Double Layer," *J. Electrochem. Soc.*, 98, 343 (1951).
128. Kar, G., Chander, S. and Mika, T.S., "The Potential Energy of Interaction Between Dissimilar Electrical Double Layers," *J. Colloid Interface Sci.*, 44, 347 (1973).
129. Overbeek, J.Th.G., "Recent Developments in the Understanding of Colloid Stability," *J. Colloid Interface Sci.*, 58, 408 (1976).
130. Smith, A.L., "Electrical Phenomena Associated with the Solid-Liquid Interface," in *Dispersions of Powders in Liquids*, ed. by Parfitt, G.D., Elsevier Publishing Company, Inc., Amsterdam, 39 (1969).
131. Frens, G. and Overbeek, J.Th.G., "Repeptization and the Theory of Electrocratic Colloids," *J. Colloid Interface Sci.*, 38, 376 (1972).
132. Overbeek, J.Th.G., "The Interaction between Colloidal Particles," in *Colloid Science*, ed. by Kruyt, H.R., Elsevier, Amsterdam, 1, 245 (1952).
133. Derjaguin, B.V., "A Theory of the Heterocoagulation, Interaction, and Adhesion of Dissimilar Particles in Solutions of Electrolytes," *Discuss. Faraday Soc.*, 18, 85 (1954).
134. Usui, S., "Heterocoagulation," in *Progress in Surface and Membrane Science*, ed. by Danielli, J.F., Rosenberg, M.D., and Cadenhead, , D.A., Academic Press, New York, 5, 223 (1972).
135. Hogg, R., Healy, T.W., and Fuerstenau, D.W., "Mutual Coagulation of Colloidal Dispersions," *Trans. Faraday Soc.*, 62, 1638 (1966).
136. Frens, G. and Overbeek, J.Th.G., "Carey Lea's Colloidal Silver," *Kolloid Z.*, 233, 922 (1969).
137. Bell, G.M. and Peterson, G.C., "Calculation of the Electric Double-Layer Force Between Unlike Spheres," *J. Colloid Interface Sci.*, 44, 542 (1972).
138. Kar, G., Chander, S. and Mika, T.S., "The Potential Energy of Interaction Between Dissimilar Electrical Double Layers," *J. Colloid Interface Sci.*, 44, 347 (1973).

139. Frens, G., Engel, D.J.C., and Overbeek, J.Th.G., "Nonequilibrium Method for the Direct Determination of Potentials of Zero Charge," *Trans. Faraday Soc.*, 63, 418 (1967).
140. Jones, J.E. and Levine, S., "A Comparison of the Conditions of Constant Surface Potential and Constant Surface Charge in the D.L.V.O. Theory of Colloid Stability," *J. Colloid Interface Sci.*, 30, 241 (1969).
141. Ninham, B.W. and Parsegian, V.A., "Electrostatic Potential between Surfaces Bearing Ionizable Groups in Ionic Equilibrium with Physiologic Saline Solution," *J. Theor. Biol.*, 31, 405 (1971).
142. Chan, D., Perram, J.W., White, L.R., and Healy, T.W., "Regulation of Surface Potential at Amphoteric Surfaces during Particle-Particle Interaction," *JCS Faraday Trans. I*, 71, 1046 (1975).
143. Chan, D., Healy, T.W., and White, L.R., "Electrical Double Layer Interactions under Regulation by Surface Ionization Equilibria-Dissimilar Amphoteric Surfaces," *JCS Faraday Trans. I*, 72, 2844 (1976).
144. Derjaguin, B.V., "On the Repulsive Forces between Charged Colloid Particles and the Theory of Slow Coagulation and Stability of Lyophobic Sols," *Trans. Faraday Soc.*, 36, 203 (1940).
145. Wiese, G.R. and Healy, T.W., "Effect of Particle Size on Colloid Stability," *Trans. Faraday Soc.*, 66, 490 (1970).
146. Overbeek, J.Th.G., "Strong and Weak Points in the Interaction of Colloid Stability," *Adv. Colloid Interface Sci.*, 16, 17 (1982).
147. Levine, S. and Bell, G.M., "The Discrete-Ion Effect and Colloid Stability Theory: Two Parallel Plates in a Symmetrical Electrolyte," *J. Phys. Chem.*, 67, 1408 (1963).
148. Levines, S., Mingins, J., and Bell, G.M., "The Discrete Ion Effect and Surface Potentials of Ionized Monolayers," *J. Phys. Chem.*, 67, 2095 (1963).
149. Read, A.D. and Kitchener, J.A., "Wetting Films on Silica," *J. Colloid Interface Sci.*, 30, 391 (1969).
150. Lyklema, J. and Mysels, K.J., "A Study of Double Layer Repulsion and van der Waals Attraction in Soap Films," *J. Am. Chem. Soc.*, 87, 2539 (1965).
151. Aronson, M.P. and Princen, H.M., "Aqueous Films on Silica in the Presence of Cationic Surfactants," *Colloid Polym. Sci.*, 256, 140 (1978).
152. Devereux, O.F. and de Bruyn, P.L., *Interactions of Plane-Parallel Double Layers*, MIT Press, Massachusetts, (1963).
153. Mysels, K.J. and Jones, M.N., "Direct Measurement of the Variation of Double-Layer Repulsion with Distance," *Discuss. Faraday Soc.*, 42, 42 (1966).

154. Barclay, L. and Ottewill, R.H., "Measurement of Forces between Colloidal Particles," *Special Discuss. Faraday Soc.*, 1, 138 (1970).
155. Roberts, A.D. and Tabor, D., "The Extrusion of Liquids between Highly Elastic Solids," *Pro. R. Soc. Lond.*, A325, 323 (1971).
156. Israelachvili, J.N., "Measurement of Forces between Surfaces Immersed in Electrolyte Solutions," *Faraday Discuss. Chem. Soc.*, 65, 20 (1978).
157. Horn, R.G., Smith, D.T., and Haller, W., "Surface Forces and Viscosity of Water Measured between Silica Sheets," *Chem. Phys. Lett.*, 162, 404 (1989).
158. Rabinovich, Ya.I., Derjaguin, B.V., and Churaev, N.V., "Direct Measurements of Long-Range Surface Forces in Gas and Liquid Media," *Adv. Colloid Interface Sci.*, 16, 63 (1982).
159. Ducker, W.A. and Pashley, R.M., "The Forces between Mica Surfaces in Ammonium Chloride Solutions," *J. Colloid Interface Sci.*, 131, 433 (1989).
160. Pashley, R.M., "Hydration Forces between Mica Surfaces in Aqueous Electrolyte Solutions," *J. Colloid Interface Sci.*, 80, 153 (1981).
161. Pashley, R.M., "The Effects of Hydrated Cation Adsorption on Surface Forces between Mica Crystals and Its Relevance to Colloidal Systems," *Chemica Scripta*, 25, 22 (1985).
162. Schulze, H., "Antimontrisulfid in Wässeriger Lösung," *J. Prakt. Chem.*, 27, 320 (1883).
163. Hardy, W.B., "On the Mechanism of Gelation in Reversible Colloidal Systems," *Proc. Roy. Soc.*, 66, 95 (1900).
164. Overbeek, J.Th.G., "The Rule of Schulze and Hardy," *Pure Appl. Chem.*, 52, 1151 (1980).
165. Ottewill, R.H., "Stability and Instability in Disperse Systems," in *Colloid Interface Sci.*, ed. by Milton Kerker, Rowell, R.L., and Zettlemoyer, A.C., Academic Press Inc., New York, 1, 379 (1977).
166. Fuchs, N., "Effect of the Charge of Aerosols on Their Stability," *Z. Physik.*, 89, 736 (1934).
167. Parfitt, G.D. and Picton, N.H., "Stability of Dispersions of Graphitized Carbon Blacks in Aqueous Solutions of Sodium Dodecyl Sulphate," *Trans. Faraday Soc.*, 64, 1955 (1968).
168. McGown, D.N.L. and Parfitt, G.D., "Stability of Non-Aqueous Dispersions IV. Rate of Coagulation of Rutile in Aerosol OT + p-Xylene Solutions," *Discuss. Faraday Soc.*, 42, 225 (1966).

169. Parfitt, G.D. and Willis, E., "Stability of Non-Aqueous Dispersions II. Graphon in Solutions of Alkyl Benzenes in n-Heptane," *J. Colloid Interface Sci.*, 22, 100 (1966).
170. Lewis, K.E. and Parfitt, G.D., "Stability of Non-Aqueous Dispersions III. Rate of Coagulation of Sterling MTG in Aerosol OT + n-Heptane Solutions," *Trans. Faraday Soc.*, 62, 1652 (1966).
171. Israelachvili, J.N., "Van der Waals Forces in Biological Systems," *Quart. Rev. Biophys.*, 6, 341 (1974).
172. Gingell, D. and Todd, I., "Adhesion of Red Blood Cells to Charged Interfaces between Immiscible Liquids. A New Method," *J. Cell Sci.*, 18, 227 (1975).
173. Gingell, D. and Fornes, J.A., "Interaction of Red Blood Cells with a Polarized Electrode," *Biophys. J.*, 16, 1131 (1976).
174. Israelachvili, J.N. and Ninham, B.W., "Intermolecular Forces- The Long and Short of It," *J. Colloid Interface Sci.*, 58, 14 (1977).
175. Christenson, H.K., "Non-DLVO Forces between Surfaces- Solvation, Hydration and Capillary Effects," *J. Dispersion Sci. Tech.*, 9, 171 (1988).
176. Ash, S.G., Everett, D.H., and Radke, C., "Thermodynamics of the Effects of Adsorption on Interparticle Forces," *J.C.S. Faraday Trans. II*, 69, 1256 (1973).
177. Claesson, P.M., "Experimental Evidence for Repulsive and Attractive Forces Not Accounted for by Conventional DLVO Theory," *Progr. Colloid Polymer Sci.*, 74, 48 (1987).
178. Derjaguin, B.V. and Churaev, N.V., "The Current State of the Theory of Long-Range Surface Forces," *Colloids Surfaces*, 41, 223 (1989).
179. Israelachvili, J.N., "Forces between Surfaces in Liquids," *Adv. Colloid Interface Sci.*, 16, 31 (1982).
180. Langmuir, I., "The Role of Attractive and Repulsive Forces in the Formation of Tactoids, Thixotropic Gels, Protein Crystals and Coacervates," *J. Chem. Phys.*, 6, 873 (1938).
181. Ninham, B.W., "Long-Range vs. Short-Range Forces. The Present State of Play," *J. Phys. Chem.*, 84, 1423 (1980).
182. Derjaguin, B.V. and Zorin, Z.M., "The Surface Condensation and Adsorption of Vapors near Saturation by an Optical Micropolarization Method I.," *Zh. Fiz. Khim.*, 29, 1010, 1755 (1955).
183. Churaev, N.V. and Derjaguin, B.V., "Inclusion of Structural Forces in the Theory of Stability of Colloids and Films," *J. Colloid Interface Sci.*, 103, 542 (1985).

184. Pashley, R.M. and Kitchener, J.A., "Surface Forces in Adsorbed Multilayers of Water on Quartz," *J. Colloid Interface Sci.*, 71, 491 (1979).
185. Allen, L.H. and Matijevic, E., "Stability of Colloidal Silica I. Effect of Simple Electrolytes," *J. Colloid Interface Sci.*, 31, 287 (1969).
186. Depasse, J. and Watillon, A., "The Stability of Amorphous Colloidal Silica," *J. Colloid Interface Sci.*, 33, 430 (1970).
187. Harding, R.D., "Stability of Silica Dispersions," *J. Colloid Interface Sci.*, 35, 172 (1971).
188. Johnson, G.A., Goldfarb, J., and Pethica, B.A., "Flocculation Studies on Model Systems: Octadecanol and Arachidic Acid Sols," *Trans. Faraday Soc.*, 61, 2321 (1965).
189. Johnson, G.A., Lecchini, S.M.A., Smith, E.G., Clifford, J., and Pethica, B.A., "Role of Water Structure in the Interpretation of Colloid Stability," *Discuss. Faraday Soc.*, 42, 120 (1966).
190. Lessard, R.R. and Ziemanski, S.I., "Bubble Coalescence and Gas Transfer in Aqueous Electrolytic Solutions," *Ind. Eng. Chem. Fundam.*, 10, 260 (1971).
191. Ninham, B.W., "Hierarchies of Forces: The Last 150 Years," *Adv. Colloid Interface Sci.*, 16, 3 (1982).
192. LeNeveu, D.M., Rand, R.P., and Parsegian, V.A., "Measurement of Forces between Lecithin Bilayers," *Nature*, 259, 601 (1976).
193. Low, P.F., "Structural Component of the Swelling Pressure of Clays," *Langmuir*, 3, 18 (1987).
194. Pashley, R.M. and Israelachvili, J.N., "DLVO and Hydration Forces between Mica Surfaces in Mg^{2+} , Ca^{2+} , Sr^{2+} , and Ba^{2+} Chloride Solutions," *J. Colloid Interface Sci.*, 97, 446 (1984).
195. Pashley, R.M., "Hydration Forces between Mica Surfaces in Aqueous Electrolyte Solutions," *Adv. Colloid Interface Sci.*, 18, 57 (1982).
196. Afzal, S., Tesler, W.J., Blessing, S.K., Collins, J.M., and Lis, L.J., "Hydration Force between Phosphatidylcholine Surfaces in Aqueous Electrolyte Solutions," *J. Colloid Interface Sci.*, 97, 303 (1984).
197. Peschel, G., Belouschek, P., Muller, M.M., Muller, M.R., and Konig, R., "The Interaction of Solid Surfaces in Aqueous Systems," *Colloid Polym. Sci.*, 260, 444 (1982).
198. Luck, W.A.P., "Water in Biological Systems," *Top. Curr. Chem.*, 64, 113 (1976).
199. Lyklema, J., "General Discussion," *Discuss. Faraday Soc.*, 65, 47 (1978).

200. Israelachvili, J.N. and Kott, S.J., "Liquid Structuring at Solid Interfaces as Probed by Direct Force Measurements: The Transition from Simple to Complex Liquids and Polymer Fluids," *J. Chem. Phys.*, 88, 7162 (1988).
201. Christenson, H.K., "Interaction between Hydrocarbon Surfaces in a Nonpolar Liquid: Effect of Surface Properties on Solvation Forces," *J. Phys. Chem.*, 90, 4 (1986).
202. Pashley, R.M., "Hydration Forces between Mica Surfaces in Electrolyte Solutions," *Adv. Colloid Interface Sci.*, 16, 57 (1982).
203. Christenson, H.K., Claesson, P.M., and Pashley, R.M., "The Hydrophobic Interaction between Macroscopic Surfaces," *Proc. Indian Acad. Sci. (Chem. Sci.)*, 98, 379 (1987).
204. Pashley, R.M. and Israelachvili, J.N., "A comparison of Surface Forces and Interfacial Properties of Mica in Purified Surfactant Solutions," *Colloids Surfaces*, 2, 169 (1981).
205. Israelachvili, J.N. and Pashley, R.M., "The Hydrophobic Interaction Is Long Range, Decaying Exponentially with Distance," *Nature*, 300, 341 (1982).
206. Israelachvili, J.N. and Pashley, R.M., "Measurement of the Hydrophobic Interaction between Two Hydrophobic Surfaces in Aqueous Electrolyte Solutions," *J. Colloid Interface Sci.*, 98, 500 (1984).
207. Pashley, R.M., McGuiggan, P.M., and Ninham, B.W., "Attractive Forces Between Uncharged Hydrophobic Surface: Direct Measurements in Aqueous Solution," *Science*, 229, 1088 (1985).
208. Claesson, P.M., Christina, E.B., Herder, P.C., and Ninham, B.W., "Interactions between Water-Stable Hydrophobic Langmuir-Boldgett Monolayers on Mica," *J. Colloid Interface Sci.*, 114, 234 (1986).
209. Rabinovich, Ya.I. and Derjaguin, B.V., "Interaction of Hydrophobized Filaments in Aqueous Electrolyte Solutions," *Colloids Surfaces*, 30, 243 (1988).
210. Claesson, P.M. and Christenson, H.K., "Very Long Range Attractive Forces between Uncharged Hydrocarbon and Fluorocarbon Surfaces in Water," *J. Phys. Chem.*, 92, 1650 (1988).
211. Parker, J.L., Christenson, H.K., and Ninham, B.W., "Forces between Bilayers of a Cationic Surfactant with Hydroxylated Headgroups: Effects of Interbilayer Adhesion on the Interactions," *J. Phys. Chem.*, 92, 4155 (1988).
212. Christenson, H.K. and Claesson, P.M., "Cavitation and the Interaction between Macroscopic Hydrophobic Surfaces," *Science*, 239, 390 (1988).
213. Christenson, H.K., Claesson, P.M., and Herder, P.C., "Forces between Fluorocarbon Surfactant Monolayers: Salt Effects on the Hydrophobic Interaction," *J. Phys. Chem.*, 93, 1472 (1989).

214. Claesson, P.M., Kjellander, R., Stenius, P., and Christenson, H.K., "Direct Measurement of Temperature-Dependent Interactions between Non-ionic Surfactant Layers," *JCS Faraday Trans. I*, 82, 2735 (1986).
215. Claesson, P.M., Horn, R.G., and Pashley, R.M., "Measurement of Surface Forces between Mica Sheets Immersed in Aqueous Quaternary Ammonium Ion Solutions," *J. Colloid Interface Sci.*, 100, 250 (1984).
216. Claesson, P.M., Herder, P.C., Bolm, C.E., and Ninham, B.W., "Interactions between a Positively Charged Hydrophobic Surface and a Negatively Charged Bare Mica Surface," *J. Colloid Interface Sci.*, 118, 68 (1987).
217. Marcelja, S. and Radic, N., "Repulsion of Interfaces due to Boundary Water," *Chem. Phys. Lett.*, 42, 129 (1976).
218. Eriksson, J.C., Ljunggren, S., and Claesson, P.M., "A Phenomenological Theory of Long-Range Hydrophobic Attraction Forces Based on a Square-Gradient Variational Approach," *JCS Faraday Trans. II*, 85, 163 (1989).
219. Cevc, G., Podgornik, R., and Zeks, B., "The Free Energy, Enthalpy, and Entropy of Hydration of Phospholipid Bilayer Membranes and Their Dependence on the Interfacial Separation," *Chem. Phys. Lett.*, 91, 193 (1982).
220. Marcelja, S., Mitchell, D.J., Ninham, B.W., and Sculley, M., "Role of Solvent Structure in Solution Theory," *JCS Faraday Trans. II*, 73, 630 (1977).
221. van Megen, W.J. and Snook, I.K., "Solvent Structure and Solvation Forces between Solid Bodies," *JCS Faraday Trans. II*, 75, 1095 (1979).
222. Snook, I.K. and van Megen, W.J., "Solvation Forces in Simple Dense Fluids I," *J. Chem. Phys.*, 72, 2907 (1980).
223. Snook, I.K. and van Megen, W.J., "Solvation Forces in Simple Dense Fluids III. Monolayer and Submonolayer Region," *J. Chem. Phys.*, 75, 4738 (1981).
224. Ravishanker, G., Mezei, M., and Beveridge, D.L., "Monte Carlo Computer Simulation Study of the Hydrophobic Effect," *Faraday Symp. Chem. Soc.*, 17, 79 (1982).
225. Dashevsky, V.G. and Sarkisov, G.N., "The Solvation and Hydrophobic Interaction of Non-polar Molecules in Water in the Approximation of Interatomic Potentials: The Monte Carlo Method," *Molecular Phys.*, 27, 1271 (1974).
226. Wallqvist, A. and Berne, B.J., "Hydrophobic Interaction between a Methane Molecule and a Paraffin Wall in Liquid Water," *Chem. Phys. Lett.*, 145, 26 (1988).
227. Marchesi, M., "Molecular Dynamics Simulation of Liquid Water between Two Walls," *Chem. Phys. Lett.*, 97, 224 (1983).

228. Barabino, G., Gavotti, C., and Marchesi, M., "Molecular Dynamics Simulation of Water near Walls Using an Improved Wall-Water Interaction Potential," *Chem. Phys. Lett.*, 104, 478 (1984).
229. Kjellander, R. and Marcelja, S., "Perturbation of Hydrogen Bonding in Water near Polar Surfaces," *Chem. Phys. Lett.*, 120, 393 (1985).
230. Horn, R.G. and Israelachvili, J.N., "Direct Measurement of Structural Forces between Two Surfaces in a Nonpolar Liquid," *J. Chem. Phys.*, 75, 1400 (1981).
231. Christenson, H.K. and Blom, C.E., "Solvation Forces and Phase Separation of Water in a Thin Film of Nonpolar Liquid between Mica Surfaces," *J. Chem. Phys.*, 86, 419 (1987).
232. Snook, I.K. and van Megen, W.J., "Solvation Forces in Simple Dense Fluids I.," *J. Chem. Phys.*, 72, 2907 (1980).
233. van Megen, W.J. and Snook, I.K., "Solvation Forces in Simple Dense Fluids II. Effect of Chemical Potential," *J. Chem. Phys.*, 74, 1409 (1981).
234. Luzar, A., Bratko, D., and Blum, L., "Monte Carlo Simulation of Hydrophobic Interaction," *J. Chem. Phys.*, 86, 2955 (1987).
235. Henderson, J.R., "Compressibility Route to Solvation Structure," *Mol. Phys.*, 59, 89 (1986).
236. Rabinovich, Ya.I., Derjaguin, B.V., and Churaev, N.V., "Direct Measurements of Long-Range Surface Forces in Gas and Liquid Media," *Adv. Colloid Interface Sci.*, 16,63 (1982).
237. Yushchenko, V.S., Yaminsky, V.V., and Schukin, E.D., "Interaction between Particles in Nonwetting Liquid," *J. Colloid Interface Sci.*, 96, 307 (1983).
238. Jonsson, B., "Monte Carlo Simulations of Liquid Water between Two Rigid Walls," *Chem. Phys. Lett.*, 82, 520 (1981).
239. Matsouka, O., Yoshimine, M., and Clementi, E., "CI Study of Water Dimer Potential Surface," *J. Chem. Phys.*, 64, 1351 (1976).
240. Christou, N.I., Whitehouse, J.S., Nicholson, D., and Parsonage, N.G., "A Monte Carlo Study of Fluid Water in Contact with Structureless Walls," *Faraday Symp. Chem. Soc.*, 16, 139 (1981).
241. Rowlinson, J.S., "The Lattice Energy of Ice and the Second Virial Coefficient of Water Vapour," *Trans. Faraday Soc.*, 47, 120 (1951).
242. Lee, C.Y. and McCammon, J.A., "The Structure of Liquid Water at an Extended Hydrophobic Surface," *J. Chem. Phys.*, 80, 4448 (1984).
243. Reimers, J.R. and Watts, R.O., "A Local Model Potential Function for the Water Molecule," *Mol. Phys.*, 52, 357 (1984).

244. Stillinger, F.H. and Rahman, A., "Improved Simulation of Liquid Water by Molecule Dynamics," *J. Chem. Phys.*, 60, 1545 (1974).
245. Sonnenschein, R. and Heinzinger, K., "A Molecular Dynamics Study of Water between Lennard-Jones Walls," *Chem. Phys. Lett.*, 102, 550 (1983).
246. Low, P.F., Cushman, J.H., and Diestler, D.J., "A Molecular Dynamics Study of Water near Silicate Surfaces," *J. Colloid Interface Sci.*, 100, 576 (1984).
247. Kjellander, R. and Marcelja, S., "Polarization of Water between Molecular Surfaces: A Molecular Dynamic Study," *Chem. Scripta*, 25, 73 (1985).
248. Attard, P. and Batchelor, M.T., "A Mechanism for the Hydration Force Demonstrated in Model System," *Chem. Phys. Lett.*, 149, 206 (1988).
249. Jonsson, B. and Wennerstrom, H., "Image-Charge Forces in Phospholipid Bilayer Systems," *JCS Faraday Trans. II*, 79, 19 (1983).
250. Kjellander, R., "On the Image-Charge Model for the Hydration Force," *JCS Faraday Trans. II*, 80, 1323 (1984).
251. Israelachvili, J.N. and Christenson, H.K., "Liquid Structure and Short-Range Forces between Surfaces in Liquids," *Physica*, A140, 278 (1986).
252. Israelachvili, J.N., "Measurements of Hydration Forces between Macroscopic Surfaces," *Chemica. Scripta*, 25, 7 (1985).
253. Lyklema, J., "Progress in Interfacial Chemistry in Relation to Colloid Stability," *Pure Appl. Chem.*, 53, 2199 (1981).
254. Attard, P., "Long-Range Attraction between Hydrophobic Surfaces," *J. Phys. Chem.*, 93, 6441 (1989).

CHAPTER 3 HYDROPHOBIC INTERACTION IN COAGULATION

3.1 Introduction

As has been discussed in Chapter 2, the classical DLVO theory of colloid stability has been successfully applied to many aqueous colloidal systems, particularly, to those in which only attractive dispersion and repulsive electrostatic interactions are operating between particles. However, some colloidal systems exhibit unusually strong interaction forces other than those considered in the DLVO theory (1). The additional forces may be repulsive or attractive, depending on the nature of the system (2).

The steric repulsion between adsorbed polymer layers (3-5) and repulsive hydration forces (1-2, 6-10) are well known. It is also well documented that for very hydrophobic substances, the attractive forces predicted by the DLVO theory are far weaker than those which can actually be measured in experiments (1, 11-18). These unexpectedly large attractive forces have been observed for hydrophobized mica and methylated silica using the apparatus developed by Israelachvili (1, 7, 11-14) or by Derjaguin (15-16) and are generally referred to as the hydrophobic effect.

Even though the hydrophobic interaction has been intensively studied as a function of distance (17-25), it is still an open question as to how hydrophobic interaction is related to the hydrophobicity of surfaces (25). It is of more practical importance to

quantitatively describe the role of hydrophobic interaction in a coagulation/dispersion process. The purpose of this chapter is to study the magnitude of hydrophobic interaction as a function of the surface hydrophobicity by means of examining the coagulation behavior of hydrophobic colloid systems.

In this chapter, a series of coagulation experiments has been carried out using coal samples oxidized to different extents and silica samples with and without methylation. The hydrophobic effects observed in these experiments have been quantitatively evaluated so that the DLVO theory can be extended to describe the stability of very hydrophobic particle suspensions as well.

3.2 Experimental

3.2.1 Sample Preparation

A run-of-mine coal (1.4% ash) from the Lower Cedar Grove seam, Virginia, was the primary coal sample used in this study. For contact angle measurements, chunky specimens were cut by a diamond saw and wet polished successively using 6-, 3-, and 1/4- μm diamond pastes on a Texmet-covered disk. The final polishing was made with 0.05- μm alumina powder on a microcloth-covered disk to obtain a mirror-like, smooth surface.

The rest of the run-of-mine sample was crushed to -6 mm using a laboratory hammer mill. The crushed coal was then split into representative lots of approximately 500 gram each, placed in air-tight containers, and stored in a freezer at -20 °C to minimize unintentional oxidation. Prior to the experiments, the crushed coal samples were dry-pulverized in a bench-scale hammer mill and the products were dry-screened. The -400 mesh fraction with an average particle size of 5 μm was used for the coagulation

experiments, and -210 + 125- μm fraction was saved for heat of wetting and heat of displacement measurements. Some of the coal samples were artificially oxidized for 24 hours at elevated temperatures in an air convection oven.

A 10- μm silica sample with an average diameter of 3.2 μm was obtained from the Pennsylvania Glass Sand Corp. A portion of the silica sample was methylated using a procedure similar to those described by Laskowski and Kitchener (26) and by Blake and Ralston (27). A 100-gram silica sample preheated at 75 °C in an air convection oven for 24 hours was contacted with 450 ml of trimethylchlorosilane (TMCS) solution (20% by volume) prepared in cyclohexane. The initial contact was made in an ultrasonic bath for 10 minutes, and then the mixture was left to stand in an ambient environment for 15 hours to complete the reaction. The methylated silica was separated from the solution by filtering and washing with pure cyclohexane and dried at 75 °C for 24 hours. For the contact angle measurements, fused silica plates were methylated in a similar manner. All the liquid chemicals used in this study are of spectral-grade. They were used without any further purification except dehydration with molecular sieves.

3.2.2 Coagulation Tests

A 10-gram coal sample (-400 mesh) suspended in a 500-ml *KCL* solution of 10^{-3} *M* concentration and given *pH* was agitated for 5 minutes at 1000 rpm. The mixing tank is schematically shown in Appendix I as Figure I.1. It was made of a 3 ½-in.-diameter Plexiglas cylinder and equipped with four baffles and a variable-speed impeller of 1 ¼ inch diameter. After the agitation, the suspension was allowed to settle for 3 minutes and then 300 ml of the supernatant was removed by siphoning. The solids in the supernatant were weighed after filtration and drying. The coagulation efficiency (E_c) was calculated as:

$$E_c = \frac{W_i - W_f}{W_i} \times 100 , \quad [3.1]$$

in which W_i refers to the initial weight of solids in a given volume (300 ml) of the suspension before coagulation, and W_f refers to that in the supernatant after coagulation.

For the coagulation of silica, a 5-gram sample was used in each experiment. The suspension was agitated at 500 rpm, and a 1 minute settling time was employed.

3.2.3 Contact Angle Measurements

Contact angles were measured at $25 \pm 2^\circ\text{C}$ using a contact angle goniometer (Rame-Hart). The sessile drop technique was employed inside a closed container in order to take the measurements at equilibrium vapor pressure. The drops were formed by introducing roughly 1 microliter liquid onto the plates with the help of a microliter syringe. At least 20 equilibrium contact angles were measured at different sites and specimens and averaged. The technique was checked by measuring the contact angles of water droplets on a paraffin-covered glass plate. The average value of 107.3° with a standard deviation of 2.1° was in good agreement with the published value of 110° (28).

3.2.4 Heat of Wetting and Heat of Displacement Measurements

Approximately 0.1 grams of coal sample ($-210 + 125 \mu\text{m}$) were placed inside a Microscal flow microcalorimeter, evacuated at 10^{-4} Torr and room temperature for about 5 hours, and then contacted by heptane while monitoring the heat of wetting. After the sample was completely wetted as indicated by a steady state base line, double-distilled water was introduced into the cell at a flow rate of 3.3 ml/hr using a

microsyringe pump. The heat measured as such represents the enthalpy change in the displacement of heptane by water primarily from the polar sites of the sample.

3.2.5 *Electrokinetic Studies*

Zeta potentials were measured using a Pen Kem Model 501 laser zee meter. The sample suspension was prepared by dispersing 0.02 grams of the $-5 \mu\text{m}$ sample in 500 ml of 10^{-3} M KCl solution. At a given experimental condition, at least three ζ -potential readings of different runs were taken and averaged.

3.3 Experimental Results

3.3.1 *Coagulation and Electrokinetic Studies*

Figure 3.1 shows the coagulation and ζ -potential data obtained as a function of pH on both fresh and oxidized (140°C) coal samples. The fresh coal is shown to coagulate over a wide range of pH values, from 3.8 to 8.9. The dotted lines in Figure 3.1 show how the upper critical coagulation pH limit and the corresponding ζ -potential are determined. The low pH limit and the corresponding ζ -potential can be determined likewise. It is interesting to note that at the upper and lower critical coagulation pH limits, the ζ -potentials, i.e., 42 and -43 mV, respectively, are of approximately the same magnitude. The fact that the fresh coal can coagulate at such high ζ -potentials suggests that there exists a highly attractive force which can overcome the strong electrostatic repulsive force. As will be evident later in this chapter, the attractive force is much larger than the dispersion forces considered in the DLVO theory. This excess attractive force may be referred to as the hydrophobic interaction force.

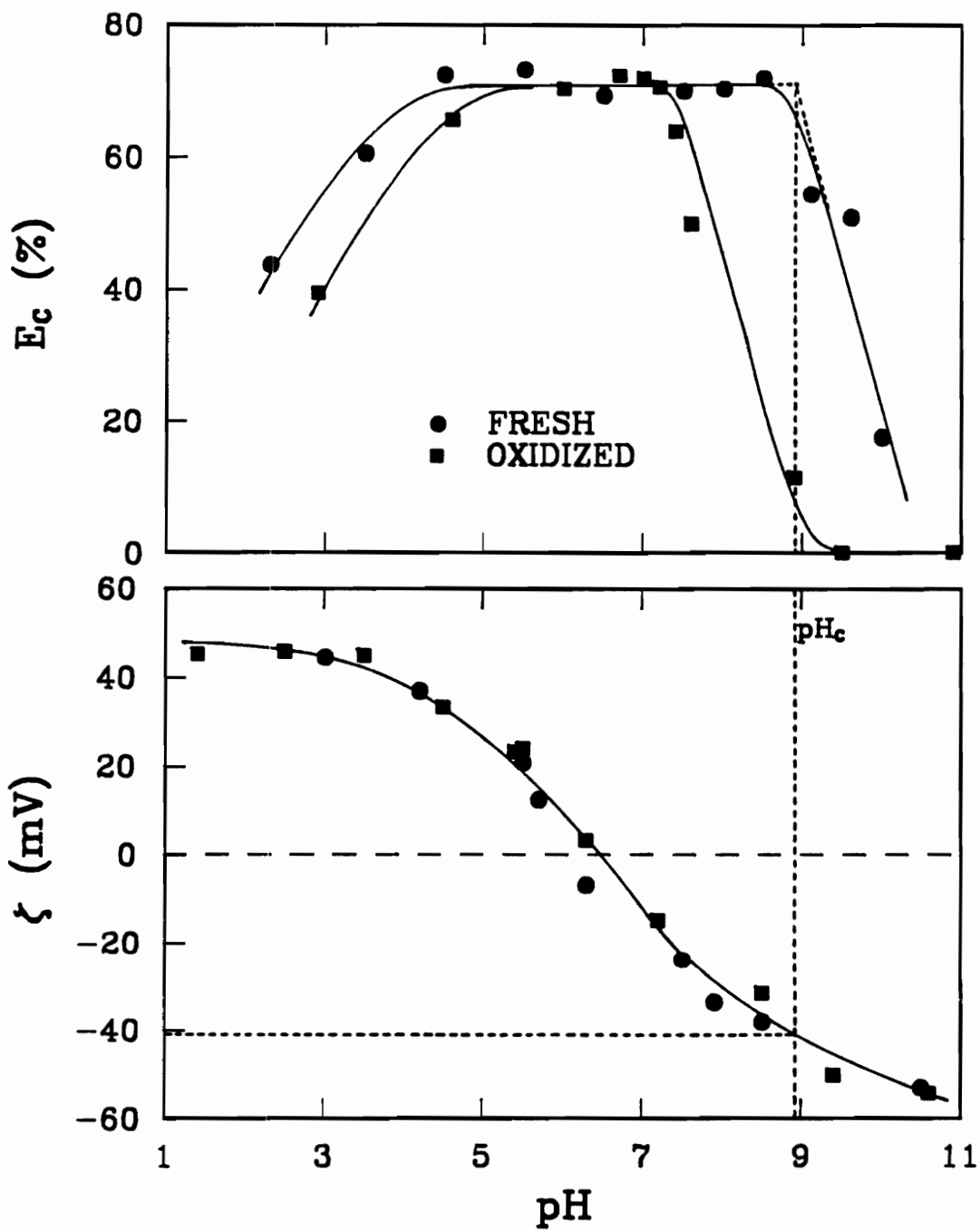


Figure 3.1. Coagulation and ζ -potential Measurements on Fresh and Oxidized (140 °C) Coal Samples as a Function of pH

Figure 3.1 also shows that the oxidation of the coal samples at 140 °C did not change the ζ -potential values appreciably, while the effective pH range for coagulation was reduced significantly. The upper critical coagulation pH limit, which will be designated as pH_c , was lowered to 7.3, at which point the corresponding ζ -potential value (ζ_c) was only -23 mV. The fact that no coagulation is possible at higher ζ -potentials suggests that oxidation significantly reduced the hydrophobic interaction force. It appears that only some phenol surface groups, which are not very sensitive surface potential determining groups, were generated by the mild oxidation at 140 °C. However, these phenol groups may reduce the surface hydrophobicity slightly, resulting in a significant reduction in the hydrophobic interaction force as observed experimentally.

The results obtained with coal samples oxidized at higher temperatures, i.e., 170 and 200 °C, are shown in Figure 3.2. One can see that after such a severe oxidation, the hydrophobic interaction force was further reduced, so that coagulation could occur only at pH near the *i.e.p.* of the coal sample. The ζ -potential values at pH_c 's were less than 5 mV in magnitude. At these low ζ -potentials, the dispersion forces would be sufficient to overcome the electrostatic repulsive force, in which case the DLVO theory may be perfectly applicable. It is possible that the hydrophobic force is still operating in these systems, but its magnitude must be smaller than that of the dispersion and electrostatic forces.

The results of the coagulation experiments conducted with natural and methylated silica samples are shown in Figure 3.3 along with their ζ -potential data. It shows that natural silica did not coagulate at any pH , even at its *i.e.p.*, which is difficult to explain on the basis of the DLVO theory. Other investigators (29-31) reported similar results, which Churaev and Derjaguin (2) attributed to the repulsive hydration (or structural) force. On the contrary, with the methylated silica, the coagulation occurred over a wide pH range extending up to pH 10.7, which is well above its *i.e.p.*. At this

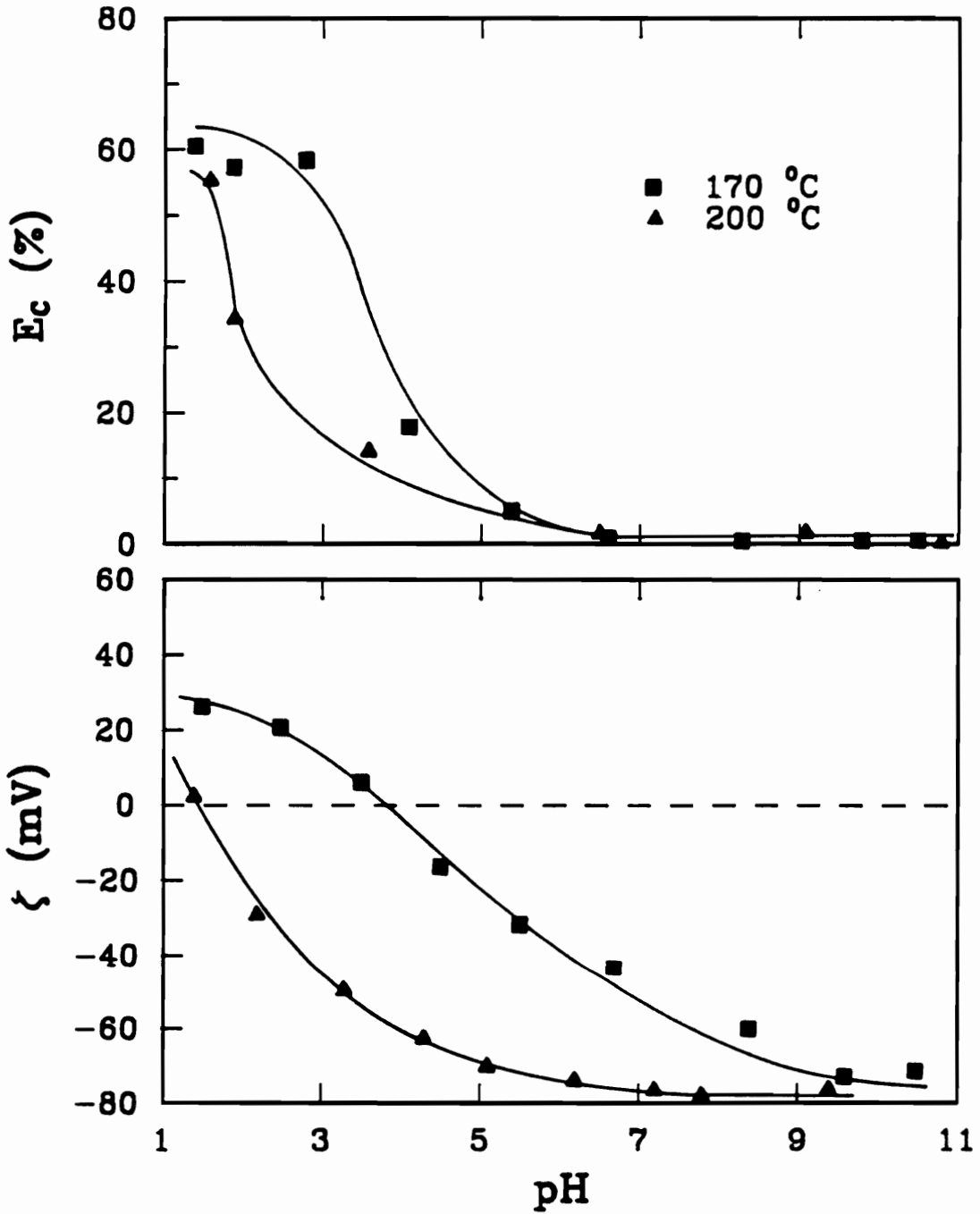
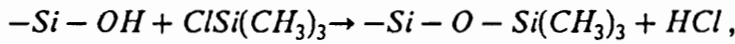


Figure 3.2. Coagulation and ζ -potential Measurements on Coal Samples Oxidized at 170 and 200 °C as a Function of pH

pH_c , the ζ -potential was as high as -51 mV. As proposed (32), the surface methylation of silica samples occurs in terms of the following reaction:



which forms hydrocarbon groups on the surface and reduces surface concentration of OH groups. As a result, the surface hydrophobicity of silica samples increases significantly upon methylation. This finding suggests that a strong attractive interaction force, which has not been considered in the classical DLVO theory, is induced due to the increased hydrophobicity of the solid surface.

Table 3.1. Critical pH and ζ -Potential Values Obtained Experimentally for Coagulation of Coal and Silica Samples

Parameters	COAL				Silica	
	Oxidation Temperature (°C)				Methy.	Natural
	25	140	170	200		
pH_c	8.9	7.3	3.8	1.5	10.7	---
ζ_c (mV)	-43.0	-22.0	-5.0	-5.0	-51.0	---

Table 3.1 summarizes the results presented in Figures 3.1-3.3. It shows that very hydrophobic solids, such as fresh coal and methylated silica, can coagulate at pH values far above their *i.e.p.*'s, where the ζ -potential values are in excess of -40 mV. This was possible most likely because of the presence of a large hydrophobic interaction force. As the coal was oxidized, however, the hydrophobic interaction force was reduced and,

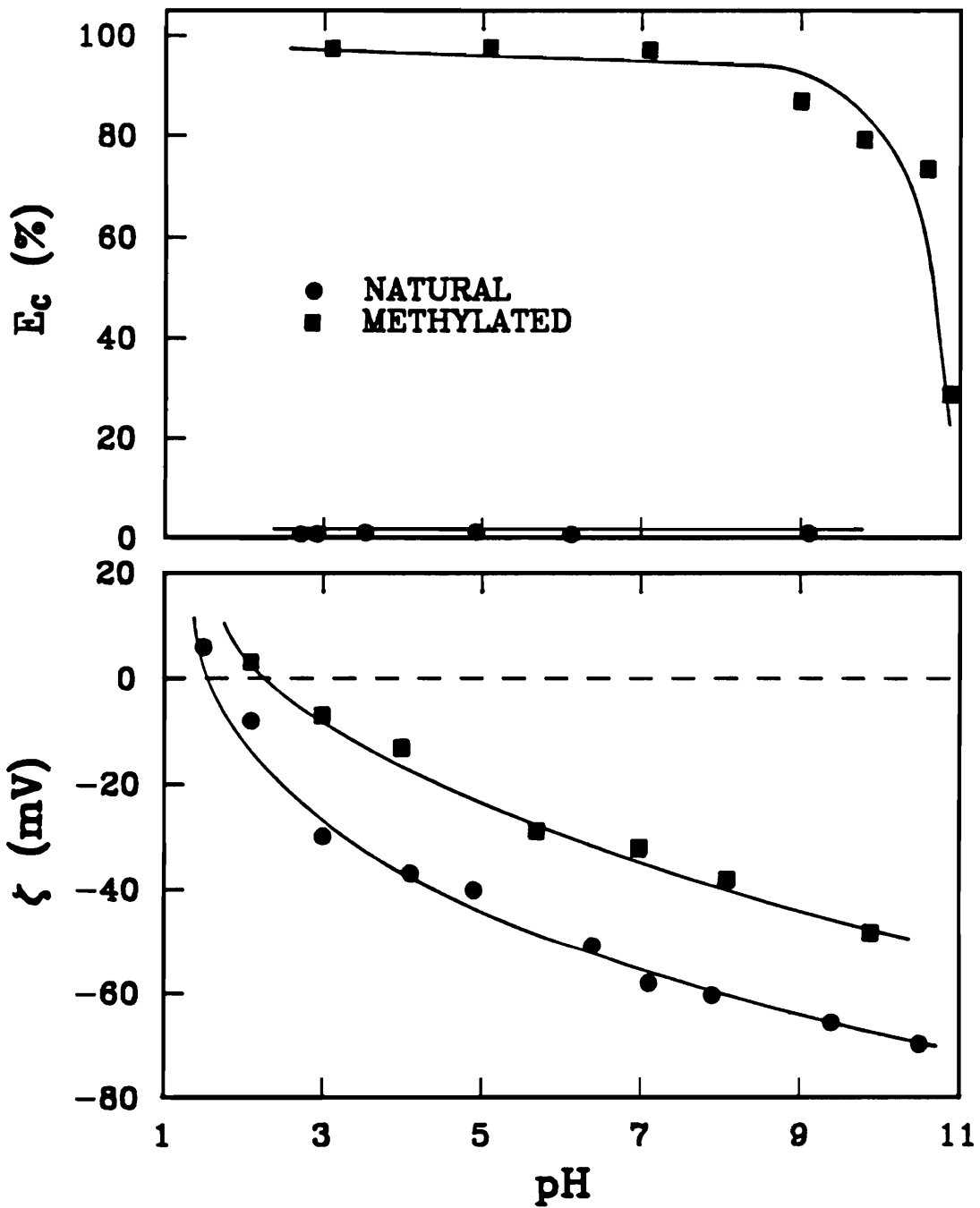


Figure 3.3. Coagulation and ζ -potential Measurements on Silica Samples with and without Methylation as a Function of pH

as a result, the coagulation occurred at *pH* values close to its *i.e.p.*, where the ζ -potential was low.

3.3.2 Characterizations of Surface Forces

In order to have a better understanding of the surface forces operating during coagulation, a series of methylene iodide and water contact angle measurements were carried out. Since the nondispersion component of surface free energy (γ_m^{nd}) of methylene iodide is negligible (2.3 erg/cm^2) (33), it is possible to determine the dispersion component of the surface free energy of a solid (γ_s^d) using the equation (33):

$$\gamma_s^d = \left[\frac{(1 + \cos \theta_m) \gamma_m}{2 \sqrt{\gamma_m^d}} \right]^2, \quad [3.2]$$

in which θ_m is the contact angle of methylene iodide on solid, γ_m ($= 50.8 \text{ erg/cm}^2$) is the surface free energy of methylene iodide, and γ_m^d ($= 48.5 \text{ erg/cm}^2$) is its dispersion component. The methylene iodide was chosen as a reference liquid also because of its high boiling point ($180 \text{ }^\circ\text{C}$), low viscosity and relatively high surface free energy.

The experimental contact angles and the calculated γ_s^d values for the coal and silica samples used in the present work are given in Table 3.2. It is shown that γ_s^d value increases slightly as the coal becomes severely oxidized at higher temperatures. This can be attributed to the increased concentration of oxygen-containing functional groups such as carbonyl, carboxyl, and hydroxyl groups that are more polarizable than the hydrocarbon groups of the unoxidized coal surface. According to these results, the dispersion interaction energy should increase with increasing oxidation, which in turn suggests, based on the DLVO theory, that coagulation should be favored with an increasing degree of oxidation. Of course, this is contrary to what has been observed in

experiments as shown in Table 3.1 and Figures 1-3. Similarly, the results obtained with methylated silica show that γ_s^d value decreased substantially after methylation, yet the methylated silica coagulated more readily while natural silica did not. These findings further substantiate the presence of a hydrophobic interaction force.

Table 3.2. Dispersion Component of Surface Free Energies of Coal and Silica Samples as Calculated from Methylene Iodide Contact Angles

Parameters	COAL					Silica	
	Oxidation Temperature (°C)					Methy.	Natural
	25	75	140	170	200		
θ_w (degree)	38.8	35.0	32.2	26.6	23.3	60.0	0.0
γ_s^d (erg/cm ²)	42.1	44.0	45.2	47.7	49.0	29.9	76.0 ⁽³⁷⁾

Since γ_s^d fails to adequately describe the coagulation behavior of hydrophobic solids, the nondispersion component of work of adhesion (W_a^{nd}) of water on solids was determined from the contact angle measurements using the relationship:

$$W_a^{nd} = \gamma_w(1 + \cos \theta_w) - 2\sqrt{\gamma_s^d \gamma_w^d} \quad , \quad [3.3]$$

in which θ_w is the water contact angle, γ_w is the surface free energy of liquid water and γ_w^d is its dispersion component. The first term on the right hand side of Equation [3.3] represents the work of adhesion (W_a) of water on a solid, and the second term represents its dispersion component (W_a^d). Equation [3.3] can be derived as follows. The work of adhesion is related to the surface and interfacial tensions by Equation [3.4],

$$W_a = \gamma_s + \gamma_w - \gamma_{sw} = W_a^d + W_a^{nd} , \quad [3.4]$$

in which γ_{sw} is the solid/water interfacial tension. The second equal sign follows that the work of adhesion can be decomposed into two major components, i.e., dispersion and nondispersion components. Rearranging the equation expressed by the second equal sign of Equation [3.4] results in:

$$W_a^{nd} = \gamma_s + \gamma_w - \gamma_{sw} - W_a^d . \quad [3.5]$$

By introducing Young's equation into Equation [3.5], Equation [3.6] is readily obtained:

$$W_a^{nd} = \gamma_w(1 + \cos \theta_w) - W_a^d . \quad [3.6]$$

Expressing W_a^d explicitly in Equation [3.6] by Equation [3.7] (34) yields the above Equation [3.3] for calculating the values of W_a^{nd} from the contact angle data.

$$W_a^d = 2\sqrt{\gamma_w^d \gamma_s^d} . \quad [3.7]$$

The values of experimentally measured contact angles of water on the solids are given in Table 3.3. From these measured contact angles, the nondispersion component of work of adhesion (W_a^{nd}) is calculated using Equation [3.3] and the results are given in Table 3.3 and Figure 3.4. Also shown in Figure 3.4 is the dispersion component of work of adhesion (W_a^d) of water on solids as a function of oxidation temperature.

As shown, W_a^{nd} is much more sensitive to changes in surface chemistry due to oxidation than W_a^d , particularly when the exposure temperature is higher than approximately 140 °C. Since the samples oxidized at the temperature above 140 °C were coagulated only when the ζ -potentials were low, as shown in Figure 3.2 and Table 3.1, which

is in accordance with the DLVO theory, one can see that hydrophobic interaction force becomes insignificant after a high temperature oxidation. Similarly, there was a significant reduction in W_a^{nd} due to the methylation, which induced a strong hydrophobic interaction that cannot be described by the DLVO theory. Therefore, W_a^{nd} may be a useful parameter in relating the hydrophobic interaction energy to changes in surface chemistry.

Table 3.3. W_a^{nd} Values for Coal and Silica Samples Calculated from the Water Contact Angles

Parameters	COAL					Silica	
	Oxidation Temperature (°C)					Methy.	Natural
	25	75	140	170	200		
θ_w (degree)	73.5	70.3	66.7	50.6	39.2	92.6	0.0
W_a^{nd} (erg/cm ²)	32.9	35.1	38.5	52.9	63.6	18.4	>63.8

Figure 3.5 shows the heats of wetting of coal by heptane and the heats of heptane displacement by water from the coal surface. It shows that the heat of wetting does not change significantly as coal undergoes oxidation with increasing temperature. This is not surprising because heptane would interact with coal primarily through a dispersion interaction, and γ_a^d does not change considerably with oxidation as shown in Table 3.2 and Figure 3.4. On the other hand, the heat of heptane displacement by water is shown to increase significantly for the coal samples oxidized with increasing temperature. Note that the sharp increase above 140 °C corresponds closely to that observed for W_a^{nd} as shown in Figure 3.4. This close correlation between heats of displacement and W_a^{nd} sim-

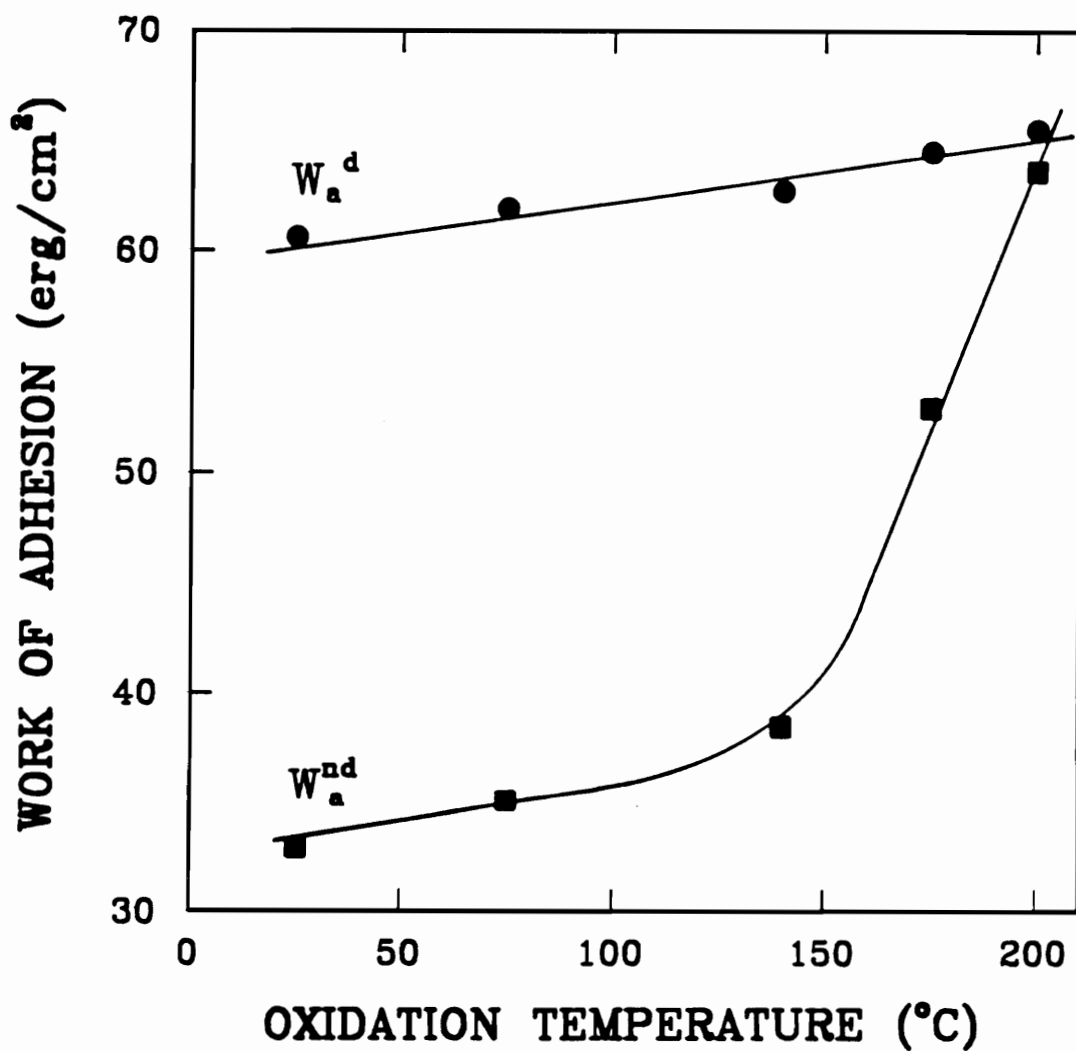


Figure 3.4. Dispersion and Nondispersion Components of Work of Adhesion of Water on Coal as a Function of Oxidation Temperature

ply shows that water interacts primarily with polar sites on the oxidized coal surface. Thus the results shown in Figures 3.4 and 3.5 support the view that W_a^{nd} plays a more important role than does W_a^d in determining the hydrophobicity of a solid (34-35).

3.4 Discussion

As has been reviewed in Chapter 2, the stability of lyophobic colloids is, according to the classical DLVO theory, determined by the sum of electrostatic repulsive energy (V_R) and London-van der Waals dispersion interaction energy (V_A), i.e.,

$$V_T = V_R + V_A \quad . \quad [3.8]$$

For convenience, the equations used in this chapter for calculating the values of V_R and V_A are briefly summarized here. For spherical particles of radius, a , separated by a distance, H , the electrostatic repulsive energy becomes (36-37):

$$V_R = \frac{\epsilon a \psi_d^2}{2} \ln[1 + \exp(-\kappa H)] \quad , \quad [3.9]$$

in which ϵ is the dielectric constant of the medium, κ is the Debye reciprocal length, and ψ_d is the stern potential. Although Equation [3.9] is derived based on the assumption that ψ_d is less than 25 mV in magnitude, Hogg et al. (37) showed that Equation [3.9] is valid for ψ_d up to approximately 60 mV.

The dispersion interaction energy can be calculated using the equation (38):

$$V_A = - \frac{aA_{131}}{12H} \quad , \quad [3.10]$$

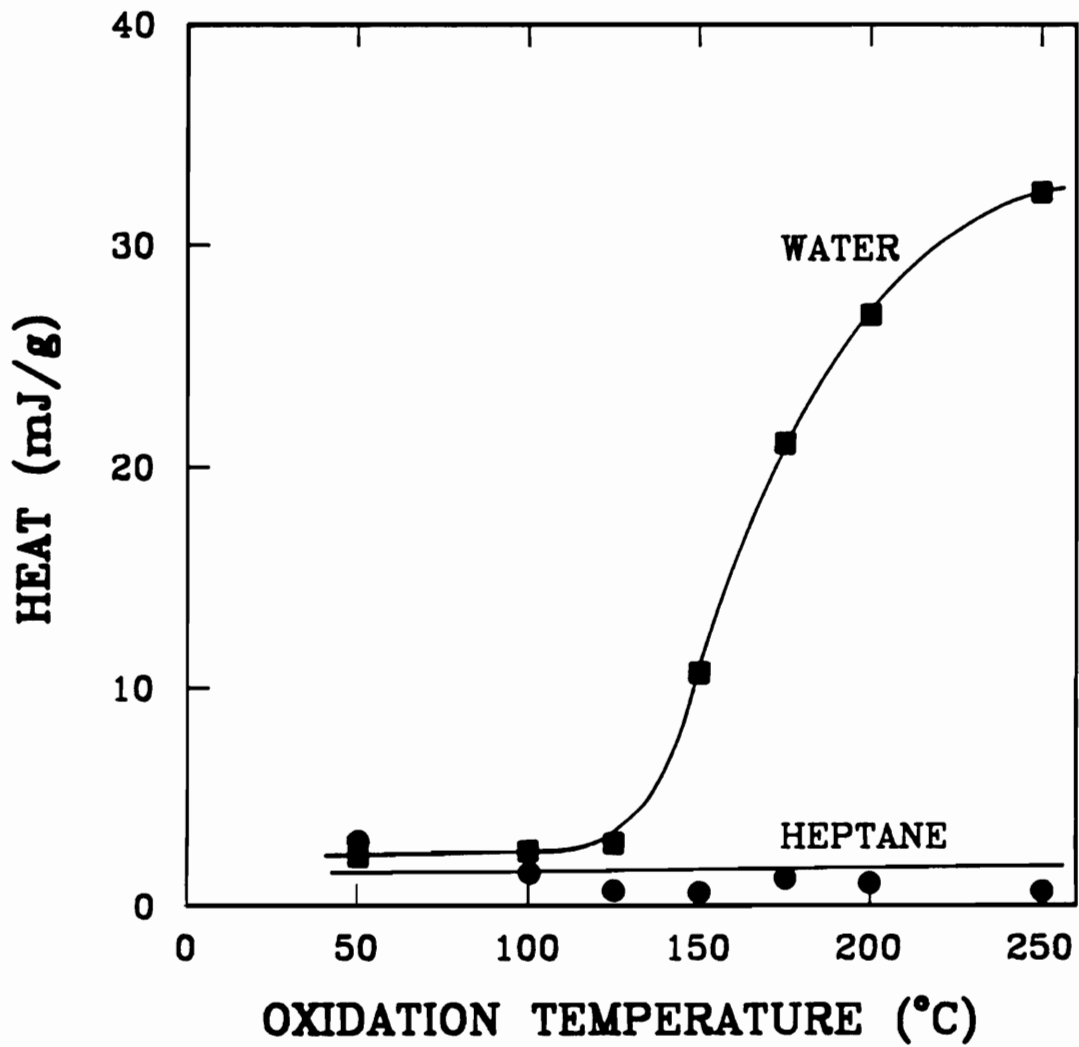


Figure 3.5. Heat of Wetting of Coal in Heptane and Heating of Heptane Displacement by Water as a Function of Oxidation Temperature

in which A_{131} is the combined Hamaker constant. Equation [3.10] is valid when $a > H$. The combined Hamaker constant (A_{131}) for two spheres in a medium can be estimated (39) by Equation [3.11] which is simplified from Lifshitz theory:

$$A_{131} = \frac{[\sqrt{A_{11}} - \sqrt{A_{33}}]^2}{1 - 2.5 \times 10^{18} \sqrt{A_{11}A_{33}}} \quad [3.11]$$

In Equation [3.11], A_{11} and A_{33} refer to the Hamaker constants of the solid and the medium, respectively, in vacuum. Fowkes (33, 40) showed that these two Hamaker constants can be determined by:

$$A_{ii} = 6\pi r_{ii}^2 \gamma_i^d \quad [3.12]$$

in which r_{ii} is the intermolecular distance within the interacting body of the substance in question and γ_i^d refers to the dispersion component of the surface free energy of the substance in question. Fowkes suggested that $6\pi r_{ii}^2$ approximates $1.44 \times 10^{-14} \text{ cm}$ for most materials.

The typical total interaction energy calculated using Equation [3.8] as a function of interparticle separation shows a maximum at certain separation. According to the classical DLVO theory, the stability of suspension is mostly controlled by the magnitude of energy maximum (V_{\max}) called energy barrier. The interaction energy barrier has been calculated as a function of ζ -potential in the range of -10 mV to 0 mV for the fresh and oxidized (200 °C) coal samples and for silica samples with and without methylation in view of the DLVO theory, i.e., using Equations [3.8], [3.9] and [3.10] in combination. The results are given in Figure 3.6. In the above calculations, the value of κ is assumed to be 10 nm which corresponds to a solution concentration of 10^{-3} M KCl as used in the coagulation experiments and ζ -potential measurements. The Hamaker constants were

estimated by means of Equations [3.11] and [3.12] using the γ_f^d values given in Table 3.2. The values of Hamaker constant calculated as such are given in Table 3.4.

Table 3.4. Potential Energy Barriers at Critical pH of Coagulation and Hamaker Constants of Coal and Silica Samples

Parameters	COAL				Silica	
	Oxidation Temperature ($^{\circ}\text{C}$)				Methy.	Natural
	25	140	170	200		
$A_{11} \times 10^{20}(\text{J})$	6.07	6.51	6.87	7.06	4.31	10.9
$A_{131} \times 10^{21}(\text{J})$	5.24	6.71	8.00	8.72	0.96	22.6
$V_{\max} (kT)$	2924	548	3.3	2.3	2901	---

As shown in Figure 3.6, V_{\max} increases in the order of natural silica, oxidized coal, fresh coal and methylated silica at the same surface potential. Therefore, the suspension of methylated silica should, theoretically, be most stable followed by that of fresh coal, oxidized coal and natural silica, which is in an opposite order to what was experimentally observed. If 15 kT of potential energy barrier is considered as insurmountable, (41-43), i.e., the suspension is stable if $V_{\max} > 15 kT$, theoretical ζ_c values can be obtained by reading the ζ -potential values in Figure 3.6 which correspond to the intersections of each curve and a horizontal line of 15 kT. For the natural silica, oxidized coal, fresh coal and methylated silica, the obtained ζ_c values are -10, -76., -5.7 and -4.8 mV, respectively. They correspond to pH_c values of 2.2, 1.6, 6.4 and 2.8, respectively, as obtained from Figures 3.1, 3.2 and 3.3. Comparing these values with experimentally obtained pH_c values of 1.5, 8.9 and 10.7 for oxidized coal, fresh coal and methylated silica samples, re-

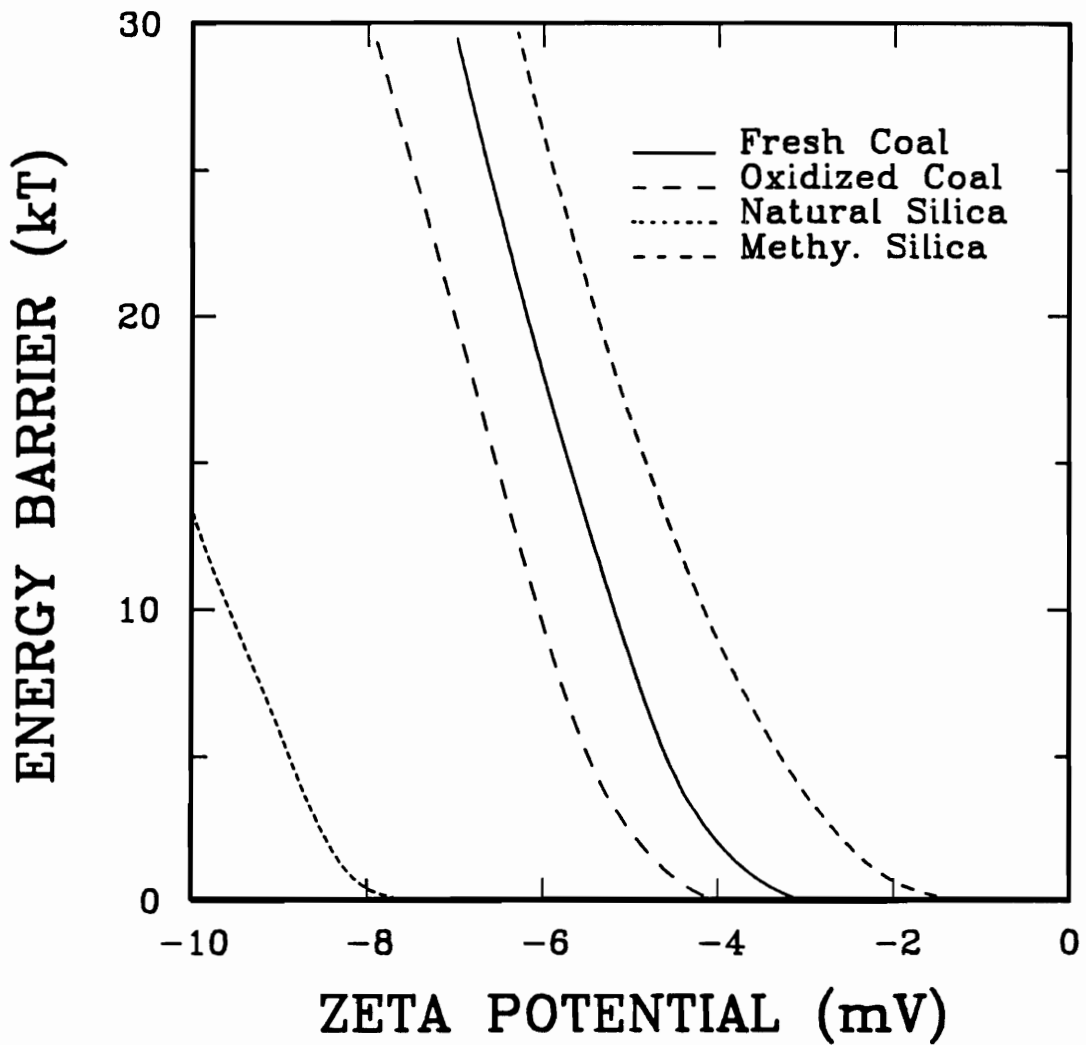


Figure 3.6. Interaction Energy Barrier as a Function of Surface Potential Calculated Using the Classical DLVO Theory

spectively, it is not difficult to see that the observed pH_c value is in excellent agreement with that calculated using the DLVO theory if the colloid is weakly hydrophobic, such as highly oxidized coal samples. However, the calculated pH_c values are much lower than that experimentally obtained if the colloids are strongly hydrophobic, such as fresh coal and methylated silica. This discrepancy indicates the limitation of the DLVO theory in describing the stability of colloidal suspensions.

In order to evaluate quantitatively the role of the hydrophobic interaction in coagulation, the interaction energy barriers at critical coagulation conditions were calculated using Equations [3.8], [3.9] and [3.10] in which ψ_d is replaced by the ζ -potential value measured at critical coagulation pH . The results are also given in Table 3.4. One can see that the V_{\max} values calculated as such decrease with increasing oxidation temperature, which suggests that coagulation should be favored as the coal becomes more oxidized. This is, of course, contrary to what was observed experimentally. As has been shown in Figures 3.1 and 3.2, fresh coal coagulates readily over a wide range of pH , while oxidized coals only coagulate over a narrow pH range near their *i.e.p.*'s. Energy barriers calculated for coal samples oxidized at 170 and 200 °C are less than 15 kT and, therefore, coagulation should be possible by thermal agitation alone. These findings therefore suggest that the DLVO theory is applicable to mildly hydrophobic particles such as those coal samples oxidized at temperatures above 140 °C but not to the strongly hydrophobic particles.

Note that the energy barriers calculated using the DLVO theory for the fresh coal and methylated silica samples are particularly large and well above 15 kT. Obviously, one must consider an additional energy term, such as hydrophobic interaction energy, which has not been considered in the DLVO theory to minimize the discrepancy between theory and experiment. Although it is not the main purpose of this chapter to discuss the nature of the hydrophobic interaction energy, it has been shown in the fore-

going section that W_a^{nd} may be a useful parameter for describing the hydrophobic interaction energy (V_H). Therefore, the V_H values, which may be taken to be equal in magnitude but opposite in sign to V_{max} , are plotted as a function of W_a^{nd} in Figure 3.7. As shown, there is a sharp transition at W_a^{nd} near 40 erg/cm^2 .

The V_H versus W_a^{nd} plot of Figure 3.7 can be represented by the functional form of:

$$V_H = \frac{-V_m}{1 + \exp[b(W_a^{nd} - c)]} \quad , \quad [3.13]$$

which requires three parameters, i.e., V_m , b and c , to fit the data. Using the nonlinear regression curve-fitting procedure, the three parameters have been determined, at a 95% confidence level, to be

$$V_m = 2924.0 \pm 4.7 \text{ kT} \quad [3.14]$$

$$b = 1.034 \pm 0.046 \text{ (erg/cm}^2\text{)}^{-1} \quad [3.15]$$

and $c = 37.08 \pm 0.07 \text{ erg/cm}^2$. [3.16]

The solid line shown in Figure 3.7 represents Equation [3.13] with the parameters being given by Equations [3.14], [3.15] and [3.16] and shows an excellent fit with the experimental data.

The physical meaning of the three parameters of Equation [3.13] may be discussed as follows. One can see that as W_a^{nd} approaches zero, which is the case for very hydrophobic solids, V_H approximates $-V_m$. Therefore, $-V_m$ represents the maximum hydrophobic interaction energy for very hydrophobic solids. This value is of the same

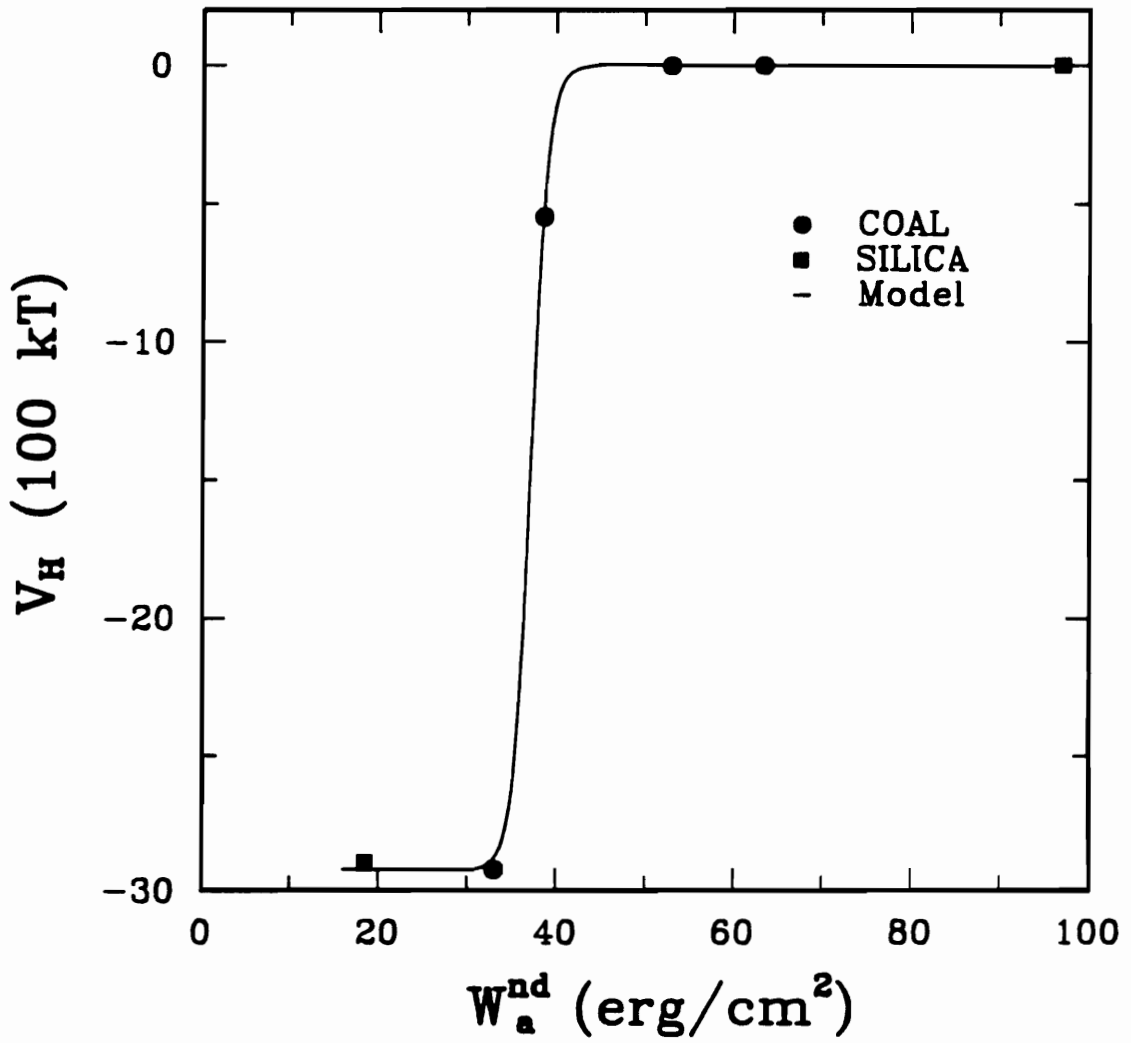


Figure 3.7. Hydrophobic Interaction Energy Plotted as a Function of Nondispersion Component of Work of Adhesion

Solid Line Represents Equation [3.13]

order of the magnitude as the hydrophobic interaction energy estimated using different approaches (44).

When $W_a^{nd} = c$, V_H becomes $-0.5V_m$. Therefore, c represents a transition point. Recently, Ström et al. (45) suggested that the hydrophobic/hydrophilic transition occurs when the hydrophilic number, which is defined as a ratio of W_a^{nd} to W_c^{nd} , the latter being the nondispersion component of work of cohesion of water (103.6 erg/cm^2), is 0.5. By substituting c for W_a^{nd} , one can obtain a hydrophilic number of 0.37 at the transition point. Since this value is less than 0.5, c may represent a transition between strongly hydrophobic and hydrophobic solids (2). It may also be noted that the hydrophobic interaction energy becomes significant when $W_a^{nd} \leq c$.

Beyond the transition point, i.e., $W_a^{nd} > c$, Equation [3.13] becomes:

$$V_H = -V_m \exp[-b(W_a^{nd} - c)], \quad [3.17]$$

which shows that the hydrophobic interaction energy decreases exponentially with increasing W_a^{nd} . The parameter b represents how quickly the hydrophobic interaction energy changes with W_a^{nd} .

Since the hydrophobic interaction energy term has been missing in the classical DLVO theory for describing the coagulation behavior of strongly hydrophobic solids, Equation [3.13] may now be incorporated into Equation [3.10] to obtain:

$$V_T = V_R + V_A + V_H. \quad [3.18]$$

It is not certain at this point, however, how universally the third term can be applied. It is likely that at least two of the three parameters, i.e., V_m and c , may be common to all the materials. It should be noted, nevertheless, that the results obtained with methylated silica samples fall on the same curve as that shown in Figure 3.7. Fur-

ther work is needed to determine the properties of the three parameters of Equation [3.17].

As an example of applying the role of hydrophobic interaction in coagulation to a practical problem, the fine coal cleaning using selective coagulation technique has been studied (46). It seems impossible to separate fine coal from mineral matter by selective coagulation because the magnitude of interaction potential energy barrier, calculated based on the DLVO theory, is of the same order of the magnitude for coal and mineral matter particles. This is chiefly due to the compensation of higher Hamaker constant of mineral matter with high polarizability for its relative high electrokinetic potential in a wide range of pH . The calculation based on the hydrophobic interaction model and the DLVO theory as well shows, however, that due to the presence of hydrophobic interaction between strongly hydrophobic coal particles, which is one or two orders of magnitude of dispersion interaction energy, the selective hydrophobic coagulation of fine coal can be achieved at pH value of 9 at which mineral matters are in a highly dispersed state. Since the hydrophobic interaction is not significant between a very hydrophobic and a hydrophilic particles as found experimentally by Claesson et al. (18) and theoretically by Il'in et al. (23), the heterocoagulation is unlikely to occur between very hydrophobic coal particles and hydrophilic mineral matter particles at such a high value of pH due to strong electrostatic repulsion between them. The batch test results of selective hydrophobic coal coagulation show the practical potential of the proposed hydrophobic interaction energy concept in mineral processing and separation science (46).

In this chapter, the role of hydrophobic interaction energy in coagulation of strongly hydrophobic colloidal particles has been demonstrated. The satisfactory explanation of selective coagulation of fine coal has been obtained on the basis of the extended DLVO theory in which hydrophobic interaction energy has been included.

However, the complete picture on the role of hydrophobic interaction in coagulation requires a quantitative description of this interaction as a function of separation distance between interacting particles. This subject will be studied in the next chapter.

3.5 Summary and Conclusions

A series of coagulation experiments has been carried out for coal samples oxidized at different temperatures and for natural and methylated silica samples. From the critical coagulation ζ -potential and the Hamaker constants determined in the present work, the maximum potential energy barrier for coagulation has been calculated using the classical DLVO theory. It has been found that for strongly hydrophobic solids, the energy barrier calculated as such is too large to explain the experimental observations. An assumption has, therefore, been made that this energy barrier must be overcome by a hydrophobic interaction energy which has not been accounted for in the classical DLVO theory.

An expression for the hydrophobic interaction energy has been derived as a function of the nondispersion component of work of adhesion, which can readily be determined from the water contact angle measurements. The expression requires three parameters to fit the data obtained with coal and methylated silica samples. The physical meaning of the three parameters has been discussed.

3.6 References

1. Claesson, P.M., "Experimental Evidence for Repulsive and Attractive Forces Not Accounted for by Conventional DLVO Theory," *Progr. Colloid Polym. Sci.*, 74, 48 (1987).
2. Churaev, N.V. and Derjaguin, B.V., "Inclusion of Structural Forces in the Theory of Stability of Colloids and Films," *J. Colloid Interface Sci.*, 103, 542 (1985).

3. Claesson, P.M. and Golander, C.G., "Direct Measurement of Steric Interactions between Mica Surfaces Covered with Electrostatically Bound Low-Molecular-Weight Polyethylene Oxide," *J. Colloid Interface Sci.*, 117, 366 (1987).
4. Tadros, Th.F., "Polymer Adsorption and Dispersion Stability," in *The Effect of Polymers on Dispersion Properties* ed. by Th.F. Tadros, Academic Press, Inc., New York, 1 (1982).
5. Mates, T.E. and Ring, T.A., "Steric Stability of Alkoxy-Precipitated TiO_2 in Alcohol Solutions," *Colloids Surfaces*, 24, 299 (1987).
6. Horn, R.G. and Israelachvili, J.N., "Direct Measurement of Forces due to Solvent Structure," *Chem. Phys. Lett.* 71, 192 (1980).
7. Israelachvili, J.N., "Measurement of Forces between Surfaces Immersed in Electrolyte Solutions," *Faraday Disc. Chem. Soc.*, 65, 20 (1978).
8. Israelachvili, J.N., "Forces between Surfaces in Liquids," *Adv. Colloid Interface Sci.*, 16, 31 (1982).
9. Pashley, R.H., "Hydration Forces between Mica Surfaces in Aqueous Electrolyte Solutions," *J. Colloid Interface Sci.*, 80, 153 (1981).
10. Pashley, R.M., "Hydration Forces between Mica Surfaces in Electrolyte Solutions," *Adv. Colloid Interface Sci.*, 18, 57 (1982).
11. Pashley, R.M., McGuiggan, P.M. and Ninham, B.W., "Attractive Forces between Uncharged Hydrophobic Surfaces: Direct Measurements in Aqueous Solution," *Science*, 229, 1088 (1985).
12. Israelachvili, J.N. and Pashley, R.M., "Measurement of the Hydrophobic Interaction between Two Hydrophobic Surfaces in Aqueous Electrolyte Solutions," *J. Colloid Interface Sci.*, 98, 500 (1984).
13. Claesson, P.M., Blom, C.E., Herder, P.C. and Ninham, B.W., "Interactions between Water-Stable Hydrophobic Langmuir-Blodgett Monolayers on Mica," *J. Colloid Interface Sci.*, 114, 234 (1986).
14. Israelachvili, J. and Pashley, R., "The Hydrophobic Interaction is Long Rang, Decaying Exponentially with Distance," *Nature*, 300, 341 (1982).
15. Rabinovich, Ya.I. and Deryagin, B.V., "Direct Measurement of Forces of Attraction of Hydrophobized Quartz Fibers in Aqueous KCl Solutions," *Kolloidn. Zh.*, 49, 682 (1987).
16. Deryagin, B.V., Rabinovich, Ya.I. and Churaev, N.V., "Direct Measurement of Molecular Forces," *Nature*, 272, 313 (1978).
17. Pashley, R.M., McGuiggan, P.M., Horn, R.G., and Ninham, B.W., "Forces between Bilayers of Cetyltrimethylammonium Bromide in Micellar Solutions," *J. Colloid Interface Sci.*, 126, 569 (1988).

18. Claesson, P.M., Herder, P.C., Bolm, C.E., and Ninham, B.W., "Interactions between a Positively Charged Hydrophobic Surface and a Negatively Charged Bare Mica Surface," *J. Colloid Interface Sci.*, 118, 68 (1987)
19. Christenson, H.K., Claesson, P.M., Berg, J., and Herder, P.C., "Forces between Fluorocarbon Surfactant Monolayers: Salt Effects on the Hydrophobic Interactions," *J. Phys. Chem.*, 93, 1472 (1989).
20. Israelachvili, J.N., "Measurements of Hydrophobic Forces between Macroscopic Surfaces," *Chemica Scripta*, 25, 7 (1985).
21. Rabinovich, Ya.I. and Derjaguin, B.V., "Interaction of Hydrophobized Filaments in Aqueous Electrolyte Solutions," *Colloids Surfaces*, 30, 243 (1988).
22. Christenson, H.K., Claesson, P.M., and Herder, P.C., "Forces between Fluorocarbon Surfactant Monolayers: Salt Effects on the Hydrophobic Interaction," *J. Phys. Chem.*, 93, 1472 (1989).
23. Derjaguin, B.V. and Churaev, N.V., "The Current State of the Theory of Long Range Surface Forces," *Colloids Surfaces*, 41, 223 (1989).
24. Claesson, P.M. and Christenson, H.K., "Very Long Range Attractive Forces between Uncharged Hydrocarbon and Fluorocarbon Surfaces in Water," *J. Phys. Chem.*, 92, 1650(1988).
25. Christenson, H.K., Claesson, P.M. and Pashley, R.M., "The Hydrophobic Interaction between Macroscopic Surfaces," *Proc. Indian. Acad. Sci. (Chem. Sci.)*, 98, 379 (1987).
26. Laskowski, J. and Kitchener, J.A., "The Hydrophilic- Hydrophobic Transition on Silica," *J. Colloid Interface Sci.*, 29, 670 (1969).
27. Blake, P. and Ralston, J., "Controlled Methylation of Quartz Particles," *Colloids Surfaces*, 15, 108, (1985).
28. Dann, J.R., "Forces Involved in the Adhesive Process: I. Critical Surface Tension of Polymeric Solids as Determined with Polar Liquids," *J. Colloid Interface Sci.*, 32, 302 (1970).
29. Allen, L.H. and Matijevic, E., "Stability of Colloidal Silica I. Effect of Simple Electrolytes," *J. Colloid Interface Sci.*, 31, 287 (1969).
30. Depasse, J. and Watillon, A., "Stability of Amorphous Colloidal Silica," *J. Colloid Interface Sci.*, 33, 430 (1970).
31. Harding, R.D., "Stability of Silica Dispersions," *J. Colloid Interface Sci.*, 35, 172 (1971).
32. Armistead, C.G. and Hockey, J.A., "Reactions of Chloromethyl Silanes with Hydrated Aerosil Silicas," *Trans. Faraday Soc.*, 63, 2549 (1967).

33. Fowkes, F.M., "Attractive Forces at Interfaces," *Ind. Eng. Chem.*, 56, 40 (1964).
34. Laskowski, J., "The Relationship between Floatability and Hydrophobicity," in *Advances in Mineral Processing*, ed. by Somasundaran, P., AIME, Inc., New York, 189 (1986).
35. Janczuk, B. and Bialopiotrowicz, T., "Adhesion of an Air Bubble to Quartz Surface in Aqueous Solution of Aliphatic Amine Hydrochloride," *J. Adhesion*, 25, 255 (1988).
36. Derjaguin, B.V., "Friction and Adhesion IV. The Theory of Adhesion of Small Particles," *Kolloid Z.*, 69, 155 (1934).
37. Hogg, R., Healy, T.W., and Fuerstenau, D.W., "Mutual Coagulation of Colloidal Dispersions," *Trans. Faraday Soc.*, 62, 1638 (1966).
38. Hamaker, H.C., "The London-van der Waals Attraction between Spherical Particles," *Physica*, 4, 328 (1937).
39. Bargeman, D. and Vader, F. Van Voorst, "van der Waals Forces between Immersed Particles," *J. Electroanal. Chem.*, 37, 45 (1972).
40. Fowkes, F.M. and Pugh, R.J., "Steric and Electrostatic Contributions to the Colloidal Properties of Non-Aqueous Dispersions," in *Polymer Adsorption and Dispersion Stability*, ed. by Goddard, E.D. and Vincent, B., 331 (1984).
41. Usui, S. and Hachisu, S., "Interaction of Electrical Double Layers and Colloid Stability," in *Surfactant Sci. Ser. (Electrical Phenomena at Interfaces)*, 15, 47 (1984).
42. Vold, R.D. and Vold, M.J., *Colloid and Interface Chemistry*, Addison-Wesley Publishing Company, Inc., 269 (1983).
43. Pugh, R.J., "Selective Coagulation in Quartz-Hematite and Quartz-Rutile Suspensions," *Colloid Polym. Sci.*, 252, 400 (1974).
44. Warren, L.J., "Shear Flocculation," *Chem. Tech.*, 181 (1981).
45. Ström, G., Fredriksson, M., and Klason, T., "Interfacial Tension and Surface Hydrophilicity in Systems of Solid Polymers in Contact with Aqueous Solutions," *J. Colloid Interface Sci.*, 123, 324 (1988).
46. Honaker, R.Q., *Development of the Selective Shear Coagulation Process for Ultrafine Coal Cleaning*, M.S. Thesis, Department of Mining and Minerals Engineering, Virginia Polytechnic Institute and State University, (1988).

CHAPTER 4 A THEORY OF HYDROPHOBIC INTERACTION

4.1 Introduction

It is widely recognized that the stability of very hydrophobic colloidal suspensions can not be adequately described by the classical DLVO theory. Many investigators have provided both theoretical and experimental evidence for the existence of force(s) other than the dispersion and electrostatic forces considered in the DLVO theory (1-11). However, the origin of this so called non-DLVO force remains controversial. Many investigators (7, 12-17) consider it entropic in origin, arising mainly from the configurational rearrangement of water molecules in the vicinity of hydrophobic surfaces, while others believe that it is due to phase changes in the interlayer between two surfaces in close proximity (1, 10, 18) or to anomalous polarization of water molecules near hydrophobic surfaces (4-5, 19-21). Churaev and Derjaguin (2) referred to it as a structural force and suggested that it can be repulsive between two interacting hydrophilic surfaces and attractive for strongly hydrophobic surfaces. They also noted that the classical DLVO theory was developed specifically for those "hydrophobic colloids" that do not exhibit any structural force.

In Chapter 3, evidence for the existence of non-DLVO forces operating in the coagulation of hydrophobic coal and methylated silica samples was presented. A

method of estimating the magnitude of the hydrophobic interaction energy from simple coagulation experiments was proposed. An expression was then formulated to relate the hydrophobic interaction energy to the nondispersion component of work of adhesion (W_a^{nd}) of water on the solids, which has been shown by Kitchener (22) and Laskowski (23) to be more important than the dispersion component (W_a^d) in determining the hydrophobicity of a solid.

In this chapter, further evidence for the existence of attractive non-DLVO forces is presented based on coagulation studies conducted on silica samples methylated to different extents. Also, the expression for the hydrophobic interaction energy has been modified to show the exponential decay of the interaction energy with increasing separation distance. The possible mechanisms of hydrophobic interaction are discussed in detail.

4.2 Experimental

The nature of the silica sample and the methylation procedure used in this chapter are the same as described in Chapter 3. The sample is methylated as a means of controlling the hydrophobicity, using trimethylchlorosilane (TMCS) solutions of different concentrations as prepared in cyclohexane. The methylated silica samples were subjected to coagulation experiments, in which 5 gram samples were mixed in a specially designed container, as shown in Appendix I, with 500 ml KCl solutions (10^{-3} M) for 5 minutes at 500 rpm. The suspension was then allowed to settle for 1 minute before 300 ml of the supernatant was siphoned off. The weight of the silica sample in the supernatant was measured to determine the coagulation efficiency (E_c) as defined in Equation [3.1]. The ζ -potentials of the methylated silica samples were determined using a Pen-Kem Lazer Zee Meter (Model 501) at 0.004% solids and 10^{-3} M KCl solution.

The Hamaker constants were determined using the methylene iodide contact angle technique (24). Further details of these experimental procedures and the calculation methods were given in Chapter 3.

The values of W_a^{nd} were determined on silica plates methylated in TMCS solutions of different concentrations using the water-in-octane contact angle technique similar to that described by David and Misra (25). This technique is based on the following relationship:

$$W_a^{nd} = \gamma_w - \gamma_o + \gamma_{wo} \cos \theta_{wo} , \quad [4.1]$$

in which γ_w and γ_o ($= 21.8 \text{ erg/cm}^2$) are the surface tensions of water and octane, respectively, and γ_{wo} ($= 49.8 \text{ erg/cm}^2$) is the interfacial tension between water and octane. The contact angle (θ_{wo}) in Equation [4.1] refers to that of the water droplet on the solid surface immersed in octane. Equation [4.1] can be readily derived by combining the following relationships:

$$W_a = W_a^d + W_a^{nd} \quad [4.2]$$

$$W_a = \gamma_s + \gamma_w - \gamma_{sw} \quad [4.3]$$

$$\gamma_{sw} = \gamma_{so} - \gamma_{wo} \cos \theta_{wo} \quad [4.4]$$

$$\gamma_{so} = \gamma_s + \gamma_o - 2\sqrt{\gamma_s^d \gamma_o^d} \quad [4.5]$$

$$\text{and } \gamma_{wo} = \gamma_w + \gamma_o - 2\sqrt{\gamma_w^d \gamma_o^d} , \quad [4.6]$$

where W_a is the work of adhesion of water on solid and W_a^d , its dispersion component, γ_s is the solid surface tension and γ_s^d , its dispersion component, and γ_{sw} and γ_{so} are the interfacial tensions of solid/water and solid/octane interfaces, respectively. Equation [4.2] shows the decomposibility of work of adhesion into dispersion and nondispersion

components, while Equation [4.3] is simply a definition of work of adhesion and Equation [4.4] represents the application of Young's equation to the present system of contact angle measurement. Fowkes' equation applied to the solid/octane and water/octane interfaces yields Equations [4.5] and [4.6], respectively. During the course of derivation of Equation [4.1], the terms of W_a^d corresponding to water/solid and octane/solid interfaces has been canceled with each other because γ_w^d equals $\gamma_o^d (= \gamma_o)$.

In the contact angle measurements, a water droplet was released on the silica plate through a microliter syringe after the plate had been immersed in octane for 15 minutes. The contact angle was then measured through the water phase using a goniometer after the droplet had rested on the surface for 10 minutes. At least 20 readings were taken from 10 different droplets formed on 4 different silica plates and averaged. The technique was checked using a fused silica plate methylated in TMCS solution of 20% (by volume) concentration. W_a^{nd} value of 16.9 erg/cm^2 obtained using this method is in good agreement with that of 18.4 erg/cm^2 obtained using the method as described in Chapter 3.

4.3 Results and Discussion

4.3.1 Theoretical Analysis

It has been shown in Chapter 3 that the total potential energy (V_T) between two particles interacting in a medium consists of three components, which include electrostatic interaction energy (V_R), dispersion interaction energy (V_A) and hydrophobic interaction energy (V_H) as given by Equation [3.18]. The first two terms on the right hand side of Equation [3.18] may be explicitly represented by Derjaguin's solution (26) and Hamaker equation (27) for spherical particles as given by Equations [3.9] and [3.10], re-

spectively. In order to show the separation distance dependence of hydrophobic interaction energy, the third term on the right hand side of Equation [3.18] may be replaced by the expression derived from mean-field gradient approach in the form of a large particle-particle separation approximation, which is identical to that obtained experimentally by Israelachvili and Pashley (6). Thus Equation [3.18] may be rewritten as:

$$V_T = \frac{\epsilon a \psi_d^2}{2} \ln[1 + \exp(-\kappa H)] - \frac{aA_{131}}{12H} - \frac{CaD_0}{2} \exp\left(-\frac{H}{D_0}\right), \quad [4.7]$$

in which C is the hydrophobic interaction parameter and D_0 is the decay length, with the other symbols being the same as that given in Equations [3.9] and [3.10]. It should be noted that in Equation [4.7], V_H is described by a single exponential term, but some of the recent investigations (3-5, 10, 12) have shown that two independent exponential terms are needed to fit the experimental results obtained from direct force measurements. However, for the purpose of describing coagulation experiments which are controlled by long range forces, one exponential term with a long decay length may be sufficient.

If all the parameters are known, Equation [4.7] can be used to calculate the potential energy barrier (V_{\max}) against coagulation and the distance (H_m) at which V_{\max} locates. H_m is also the distance where the intervening film (or disjoining film) between the two particles begins to rupture spontaneously. Until this critical film thickness is reached, the film thinning process must rely on the kinetic energy (V_k) of the system.

Thus, under dynamic conditions, the coagulation will occur when V_k of the interacting particles at the moment of collision equals or exceeds V_{\max} but is less than the adhesion energy (V_c) holding the particles together. This coagulation condition can be described mathematically by Equation [4.8]:

$$V_{\max} \leq V_k \leq V_B. \quad [4.8]$$

Substituting Equation [4.7] at $H = H_m$ into Equation [4.8] for the boundary condition of coagulation, one obtains:

$$\frac{\varepsilon a \psi_d^2}{2} \ln[1 + \exp(-\kappa H_m)] - \frac{aA}{12H_m} - \frac{CaD_0}{2} \exp\left(-\frac{H_m}{D_0}\right) - V_k = 0 \quad [4.9]$$

The kinetic energy (V_k) in Equation [4.9] is determined by the hydrodynamics of the system. For the conditions employed in the coagulation experiments, the kinetic energy of mixing can be estimated using the following equation:

$$V_k = \frac{1}{2} \mu U_r^2 \quad [4.10]$$

in which $\mu (= m_1 m_2 / (m_1 + m_2))$ is the reduced mass of interacting particles of masses m_1 and m_2 , and U_r is their relative velocity at the moment of collision which can be calculated using the method described by Delichatsios and Probst (28) and Nataga (29), as given in Appendix I. The value of V_k calculated as such for the coagulation system of silica suspensions is approximately 3 kT, which is comparable to the thermal agitation energy. Therefore, the conditions employed in the present work may be considered perikinetic and, hence, the value of V_k may be taken to be 15 kT (30-33).

At the separation distance H_m where V_{max} occurs, the following condition must be satisfied:

$$\left. \frac{dV_T}{dH} \right|_{H=H_m} = 0 \quad [4.11]$$

Substituting Equation [4.7] into Equation [4.11] and replacing H with H_m yield:

$$-\frac{\varepsilon a \psi_d^2}{2} \frac{\exp(-\kappa H_m)}{1 + \exp(-\kappa H_m)} + \frac{aA}{12H_m^2} + \frac{Ca}{2} \exp\left(-\frac{H_m}{D_0}\right) = 0 \quad [4.12]$$

Using the methods described in Chapter 3, most of the parameters except for C , D_0 and H_m , of Equations [4.9] and [4.12] can be determined experimentally. If only one of the three parameters is known, the other two unknowns can be determined by solving Equations [4.9] and [4.12] simultaneously.

Rabinovich and Derjaguin (4-5) reported that two methylated quartz fibers immersed in a 10^{-4} M KCl solution jumped into a contact position when the separation distance (H) between them reached 20 nm. Therefore, this value may be taken as H_m for the system investigated by these investigators. They reported the values of receding and advancing contact angles of water on the methylated quartz fiber to be 80° and 100° , respectively. These values are almost the same as those measured in the present work as given in Chapter 3. For the silica plate methylated in 20% (by volume) TMCS solution, the equilibrium contact angle was measured at 25°C to be 92.9° on the average. Therefore, the powdered silica sample treated in the same solution and used for coagulation experiments in the present work may be considered to have a similar surface characteristic and, hence, its H_m may be assumed to be the same (20 nm) as measured by Rabinovich and Derjaguin using the methylated quartz fibers.

Equations [4.9] and [4.12] can now be solved simultaneously to find that the values of parameter C and D_0 are -1.896 erg/cm^2 and 10.3 nm, respectively. For this calculation, the value of ψ_d has been considered to be the same as the critical ζ -potential ($\zeta_c = -51 \text{ mV}$) for coagulation and the value of A_{131} has been determined to be $0.1 \times 10^{-20} \text{ J}$ using the methylene iodide contact angle method as described in Chapter 3.

The value of the decay length (D_0) determined in the present work is close to that of 12.2 nm as obtained by Rabinovich and Derjaguin from the direct force measurement on hydrophobized quartz fibers (4-5). Also, the value of the hydrophobic interaction

parameter (C) is comparable to that of -2.51 mJ/m^2 as obtained in the same manner (4-5).

As has been noted, the value of H_m has been assumed to be 20 nm on the basis of the similar contact angle values reported by Rabinovich and Derjaguin and those obtained in the present work. It should be noted, however, that the electrolyte concentration used in the present work was different from that used in Rabinovich and Derjaguin's measurements and, hence, the value of H_m for the system studied in the present work may not be exactly 20 nm. For this reason, a series of calculations have been made using different values of D_0 in Equations [4.9] and [4.12]. The results, given in Figure 4.1, show that a larger change in H_m results in relatively small changes in both D_0 and C values when H_m is in the range of 8 to 35 nm. Therefore, an error in assuming the value of H_m may not significantly affect the outcome of the calculations of C and D_0 values. Since all the parameters of Equation [4.7] are now known for the silica sample treated in 20% TMCS solution, one can calculate each component, i.e., V_R , V_A and V_H of the total interaction energy (V_T). Figure 4.2 shows the results of the calculations made as a function of separation distance (H) at the critical pH of coagulation. It shows that for the case of strongly hydrophobic silica suspensions, the attractive dispersion interaction (V_A) plays a minor role in determining its stability. It is the repulsive electrostatic interaction (V_R) and the attractive hydrophobic interaction (V_H) energies that dominate the stability.

4.3.2 Derivation of an Expression for V_H

In order to derive a common expression of V_H for solids having different degrees of hydrophobicity, a series of coagulation tests and ζ -potential measurements have been conducted using powdered silica samples methylated at different TMCS concentrations.

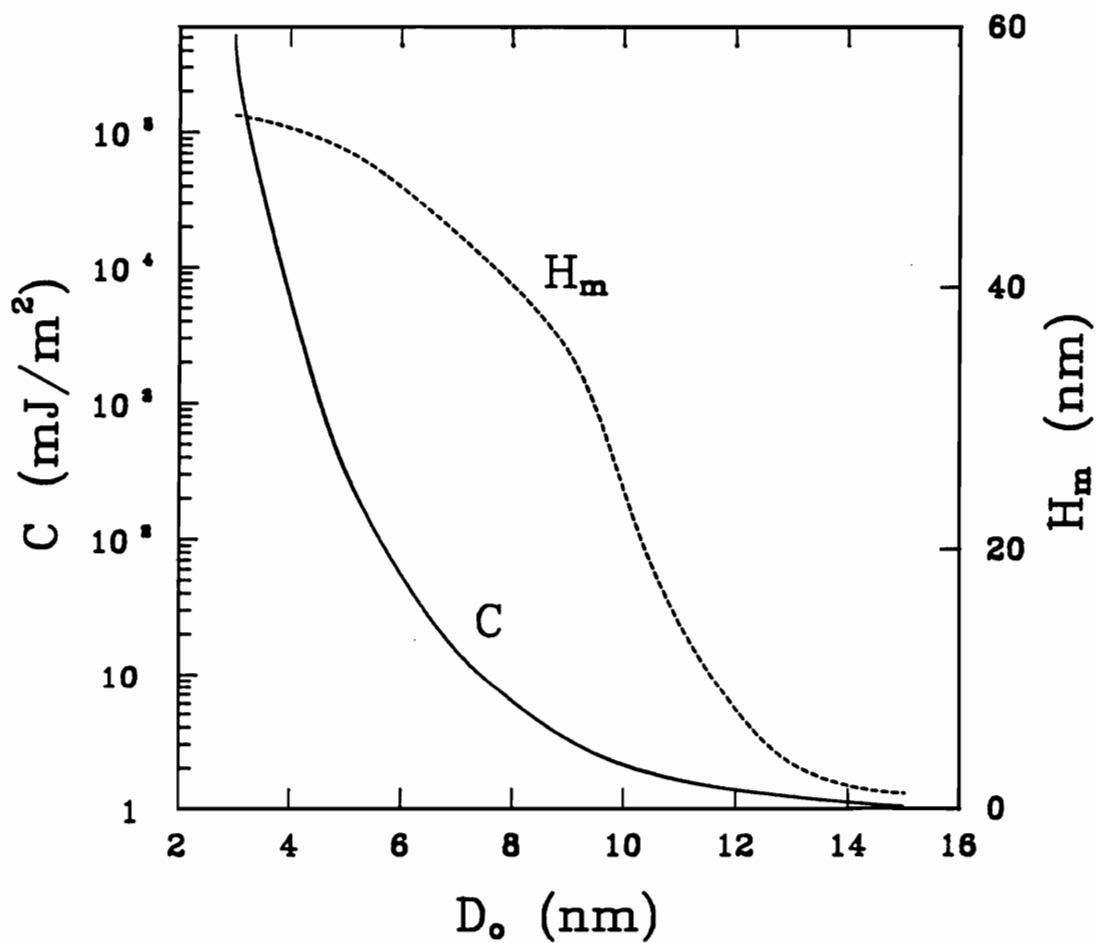


Figure 4.1. Values of C and H_m as a Function of Decay Length (D_0) as Calculated Using Equations [4.9] and [4.12]

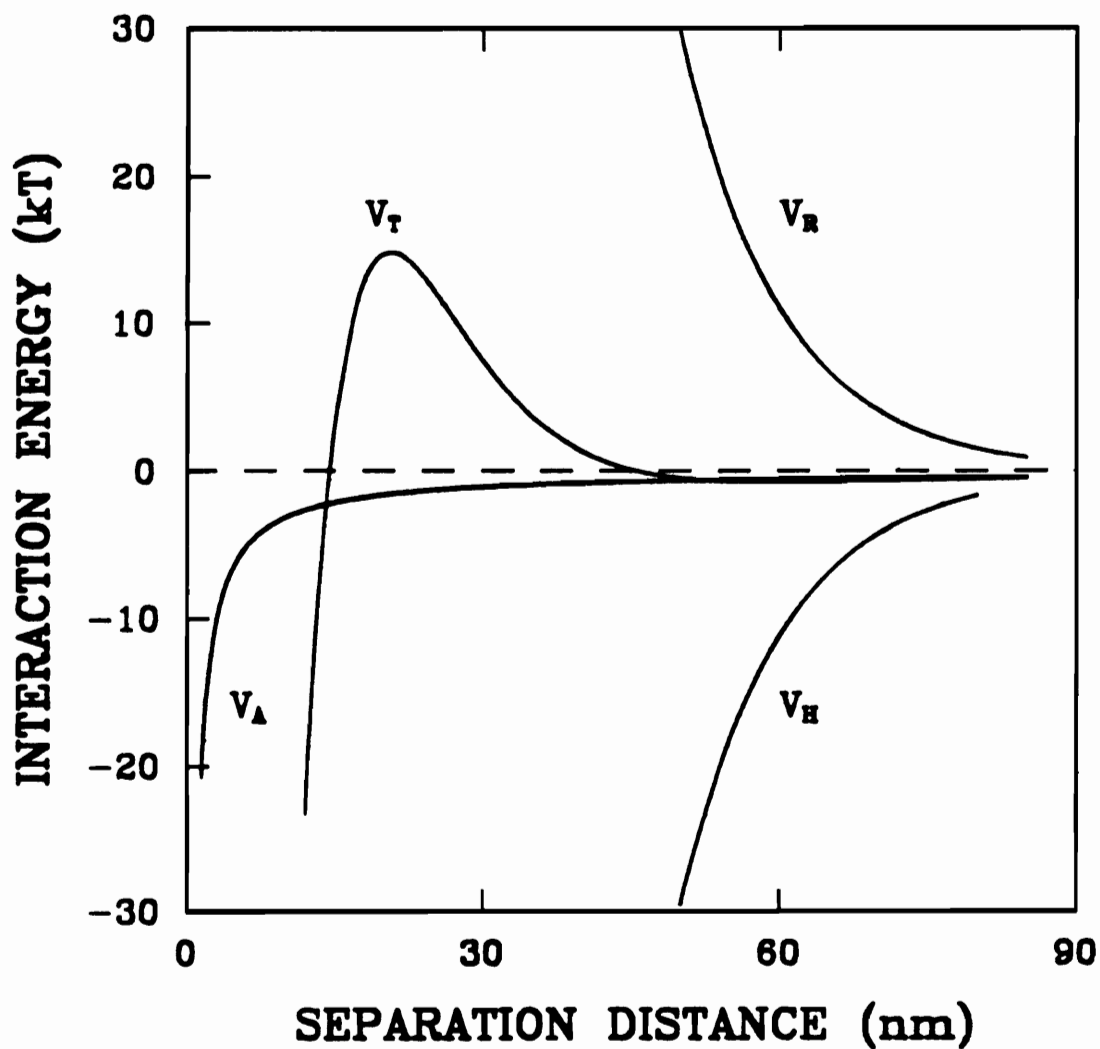


Figure 4.2. Potential Energy Profile as a Function of Separation Distance Calculated for Methylated Silica

$$\begin{array}{lll}
 KCl = 10^{-3} \text{ M}; & \psi_d = -51 \text{ mV}; & pH = 10.7; \\
 A_{131} = 0.1 \times 10^{-20} \text{ J}; & a = 1.6 \text{ } \mu\text{m}; & C = -1.896 \text{ erg/cm}^2; \\
 D_0 = 10.3 \text{ nm}. & &
 \end{array}$$

To obtain the Hamaker Constants, methylene iodide contact angles were measured on silica plates treated with the same TMCS solutions.

Table 4.1. Values of H_m and C as Calculated Using Equations [4.11] and [4.13]

Parameters	% TMCS by Volume				
	0.05	0.10	1.00	10.00	20.00
pH_c	---	5.1	9.2	10.3	10.7
ζ_c (mV)	---	-30.0	-50.0	-50.0	-51.0
θ_{m_i} (degrees)	44.1	46.1	53.7	60.2	60.0
$A_{11} \times 10^{20}$ (J)	5.66	5.49	4.86	4.29	4.31
$A_{131} \times 10^{21}$ (J)	4.01	3.53	1.99	0.93	0.96
H_m (nm)	---	15.8	20.2	20.4	20.6
C (erg/cm ²)	---	-0.612	-1.812	-1.818	-1.895

Figure 4.3 shows the results of coagulation tests and ζ -potential measurements. The silica samples methylated at a TMCS concentration of less than 0.05% by volume do not show any coagulation even at its *i.e.p.*, where the electrostatic repulsive energy is minimum. This finding is similar to what has been observed with unmethylated silica samples as shown in Chapter 3, indicating that silica samples methylated at such a low level of TMCS concentrations are still hydrophilic. However, as the silica samples are methylated at higher TMCS concentrations, coagulation occurs more readily, as shown in Figure 4.3. Note that the pH range where coagulation occurs is extended to a higher

pH with increasing TMCS concentration. Since the ζ -potential value of methylated silica increases with increasing pH , this finding suggests that the electrostatic repulsive energy can be more readily overcome with an increasing degree of methylation and, hence, hydrophobicity.

Table 4.1 summarizes the results of the coagulation tests plotted in Figure 4.3, including the results obtained using the samples methylated at 20% TMCS solution as given in Chapter 3. It is shown that the critical pH of coagulation (pH_c) and the magnitude of corresponding ζ -potential (ζ_c) for coagulation increase with increasing TMCS concentration. The method for obtaining such information from the data shown in Figure 4.3 has been described in Chapter 3. Also shown in Table 4.1 are the methylene iodide contact angles, which can be used to determine the Hamaker constants (A_{11}) and then to estimate the combined Hamaker constant (A_{131}) using Equations [3.12] and [3.11], respectively. The ζ_c and A_{131} values, obtained as such, can be used to calculate the values of V_R and V_A , respectively.

Although it is possible that the decay lengths (D_0) for the silica samples used in the present work may change with varying degrees of methylation, an assumption is made that they remain constant and that their value is 10.3 nm. According to the mean-field gradient theory as discussed in Chapter 2, the decay length is determined solely by the solution conditions. Since the suspension conditions were kept the same in the present studies, this assumption appears to be reasonable. Under this assumption, one can then calculate H_m and C values by simultaneously solving Equations [4.10] and [4.13]. The results are shown in Table 4.1. It can be seen that the calculated values of H_m increase with increasing degrees of methylation. What this means is that the thickness of the metastable water film increases with increasing degree of hydrophobicity and, therefore, that the critical distance (H_m) at which the disjoining film between two approaching particles ruptures, also increases. Jordan (34) used an interference technique

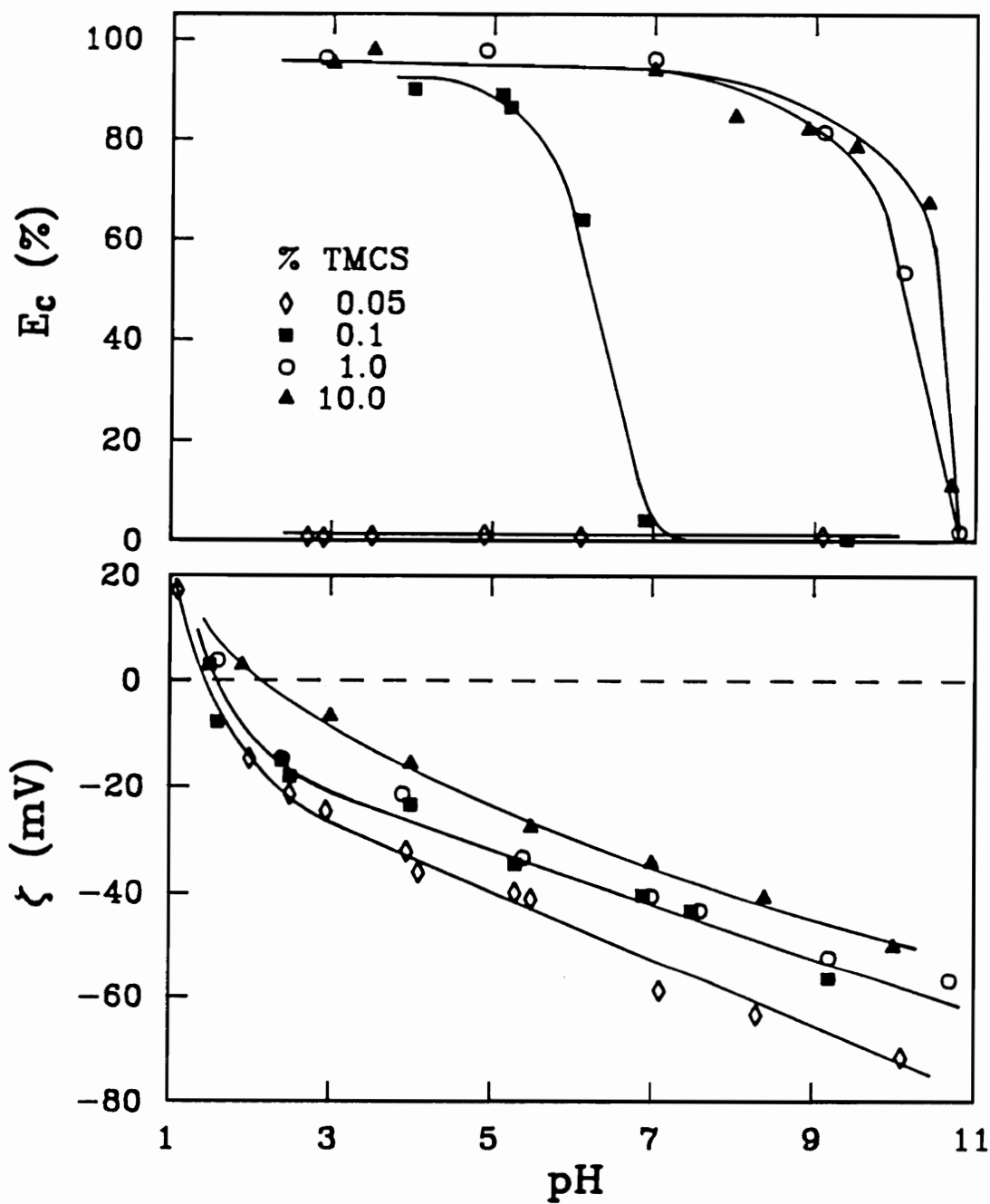


Figure 4.3. Results of Coagulation and ζ -potential Measurements on Silica Samples Methylated at Various TMCS Concentrations

All the data are obtained in 10^{-3} M KCl solutions

to determine the thickness of the metastable water film between an air bubble and the methylated quartz plate and found that it increases with increasing hydrophobicity of the solid.

It can also be seen that the value of C increases rapidly in magnitude with increasing TMCS concentration and stays above 1.8 erg/cm^2 when the concentration is higher than 1%. When the TMCS concentration is below 0.05%, the value of C approaches zero and the hydrophobic interaction energy (V_H) becomes negligible.

Table 4.2. Values of W_a^{nd} of Water on Methylated Silica as Calculated Using Equation [4.1]

Parameters	% TMCS by Volume				
	0.05	0.10	1.00	10.00	20.00
θ_{wo} (degrees)	65.1	107.53	114.9	123.0	131.0
W_a^{nd} (erg/cm^2)	72.5	36.5	30.5	24.4	18.8

Table 4.2 shows the results of the water-in-octane contact angle (θ_{wo}) measurements made on methylated silica plates and the W_a^{nd} values calculated using Equation [4.1]. It can be seen that the W_a^{nd} value decreases substantially with increasing TMCS concentration. Since it has been shown in Chapter 3 that hydrophobic interaction energy can be expressed as a function of W_a^{nd} , the C values given in Table 4.1 are plotted as a function of W_a^{nd} in Figure 4.4. Also shown in this figure are the data obtained for the coal samples oxidized at different temperatures as a means of controlling the surface hydrophobicity. Table 4.3 gives the pertinent data for the coal samples, including ζ_c , A_{131} and W_a^{nd} . The first two data sets have been used to calculate the values of C assuming

that the decay length (D_0) is the same (10.3 nm) as that of the silica samples used in the present work. In solving Equations [4.9] and [4.12] to obtain the values of C for the coal samples of various oxidation degrees, the value of V_k has been taken to be 61 kT, as calculated using Equation [4.10] for the mixing conditions employed in the coagulation experiments as described in Chapter 3.

Table 4.3. Values of C Calculated Using Equations [4.11] and [4.13] and W_a^{nd} of Water on Oxidized Coal Samples

Parameters	Coal Oxidized at Various Temperatures (°C)			
	25	140	170	200
ζ_c (mV)	-43	-22.0	-5.0	-5.0
$A_{131} \times 10^{21}$ (J)	5.24	6.71	8.00	8.72
C (erg/cm ²)	-1.247	-0.260	0.000	0.000
W_a^{nd} (erg/cm ²)	32.9	38.7	54.5	63.9

By applying a non-linear regression curve-fitting procedure to the set of W_a^{nd} and C values given in Tables [4.1], [4.2] and [4.3], one can obtain the following expression:

$$C = \frac{C_m}{1 + \exp(-b \times (W_a^{nd} - K))} \quad \text{mJ/m}^2, \quad [4.13]$$

in which C_m , b and K are the three parameters that have values of -1.89, 0.49 and 34.8, respectively. The solid line in Figure 4.4 represents Equation [4.13]. As shown, there is an excellent fit between experimental data and Equation [4.13]. Thus, this expression

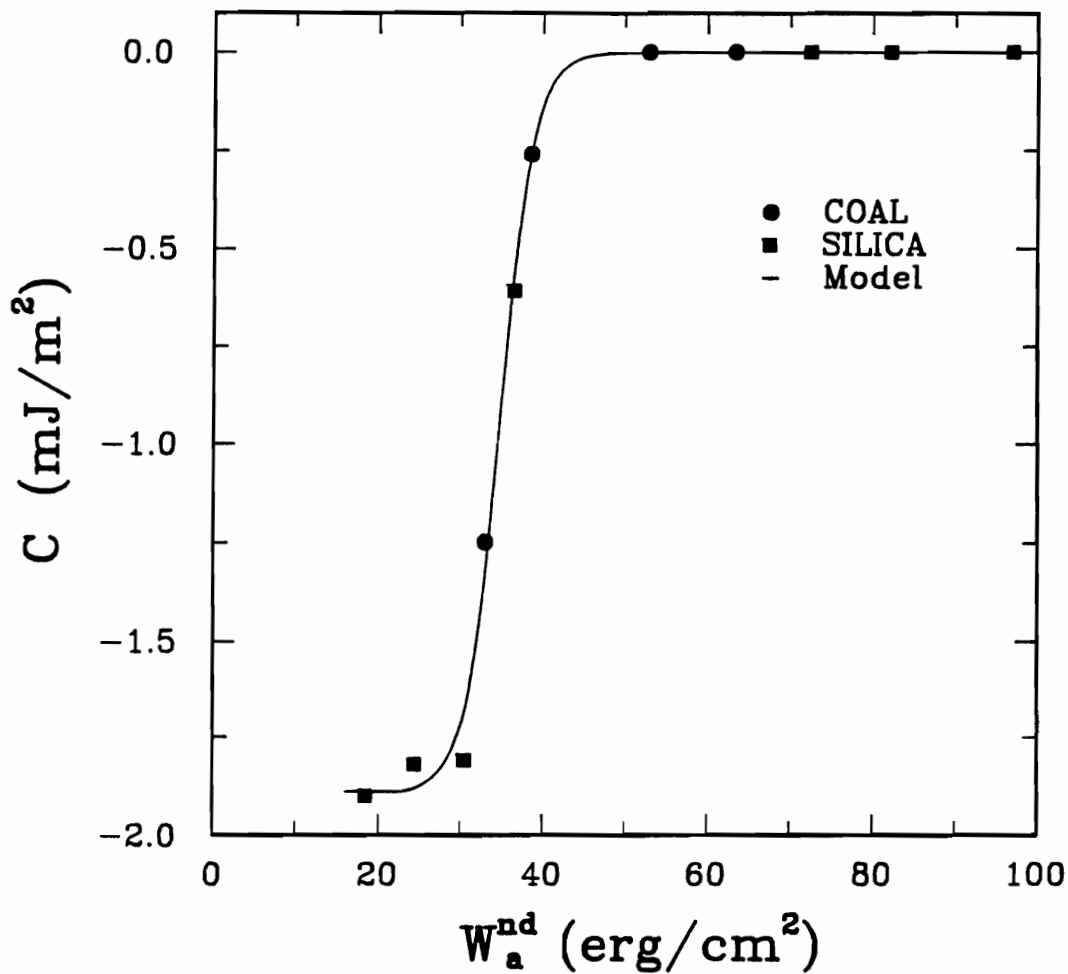


Figure 4.4. Hydrophobic Interaction Parameter (C) versus W_a^{nd} Plot for Methylated Silica and Oxidized Coal Samples

may be used for predicting the values of the hydrophobic interaction parameter (C) from the W_a^{nd} values, which can be readily determined from simple contact angle measurements. An attempt has been made to use the work of adhesion (W_a) instead of W_a^{nd} in Equation [4.13]. The values of the three parameters were found, in this attempt, to be -1.88, 0.32 and 93.91, respectively. Using these values in Equation [4.13], C values were calculated at various W_a values, and the results are given in Figure 4.5 as a solid line. Also given in this figure are the symbols corresponding to the experimental values of C . Figure 4.5 shows clearly that the correlation between the values of C and W_a is not as good as that between the values of C and W_a^{nd} , indicating that W_a^{nd} is a better representation for surface hydrophobicity.

For very hydrophobic solids, W_a^{nd} becomes zero and, then, $C = C_m$. This means that the maximum hydrophobic interaction energy would be -1.89 erg/cm^2 . When $W_a^{nd} = K$, C becomes $0.5C_m$. Thus, the value of $W_a^{nd} = 34.8 \text{ erg/cm}^2$ may be considered as the transition point between strongly hydrophobic and weakly hydrophobic solids. This value will give a hydrophilic number of 0.34, which has been defined by Ström et al. (35) as the ratio of W_a^{nd} to the nondispersion component of the work of cohesion of water ($W_c^{nd} = 103.6 \text{ erg/cm}^2$). These investigators suggested the value of 0.5 as the hydrophobic/hydrophilic transition point. It is, therefore, further evident that the hydrophobic interaction plays an important role only in the coagulation of strongly hydrophobic solids. It is interesting to note that the hydrophilic number of 0.34 obtained in this approach is similar to that of 0.37 as obtained in the previous chapter, indicating the universality of this value for distinguishing strongly hydrophobic solids from weakly hydrophobic ones.

When W_a^{nd} is significantly larger than K , Equation [4.13] becomes:

$$C = C_m \exp[-b(W_a^{nd} - K)] , \quad [4.14]$$

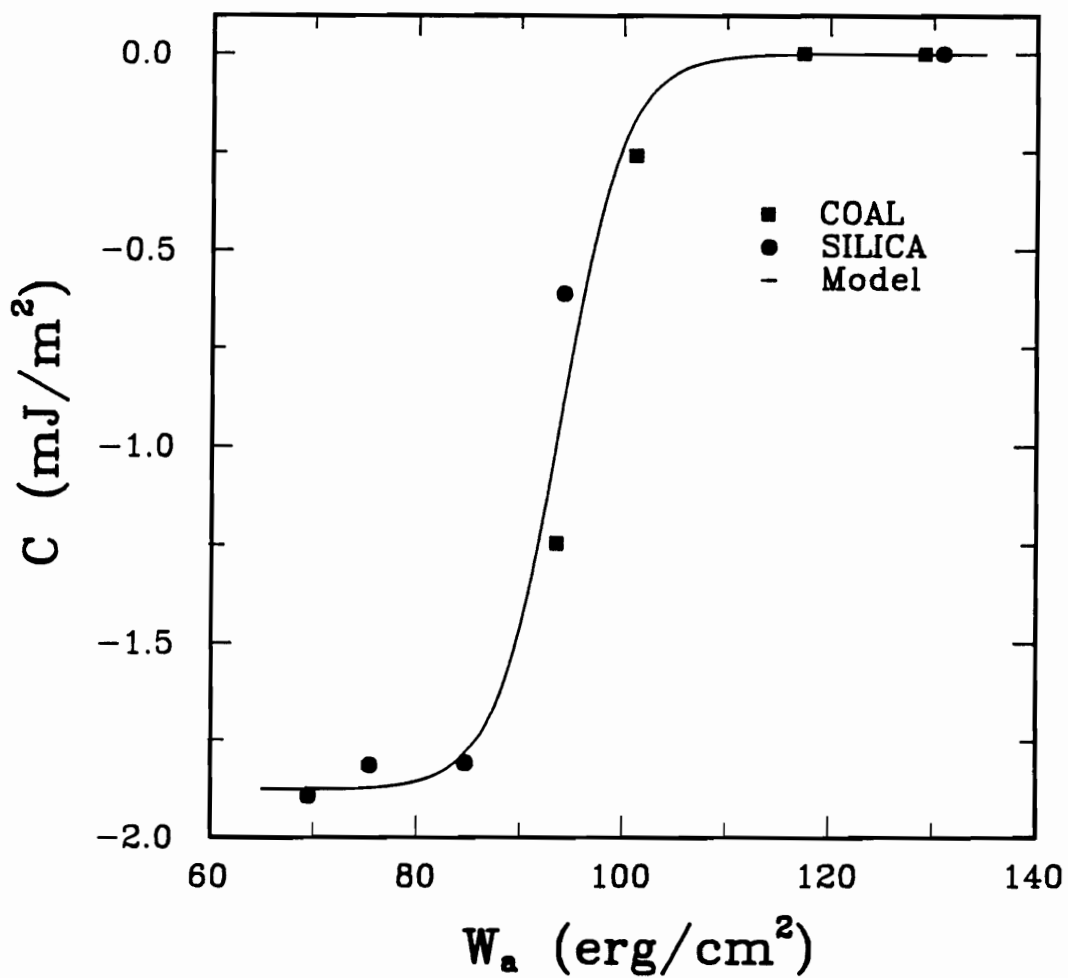


Figure 4.5. Hydrophobic Interaction Parameter (C) versus W_a Plot for Methylated Silica and Oxidized Coal Samples

which shows that C value increases exponentially with increasing W_a^{nd} for weakly hydrophobic surfaces. The parameter b , therefore, represents a gradient at which C increases with increasing W_a^{nd} .

Substituting Equation [4.13] into the general expression for hydrophobic interaction energy, i.e., the last term on the right hand side of Equation [4.7], one obtains:

$$V_H = - \frac{1.95 \times 10^{-17}}{1 + \exp[0.49(W_a^{nd} - 34.8)]} \frac{a}{2} \exp\left(-\frac{H}{10.3}\right), \quad [4.15]$$

in which a is in μm , H_m is in nm and V_H is in J. By incorporating Equation [4.15] into the classical DLVO theory, one can predict the stability of hydrophobic suspensions regardless of whether the solid is strongly hydrophobic or weakly hydrophobic.

Equation [4.15] implicitly assumes that V_H (or C) is zero for hydrophilic solids. Churaev and Derjaguin (2) showed, however, that hydrophilic solids exhibit a repulsive hydration force and its magnitude changes from one solid to another, depending on their hydrophilicity. Christenson (1), Claesson (9) and Pashley (36), among others, also showed the presence of a repulsive hydration force through direct force measurements. This repulsive force prevents the coagulation of a hydrophilic colloid even at its *i.e.p.*, where the electrostatic interaction is minimal or zero (37-39). Thus, V_H can be positive (or $C > 0$) for hydrophilic solids. Therefore, Equation [4.15] is applicable only to hydrophobic solids.

One of the most serious assumptions made in the present work is that a decay length of 10.3 nm has been assumed for all the samples used, which may need verification by further research. It is difficult to judge the validity of this assumption from the survey of published decay lengths which vary in the range of 1 to 15 nm. One possible way to experimentally verify it will be to determine the hydrophobic interaction energy

(V_H) as a function of distance for a system with varying degrees of surface hydrophobicity.

4.4 Mechanism of Hydrophobic Interaction

Unlike the electrostatic repulsion and London-van der Waals attraction, which are associated directly with the interparticle interactions, the hydrophobic attraction is mainly due to the interaction between the solids and the liquid medium, or more precisely due to the disliking of the solids for water. In order to have a better understanding of the nature of hydrophobic interaction, it is helpful to calculate the mean excess free energy of water molecules confined in an interlayer region between two strongly hydrophobic solids as a function of the distance separating solid surfaces. The hydrophobic interaction energy expressed as the last term on the right hand side of Equation [4.7] can be taken as the free energy change associated with the removal of water molecules from the interlayer region between two interacting particles to the bulk. Therefore, the expression for calculating the excess free energy, g_t , per water molecule as a function of the distance H separating two interacting particles can be derived as follows.

Based on the definition of g_t , one can obtain that:

$$g_t = \frac{\partial V_H}{\partial N} = \left(\frac{\partial V_H}{\partial H} \right) \left(\frac{\partial H}{\partial N} \right), \quad [4.16]$$

in which V_H is the hydrophobic interaction energy, i.e., the last term of Equation [4.7], and N is the total number of water molecules contained in the interlayer region. Since $(\partial H/\partial N)$ can be expressed as:

$$\left(\frac{\partial H}{\partial N}\right) = \left(\frac{\partial H}{\partial V}\right)\left(\frac{\partial V}{\partial N}\right), \quad [4.17]$$

where V is the volume of water confined between two spheres with a separation distance of H . Geometrically, V can be expressed by:

$$V = [\pi a^2(H + 2a) - \frac{4}{3}\pi a^3] = \pi a^2 H + \frac{2}{3}\pi a^3, \quad [4.18]$$

in which a is the radius of particles in question. Differentiating Equation [4.18] with respect to H yields:

$$\left(\frac{\partial V}{\partial H}\right) = \pi a^2. \quad [4.19]$$

By combining the above Equations [4.19], [4.17] and [4.16], the following equation is, then, obtained:

$$g_t = \left(\frac{\partial V_H}{\partial H}\right)\left(\frac{\partial V}{\partial N}\right)\frac{1}{\pi a^2}. \quad [4.20]$$

On the other hand, the number of water molecules can be related to the total volume through the following relationship:

$$N = \frac{\rho V}{M} N_A, \quad [4.21]$$

in which, ρ and M are the density and the molecular weight of water and N_A is the Avogadro's number. Differentiating Equation [4.21] with respect to V results in:

$$\left(\frac{\partial V}{\partial N}\right) = \frac{M}{\rho N_A}. \quad [4.22]$$

By replacing $(\partial V/\partial N)$ in Equation [4.20] with Equation [4.22], one obtains:

$$g_t = \frac{M}{\pi\rho N_A a^2} \left(\frac{\partial V_H}{\partial H} \right) . \quad [4.23]$$

Since V_H in Equation [4.23] can be written explicitly as (6):

$$V_H = - \frac{aCD_0}{2} \exp\left(-\frac{H}{D_0}\right) , \quad [4.24]$$

by differentiating Equation [4.24] with respect to H , it is readily obtained that:

$$\left(\frac{\partial V_H}{\partial H} \right) = \frac{aC}{2} \exp\left(-\frac{H}{D_0}\right) . \quad [4.25]$$

The equation for calculating g_t can, then, be obtained, by substituting $(\partial V_H/\partial H)$ in Equation [4.23] with Equation [4.25], as:

$$g_t = \frac{MC}{2\pi\rho N_A} \exp\left(\frac{-H}{D_0}\right) . \quad [4.26]$$

By replacing the constant D_0 with the value of 10.3, and the constant C with the values of -1.895 for silica samples methylated with 20% volume TMCS solution and -1.247 for the fresh coal samples, the g_t values were calculated as a function of separation distance H and the results are given in Figure 4.6. It is clearly shown in Figure 4.6 that the stronger the surface hydrophobicity, the smaller the g_t value, which means that transferring interlayer water molecules between stronger hydrophobic surfaces to the bulk will result in a greater reduction in the free energy. It is also evident that the water molecule closer to the hydrophobic surface will have greater excess free energy. However, the strong hydrophobic interaction energy observed experimentally corresponds to a free energy gain of only a few hundredths of kT per water molecule. Therefore, it is

not clear whether water between strongly hydrophobic surfaces is exposed to a force field significantly different from that in bulk water. Thus, it appears that the attractive hydrophobic interaction is essentially entropic in nature.

Experimentally, Pchelin (40) measured the volume of the precipitate of a Teflon suspension as a function of temperature, and found that the volume of precipitates increases with increasing temperature. The increase in the volume of precipitates indicates an increase in the strength of adhesion and an increase in the formation rate of contacts between the Teflon particles. The former is supported by an increase in the experimentally measured limiting shear stress with increasing temperature. He suggested that the increase in the adhesion strength is directly connected with a change in the structure of water, and concluded that hydrophobic interactions are reinforced with an increase in the temperature. His experimental results support the concept that the hydrophobic interaction is entropic in nature.

Claesson et al. (41) measured interactions between surfaces coated with penta-oxethylenedodecyl ether as a function of temperature. Their results show that at low temperatures, the hydration force between ethylene oxide units is purely repulsive while at higher temperatures, part of the force curve turns attractive. From the thermodynamics, the free energy changes associated with any physiochemical process can be expressed by:

$$\Delta G = \Delta H - T\Delta S . \quad [4.27]$$

The fact that a small change in the temperature changes the sign of ΔG and turns the repulsive to the attractive indicates that the hydrophobic interaction is associated with a significant increase in ΔS , thus it is mainly entropic in nature.

In an attempt to gain insight into whether the hydrophobic interaction is entropic orientational in nature, Israelachvili et al. (17) conducted a series of force

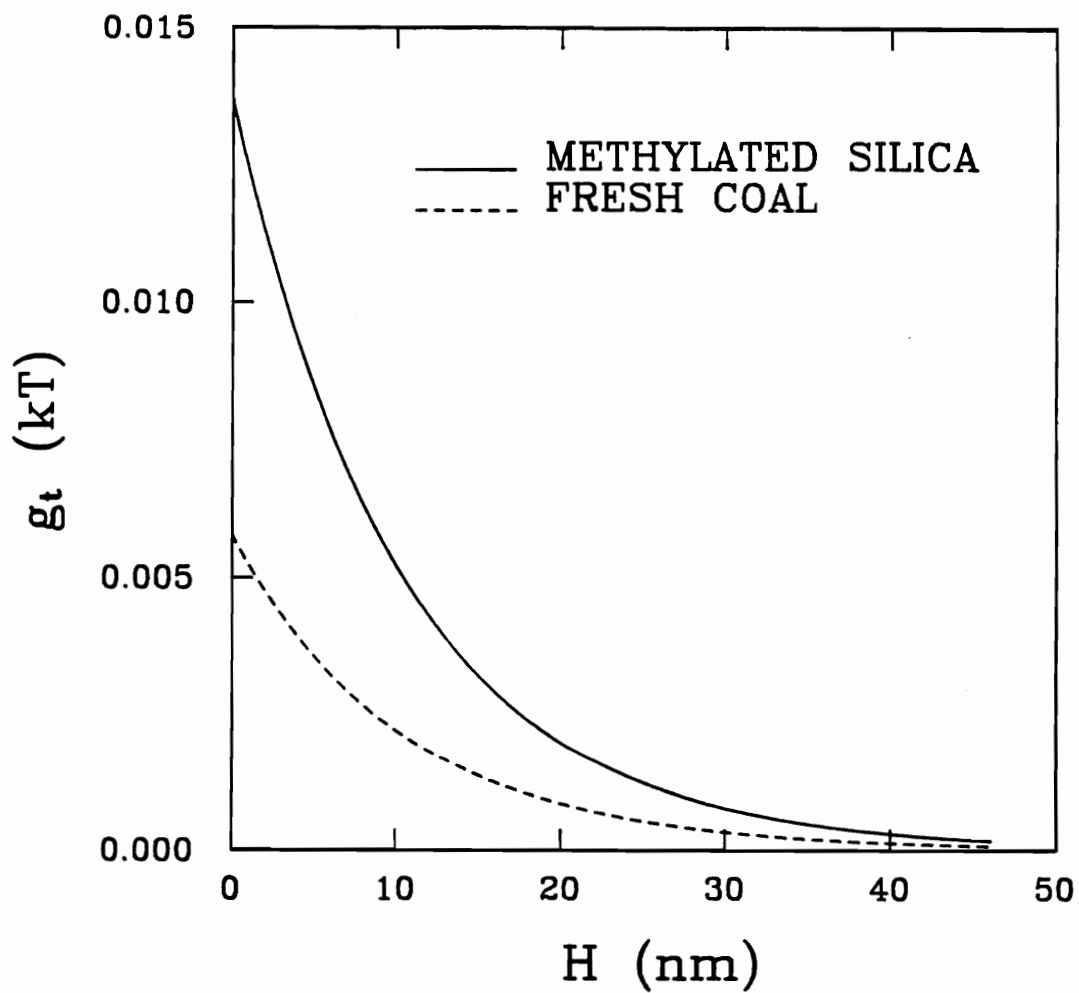


Figure 4.6. Excess Free Energy per Water Molecule Confined in the Interlayer Region between Two Strongly Hydrophobic Solids

measurement for surfaces immersed in 2-methyloctadecane, an anisotropic liquid. A hitherto unsuspected additional attractive force was observed, which they attributed to the entropic orientational effects. Although repulsive entropic orientational forces could arise, as is evident in the case of repulsive hydration forces, attractive force would be expected whenever the surface-induced ordering lowers the entropy of the adjacent liquid. Of course, in order to have a clear picture of the origin of the hydrophobic interaction, it would be helpful to conduct the force measurement with isotropic and anisotropic liquids of similar physiochemical properties.

It is well known that bulk liquid water is a very structured fluid with strong hydrogen bonds. The presence of hydrophobic entities, which are inert to hydrogen bonds because of their non-polar character, perturbs the water structure in such a way as to minimize the loss of hydrogen bonds. To accomplish this configuration, water dipoles are oriented parallel to the surface, forming a hydrophobic hydration sheath around the hydrophobic solid. Since water is an associated liquid, there is a tendency to avoid the rupture of hydrogen bonds. This causes the surface induced structure to be propagated towards the center of the water film, showing the long range effect of orientation. Such an arrangement of water molecules adjacent to the hydrophobic surface, as discussed above, is responsible for a significantly reduced density of the water near the hydrophobic surface as observed experimentally. An increased mobility of water molecules along the tangential direction as indicated by the reduction in the viscosity of boundary layer (42) also supports the view of water structure as discussed above.

Because the water structure adjacent to the hydrophobic surfaces is entropically unfavorable, it is conceivable that the water film in the immediate vicinity of the surface is thermodynamically unstable. Schulze (43) has noted that the thickness of this unstable hydration sheath is on the order of 170 nm for very hydrophobic solids. Recent studies also show that the thickness of the unstable water film is in the range of 70-145

nm for a variety of hydrophobic solids (34). When two hydrophobic particles approach each other, these films must rupture before coagulation takes place. During this process, the water molecules in the hydration sheath must be released into the bulk water phase, which will result in an increase in entropy since the water molecules in the vicinity of a hydrophobic solid have a low degree of freedom. The entropy increase may, thus, be the driving force for the hydrophobic interaction.

4.5 Summary and Conclusions

Further evidence of attractive non-DLVO interaction has been provided by conducting coagulation tests using silica sample methylated to different degrees of hydrophobicity. An expression for describing the hydrophobic interaction energy as a function of the non-dispersion component of work of adhesion of water on solids has been derived. It suggests that the interaction energy is attractive and decays exponentially. The decay length has been determined from the critical film thickness reported in the literature, the critical ζ -potential for coagulation and the Hamaker constants obtained in the present work.

It has been shown that the hydrophobic interaction energy is operating at a much longer separation distance than the dispersion energy and is the major driving force for coagulation of strongly hydrophobic particles. The origin of hydrophobic interaction has been discussed in detail and it is suggested that the hydrophobic interaction appears entropic in nature.

4.6 References

1. Christenson, H. K., "Non-DLVO Forces between Surfaces-Solvation, Hydration and Capillary Effects," *J. Dispersion Sci. Tech.*, 9, 171 (1988).
2. Churaev, N. V. and Derjaguin, B. V., "Inclusion of Structural Forces in the Theory of Stability of Colloids and Films," *J. Colloid Interface Sci.*, 103, 542 (1985).
3. Christenson, H. K., Claesson, P. M. and Pashley, R. M., "The Hydrophobic Interaction between Macroscopic Surfaces," *Proc. Indian Acad. Sci. (Chem. Sci.)*, 98, 379 (1987).
4. Rabinovich, Ya. I. and Deryagin, B. V., "Direct Measurement of Forces of Attraction of Hydrophobized Quartz Fibers in Aqueous KCl Solutions," *Kolloidn. Zh.*, 49, 682 (1987).
5. Rabinovich, Ya. I. and Deryagin, B. V., "Interaction of Hydrophobized Filaments in Aqueous Electrolyte Solutions," *Colloids Surfaces*, 30, 243 (1988).
6. Israelachvili, J.N. and Pashley, R.M., "Hydrophobic Interaction Is Long Range, Decaying Exponentially with Distance," *Nature*, 300, 341 (1982).
7. Israelachvili, J. N. and Pashley, R. M., "Measurement of the Hydrophobic Interaction between Two Hydrophobic Surfaces in Aqueous Electrolyte Solutions" *J. Colloid Interface Sci.*, 98, 500 (1984).
8. Xu, Z. and Yoon, R. H., "The Role of Hydrophobic Interactions in Coagulation," *J. Colloid Interface Sci.*, 132, 532(1989).
9. Claesson, P. M., "Experimental Evidence for Repulsive and Attractive Forces Not Accounted for by Conventional DLVO Theory," *Progr. Colloid Polym. Sci.*, 74, 48 (1987).
10. Claesson, P. M. and Christenson, H. K., "Very Long Range Attractive Forces between Uncharged Hydrocarbon and Fluorocarbon Surfaces in Water," *J. Phys. Chem.*, 92, 1650 (1988).
11. Pashley, R. M., McGuiggan, P. M. and Ninham, B. W., "Attractive Forces between Uncharged Hydrophobic Surfaces: Direct Measurements in Aqueous Solution," *Science*, 229, 1088 (1985).
12. Claesson, P. M., Blom, C. E., Herder, P. C. and Ninham, B. W., "Interactions between Water-Stable Hydrophobic Langmuir-Blodgett Monolayers on Mica," *J. Colloid Interface Sci.*, 114, 234 (1986).
13. Marcelja, S., Mitchell, D. J., Ninham, B. W. and Sculley, M. J., "Role of Solvent Structure in Solution Theory," *J. Chem. Soc. Faraday Trans. II*, 73, 630 (1977).
14. Luzar, A., Svetina, S. and Zeks, B., "The Contribution of Hydrogen Bonds to the Surface Tension of Water," *Chem. Phys. Lett.*, 96, 485 (1983).

15. Pratt, L. R. and Chandler, D. J., "Theory of the Hydrophobic Effect," *J. Chem. Phys.*, 67, 3683 (1977).
16. Rao, M., Pangali, C. and Berne, B. J., "A Monte Carlo Simulation of the Hydrophobic Interaction," *J. Chem. Phys.*, 71, 2975 (1979).
17. Israelachvili, J.N., Kott, S.J., Gee, M.L., and Witten, T.A., "Entropic Orientational Forces between Surfaces in Anisotropic Liquids," *Langmuir*, 5, 1111 (1989).
18. Christenson, H. K. and Claesson, P. M., "Cavitation and the Interaction between Macroscopic Hydrophobic Surfaces," *Science*, 239, 390 (1988).
19. Stillinger, F. H. and Ben-Naim, A., "Liquid-Vapor Interface Potential for Water," *J. Chem. Phys.*, 47, 4431 (1967).
20. Stillinger, F. H., "Structure in Aqueous Solutions of Nonpolar Solutes from the Standpoint of Scaled-Particle Theory," *J. Solution Chem.*, 2, 141 (1973).
21. Lee, C. Y. and McCammon, J. A., "The Structure of Liquid Water at an Extended Hydrophobic Surface," *J. Chem. Phys.*, 80, 4448 (1984).
22. Kitchener, J. A., "Surface Forces in Flotation- A Critique," in *Principles of Mineral Flotation*, ed. by Jones M.H. and Woodcock, J.T., The Australasian Institute of Mining and Metallurgy, Victoria, Australia, 65 (1984).
23. Laskowski, J., "The Relationship between Floatability and Hydrophobicity," in *Advances in Mineral Processing*, ed. by Somasundaran, P., AIME, Inc., New York, 189 (1986).
24. Fowkes, F. M., "Attractive Forces at Interfaces," *Ind. Eng. Chem.*, 56, 40 (1964).
25. David, D. J. and Misra, A., "Surface Energetics Characterization and Relationship to Adhesion Using a Novel Contact Angle Measuring Technique," *J. Colloid Interface Sci.*, 108, 371 (1985).
26. Derjaguin, B. V., "Friction and Adhesion IV. The Theory of Adhesion of Small Particles," *Kolloid Z.*, 69, 155 (1934).
27. Hamaker, H. C., "The London-van der Waals Attraction between Spherical Particles," *Physica*, 4, 1058 (1937).
28. Delichatsios, M. A. and Probstein, R. F., "Coagulation in Turbulent Flow: Theory and Experiment," *J. Colloid Interface Sci.*, 51, 394 (1975).
29. Nagata, S., *Mixing: Principles and Applications*, Halsted Press, New York, (1975).
30. Usui, S., "Interaction of Electrical Double Layers and Colloid Stability," *Surfactant Sci. Ser. (Electrical Phenomena at Interfaces)*, 15, 47 (1984).
31. Vold, R. D. and Vold, M. J., *Colloid and Interface Chemistry*, Addison-Wesley Publishing Company, Inc., 269 (1983).

32. Pugh, R. J., "Selective Coagulation in Quartz-Hematite and Quartz-Rutile Suspensions," *Colloid Polym. Sci.*, 252, 400 (1974).
33. Olphen, H. V., *An Introduction to Clay Colloid Chemistry: For Clay Technologists, Geologists and Soil Scientists*, John Wiley & Sons, Inc., New York, (1963).
34. Yordan, J., *Surface Forces in Bubble-Particle Adhesion*, Ph.D. Thesis, Department of Mining and Minerals Engineering, Virginia Polytechnic Institute and State University, 1989.
35. Ström, G., Fredriksson, M. and Klason, T., "Interfacial Tension and Surface Hydrophobicity in Systems of Solid Polymers in Contact with Aqueous Solutions," *J. Colloid Interface Sci.*, 123, 324 (1988).
36. Pashley, R. H., "Hydration Forces between Mica Surfaces in Aqueous Electrolyte Solutions," *J. Colloid Interface Sci.*, 80, 153 (1981).
37. Allen, L. H. and Matijevic, E., "Stability of Colloidal Silica II. Ion Exchange," *J. Colloid Interface Sci.*, 33, 420 (1970).
38. Depasse, J. and Watillon, A., "Stability of Amorphous Colloidal Silica," *J. Colloid Interface Sci.*, 33, 430 (1970).
39. Harding, R.D., "Stability of Silica Dispersions," *J. Colloid Interface Sci.*, 35, 172(1971).
40. Pchelín, V.A., "Modelling of Hydrophobic Interactions," *Kolloidn. Zh.*, 34, 783 (1972).
41. Claesson, P.M., Kjellander, R., Stenius, P., and Christenson, H.K., "Direct Measurement of Temperature-Dependent Interactions between Non-Ionic Surfactant Layers," *JCS Faraday Trans. I*, 82, 2735 (1986).
42. Derjaguin, B.V. and Churaev, N.V., "Structure of Water in Thin Layers," *Langmuir*, 3, 611 (1987).
43. Schulze, H.J., *Developments in Mineral Processing*, Elsevier, Amsterdam, (1984).

CHAPTER 5 MODEL DEVELOPMENT FOR THE COAGULATION PROCESS

5.1 Introduction

It is well known that coagulation is a result of collision and coalescence or adhesion of particles. The collision frequency is usually controlled by the hydrodynamics of the coagulation system, while the coalescence or adhesion is largely determined by the thermodynamics of the system.

The collision between particles is from the transport of particles in suspension. The relative motion of particles may be due to Brownian motion, differential sedimentation and/or fluid flow, depending upon the fluid turbulence scale and particle size. For example, if the particle size is less than $1 \mu\text{m}$, the Brownian motion is the major transport mechanism regardless of the hydrodynamics of the mixing conditions, and the coagulation is perikinetic (1-3). When the particle size is larger than $5 \mu\text{m}$ and the coagulation is conducted under severe turbulent conditions, the fluid flow is the dominating transport mechanism and the coagulation is orthokinetic (4-5).

In conventional coagulation, it is said that the thermodynamics of the system plays an important role in determining the adhesion efficiency or stability of the suspension (6-7). If there is no net repulsive interaction between approaching particles, every collision will result in adhesion and the coagulation is said to be rapid. An inter-

action energy barrier existing between two approaching particles, however, prevents every encounter from being effective. Only a fraction of the collisions leads to aggregation and the coagulation is then termed slow coagulation. The reduction in the coagulation rate depends upon the magnitude of the energy barrier which is determined from the thermodynamics of the system.

When coagulation is conducted under severe shear conditions, the kinetic energy provided by mixing may exceed the potential energy barrier, turning slow coagulation into rapid coagulation. Even if the kinetic energy is not sufficient to completely overcome the interaction energy barrier, it is still possible to increase the aggregation rate by reducing the effective energy barrier. It is, therefore, clear that both hydrodynamics and thermodynamics are important in determining the coagulation rate in the process of coagulation with mixing.

On the other hand, the stability of aggregates thus formed is mainly determined by the interfacial properties and hydrodynamics of the fluid. It is well documented (8-13) that aggregates are subjected to breakage due to shear force. The stability of aggregates in a turbulent suspension of low percent solids is governed by both the interaction of individual aggregates with the fluid and the adhesion strength between particles. The size and compactness of the aggregates, the size and shape of the primary particles and the number of interparticle contacts can all contribute to aggregate structure and the ability to withstand disruption of aggregates by fluid forces.

A complete description of the coagulation process with mixing should, therefore, include both aggregate growth and breakage. Mathematical modeling and computer simulation as applied to the coagulation process can provide a quantitative and systematic basis for understanding the mechanism of coagulation, analyzing the factors affecting the process and improving its design and operation. Three types of coagulation models have been reported, including direct simulation of particle collision, numerical

solution of the kinetic coagulation equation and exact Monte Carlo simulation of particle collision. The most important deterministic model describing size distribution evolution as a function of time is, however, the population balance, which results in a set of simultaneous first-order nonlinear ordinary differential equations for a discrete size spectrum. The significant advantage of the model is that it provides a means of including the details of both aggregation and breakage processes in terms of the physical parameters and operating conditions.

In this chapter, the coagulation process of a batch-operated unit has been analyzed in detail from a theoretical point of view. The theoretical models describing the rate processes of aggregate growth and breakage in a locally isotropic turbulent flow field have been proposed from fundamental concepts. The coagulation kinetic equations have been developed based on the first principle of population balance, with four adjustable parameters being involved.

5.2 Model for Aggregate Porosity

During the coagulation of solids in a suspension, porous aggregates are formed with volumes being greater than the sum of the volumes of individual particles consisting of the aggregates. It has been found, theoretically and experimentally, that the porosity of the aggregates increases as the aggregate size increases, but in a complicated fashion (14-17). Therefore, it is necessary to model the porosity of aggregates as a function of aggregate size for any simulation of the coagulation process to be successful.

As a model (17), an effective binary collision between an i th-fold aggregate and a j th-fold aggregate forming an $(i+j)$ th-fold aggregate is depicted in Figure 5.1. The i th-fold aggregate in the present work is defined as an aggregate consisting of i primary particles. In general, the aggregate formed through binary collision is not spherical, as

shown in Figure 5.1 (b). However, for the convenience of simulation, it is necessary to assume that the aggregate is a porous sphere with the same volume as that of an envelope surrounding the doublet, as shown in Figure 5.1 (b). The volume of an equivalent sphere of the aggregate shown in Figure 5.1 (c) equals the sum of the volumes of a cone, C, and two deficient spheres, A and B, as shown in Figure 5.1 (b). The porosity, ε , of the aggregate can, on a volume basis, be expressed as:

$$\varepsilon = 1 - \frac{V_s}{V_a} , \quad [5.1]$$

where V_s is the volume of two spheres and V_a is the volume of the aggregate. From simple geometry, it can be readily shown (17) that:

$$\varepsilon = \frac{p^2(1-p)}{1-p^5} , \quad [5.2]$$

where $p = (a_1/a_2)$. For the special case of $a_1 = a_2$, p equals 1 and Equation [5.2] becomes:

$$\varepsilon = \lim_{p \rightarrow 1} \frac{p^2(1-p)}{1-p^5} = \lim_{p \rightarrow 1} \frac{2p - 3p^2}{-5p^4} = \frac{-1}{-5} = 0.2 . \quad [5.3]$$

Equation [5.3] means that the porosity reaches a limiting value of 0.2 when two interacting particles are of the same size. It is important to realize that Equation [5.2] only gives a new volume-based porosity introduced from binary aggregation. For an aggregate consisting of z primary particles of equal size, each having a volume of V_1 , the apparent volume of the aggregate may be expressed as:

$$V_{az} = \frac{V_{a(z-1)} + V_1}{1 - \varepsilon_{pz}} , \quad [5.4]$$

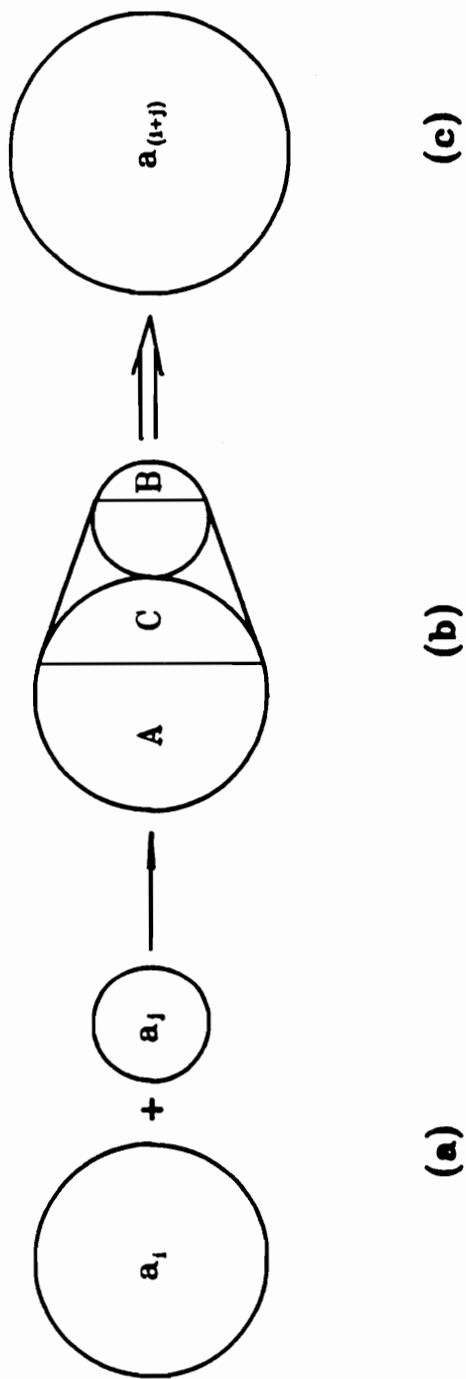


Figure 5.1 A Schematic Representation of a Binary Aggregate Formation Model

- (a) Individual particles of sizes a_i and a_j
- (b) A binary aggregate formed from individual particles a_i and a_j
- (c) Equivalent spherical aggregate of size $a_{(i+j)}$

where ε_{pz} is the new volume-basis porosity introduced due to the addition of a z th particle to a $(z-1)$ th-fold aggregate and $V_{a(z-1)}$ refers to the apparent volume of the $(z-1)$ th-fold aggregate. By the definition of porosity given in Equation [5.1],

$$V_{a(z-1)} = \frac{(z-1)V_1}{1 - \varepsilon_{z-1}} \quad [5.5]$$

Substituting Equations [5.4] and [5.5] into Equation [5.1] results in the following equation for calculating the overall porosity of the z th-fold aggregate:

$$\varepsilon_z = 1 - \frac{z(1 - \varepsilon_{z-1})(1 - \varepsilon_{pz})}{z - \varepsilon_{z-1}} \quad [5.6]$$

The new porosity, ε_{pz} in Equation [5.6] can be calculated using Equation [5.2] in which p_z is given by Equation [5.7] as obtained from substituting Equation [5.4] into the above expression for p :

$$p_z = \frac{a_1}{a_{z-1}} = \left(\frac{V_1}{V_{a(z-1)}} \right)^{1/3} = \left(\frac{1 - \varepsilon_{z-1}}{z - 1} \right)^{1/3} \quad [5.7]$$

With the overall porosity, the equivalent spherical size of a z th-fold aggregate can be readily calculated using the following equation:

$$a_z = a_1 \left(\frac{z}{1 - \varepsilon_z} \right)^{1/3} \quad [5.8]$$

The overall porosity and equivalent spherical size of an aggregate have been simulated as a function of aggregate number, z , by successive solutions of Equations [5.7], [5.2], [5.6] and [5.8]. The simulations have been made for two different primary particle sizes and the results are given in Figure 5.2. This model implicitly assumes that the aggregate structure is not historically dependent. Based on this model, the porosity

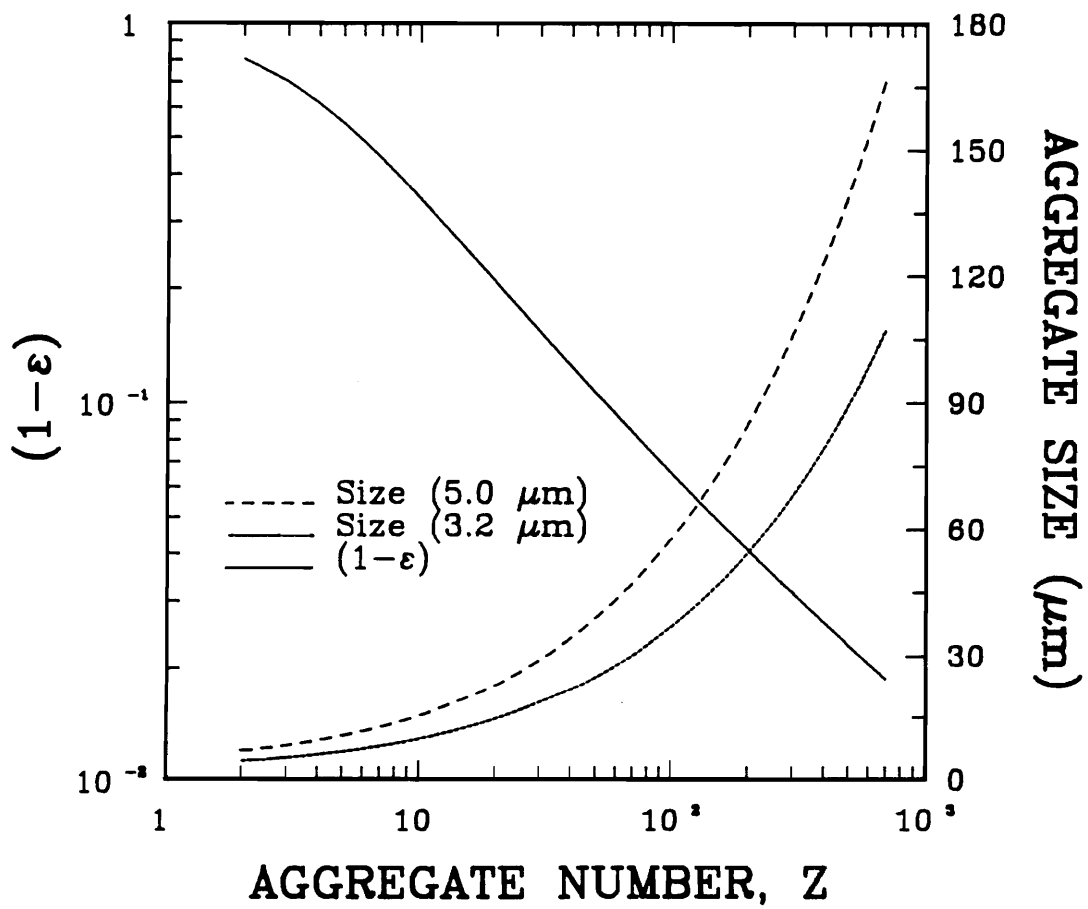


Figure 5.2. Simulation Results of Porosity and Aggregate Size as a Function of Aggregate Number Using the Model of Figure 5.1.

is a function of the aggregate number only, and is independent of primary particle size as shown in Figure 5.2. This simulation shows that over a wide range of aggregate numbers, there exists a linear relationship between the logarithm of $(1 - \varepsilon)$ and the logarithm of the aggregate number. Similar relationships have been obtained through computer simulations with various assumptions (14-15) and verified experimentally (16-17).

Figure 5.2 also shows that the aggregate size keeps increasing with increases in the aggregate number. As indicated in Equation [5.8], the aggregate size is also a function of primary particle size but the functional dependence of the aggregate size on the aggregate number is identical, i.e., the aggregate grows in the same functional form. This feature is clearly shown in Figure 5.2.

5.3 Model for Aggregate Growth

As mentioned earlier in this chapter, the aggregation rate depends upon the frequency of collision and the fraction of collisions which result in adhesion. In the present work, the shear field is applied by intense mixing, with primary particle size being larger than $1 \mu\text{m}$. Under these conditions, the fluid flow is the only important mechanism for transporting particles. The suspension used in this study is sufficiently dilute (less than 3% by volume) so that only binary collisions need to be considered (18). The aggregation in such a system is a free-in-space process (19) to which simple binary collision mean free path concepts may be applied for calculating collision frequency.

As discussed in the previous chapter, when two interacting particles approach each other, there may exist a critical separation, H_m . Upon reaching this separation, two particles will slip together spontaneously, forming a random aggregate. It is, therefore, necessary to take the surface force effect into account when formulating the collision

frequency. This is particularly true in the presence of a significant hydrophobic interaction which operates over a very long range. By incorporating the surface force effects into the collision model, the effective collision cross-sectional area becomes $\pi(a_i + a_j + H_m)^2$ instead of $\pi(a_i + a_j)^2$ which has been commonly used (18). a_i and a_j here are the radii of two colliding particles and/or aggregates.

As an example of developing an expression for collision frequency, the collision between an i th-fold aggregate and a j th-fold aggregate is considered here. According to the Kolmogorov theory of isotropic turbulence, the relative velocity, U_{ij} , with a separation distance of $(a_i + a_j + H_m)$ in the fluid, depends on the turbulent scale, and its magnitude is given by the relations (18):

$$U_{ij} = \left(\frac{1}{15}\right)^{1/2} \left(\frac{\bar{\epsilon}}{\nu}\right)^{1/2} (a_i + a_j + H_m) \quad \text{if } (a_i + a_j + H_m) < \lambda \quad [5.9]$$

or
$$U_{ij} = 1.37[\bar{\epsilon}(a_i + a_j + H_m)]^{1/3} \quad \text{if } (a_i + a_j + H_m) > \lambda, \quad [5.10]$$

where ν is the kinematic viscosity of the continuous phase, $\bar{\epsilon}$ is the rate of turbulent energy dissipation per unit mass and λ is the Kolmogorov microscale, as defined by Equation [5.11]:

$$\lambda = \left(\frac{\nu^3}{\bar{\epsilon}}\right)^{1/4}. \quad [5.11]$$

The magnitude of $\bar{\epsilon}$ is a function of the mixing hydrodynamics and the geometry of the mixing system. It can be readily evaluated using the method described by Nataga (20), and the procedures for the calculation are given in Appendix I. It is shown in Appendix I that with the increase in mixing intensity, the rate of turbulent energy dissipation increases significantly. Therefore, the relative velocity increases as the mixing becomes increasingly intense, as indicated in Equations [5.9] and [5.10].

During the course of the transport of an *i*th-fold aggregate with respect to a *j*th-fold aggregate, the apparent volume swept out by this aggregate in unit time is given by Equation [5.12]:

$$\omega(a_i, a_j) = \pi(a_i + a_j + H_m)^2 U_{ij} . \quad [5.12]$$

Since the aggregation proceeds in a free-in-space environment, the reference aggregate *i* will collide with all *j*th-fold aggregates within the volume as given by Equation [5.12]. Therefore, the total number of collisions between *i*th- and *j*th-fold aggregates of unit volume in unit time can be written as:

$$N_{ij} = \pi(a_i + a_j + H_m)^2 U_{ij} n(i) n(j) , \quad [5.13]$$

where $n(i)$ and $n(j)$ are the number concentrations of *i*th- and *j*th-fold aggregates, respectively. Equation [5.13] shows that the collision frequency is simply a product of $\omega(a_i, a_j)$ and the number concentrations of *i*th- and *j*th-fold aggregates. It is, therefore, reasonable to refer to $\omega(a_i, a_j)$ as the collision mode which is an intensive property of the system. Equation [5.13] is valid only when *i* is not equal to *j*. In the case of *i* equal *j*, Equation [5.13] is reduced to:

$$N_{ii} = \frac{1}{2} \pi(2a_i + H_m)^2 U_{ii} n(i)^2 . \quad [5.14]$$

It should be noted that (1/2) enters into Equation [5.14] to ensure that each collision between particles of the same class is counted only once. From Equations [5.13] and [5.14], it can be seen that the increased mixing promotes the collision frequency significantly.

In the absence of a net interparticle repulsive force, every such encounter will cause the formation of a new aggregate, and the aggregation rate will be determined

solely by the hydrodynamics of the system, as shown in Equations [5.9]-[5.14]. However, only a fraction of the collisions described by Equations [5.13] and [5.14] are effective in the presence of a net repulsive force between i th- and j th-fold aggregates, regardless of the nature of the forces. In the classical stability theory, this fraction is determined exclusively by the thermodynamic properties of the system. A common way to evaluate the magnitude of this fraction is to integrate a potential energy function with respect to a separation distance, as given by Equation [5.15] (1, 6-8, 21-23):

$$\frac{1}{\alpha} = (a_i + a_j)^2 \int_{a_i + a_j}^{\infty} \exp\left(\frac{V_T}{kT}\right) \frac{dH}{H^2} , \quad [5.15]$$

where V_T is the total interaction potential between i th- and j th-fold aggregates, which is a function of the separation distance, H . Since a small range of separation around the energy barrier, V_{\max} , contributes predominantly to the above integration, an approximation as given by Equation [5.16] is useful (22):

$$\frac{1}{\alpha} = \frac{1}{\kappa(a_i + a_j)} \exp\left(\frac{V_{\max}}{kT}\right) . \quad [5.16]$$

The above stability theory has been widely used in conventional coagulation/dispersion studies. However, this theory may not be appropriate when applied to a coagulation system under severe mixing conditions. Conceptually, if intense mixing is applied to the suspension, the particles may obtain a kinetic energy which is sufficient to overcome the interaction energy barrier. As a result, the particles can still reach a very close proximity where the strong net attractive forces are operating. In this case, every collision is actually effective and results in aggregation. It is, therefore, necessary to

develop a new expression for collision efficiency as a function of both interaction energy barrier and kinetic energy.

In the present work, the collision efficiency is taken as unity if the kinetic energy is larger than or equal to the interaction energy barrier. Otherwise, an exponential distribution of collision efficiency is used, which can be expressed as:

$$\alpha = 1 \quad \text{if } V_k \geq V_{\max} \quad [5.17]$$

$$\text{or } \alpha = \exp[-\beta(V_{\max} - V_k)] \quad \text{if } V_k < V_{\max} , \quad [5.18]$$

in which β is an adjustable parameter with a unit of $(kT)^{-1}$, describing the rate at which collision efficiency decreases with increasing $(V_{\max} - V_k)$, where V_{\max} is the interparticle potential energy barrier and V_k is the kinetic energy of the particles at the moment of collision. The value of V_k can be calculated using Equation [4.10].

It is interesting to note that Equations [5.17] and [5.18] in combination are equivalent to Equation [5.16] if the effect of kinetic energy is neglected and β is set to be unity. They differ only by a factor of $\kappa(a_i + a_j)$, i.e., Equation [5.16] predicts a collision efficiency of $\kappa(a_i + a_j)$ instead of unity which is expected for barrierless coagulation conditions. Therefore, to describe the collision efficiency, Equations [5.17] and [5.18] in combination seem more reasonable, in particular when coagulation is conducted under severe mixing conditions. Figure 5.3 shows the dependence of collision efficiency on $(V_{\max} - V_k)$, as calculated using Equations [5.17] and [5.18] with various values of β . It can be seen that over the range of $V_{\max} > V_k$, the collision efficiency is very sensitive to the interaction energy barrier through its exponential dependence. The sensitivity can be controlled by adjusting the value of parameter β . The value of parameter β may be

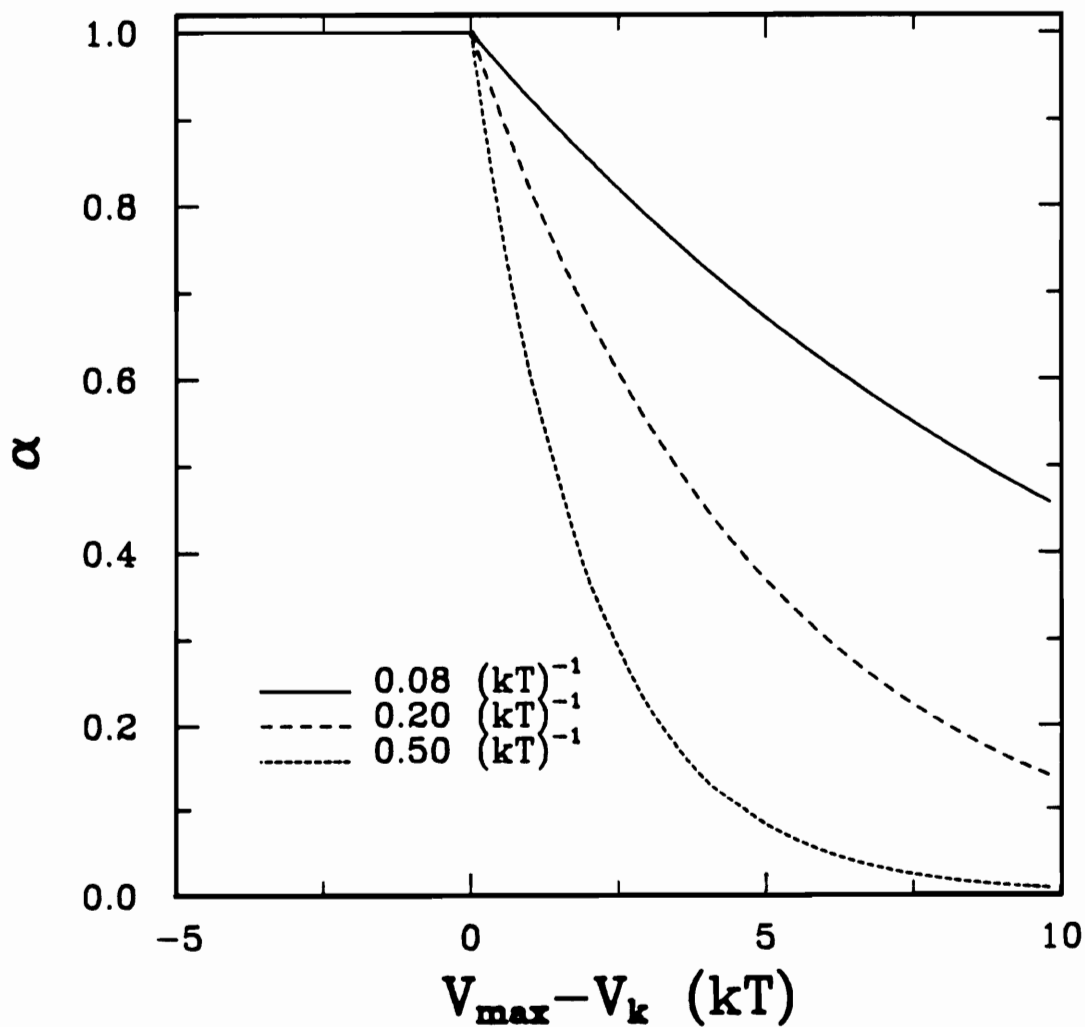


Figure 5.3. Comparison of Collision Efficiency for Three Different Values of Model Parameter β

determined by measuring initial coagulation rates experimentally and matching them with simulation results obtained using different values of β .

Based on the above discussion, the following expressions can be obtained to give the overall aggregation rate between i th- and j th-fold aggregates:

$$R(i, j) = \alpha\pi(a_i + a_j + H_m)^2 U_{ij} n(i)n(j), \quad \text{if } i \neq j \quad [5.19]$$

or
$$R(i, j) = \frac{1}{2} \alpha\pi(a_i + a_j + H_m)^2 U_{ij} n(i)n(j), \quad \text{if } i = j . \quad [5.20]$$

It is convenient to use rate constant instead of rate in formulating coagulation kinetic equations since rate constant is an intensive property, independent of the concentration of the species. It can be readily shown that the aggregation rate constants $k(i, j)$ are given by:

$$k(i, j) = \alpha\pi(a_i + a_j + H_m)^2 U_{ij}, \quad \text{if } i \neq j \quad [5.21]$$

or
$$k(i, j) = \frac{1}{2} \alpha\pi(a_i + a_j + H_m)^2 U_{ij}, \quad \text{if } i = j . \quad [5.22]$$

Two important roles of mixing in promoting the aggregation rate are illustrated in Equations [5.19] and [5.20]. On one hand, an increase in mixing intensity will increase the kinetic energy and, thus, increase the collision efficiency in the presence of an interaction energy barrier. On the other hand, an increase in mixing intensity increases the collision frequency as indicated by an increase in U_{ij} . Apparently, shear conditioning of a coagulation system is favorable for aggregation kinetics. However, it should be noted that the shear conditioning will unavoidably create a mechanical force which may be strong enough to break aggregates of a certain size, as will be discussed in the following.

5.4 Model for Aggregate Breakage

In the previous section of this chapter, the importance of shear conditioning of a suspension for promoting aggregation has been discussed in detail. It is obvious that intense mixing increases particle-particle collision frequency. At same time, it increases the collision efficiency by providing interacting particles with a high level of kinetic energy. If the kinetic energy is sufficient to overcome the interaction energy barrier, every collision will then be effective for aggregation. Even if the kinetic energy is less than the interaction energy barrier, it will still increase the collision efficiency by increasing the probability of overcoming this energy barrier.

It is also noted (8-9, 12-13, 24-27) that if the mixing is too vigorous, the shear force produced may break large aggregates into small ones. Therefore, successful modeling of coagulation under mixing conditions should focus on both aggregate growth and breakage. In this section, the breakage rate and breakage mode will be proposed through theoretical analysis of the breakage event.

It is evident that there are two major forces which control the breakage rate. The surface forces between particles tend to hold them together, forming a stable aggregate, while the hydrodynamic shear force tends to break the bonds between particles so that only random aggregates can form. Therefore, it is reasonable to relate the breakage rate constant to these two counteracting forces.

It is obvious that when two or more particles form an aggregate, there is a reduction in the solid/water interface due to the direct contact of particles. The binding force is, therefore, a function of solid/water interfacial tension and contact area. The former can be evaluated from contact angle measurements while the latter is a function of the mechanical properties of particles, the number of primary particles composing the aggregate, and the structure of the aggregate. In general, the magnitude of the binding

force, F_b , can be considered as a product of twice the net contact area and the interfacial tension, as given by Equation [5.23]:

$$F_b = 2\gamma_{sw}A_n , \quad [5.23]$$

where γ_{sw} is the solid/water interfacial tension and A_n is the net contact area. Since our knowledge about the relation between the net contact area and aggregate size and structure is rather limited, an assumption has been made (10) that the net contact surface area is proportional to the cross-sectional area of the aggregate, i.e.,

$$A_n = k_1 a^2 (1 - \epsilon)^{2/3} , \quad [5.24]$$

where ϵ is the porosity of an aggregate, a is the radius of the aggregate and k_1 is an adjustable parameter. Substituting Equation [5.24] into Equation [5.23] results in Equation [5.25], which can be used to evaluate the binding force:

$$F_b = 2k_1 \gamma_{sw} a^2 (1 - \epsilon)^{2/3} . \quad [5.25]$$

The binding force, F_b , has been calculated as a function of aggregate size using Equation [5.25] with various values of k_1 . The results given in Figure 5.4 show that the binding force increases with increasing aggregate size. This is obvious since, with the increase in aggregate size, the number of contacts per aggregate increases. It can be seen from Figure 5.4 that the rate at which the binding force increases with aggregate size is also very sensitive to the parameter k_1 . Since the structure of the aggregate determines the number of contacts for a given aggregate number, while the mechanical properties of the particles and the net normal forces at the contact position determine the contact area per contact, the value of k_1 varies from system to system. Even with the same system, different hydrodynamic conditions will produce aggregates with different structures.

More open structures will form under gentle mixing conditions, while compact aggregates are most probable with severe mixing. Different mixing intensities also produce different pressure drops over certain distances, which changes the magnitude of the normal forces acting across the contact region. As a result, the contact area per contact changes with varying mixing intensities. Usually, intense mixing gives higher values of k_1 since the more compact structure of the aggregates allows more interparticle contacts and greater contact area per contact. It is, therefore, important to characterize the parameter k_1 for each system under the given operating conditions in order to obtain a successful simulation.

On the other hand, the shear force (F_s) acting on a unit area of opposite sides of an aggregate is proportional to the average value of the relative velocity fluctuations of the two sides (28), which can be written as:

$$F_s = k_2 A_s \rho_w U_a^2 \quad , \quad [5.26]$$

where k_2 is a proportionality constant, A_s is cross-sectional area of shear and U_a is average value of the velocity fluctuation evaluated at a separation distance of a . From the Kolmogorov theory of isotropic turbulence, the average value of relative velocity fluctuation depends upon the turbulent scales. Under conditions where the inertial convection subrange of turbulence exists, Equation [5.10] can be used to calculate the average value of velocity fluctuation. Otherwise, Equation [5.9] should be used in the viscous dissipation subrange of turbulence.

Substituting Equation [5.9] or [5.10] into Equation [5.26], and expressing A_s explicitly yield Equation [5.27] or [5.28]:

$$F_s = \frac{2\pi}{15} k_2 \rho_w \alpha^4 \frac{\bar{\epsilon}}{\nu} \quad \text{if } 2a < \lambda \quad [5.27]$$

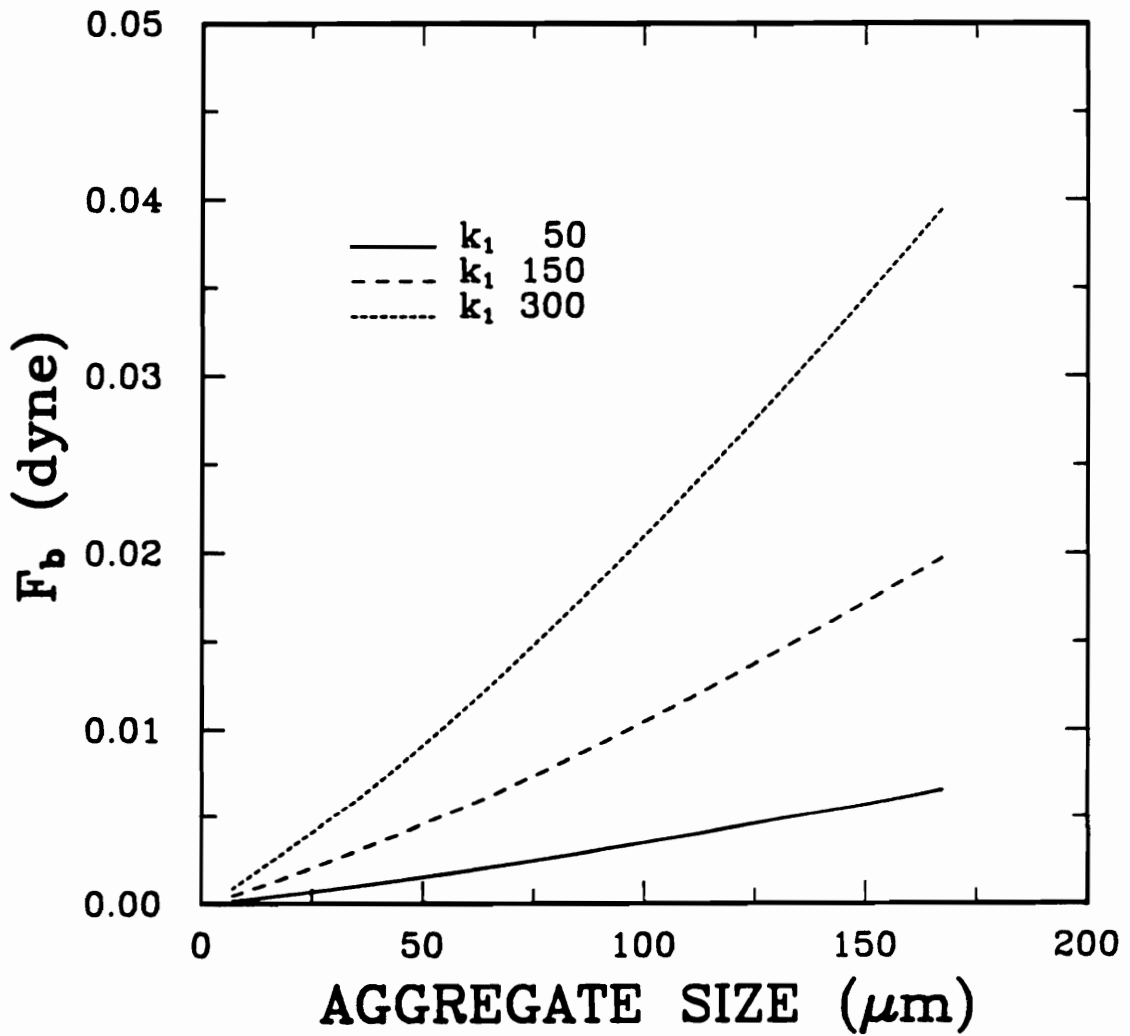


Figure 5.4. Variation of Binding Force as a Function of Aggregate Size for Three Different Values of Model Parameter k_1

$$\text{or } F_s = 1.09k_2\pi\rho_w a^{8/3}\bar{E}^{2/3} \quad \text{if } 2a > \lambda . \quad [5.28]$$

By using Equation [5.27] or [5.28], the shear force has been calculated as a function of aggregate size for the system of a 5% by weight coal suspension with the primary coal particles being $5 \mu\text{m}$. The mixing has been assumed to be provided with a mixer, as described in Appendix I, operating at 500, 1000 and 1500 *rpm*, respectively. The results given in Figure 5.5 were obtained by using the value of unity for parameter k_2 in the calculation. The figure shows that the shear force increases with increasing aggregate size. Under intense shear conditions, this aggregate size dependence is more significant. Figure 5.5 also shows that with a given aggregate size, the shear force increases dramatically as shear intensities increase, indicating that the mixing which is too vigorous will break the aggregates that are relatively small in size and reduce the aggregate top size.

By comparing Figure 5.5 with Figure 5.4, it can be seen that the shear force increases with aggregate size more rapidly than the binding force. At small aggregate sizes, the shear force being exerted on the aggregate is insignificant. Therefore, the breakup of aggregates is unlikely to occur. However, as the aggregate size increases, the shear force becomes increasingly significant. It is expected that at a certain aggregate size, the shear force starts to exceed the binding force and the breakup of aggregates begins.

It has been found that there are two major aggregate breakage mechanisms, surface erosion of primary particles (29) and bulgy deformation-aggregate splitting (30). It is obvious, however, that the breakup of an aggregate will not occur until the shear force provided by intense mixing is greater than the binding forces between particles, regardless of the breakage mechanisms. In the present breakage model, no special consideration is given to the breakage mechanisms. As long as the shear force is greater

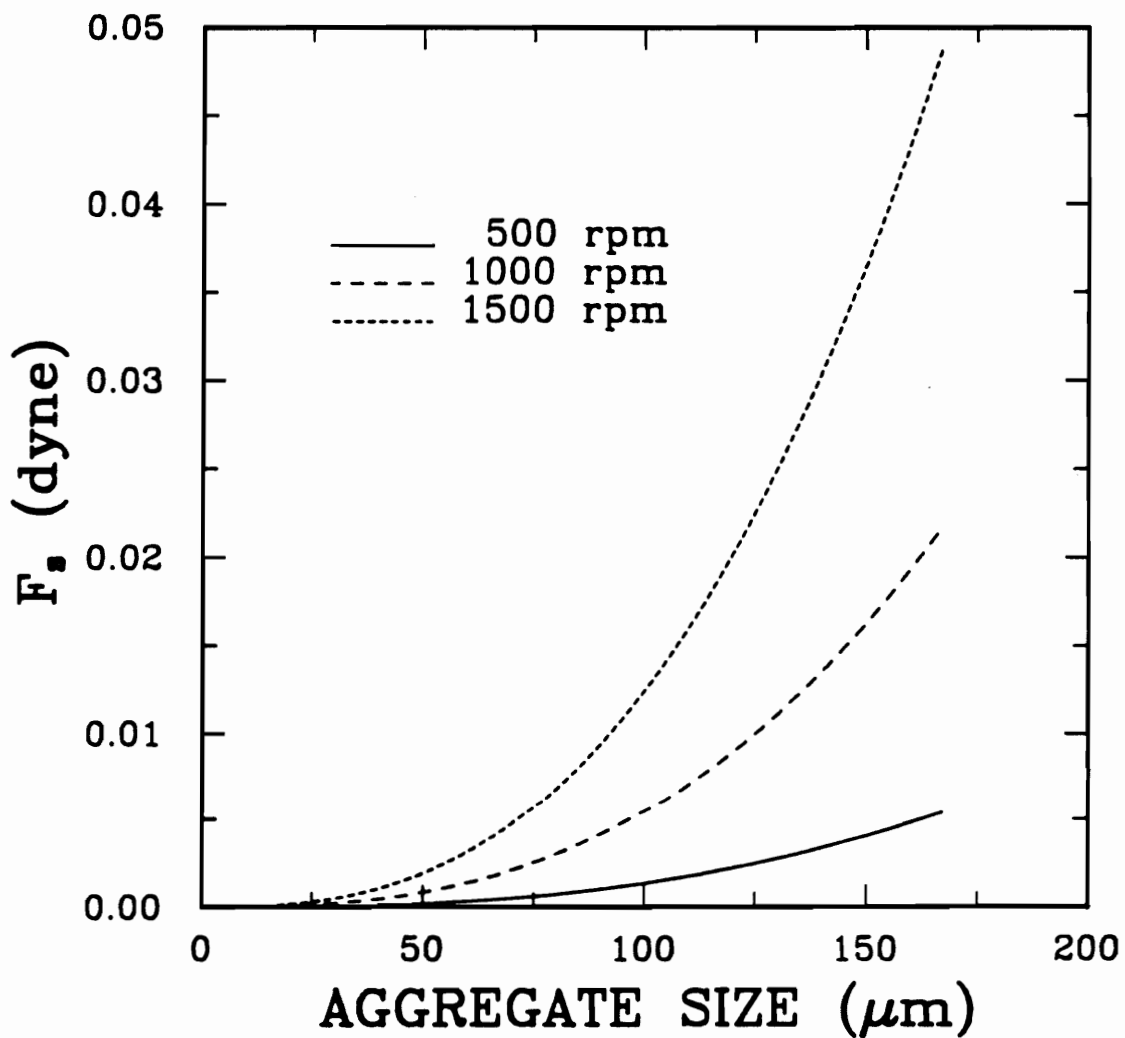


Figure 5.5. Variation of Shear Force as a Function of Aggregate Size for Three Different Mixing Rates

than the binding force, the aggregate will be subjected to disintegration, forming a spectrum of daughter particles. The breakage rate constant, $S(a)$, is defined as such that $S(a)n(a)dt$ is the number of aggregates having size a that split per unit volume in the infinitesimal time interval dt . The breakage rate constant defined in this manner has the unit of sec^{-1} . The following functional formula is proposed to describe the breakage rate constant:

$$S(a) = 0 \quad \text{if } F_b > F_s, \quad [5.29]$$

or
$$S(a) = A\{1 - \exp[k_3(F_b - F_s)]\} \quad \text{if } F_b \leq F_s, \quad [5.30]$$

where A and k_3 are adjustable parameters which can be determined by fitting experimental data to the simulation results. The binding force (F_b) and shear force (F_s) in Equations [5.29] and [5.30] can be calculated using Equations [5.25] and [5.27] or [5.28], respectively.

Equation [5.29] simply means that breakage will not occur if the binding force is greater than shear force, while Equation [5.30] indicates that the breakage rate is exponentially proportional to the net breakup force in the regime that shear force is greater than the binding force. The exponential form is used without any justification since it is a widely used function in describing the relationship between rate constant and activation energy for most chemical processes. Equation [5.30] ensures that the breakage rate approaches a finite value asymptotically as is required physically.

The behavior of this breakage rate constant function is illustrated in Figure 5.6 as a function of aggregate size. In the calculation of breakage rates as shown in Figure 5.6, Equations [5.25], [5.27], [5.28], [5.29] and [5.30] have been used in combination. The calculation has been conducted for a 5% by weight suspension of 5- μm coal conditioned

at 1000 rpm using the mixer illustrated in Appendix I. To be simple, the value of parameter k_2 in Equations [5.27] and [5.28] has been assumed to be unity. This will not change the calculated breakage rate constants since we can pull k_2 out of the expressions for F , and assign two new equivalent values to parameters k_1 and k_3 , respectively. This indicates that only three instead of four independent parameters are required in the present breakage model for describing the breakage rate. For convenience, A in Equation [5.30] has been set to be unity in the calculations.

Figure 5.6 shows that the breakage will not occur until the aggregate grows to a certain size. The size at which the aggregates start to break increases significantly as k_1 increases. This finding suggests that compact aggregates of soft material can be subjected to a higher shear field without breakage, forming aggregates of larger size due to the larger value of k_1 . Figure 5.6 also shows that by assuming the same value of k_1 , the breakage rate increases substantially with an increase in the value of k_3 . However, the aggregate size at which the aggregates start to break does not change.

In order to study the influence of shear force on aggregate breakage, the calculation of breakage rate constants as a function of aggregate size has also been performed using different mixing intensities. The k_1 and k_3 values have been fixed at 150 and 100, respectively. The results given in Figure 5.7 show that not only the breakage rate but also the size at which the aggregates start to break up changes with changes in mixing intensity. This finding suggests that mixing intensity is a most sensitive adjustable operation variable to control the ultimate aggregate size and its distribution.

The above discussion indicates that this simple three-parameter model seems appropriate for describing the breakage rate. The values of these three parameters can be determined by curve-fitting of the experimental results.

Upon breakage, an aggregate of size a turns into a number of daughter fragments which are distributed in the size space according to a distribution function, $B(a', a)$.

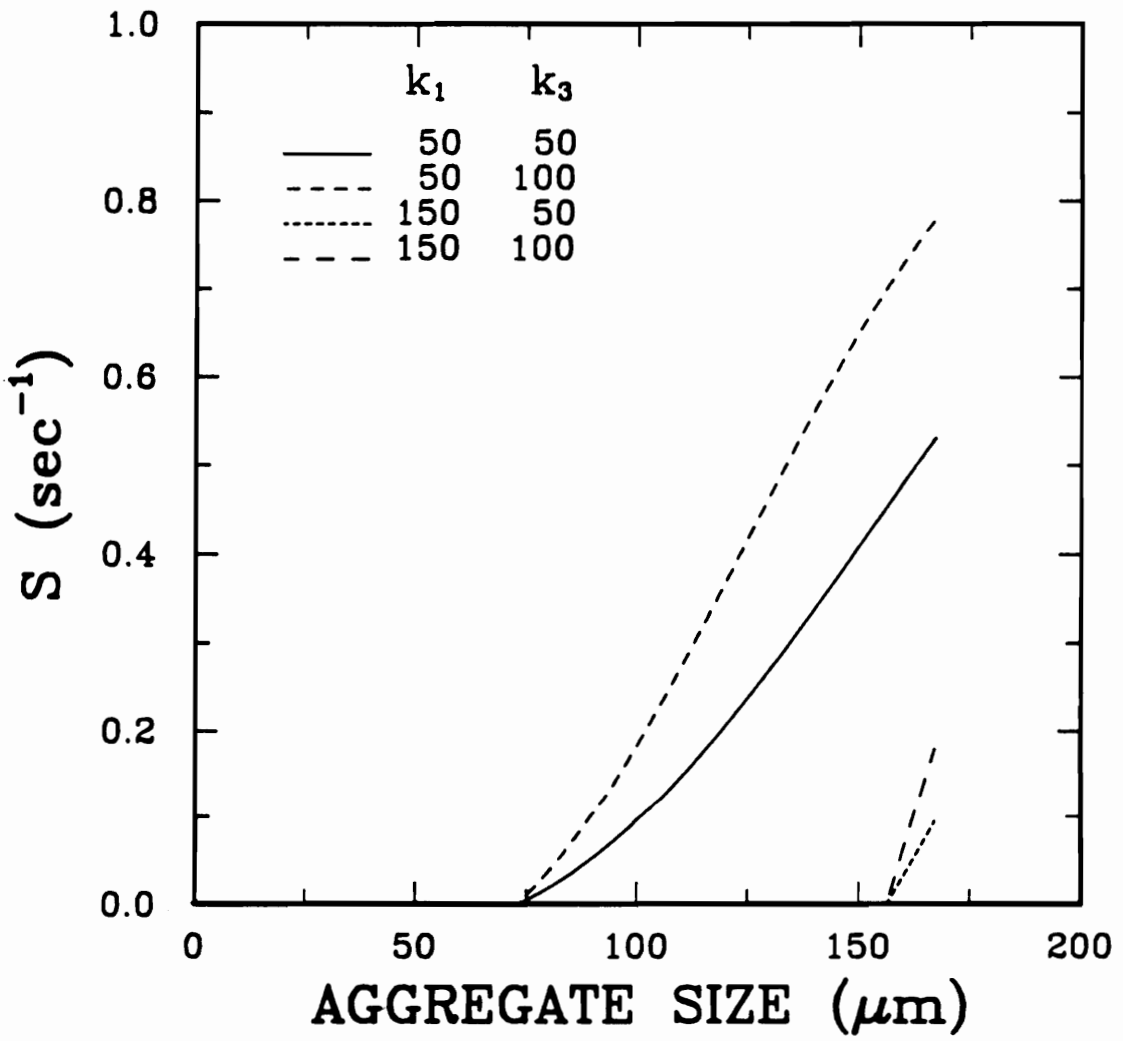


Figure 5.6. Variation of Breakage Rate Constant as a Function of Aggregate Size for Different Values of Model Parameters k_1 and k_3

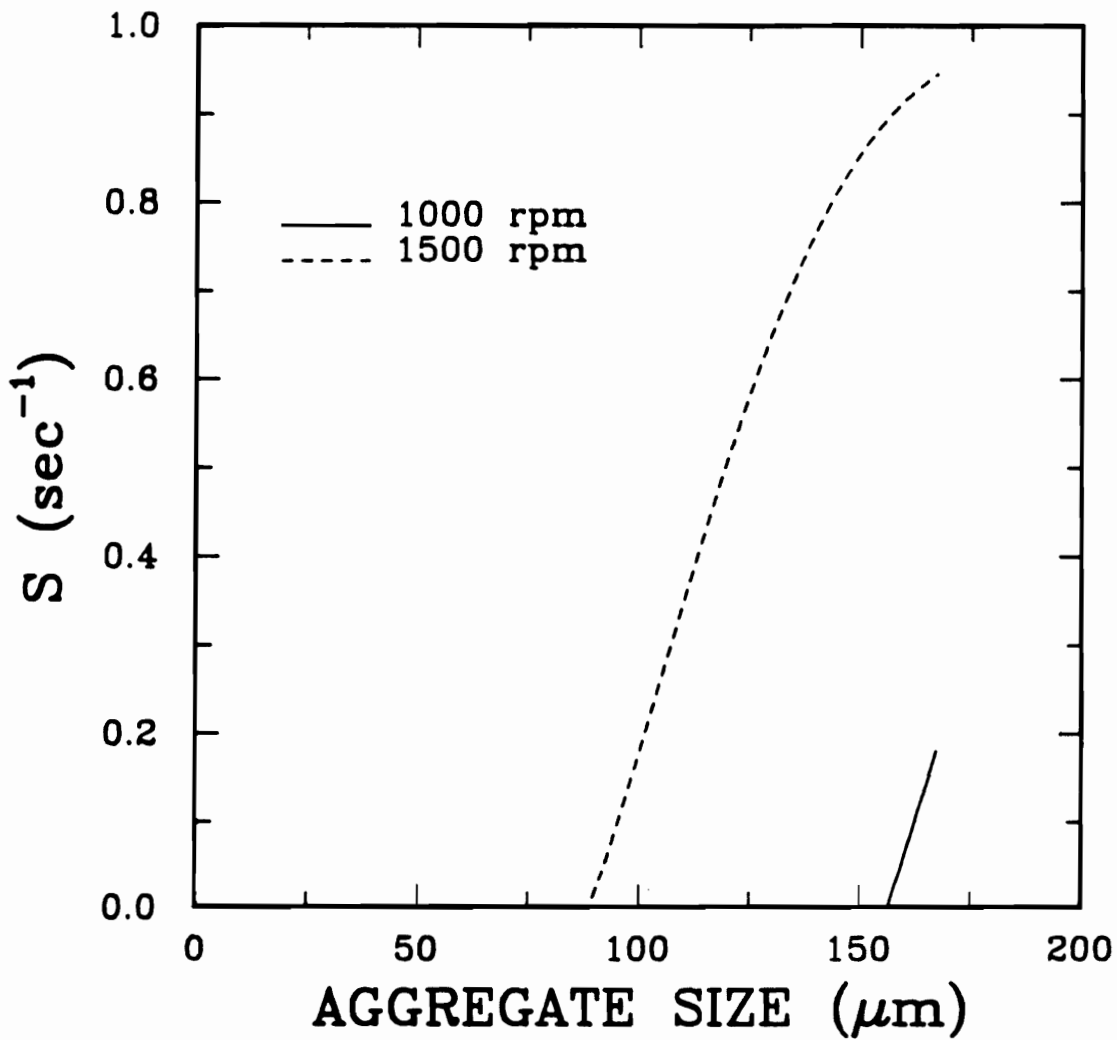


Figure 5.7. Variation of Breakage Rate Constant as a Function of Aggregate Size for Two Different Mixing Rates

$$k_1 = 150 \text{ sec}^{-1}; \quad k_3 = 100 \text{ dyne}^{-1}.$$

$B(a', a)$ is the number fraction of aggregates of size a that report into a size class of a' after their disintegration. To complete the description of the breakage event, it is necessary to know the distribution function of the fragments resulting from the breakage of a larger aggregate, known as the breakage function.

To date, there is not enough knowledge to help in deriving a theoretical aggregate breakage function. However, numerous studies on the breakage behavior that occurs in grinding processes have been conducted, from which various breakage modes have been developed (31-35). It is, therefore, helpful to analyze briefly the similarities and dissimilarities between the grinding process and the aggregate breakage process.

It is well known that erosion due to abrasion and splitting due to compression and chipping are the major mechanisms of breakage in a grinding mill. Therefore, the mechanisms of breakage in both processes are similar even though the forces that cause the breakage are different. It has also been found that grinding produces daughter particles that can be distributed over a continuous size spectrum. However, it is unlikely that the shear force provided by mixing in coagulation is strong enough to break the matrix of the particles. What usually happens is that the interparticle bonds break preferentially, forming a discrete size spectrum. Nevertheless, both processes will produce a particle spectrum where the top size is smaller than the size of the particles or aggregates from which the daughter particles result. Also the total solid mass of all the particles must be conservative after undergoing either size reduction process.

The above analysis shows that the breakage rates for both size reduction processes may differ significantly, but the breakage function appears similar. Therefore, it is reasonable to adopt the functional form of breakage function developed by grinding researchers to describe the aggregate breakage. In the present work, the Broadbent and Callcott breakage function (31) is used without considerable modifications to describe

the aggregate breakage function. For convenience, the aggregate number instead of aggregate size is used in the following:

$$B(z', z) = \frac{e^{-(z'-1)/z} - e^{-z'/z}}{1 - e^{-1}} \frac{z}{z'} , \quad [5.31]$$

where z and z' refer to z th- and z' th-fold aggregates, respectively. $B(z', z)$ in Equation [5.31] represents the fractional number of z' th-fold aggregates formed by the breakage of a z th-fold aggregate. It should be noted that a factor of (z/z') appears in Equation [5.31]. This is due to the fact that every z th-fold aggregate produces (z/z') z' th-fold daughter aggregates if all daughter aggregates are of the same aggregate number, z' . Apparently, the following relation is satisfied for the present breakage function:

$$\sum_{z'=1}^{\infty} B(z', z) = \sum_{z'=1}^{z-1} B(z', z) = z . \quad [5.32]$$

The first equality follows from Equation [5.33],

$$B(z', z) = 0, \quad z' \geq z , \quad [5.33]$$

indicating that all daughter aggregates must be smaller than the father aggregate. Equation [5.33] implicitly assumes that aggregates of a given size do not break into its own class, which is a sound assumption if the primary particles are of a mono size and the spectrum of aggregate size is classified in such a way that the aggregate in each successive class contains one more primary particle than the aggregate in the previous class. Although the above classification method takes more size classes to cover a wide size range, it does not suffer the rounding error of mass balance.

From the development of the aforementioned aggregate growth and breakage models, it is possible to develop a general model describing the dynamic behavior of coagulation under the mixing. For this purpose, the theorem of population balance will be applied to these rate processes in the next section.

5.6 Population Balance Model

As a general theorem, population balance has been widely used in any particulate system where many problems cannot be solved using usual continuity of mass and rate expressions (36-40). It has been found that particulate processes are unique in that the disperse phase is made up of a countable number of entities where these entities form a distribution of properties (36-38). The population balance as a basis for describing the behavior of such systems has been developed from the general conservation equation:

$$\text{Accumulation} = \text{Input} - \text{Output} + \text{Net Generation} . \quad [5.34]$$

In coagulation processes, the size evolution in a population of aggregates is of significant interest. Therefore, the aggregate size is the only property considered in the present population balance model. Applying the general theorem of Equation [5.34] to a closed system of coagulation processes under proper mixing conditions, the basic deterministic equation for the number balance of any fold aggregates, say z th-fold, is obtained as:

$$\begin{aligned} \frac{\partial n(z, t)}{\partial t} = & \frac{1}{2} \sum_{i=1}^{z-1} RC(z-i, i)n(z-i, t)n(i, t) - n(z, t) \sum_{i=1}^{\infty} RC(z, i)n(i, t) \\ & + \sum_{i=z+1}^{\infty} S(i)B(z, i)n(i, t) - S(z)n(z, t), \quad z = 3, 4, \dots \end{aligned} \quad [5.35]$$

The symbol of $n(z,t)$ for the number concentration of z th-fold aggregate in Equation [5.35] indicates the time dependence of concentration. The descriptions of all other symbols in Equation [5.35] are the same as those described in the above context.

The left-hand side of Equation [5.35] represents the change in the number concentration of z th-fold aggregates per unit time. This term is also referred to as an accumulation of z th-fold aggregates, which is equivalent to the left-hand side of Equation [5.34]. On the right-hand side of Equation [5.35], the first term accounts for the increase in the number concentration of z th-fold aggregates which are formed by binary aggregation of smaller aggregates and/or particles in this unit time interval, and the second term describes the decrease in the number concentration of z th-fold aggregates due to the binary combination of a z th-fold aggregate with the aggregate of any class, forming an aggregate larger than the z th-fold aggregate. These two terms in combination describe the aggregate growth behavior, and the other two terms on the right-hand side of Equation [5.35] collectively show the aggregate breakage behavior. The third term shows the appearance of a z th-fold aggregate by the breakage of a larger aggregate, and the fourth term represents the disappearance of the z th-fold aggregate due to its disintegration, forming a spectrum of smaller daughter aggregates. It can be readily seen that the right-hand side of Equation [5.35] corresponds to the net generation term of Equation [5.34]. Since the system in question is a closed system, both input and output terms must be zero. Thus, Equation [5.35] satisfies the general conservation theorem of Equation [5.34]. Equation [5.35] is similar to that derived by Vigil and Ziff (41) but in a discrete size spectrum.

In Equation [5.35], it is implicitly assumed that the aggregate can grow without any limitation on the aggregate size as indicated by the summation to infinity. It has been found experimentally that a characteristic finite maximum aggregate size exists for every coagulation system (42). It is therefore reasonable and practical to replace the

infinity sign in Equation [5.35] with a maximum aggregate number, N , which varies from one system to another.

Applying this general theorem to the primary particle, the dimer and the top aggregate classes yields the following equations:

$$\frac{\partial n(1,t)}{\partial t} = -n(1,t) \sum_{i=1}^N RC(1,i)n(i,t) + \sum_{i=2}^N S(i)B(1,i)n(i,t) , \quad [5.36]$$

$$\frac{\partial n(2,t)}{\partial t} = RC(1,1)n(1,t)^2 - n(2,t) \sum_{i=1}^N RC(2,i)n(i,t) + \sum_{i=3}^N S(i)B(2,i)n(i,t) - S(2)n(2,t) , \quad [5.37]$$

and

$$\frac{\partial n(N,t)}{\partial t} = \frac{1}{2} \sum_{i=1}^{N-1} RC(i,N-i)n(i,t)n(N-i,t) - n(N,t) \sum_{i=1}^N RC(i,N)n(i,t) - S(N)n(N,t) . \quad [5.38]$$

Equations [5.36], [5.37] and [5.38] can be interpreted in a similar way as interpreting Equation [5.35]. An additional constraint, Equation [5.39], should be imposed on Equations [5.35]-[5.38] in order to complete the description of a closed system of coagulation under mixing conditions:

$$\frac{\partial \sum_{z=1}^N zn(z,t)}{\partial t} = 0 . \quad [5.39]$$

Equation [5.39] indicates that the total mass of the solids in a system does not change with time, which is a common character of any closed system. It can be written in an integral form as:

$$\sum_{z=1}^N zn(z,t) = n(1,0) . \quad [5.40]$$

It should be noted that the above equations ([5.35]-[5.38]) have been derived from a macroscopic point of view where spatial dependence is suppressed. However, in the case of batch-operated coagulation where the system is well mixed, this approach turns out to be exact. These coagulation kinetic equations can also be obtained by using the universal microscopic population balance approach if the same assumption of a well-mixed, batch-operated system is made.

It is interesting to note that if the breakage event is neglected in these coagulation kinetic equations, the equations are simplified to a discrete form of the well-known Smoluchowski's coagulation equations (43-47). Therefore, the present model can be applied to more general coagulation systems while the model developed by Smoluchowski only accounts for special cases. It is also important to know that although the functional form describing aggregate growth kinetics is the same in the present model as in Smoluchowski's coagulation equation, the detailed information regarding calculation of the rate constants is different in each case.

5.7 Summary and Conclusions

The application of the deterministic population balance equation has been illustrated through the analysis of aggregate size distribution in a batch-operated coagulation system of isotropic turbulent flow. Theoretical models have been proposed to describe the aggregate growth and breakage dynamic behaviors. Both interparticle potential energy and kinetic energy have been considered in formulating the aggregation rate constant, which extends the classical colloidal stability theory to a more general form. The breakage rate process has been analyzed through the force balance by considering the internal adhesion force and the external shear force exerting on an aggregate. By including both aggregate growth and breakage rate processes in the population balance

model, a set of first-order non-linear differential equations has been derived to complete the description of coagulation kinetics, in which four adjustable parameters are involved to make the model more flexible. The importance of mixing intensity in the coagulation has been discussed through the model analysis of both rate processes. A model of aggregate structure has also been considered to account for the effects of the apparent density and porosity on the collision kinetic energy and frequency.

5.8 References

1. Strauss, M., Ring, T., Bleier, A. and Bowen, H.K., "The Effect of Particle Size Distribution on the Coagulation of Ceramic Suspensions," in *Particulate and Multiphase Processes (Colloidal and Interfacial Phenomena)*, ed. by Ariman, T. and Veziroglu, T.N., Hemisphere Publishing Corporation, 3 (1987).
2. Spielman, L.A., "Viscous Interactions in Brownian Coagulation," *J. Colloid Interface Sci.*, 33, 562 (1970).
3. Honig, E.P., Roeberson, G.J. and Wiersema, P.H., "Effect of Hydrodynamic Interaction on the Coagulation Rate of Hydrophobic Colloids," *J. Colloid Interface Sci.*, 36, 97 (1971).
4. Curtis, A.S.G. and Hocking, L.M., "Collision Efficiency of Equal Spherical Particles in a Shear Flow," *Trans. Far. Soc.*, 66, 1381 (1970).
5. van de Ven, T.G.M. and Mason, S.G., "The Microrheology of Colloidal Dispersions VII. Orthokinetic Doublet Formation of Spheres," *Colloid Polym. Sci.*, (1977).
6. Fuchs, N., "Effect of the Charge of Aerosols on Their Stability," *Z. Physik*, 89, 736 (1934).
7. Verwey, E.J.W. and Overbeek J. Th. G., *Theory of the Stability of Lyophobic Colloids*, Elsevier, Amsterdam, (1948).
8. Spielman, L.A., "Hydrodynamic Aspects of Flocculation," in *The Scientific Basis of Flocculation*, ed. by Ives, K.J., Sijthoff & Noordhoff, (1978).
9. Kim, Y.H. and Glasgow, L.A., "Simulation of Aggregate Growth and Breakage in Stirred Tanks," *Ind. Eng. Chem. Res.*, 26, 1604 (1987).
10. Tambo, N. and Hozumi, H., "Physical Characteristics of Floccs-II. Strength of Flocc," *Water Research*, 13, 421 (1979).

11. Fair, G.M. and Gemmel, R.S., "A Mathematical Model of Coagulation, *J. Colloid Sci.*, 19, 360 (1964).
12. Parker, D.S., Kaufman, W.J. and Jenkins, D., "Floc Breakup in Turbulent Flocculation Processes," *J. Sanitary Eng. Div., ASCE*, 102, 79 (1972).
13. Pandya, J.D. and Spielman, L.A., "Floc Breakage in Agitated Suspensions: Theory and Data Processing Strategy," *J. Colloid Interface Sci.*, 90, 517 (1982).
14. Vold, M.J., "Computer Simulation of Floc Formation in a Colloidal Suspension," *J. Colloid Sci.*, 18, 684 (1963).
15. Goodarz-Nia, I., "Floc Density, Porosity and Void Ratio in Colloidal Systems and Aerosols," *J. Colloid Interface Sci.*, 62, 131 (1977).
16. Tambo, N. and Watanabe, Y., "Physical Characteristics of Floccs-I. The Floc Density Function and Aluminium Floc," *Water Research*, 13, 409 (1979).
17. Hogg, R., "Modelling of Porous Agglomerate Formation and Growth," *Proceedings, Third International Symposium on Agglomeration*, Nuremberg, West Germany, May (1981).
18. Delichatsios, M.A. and Probstein, R.F., "Coagulation in Turbulent Flow: Theory and Experiment," *J. Colloid Interface Sci.*, 51, 394 (1974).
19. Sastry, K.V.S. and Fuerstenau, D.W., "Size Distribution of Agglomerates in Coalescing Dispersed Phase Systems," *Ind. Eng. Chem. Fundam.*, 9, 145 (1970).
20. Nagata, S., *Mixing: Principles and Applications*, Halsted Press, New York, (1975).
21. Hogg, R., Healy, T.W. and Fuerstenau, D.W., "Mutual Coagulation of Colloidal Dispersions," *Trans. Faraday Soc.*, 62, 1638 (1966).
22. Usui, S. and Hachisu, S., "Interaction of Electrical Double Layers and Colloid Stability," in *Surfactant Sci. Ser. (Electrical Phenomena at Interfaces)*, 15, 47 (1984).
23. Sonntag, H. and Strenge, K., *Coagulation Kinetics and Structure Formation*, Plenum Press, New York, (1978).
24. Glasgow, L.A., Kim, Y.H. and Hsu, Y.P., "Aggregate Growth and Breakage in Inhomogeneous Turbulence," in *Particulate and Multiphase Processes (General Particulate Phenomena)*, ed. by Ariman, T. and Veziroglu, T.N., Hemisphere Publishing Co., New York, 1, 539 (1988).
25. Hsu, J.P. and Glasgow, L.A., "Floc Size Reduction in the Turbulent Environment," *Particulate Sci. Tech.*, 1, 205 (1983).
26. Ham, R.K. and Christman, R.F., "Agglomerate Size Changes in Coagulation," *J. San. Engr. Div. ASCE*, 95, 481 (1969).

27. Sonntag, R.C. and Russel, W.B., "Structure and Breakup of Floccs Subjected to Fluid Stresses I. Shear Experiments," *J. Colloid Interface Sci.*, 113, 399 (1986).
28. Levich, V.G., *Physicochemical Hydrodynamics*, Prentice-Hall Inc., Englewood Cliffs, N.J., (1962).
29. Argaman, Y. and Kaufman, W.J., "Turbulence and Flocculation," *J. Sanitary Eng. Div., ASCE*, 96, 223 (1970).
30. Thomas, D.G., "Turbulent Disruption of Floccs in Small Particle Size Suspension," *AICHE J.*, 10, 517 (1964).
31. Broadbent, S.R. and Callcott, T.G., "Coal Breakage Processes," *J. Institute Fuel*, 29, 524 (1956).
32. Lynch, A.J., et al., *Mineral Crushing and Grinding Circuits*, Elsevier Scientific Publishing Co., New York, (1977).
33. Austin, L.G., Klimpel, R.R. and Luckie, P.T., *Process Engineering of Size Reduction: Ball Milling*, AIME, Inc., New York, N.Y., (1984).
34. Herbst, J.A. and Fuerstenau, D.W., "The Zero Order Production of Fine Sizes in Comminution and Its Implications in Simulation," *Trans. SME-AIME*, 241, 538 (1968).
35. Herbst, J.A., Grandy, G.A., and Fuerstenau, D.W., "Population Balance Models for the Design of Continuous Grinding Mills," in *Proc. X Int. Miner. Processing Congr. (London)*, ed. by Jones, M.J., The Institute of Mining and Metallurgy, 23 (1974).
36. Hulbert, H.M. and Katz, S., "Some Problems in Particle Technology: A Statistical Mechanical Formulation," *Chem. Eng. Sci.*, 19, 555 (1964).
37. Randolph, A.D., "A Population Balance for Countable Entities," *The Canadian J. of Chem. Eng.*, 42, 280 (1964).
38. Herbst, J.A., "Rate Processes in Multiparticle Metallurgical Systems," in *Rate Processes of Extractive Metallurgy*, ed. by Sohn, H.Y. and Wadsworth, M.E., Plenum Press, New York, (1979).
39. Lee, C.H., Erickson, L.E. and Glasgow, L.A., "Dynamics of Bubble Size Distribution in Turbulent Gas-Liquid Dispersions," *Chem. Eng. Comm.*, 61, 181 (1987).
40. Sastry, K.V.S. and Gaschignard, P., "Discretization Procedure for the Coalescence Equation of Particulate Processes," *Ind. Eng. Chem. Fundam.*, 20, 355 (1981).
41. Vigil, R.D. and Ziff, R.M., "On the Stability of Coagulation-Fragmentation Population Balances," *J. Colloid Interface Sci.*, 133, 257 (1989).
42. Tambo, N. and Watanabe, Y., "Physical Aspect of Flocculation Process-I. Fundamental Treatise," *Water Research*, 13, 429 (1979).

43. Smoluchowski, M. V., "drei Vortrage uber Diffusion, Brownsche Molekularbewegung und Koagulation von Kolloidteilchen," *Z. Phys.*, 17, 557 (1916).
44. Smoluchowski, M.V., "Versuch einer Mathematischen Theorie der Koagulationskinetik Kolloide Losungen," *Z. Phys. Chem.*, 92, 129 (1917).
45. Friedlander, S.K., *Smoke, Dust and Haze*, Wiley-Interscience, New York, (1977).
46. Valioulis, I.A., "Coagulation in the Aquatic Environment: Theory and Practice," *Adv. Colloid Interface Sci.*, 24, 81 (1986).
47. Overbeek, J.Th.G., "Kinetics of Flocculation," in *Colloid Science*, ed. by Kruyt, H.R., Elsevier, Amsterdam, 1, 278 (1952).

CHAPTER 6 A SIMULATION OF THE COAGULATION PROCESS

6.1 Introduction

In the preceding chapter, a set of generalized equations of coagulation kinetics has been derived for the discrete size spectrum from the theoretical point of view. In order to study the coagulation kinetics, however, this set of equations needs to be solved. Since there is no simple functional form to describe the aggregate birth and death rate constants as a function of aggregate size, properties of the system, geometry of the unit and the operation conditions, it is impossible to obtain a general, explicit, and time-dependent solution to the kinetic equations of coagulation, i.e., equations [5.35], [5.36], [5.37], [5.38] and [5.39] (1-6). Analytical solutions are possible only for very special systems where either a constant rate constant (7-8) or a rate constant of simple functional form (1-2, 9-10) is assumed. However, it is still very difficult to get the analytical solutions for the coagulation under the mixing where the breakage of aggregates is important. It has been pointed out by Vigil and Ziff (6) that a system described by equations [5.35], [5.36], [5.38], and [5.39] cannot, in general, reach a dynamic equilibrium in which detailed balance is satisfied. For a stable system, which has steady state solutions to coagulation kinetic equations, the study of dynamic behavior of coagulation using analytical method has been proven to be very difficult even under simplified conditions. It

is, however, practical to solve those first order nonlinear ordinary differential equations of coagulation kinetics using numerical methods.

In this chapter, numerical procedures have been described based on the model developed in Chapter 5. Using the proposed numerical technique, the coagulation process has been simulated by monitoring the aggregate size evolution. The influence of model parameters on the simulation results has been studied to have a better understanding on the model. The system conditions such as mixing intensity, surface potential, and surface hydrophobicity have been examined by the simulation to study the effect of these operation variables on the coagulation performance. Although the discussion has been focused on the qualitative comparison between simulation predictions and the experimental results, the aggregate size distribution measured using classical Andreasen pipette technique has been presented as a comparison for the simulation results.

6.2 Numerical Procedures

In order to solve the coagulation kinetic equations numerically, it is important to define the size classes over the size spectrum of interest. For a system of mono size primary particles, it is convenient to define size class based on the number of particles composing the aggregates. In the present work, the classes are defined in such a way that any aggregate in every successive class contains one more primary particle than it does in its previous class. It is obvious that each class has a constant property of aggregate number. It requires a large number of classes, say 500 classes (11), to cover the size spectrum of interest using this method. However, this scheme of classification is more convenient as will be shown later in this chapter. This method also gives a more accurate mass balance in the simulation since all the aggregates in the same class have

identical solid mass. With the classes being specified, the porosity for each class is calculated using the Equations [5.7], [5.2] and [5.6], successively, while the equivalent spherical aggregate size is calculated using Equation [5.8] in which the porosities have been previously obtained.

The interaction energy barrier, V_{\max} , and the critical film thickness, H_m , between particles of each pair of classes are then calculated by finding the maximum value of Equation [4.7] and its location. In these calculations, the particle sizes are replaced by the corresponding spherical aggregate sizes, and the zeta potential and Hamaker constant of the aggregates are assumed to be the same as that of the primary particles. The kinetic energy, V_k , for the aggregates of each pair of classes at the separation of critical film thickness is calculated using Equation [4.10]. The reduced mass of interacting aggregates is calculated from the apparent masses of individual equivalent spherical aggregates, which include the masses of solids and inclusion water. The relative velocity between two approaching aggregates is then calculated using Equation [5.9] or [5.10], depending on whether the flow of suspension is viscous dissipation or inertial convection in nature, where the energy dissipation rate per unit mass of suspension is calculated using the procedures as described in Appendix I. With the obtained energy barriers and kinetic energies, the collision efficiency between aggregates of each pair of classes is calculated using Equation [5.17] or [5.18]. Coagulation rate constants for each pair of aggregates of any two different classes is then calculated using Equation [5.21] or [5.22].

In the calculation of the breakage rate constants, the adhesion force and breakup force are calculated using Equations [5.25] and [5.27] or [5.28], respectively. The breakage rate constant is calculated for each class using Equation [5.29] or [5.30] with parameters of A and k_3 being fixed at the reasonable values. Finally, the daughter aggregate distribution function of aggregate breakage is calculated for each class using Equation [5.31].

After predeterminations and calculations of all parameters and constants, the coagulation kinetic equations, i.e., Equations [5.35]-[5.38], are solved numerically using the backward differentiation formula called Gear's stiff method (12), which has been coded as a standard subroutine in IMSL package. From the trial and fail tests, it has been found that the problem is very stiff. Therefore, it is necessary to provide a subroutine with a user's Jacobian matrix to get the solution for the problem (12). The general Jacobian matrix has the form of the following equation:

$$J = \begin{bmatrix} \frac{\partial f_1}{\partial n(1)} & \frac{\partial f_1}{\partial n(2)} & \cdots & \frac{\partial f_1}{\partial n(N)} \\ \frac{\partial f_2}{\partial n(1)} & \frac{\partial f_2}{\partial n(2)} & \cdots & \frac{\partial f_2}{\partial n(N)} \\ \cdot & \cdot & \cdots & \cdot \\ \cdot & \cdot & \cdots & \cdot \\ \frac{\partial f_N}{\partial n(1)} & \frac{\partial f_N}{\partial n(2)} & \cdots & \frac{\partial f_N}{\partial n(N)} \end{bmatrix} \quad [6.1]$$

In Equation [6.1], f_z represents the left hand sides of Equations [5.35], [5.36], [5.37] and [5.38]. The elements of the above Jacobian matrix, J_{zj} , can be expressed explicitly by differentiating z th ordinary differential equation with respect to the concentration of j th-fold aggregate as given collectively in the following:

$$J_{11} = \frac{\partial f_1}{\partial n(1)} = -2k(1,1)n(1) - \sum_{i=2}^N k(1,i)n(i), \quad [6.2]$$

$$J_{1i} = \frac{\partial f_1}{\partial n(i)} = -k(1,i)n(1) - B(1,i)S(i), \quad i = 2, \dots, N \quad [6.3]$$

$$J_{21} = \frac{\partial f_2}{\partial n(1)} = 2k(1,1)n(1) - k(2,1)n(2), \quad [6.4]$$

$$J_{22} = \frac{\partial f_2}{\partial n(2)} = -k(2,1)n(1) - 2k(2,2)n(2) - \sum_{i=3}^N k(2,i)n(i) - S(2) \quad [6.5]$$

$$J_{2i} = \frac{\partial f_2}{\partial n(i)} = -k(2,i)n(2) - B(2,i)S(i), \quad i = 3, \dots, N \quad [6.6]$$

$$J_{zz} = \frac{\partial f_z}{\partial n(z)} = - \sum_{i=qz} k(z,i)n(i) - 2k(z,z)n(z) - S(z), \quad z = 3, \dots, N-1 \quad [6.7]$$

$$J_{zi} = \frac{\partial f_z}{\partial n(z)} = k(i,z-i)n(z-i) - k(z,i)n(z), \quad z > i, \quad i = 1, \dots, z-1 \quad [6.8]$$

$$J_{zi} = \frac{\partial f_z}{\partial n(i)} = -k(z,i)n(z) + B(z,i)S(i), \quad z < i, \quad i = z+1, \dots, N \quad [6.9]$$

$$J_{Ni} = \frac{\partial f_N}{\partial n(i)} = k(N-i,i)n(N-i) - k(N,i)n(N) \quad i = 1, 2, \dots, N-1, \quad [6.10]$$

$$\text{and} \quad J_{NN} = \frac{\partial f_N}{\partial n(N)} = -2k(N,N)n(N) - \sum_{i=1}^{N-1} k(N,i)n(i). \quad [6.11]$$

By incorporating the above Jacobian matrix into the IMSL subroutine, the coagulation kinetic equations are solved at each given time interval. The solutions are then tested using the constraint equation, i.e., Equation [5.39], for the acceptance of the results. If the relative error is larger than a given value, the solutions are rejected and the time interval is reduced for another try, otherwise, the solutions are accepted and sent to the output device. The steady state is then checked by comparing the total number of aggregates of two successive runs. If the steady state is recognized, the program is terminated. Otherwise, the numerical solution will start again with a new starting time which is the ending time of the previous run, unless the desired time range has been covered. The numerical procedures described previously can be summarized by the

schematic flow chart, as given in Figure 6.1, with the program being given in Appendix II.

6.3 A Typical Example of Simulation

Using the numerical procedures proposed in the preceding section, the aggregate size distribution as a function of evolution time has been simulated for a fine coal particle suspension mixed at 1000 rpm and the results are given in Figure 6.2. The zeta potential value of -43 mV , Hamaker constant of $6.07 \times 10^{-20} \text{ J}$, and hydrophobic interaction parameter of -1.247 mJ/m^2 as determined at critical coagulation pH have been used in this simulation. A solid/water interfacial tension of 26.72 dyne/cm as determined from contact angle measurement has also been used. The values of other model parameters for calculating the collision efficiency and breakage rate have been chosen so that a reasonable dynamic equilibrium aggregate size distribution can be obtained. They are $0.138 (kT)^{-1}$, 139.89 , 507.38 dyne^{-1} and $1 \times 10^5 \text{ sec}^{-1}$, with respect to β , k_1 , k_3 and A .

Figure 6.2 shows that starting with mono size primary particles of $5 \mu\text{m}$, three distinct size zones are developed as the coagulation proceeds. The first size zone covers 5 to $26.7 \mu\text{m}$ size range. This zone is characterized by relative low coagulation rate constants. Its existence is due to the breakage of the larger aggregates of zone 3. Following this first zone, a second zone is developed with evolution of coagulation time, which is characterized with a coagulation rate larger than its breakage rate. This zone covers a wide range of the aggregate size, from $29.6 \mu\text{m}$ to $99 \mu\text{m}$. Most aggregates formed fall in this zone. The wide range of aggregate size covered by this zone shows that the aggregates formed under severe shear conditions differ significantly in size. The last zone starts from aggregate size of $100 \mu\text{m}$. Inside this zone, only random aggregates are pos-

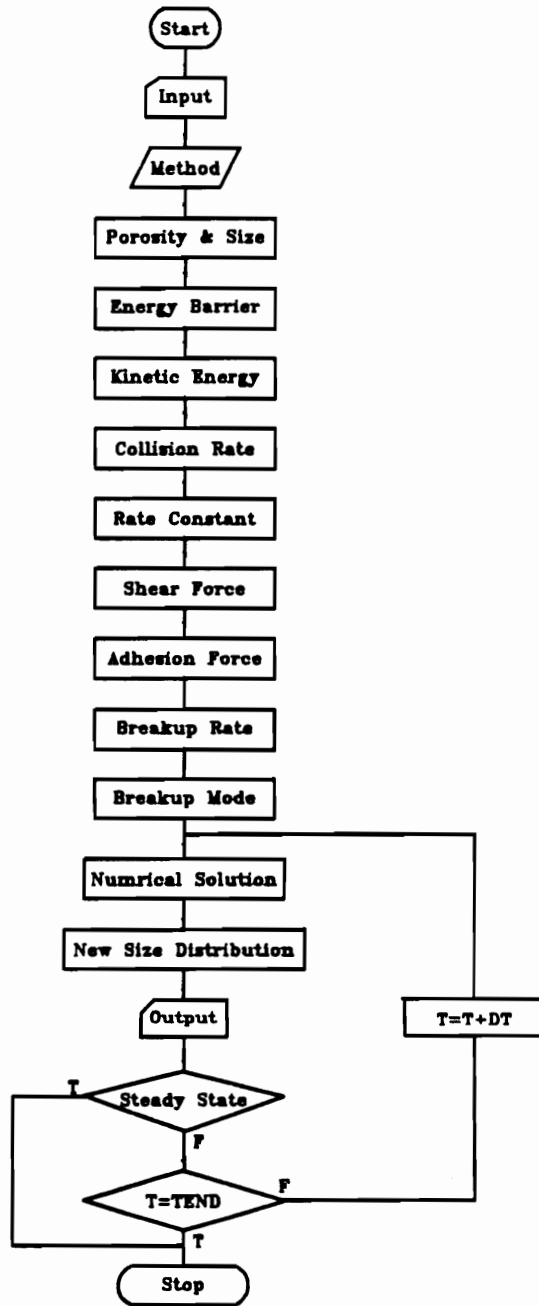


Figure 6.1. Schematic Diagram of the Computer Program for Simulating Coagulation Kinetic Behaviors

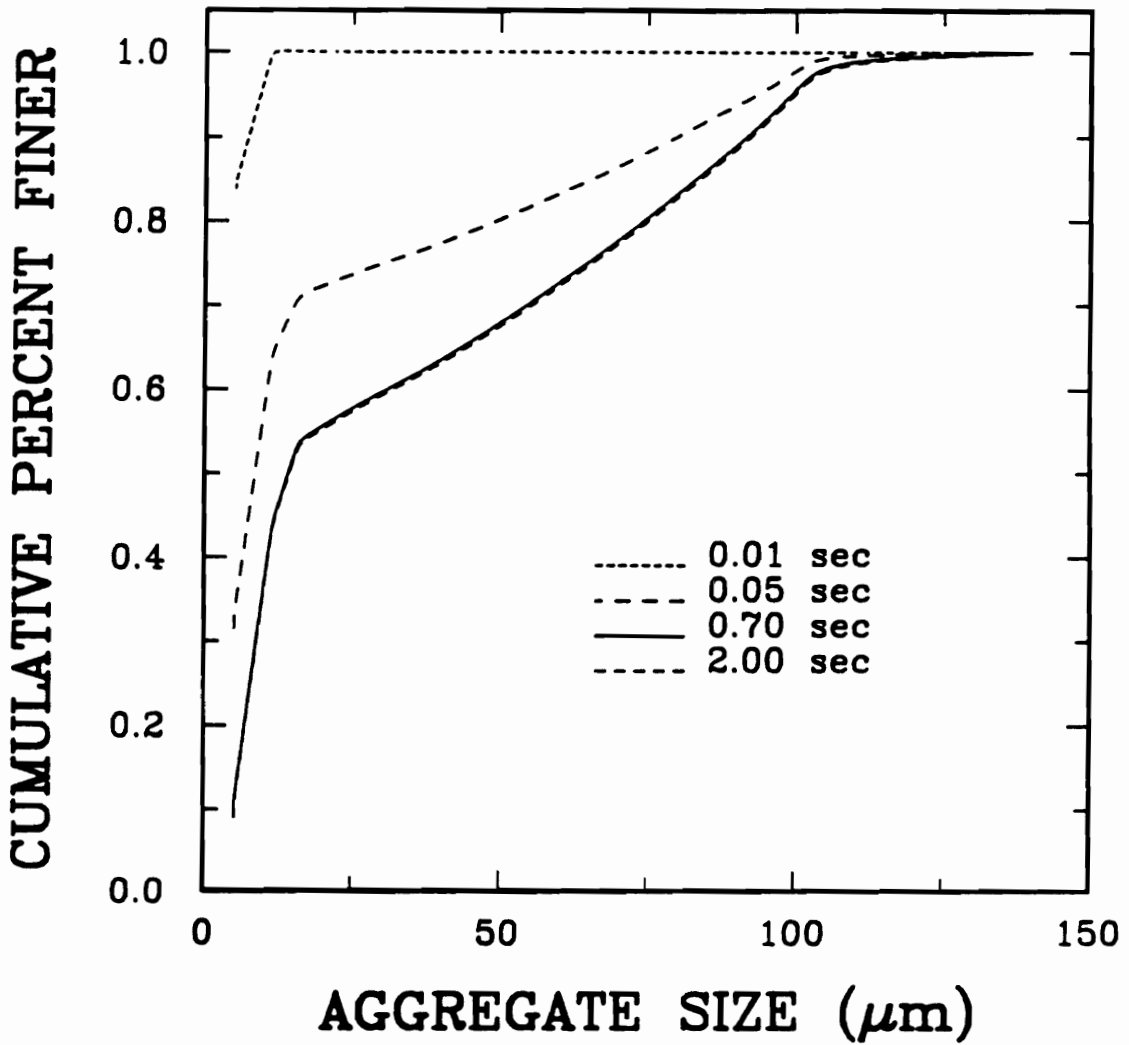


Figure 6.2. Cumulative Aggregate Size Distributions of Fine Coal Particles at Various Coagulation Time

$\beta = 0.138 (kT)^{-1}$;	$k_1 = 139.89$;	$k_3 = 507.38 \text{ dyne}^{-1}$;
$A = 1.0 \times 10^5 \text{ sec}^{-1}$;	Mixing = 1000 rpm;	$\zeta = -43 \text{ mV}$;
$A_{131} = 3.31 \times 10^{-21} \text{ J}$;	$C = -1.247 \text{ mJ/m}^2$;	$\gamma_{sw} = 26.72 \text{ dyne/cm}$.

sible to form since the breakage rate of aggregates in this zone is much greater than their formation rate. Therefore, upon formation, the aggregates break into a spectrum of daughter aggregates of smaller size.

Figure 6.2 also shows that after 0.7 seconds, the aggregate size distribution does not change significantly as the coagulation proceeds further. This finding suggests that coagulation under severe mixing conditions reaches its equilibrium in a short time period, indicating the experimental difficulties of kinetic studies of coagulation with severe mixing.

The variation of mass fraction of the aggregates in each individual size class has also been traced as a function of coagulation time in this simulation. In Figure 6.3, the typical patterns are shown for sizes of primary particles and the aggregates of size ranging from 5.0 to 11.7 μm and from 89.6 to 100.2 μm . Figure 6.3 clearly shows that the total mass of the primary particles continues decreasing significantly as the coagulation proceeds to 0.7 seconds, and after that it levels off at 9 percent.

Unlike the primary particles, the mass fraction of the aggregates in the 5.0 to 11.7 μm size range increases at the very beginning of coagulation, reaching its maximum at 0.03 seconds. During this period of coagulation, the aggregate formation of this size range by binary aggregation of the primary particles and the aggregate of smaller size is dominating since the number of the aggregates in this size range is not sufficient in this period for inducing the formation of any higher order aggregates. Upon reaching a certain number of aggregates in this size range, the aggregation between the primary particles or aggregates of smaller size and the aggregates of this size range begins at a rate greater than that of the formation of aggregates falling in this size range. As a result, the mass fraction of the aggregates starts decreasing, which is a common phenomenon in coagulation. However, it is interesting to note that at a certain coagulation time, the mass fraction of the aggregates in this size range reaches a minimum, and after

that, it starts increasing slightly. Eventually, it levels off after the coagulation time of 0.7 seconds. This behavior may be attributed to the disintegration of larger aggregates. These characteristics will disappear if the breakage event is neglected in the population balance model as will be illustrated in detail in the later section of this chapter. The time at which the mass fraction of the aggregates in this size range starts increasing again may be considered as the time at which substantial breakage of the aggregates of larger size begins.

The mass fraction of aggregates with sizes in the range of 89.6 and 100.2 μm does not show any change until 0.03 seconds at which time the mass fraction of the aggregates in the size range of 5.0 to 11.7 μm reaches maximum. After that time, it increases to a certain value and then levels off at a coagulation time of 0.7 seconds, having reached a dynamic equilibrium state.

6.4 Simulations with Varying Model Parameters

To examine the response of simulation results to each model parameter, the effects of each model parameters, such as β , k_1 , k_3 and A , on the coagulation kinetic behavior and ultimate aggregate size distributions, have been studied through the simulation. The results are given collectively in Figures 6.4 to 6.11.

6.4.1 *Effect of Model Parameter β on Coagulation Kinetics*

It is convenient to define a dimensionless number concentration as a ratio of the total number of aggregates in unit volume at any time, t , to that at time 0. Although this quantity does not give any detailed information about aggregate size distribution, it does provide a simple way to present a general idea as to the coagulation against

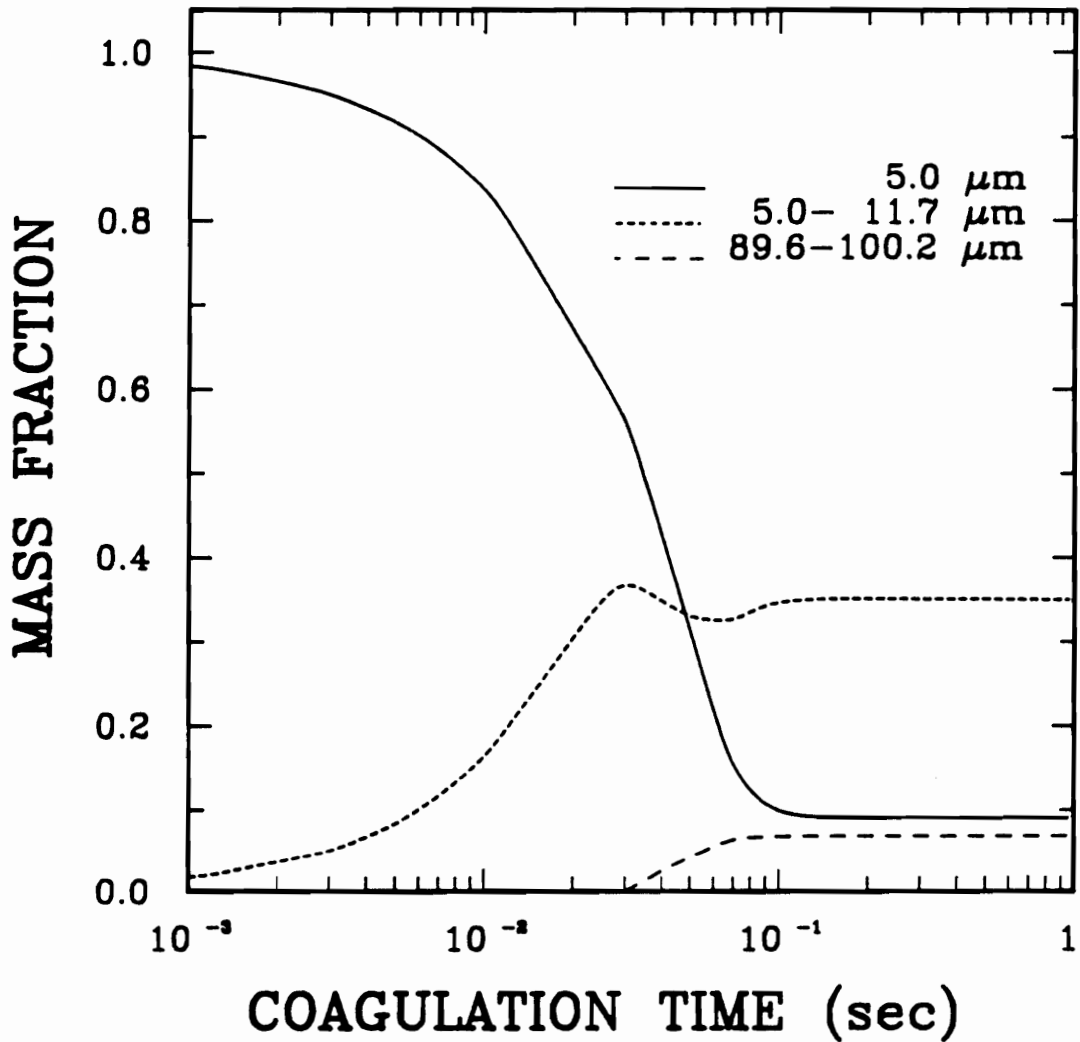


Figure 6.3. Changes of Mass Fraction of Primary Particles and Aggregates in Different Size Ranges as a Function of Coagulation Time

$\beta = 0.138 (kT)^{-1}$;	$k_1 = 139.89$;	$k_3 = 507.38 \text{ dyne}^{-1}$;
$A = 1.0 \times 10^5 \text{ sec}^{-1}$;	Mixing = 1000 rpm;	$\zeta = -43 \text{ mV}$;
$A_{131} = 3.31 \times 10^{-21} \text{ J}$;	$C = -1.247 \text{ mJ/m}^2$;	$\gamma_{sw} = 26.72 \text{ dyne/cm}$.

dispersion and reflect the kinetic behavior of coagulation systems. A smaller value of this quantity indicates a better coagulation.

In Figure 6.4, the dimensionless number concentration is given as a function of coagulation time. This figure shows that with other model parameters and system variables being the same, an increase in the value of model parameter β slows down the coagulation kinetics as expected theoretically. By increasing the value of model parameter β , the collision efficiency decreases as indicated in Equation [5.18] and illustrated in Figure 5.3. Therefore, the proportion of collisions which result in aggregation is reduced. As a result, a longer coagulation time is required to reach the equilibrium as found in the simulation.

It is interesting to note that upon reaching the equilibrium, the dimensionless number concentration has almost the same value regardless of the values of model parameter β as used in the simulation, indicating that there is no significant effect on the final aggregate size distribution by the value of model parameter β . This behavior is more clearly shown in Figure 6.5 where the equilibrium aggregate size distributions are given for different values of model parameter β .

Figure 6.5 shows that the equilibrium aggregate size distributions for three different values of model parameter β are almost identical. It is not difficult to understand that the values of model parameter β only affect the aggregation rate constant of those pairs of particles or aggregates whose kinetic energy is less than the interaction energy barrier. Since the kinetic energy obtained by the particles or aggregates of small size is usually less than the interaction energy barrier, the aggregation rate constants between those particles and aggregates are reduced as the value of model parameter β increases. However, the aggregation rate constants for the pairs of particles or aggregates, whose kinetic energy is greater than the energy barrier, are not affected by changing the value of model parameter β , because the collision efficiency is considered as unity in these

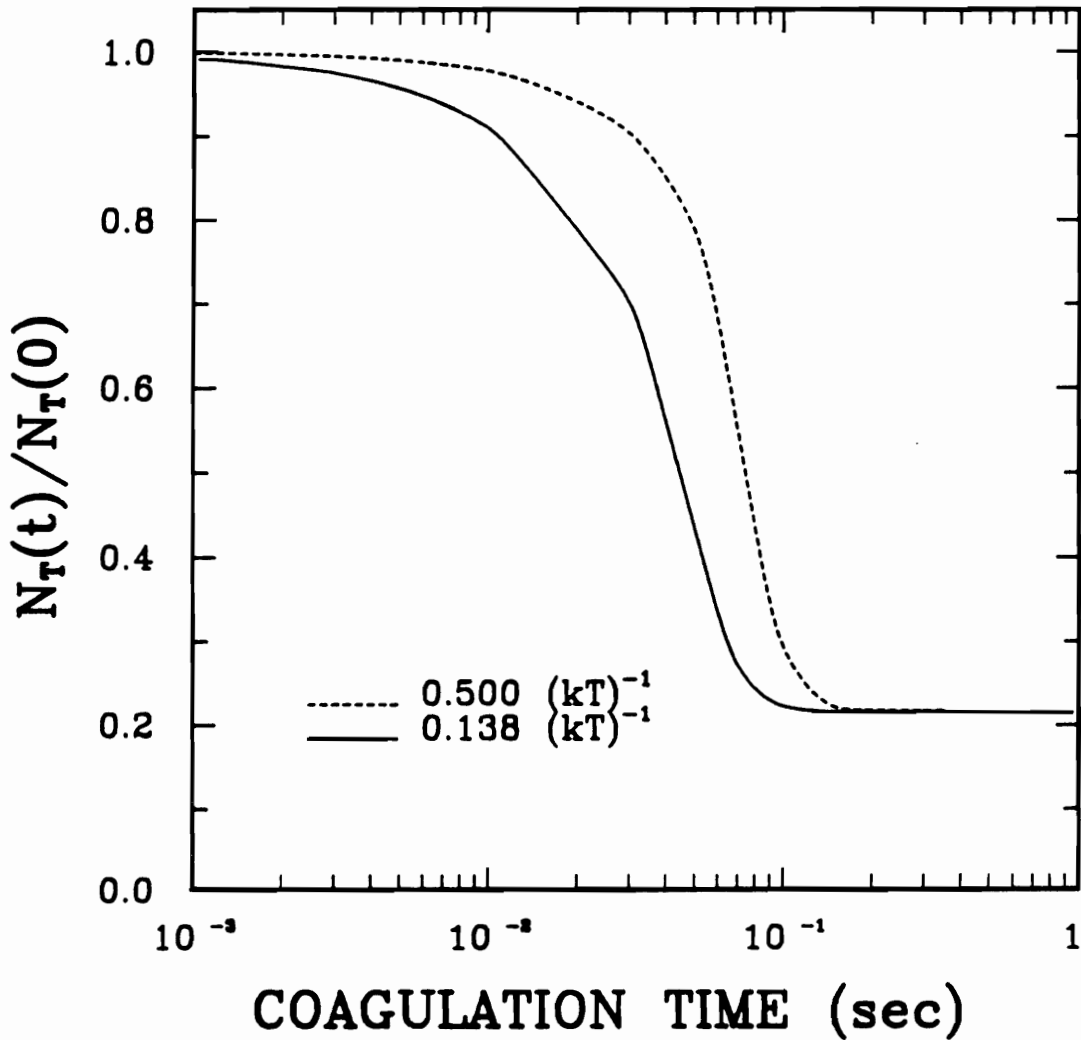


Figure 6.4. Changes of Dimensionless Number Concentration as a Function of Coagulation Time for Different β Values

$k_1 = 139.89$;	$k_3 = 507.38 \text{ dyne}^{-1}$;	$A = 1.0 \times 10^5 \text{ sec}^{-1}$;
Mixing = 1000 rpm;	$\zeta = -43 \text{ mV}$;	$A_{131} = 3.31 \times 10^{-21} \text{ J}$;
$C = -1.247 \text{ mJ/m}^2$;	$\gamma_{sw} = 26.72 \text{ dyne/cm}$.	

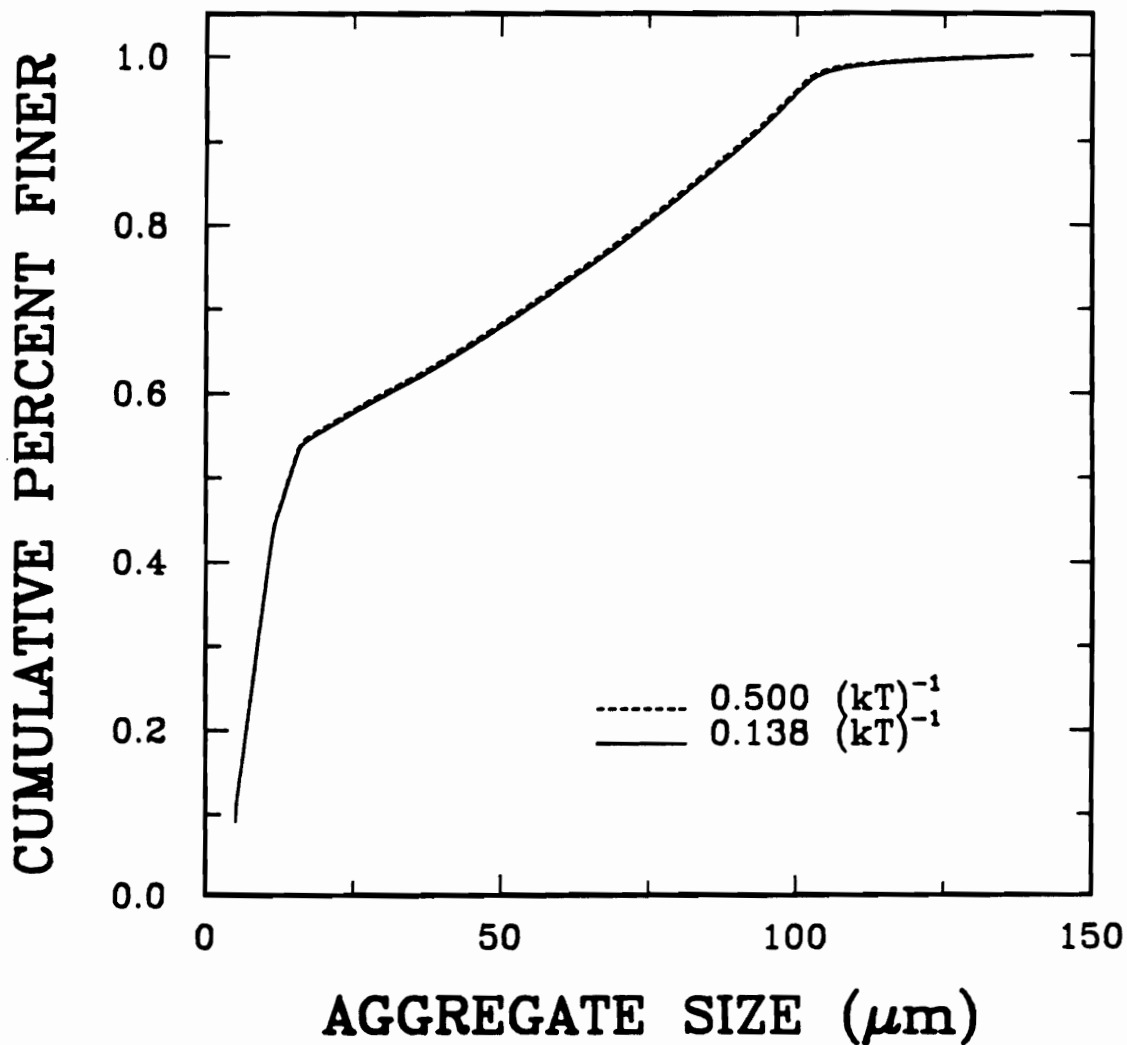


Figure 6.5. Equilibrium Cumulative Aggregate Size Distributions for Two Different β Values

$k_1 = 139.89;$	$k_3 = 507.38 \text{ dyne}^{-1};$	$A = 1.0 \times 10^5 \text{ sec}^{-1};$
$\text{Mixing} = 1000 \text{ rpm};$	$\zeta = -43 \text{ mV};$	$A_{131} = 3.31 \times 10^{-21} \text{ J};$
$C = -1.247 \text{ mJ/m}^2;$	$\gamma_{sw} = 26.72 \text{ dyne/cm}.$	

cases. Therefore, it takes a longer time for a certain amount of smaller aggregates to form when the aggregation rate constant is reduced due to the increase of the value of model parameter β . As soon as the aggregation between primary particles or small aggregates and larger aggregates previously formed begins, it dominates the consumption of primary particles and smaller aggregates since the aggregation rate constants are much greater in this case. As a result, the value of model parameter β has no effect on the equilibrium aggregate size distribution since it does not affect the aggregation rate constant of these size ranges. This finding suggests that the true value of model parameter β can only be evaluated from coagulation kinetic studies.

6.4.2 *Effect of Model Parameter k_1 on Coagulation Kinetics*

The dimensionless number concentration of a suspension mixed at 800 rpm has been simulated by using different values of the model parameter k_1 to study the effect of this model parameter on coagulation kinetics. The results given in Figure 6.6 show that increasing the value of parameter k_1 only slightly affects the coagulation kinetic behavior, but the total number of aggregates at steady state decreases significantly.

As discussed earlier, a higher value of parameter k_1 corresponds to a more compact aggregate structure, which gives rise to a larger number of contacts per particle and a higher value of contact area per contact. In this case, the binding forces between particles are much stronger, resulting in a reduced breakage rate constant as indicated in Equations [5.25] and [5.30]. Therefore, it is not surprising to observe that the increased k_1 value causes the equilibrium aggregate size distribution to shift in the direction of increasing aggregate size as shown in Figure 6.7.

Figure 6.7 also shows that by changing the model parameter k_1 , the equilibrium aggregate size distribution function varies significantly. A distinct zone of 3 observed in

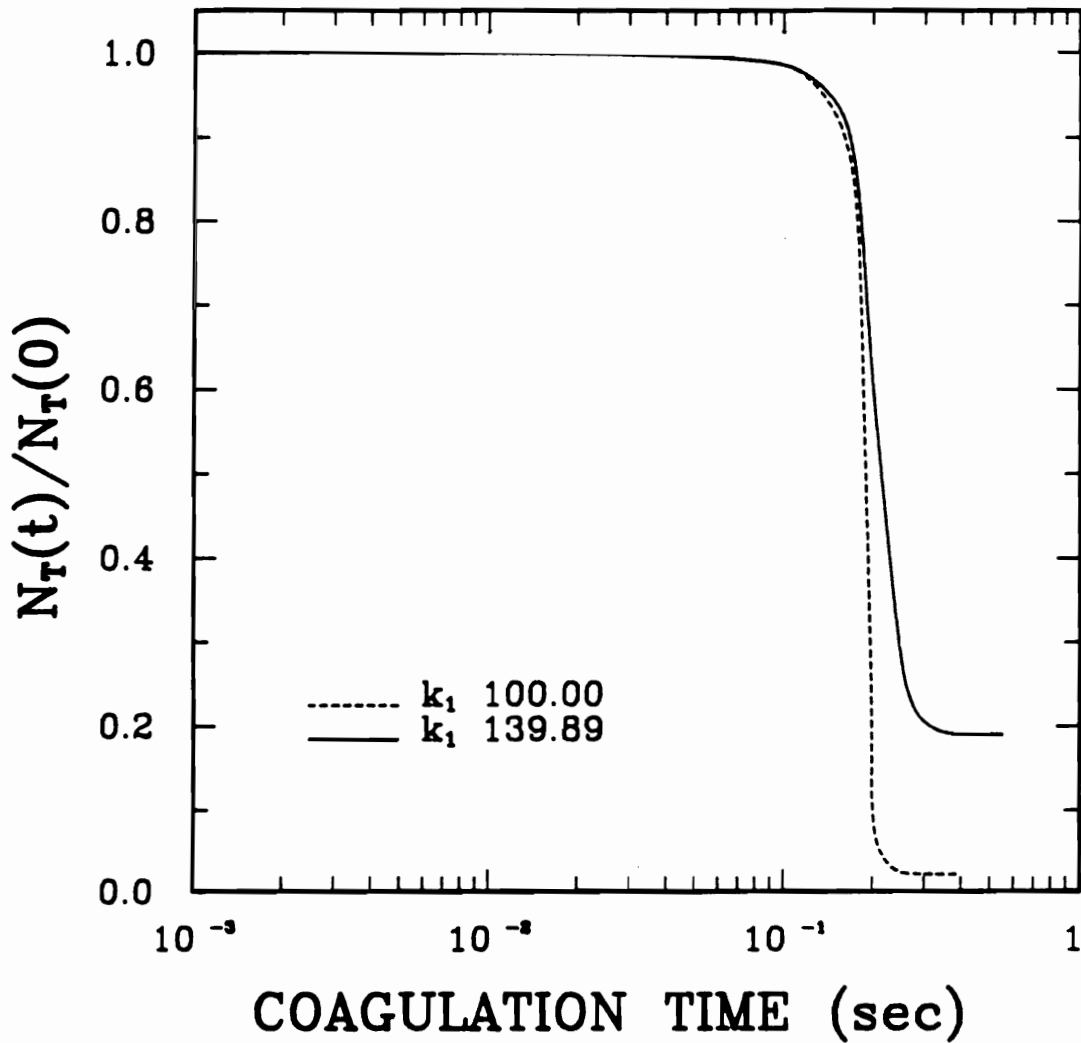


Figure 6.6. Changes of Dimensionless Number Concentration as a Function of Coagulation Time for Different k_1 Values

$$\begin{array}{lll}
 \beta = 0.138 (kT)^{-1}; & k_3 = 507.38 \text{ dyne}^{-1}; & A = 1.0 \times 10^5 \text{ sec}^{-1}; \\
 \text{Mixing} = 800 \text{ rpm}; & \zeta = -43 \text{ mV}; & A_{131} = 3.31 \times 10^{-21} \text{ J}; \\
 C = -1.247 \text{ mJ/m}^2; & \gamma_{sw} = 26.72 \text{ dyne/cm}. &
 \end{array}$$

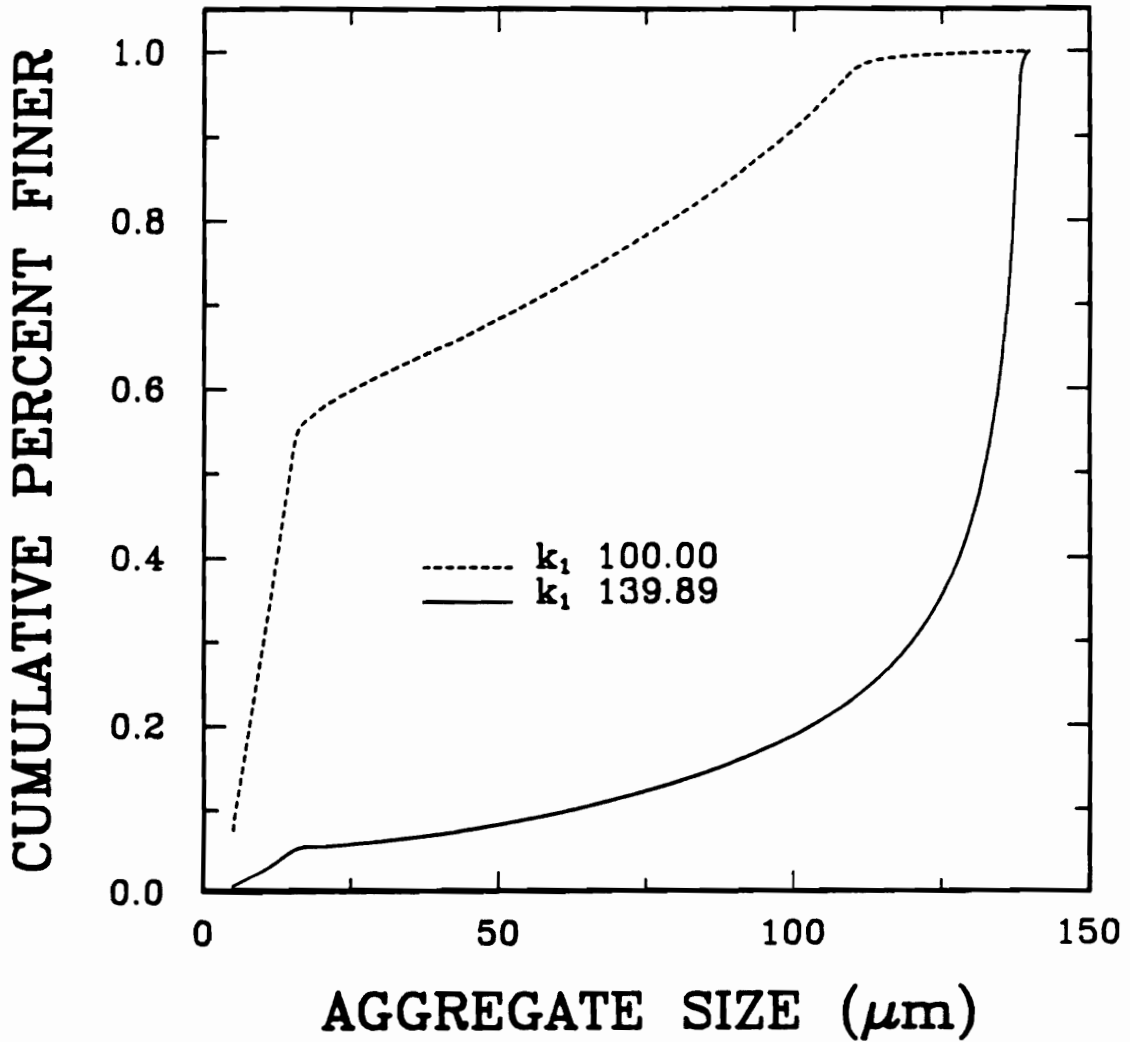


Figure 6.7. Equilibrium Cumulative Aggregate Size Distributions for Different k_1 Values

$\beta = 0.138 (kT)^{-1}$;	$k_3 = 507.38 \text{ dyne}^{-1}$;	$A = 1.0 \times 10^5 \text{ sec}^{-1}$;
Mixing = 800 rpm;	$\zeta = -43 \text{ mV}$;	$A_{131} = 3.31 \times 10^{-21} \text{ J}$;
$C = -1.247 \text{ mJ/m}^2$;	$\gamma_{sw} = 26.72 \text{ dyne/cm}$.	

Figure 6.5 almost disappeared. This phenomenon can be attributed to the fact that at such a high value of model parameter k_1 , the breakage is unlikely to occur under the current mixing conditions. This finding of the simulation suggests that the value of parameter k_1 can be estimated by matching the experimental value of d_{\max} , the maximum aggregate size, with the values obtained during the simulation when a series of values are assigned to k_1 .

6.4.3 Effect of Model Parameter k_3 on Coagulation Kinetics

The effects of model parameter k_3 on coagulation kinetics and equilibrium aggregate size distribution are illustrated in Figures 6.8 and 6.9. Figure 6.8 shows that an increase in model parameter k_3 does not change the coagulation kinetics substantially, which is similar to what has been observed in Figure 6.6. However, a slightly higher dimensionless number concentration has been obtained with higher values of model parameter k_3 at the equilibrium condition. This is due chiefly to the significant breakage of aggregates which starts at a lower aggregate size with the higher value of model parameter k_3 , as indicated in Equation [5.30] and Figure 5.6.

Unlike the effect of model parameter k_1 on the equilibrium aggregate size distribution, the change of value of model parameter k_3 changes the distribution of the aggregate size but the functional form of aggregate size distribution remains the same as shown in Figure 6.9. This is because the aggregate size above which aggregates are subjected to breakup is not affected by changing the value of the parameter k_3 . Therefore, this model parameter can most likely be determined by matching the experimental aggregate size distribution function with that obtained from simulation using different values of the parameter.

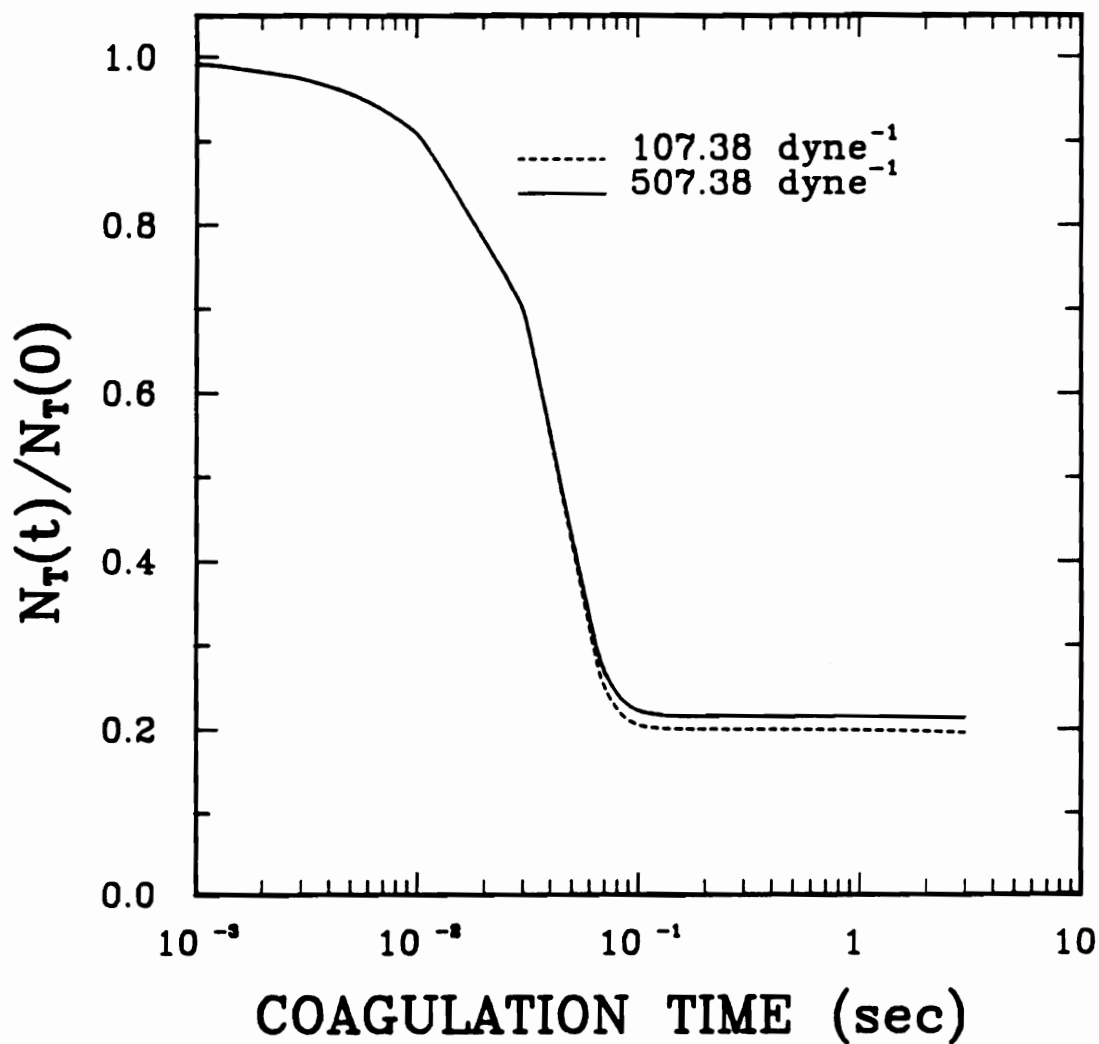


Figure 6.8. Changes of Dimensionless Number Concentration as a Function of Coagulation Time for Different k_3 Values

$$\begin{array}{lll}
 \beta = 0.138 (kT)^{-1}; & k_1 = 139.89; & A = 1.0 \times 10^5 \text{ sec}^{-1}; \\
 \text{Mixing} = 1000 \text{ rpm}; & \zeta = -43 \text{ mV}; & A_{131} = 3.31 \times 10^{-21} \text{ J}; \\
 C = -1.247 \text{ mJ/m}^2; & \gamma_{sw} = 26.72 \text{ dyne/cm}. &
 \end{array}$$

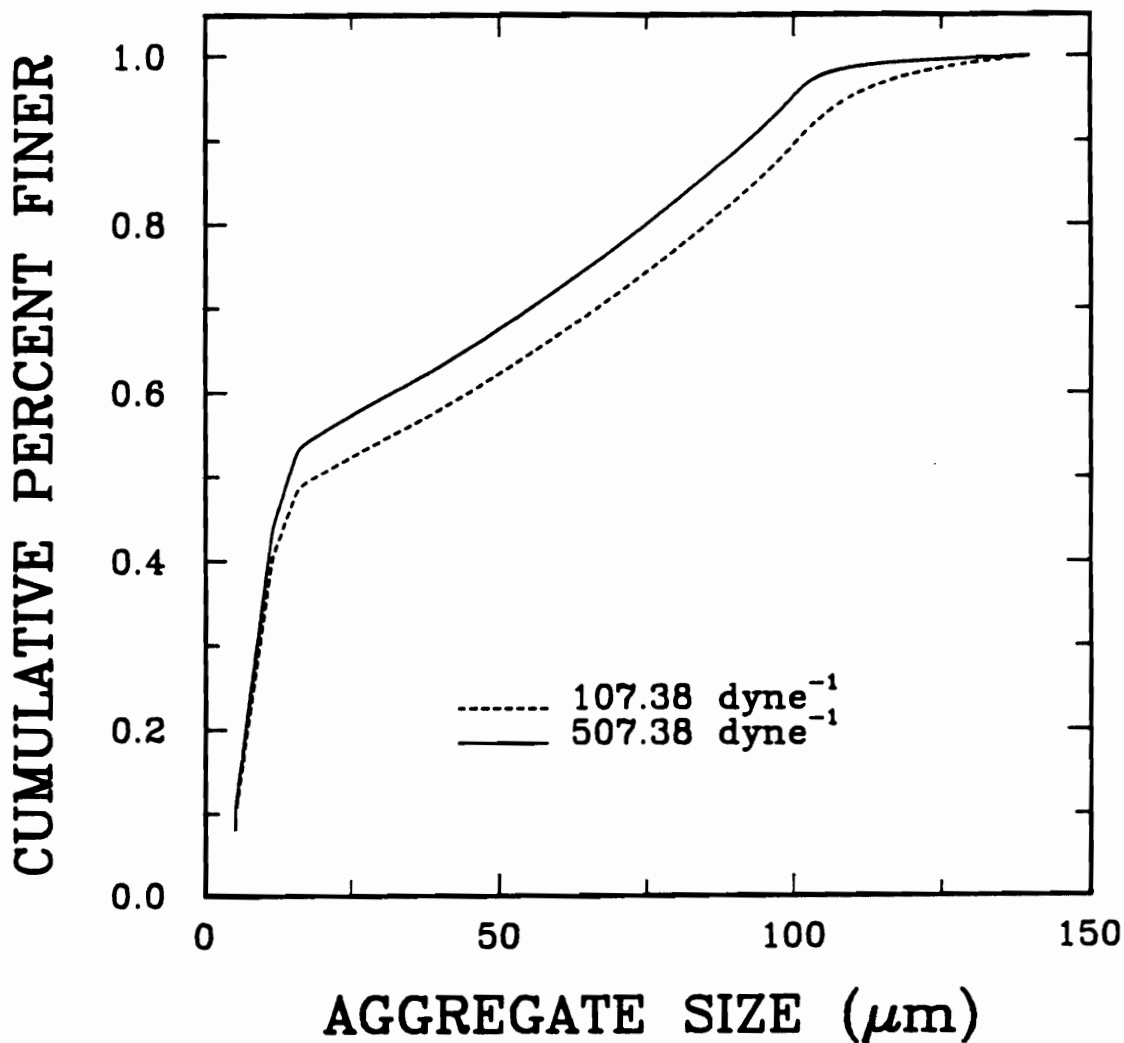


Figure 6.9. Equilibrium Cumulative Aggregate Size Distributions for Different k_3 Values

$\beta = 0.138 (kT)^{-1}$;	$k_1 = 139.89$;	$A = 1.0 \times 10^5 \text{ sec}^{-1}$;
Mixing = 1000 rpm;	$\zeta = -43 \text{ mV}$;	$A_{131} = 3.31 \times 10^{-21} \text{ J}$;
$C = -1.247 \text{ mJ/m}^2$;	$\gamma_{sw} = 26.72 \text{ dyne/cm}$.	

6.4.4 Effect of Model Parameter A on Coagulation Kinetics

Finally, Figures 6.10 and 6.11 show the influence of model parameter A on the coagulation kinetics and equilibrium aggregate size distributions. It is not surprising to find that varying the value of breakage model parameter A affects, slightly, the time at which the coagulation reaches a steady state as illustrated in Figure 6.10.

The dimensionless number concentration of aggregates, however, decreases significantly with decreasing the value of model parameter A . It reaches almost zero if the unity value of A is used in the simulation, even though the breakage of the aggregate occurs at exactly the same aggregate size. This is because the breakage rate is negligible compared with the aggregate formation rate in this particular case. By examining the equilibrium aggregate size distribution as shown in Figure 6.11, it can be seen that using unity value of A causes coagulation to generate the mono-size aggregates of top size. Figure 6.11 also shows that a change in the value of model parameter A changes not only the aggregate size distribution but also the functional form of the distribution, which makes this parameter most interesting.

In summary, the above simulation results show that this four parameter population balance model seems very flexible with β mostly dominating the aggregation kinetics, k_1 adjusting the breakup point, A determining the functional form of aggregate size distribution and k_2 controlling the aggregate size distribution. Although Broadbent and Callcott breakage function has been used throughout these simulations, the use of other types of breakage function may have significant influence on the simulation results and could be a very important factor affecting the coagulation kinetic behavior. This aspect will be discussed briefly later in this chapter.

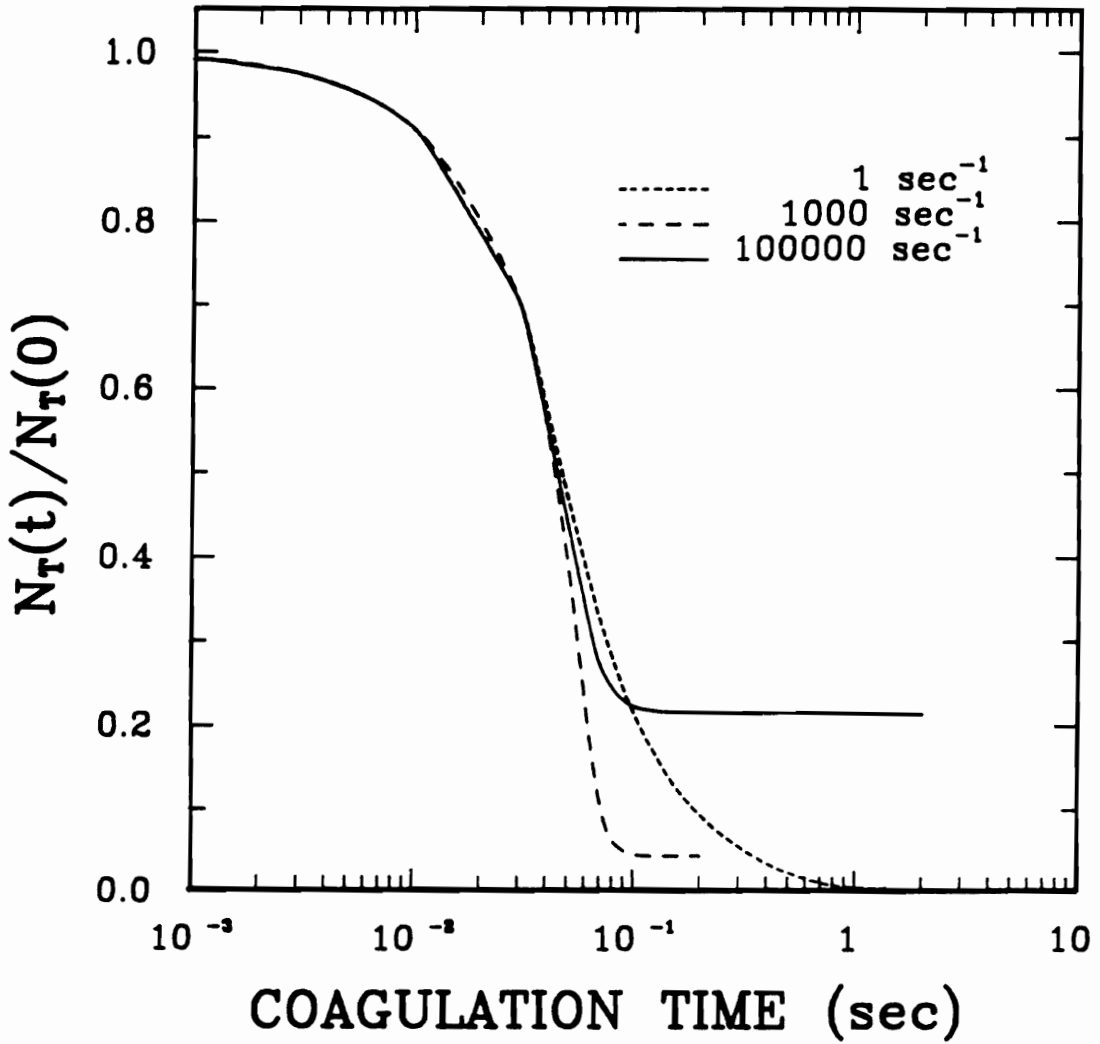


Figure 6.10. Changes of Dimensionless Number Concentration as a Function of Coagulation Time for Different A Values

$\beta = 0.138 (kT)^{-1}$;	$k_1 = 139.89$;	$k_3 = 507.38 \text{ dyne}^{-1}$;
Mixing = 1000 rpm;	$\zeta = -43 \text{ mV}$;	$A_{131} = 3.31 \times 10^{-21} \text{ J}$;
$C = -1.247 \text{ mJ/m}^2$;	$\gamma_{sw} = 26.72 \text{ dyne/cm}$.	

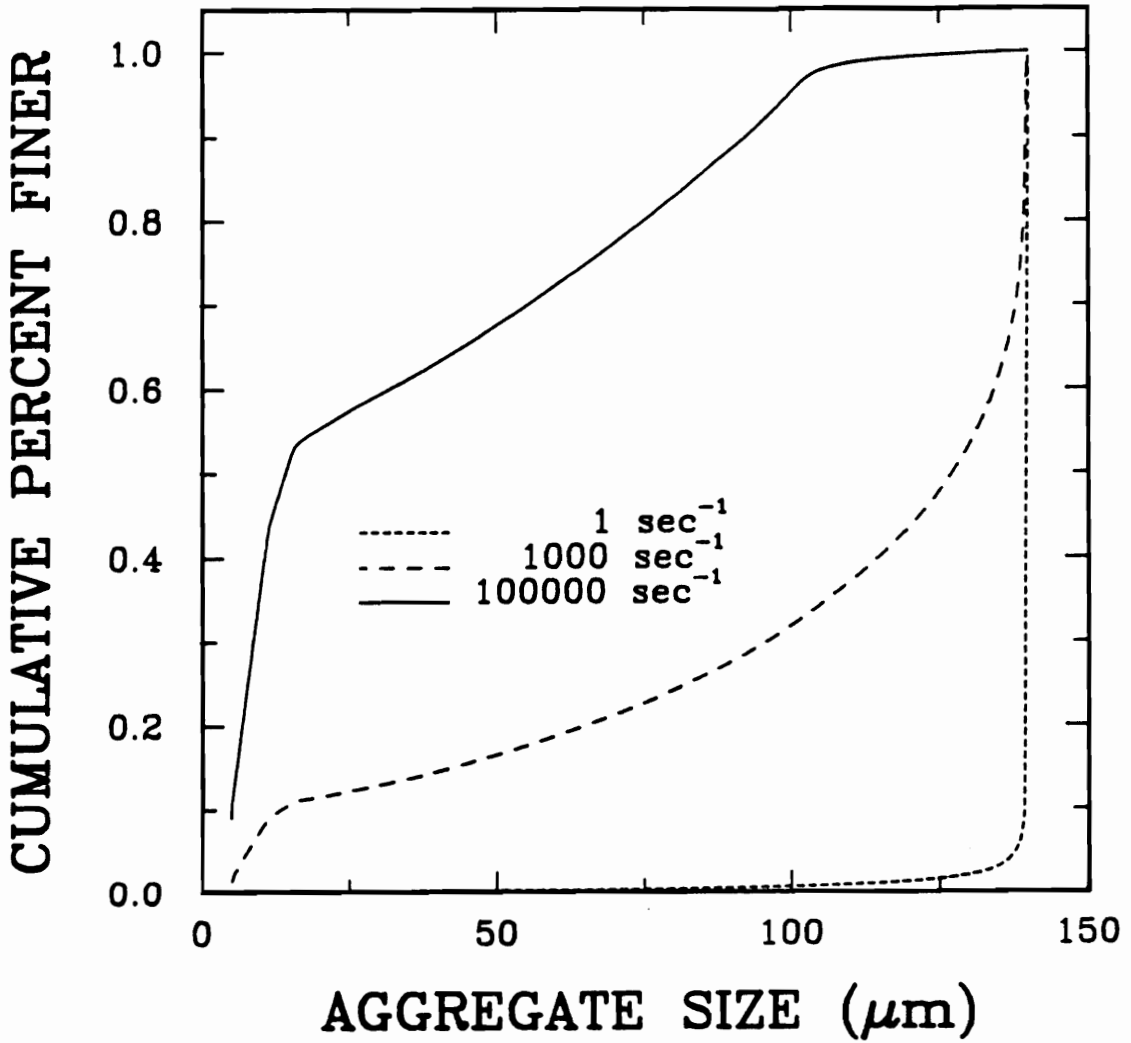


Figure 6.11. Equilibrium Cumulative Aggregate Size Distributions for Different A Values

$\beta = 0.138 (kT)^{-1}$;	$k_1 = 139.89$;	$k_3 = 507.38 \text{ dyne}^{-1}$;
Mixing = 1000 rpm;	$\zeta = -43 \text{ mV}$;	$A_{131} = 3.31 \times 10^{-21} \text{ J}$;
$C = -1.247 \text{ mJ/m}^2$;	$\gamma_{sw} = 26.72 \text{ dyne/cm}$.	

6.5 Simulations with Varying System Variables

6.5.1 *Effect of Mixing Rate on Coagulation Kinetics*

After choosing the reasonable values of the model parameters, the effects of the system variables on coagulation kinetics and equilibrium aggregate size distribution have been studied by varying one system variable at a time in each simulation. Figure 6.12 shows the changes of mass fraction of individual size class as a function of coagulation time. The model parameters and other system variables used in this simulation are the same as those used in the previous simulation with the results shown in Figure 6.2, except that the mixing is assumed to be conducted at 800 rpm.

In contrast to Figure 6.2 where mixing rate has been assumed to be 1000 rpm, the coagulation is delayed at a lower mixing condition as shown in Figure 6.12. Figure 6.2 shows that the coagulation starts at 0.001 seconds, while Figure 6.12 shows that coagulation does not begin until coagulation proceeds to 0.1 seconds. However, as soon as the coagulation is initiated at a certain time, approximately 0.1 seconds, the reduction of the number of primary particles becomes much more significant as the coagulation proceeds further in the case of lower mixing intensity. It is also shown that with lower mixing intensity, the mass fraction of the aggregates in the size range of 5.0 to 11.7 μm never exists at a substantial level as opposed to what has been observed with higher mixing intensity. The complicated behavior of mass fraction of the aggregates in this size range observed at higher mixing rate disappears, indicating that the breakage of aggregates of larger size becomes, as expected, less significant at a lower mixing rate.

The effects of a further reduction in the mixing intensity on the coagulation behavior are shown in Figure 6.13. These results have been obtained from simulation by assuming a mixing rate of 500 rpm. At this mixing rate, the simulation has shown that

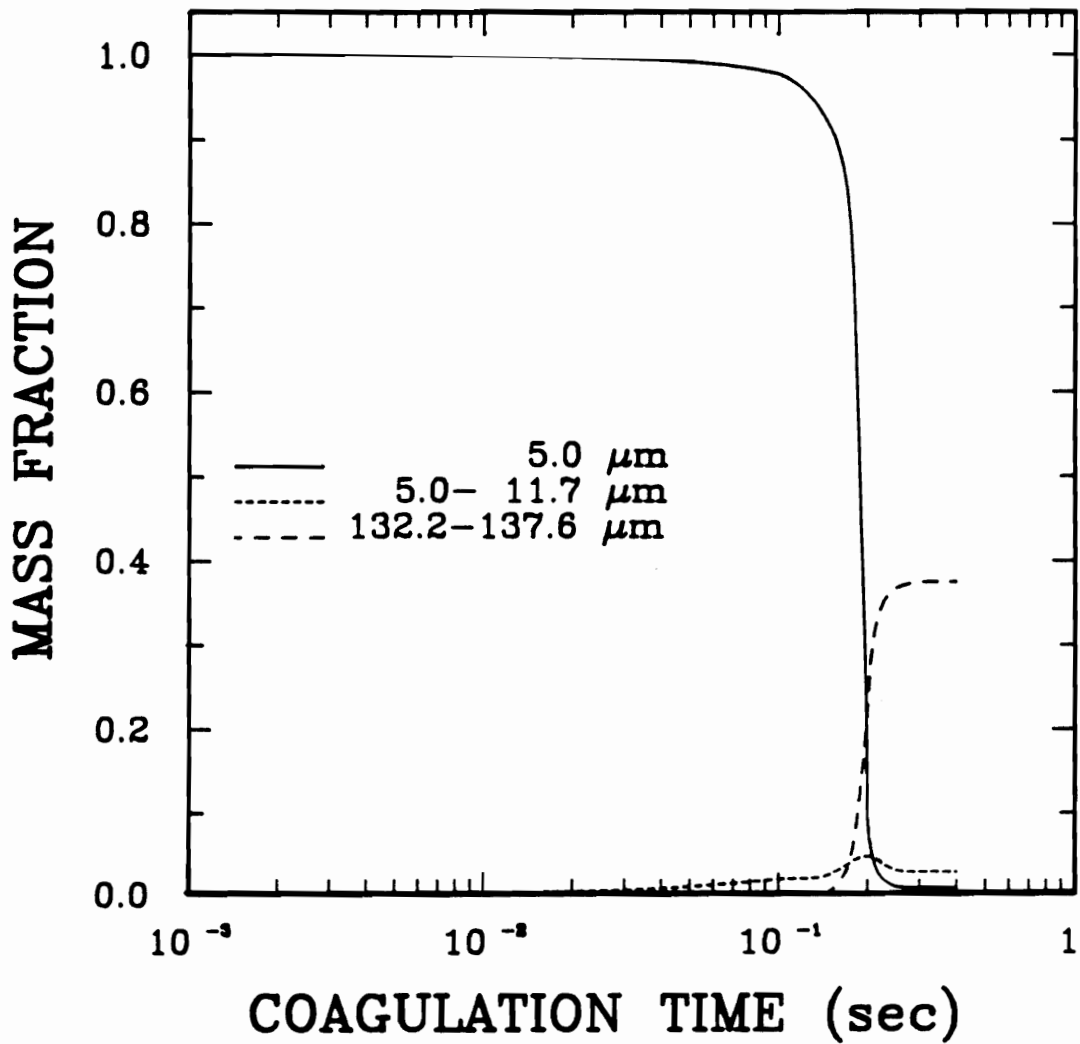


Figure 6.12. Evolution of Mass Fraction of Primary Particles and Aggregates in Different Size Ranges under Mixing Rate of 800 rpm

$$\begin{array}{lll}
 \beta = 0.138 (kT)^{-1}; & k_1 = 139.89; & k_3 = 507.38 \text{ dyne}^{-1}; \\
 A = 1.0 \times 10^5 \text{ sec}^{-1}; & \text{Mixing} = 800 \text{ rpm}; & \zeta = -43 \text{ mV}; \\
 A_{131} = 3.31 \times 10^{-21} \text{ J}; & C = -1.247 \text{ mJ/m}^2; & \gamma_{sw} = 26.72 \text{ dyne/cm}.
 \end{array}$$

there is no breakage of aggregates over the whole size spectrum studied. It is noted that the coagulation does not occur until 1 second, which is a 1000 times delay as compared with the coagulation conducted at 1000 rpm. Compared with Figures 6.2 and 6.12, the most remarkable feature in Figure 6.13 is that as the coagulation proceeds, the mass fraction of the aggregates in the size range of 5.0 to 11.7 μm increases considerably first, reaches the maximum at a certain time and, then, begins to decrease and continues to almost zero. This is a commonly observed behavior in coagulation simulation in which the breakage event of aggregates has been neglected.

The dimensionless number concentrations as a function of coagulation time obtained from simulation using various mixing conditions are given in Figures 6.14 and 6.15. Figure 6.14 shows that a decrease of mixing rate from 1000 rpm to 800 rpm delays the starting time of coagulation substantially, from 0.001 seconds to 0.2 seconds. It appears that the change of the mixing rate at this level does not significantly affect the system reaching steady state. The coagulation reaches a steady state at coagulation time of 0.2 and 0.3 seconds, respectively.

However, a further reduction in mixing rate to 500 rpm causes the system to reach the steady state after 10 minutes of coagulation as shown in Figure 6.15. Figure 6.15 also shows that if the coagulation is conducted at a mixing rate of 300 rpm, the dimensionless number concentration still shows a tendency of significant decline at the coagulation time of 10 minutes, which indicates that the steady state has not been reached. Figures 6.14 and 6.15 in combination show that the dimensionless number concentration at the steady state decreases significantly as the mixing rate decreases from 1000 rpm to 800 rpm and then levels off at a value of 0.02 with a further decrease in the mixing rate. The higher value of the dimensionless number concentration at a higher mixing rate illustrates the adverse effect of severe shear force on coagulation.

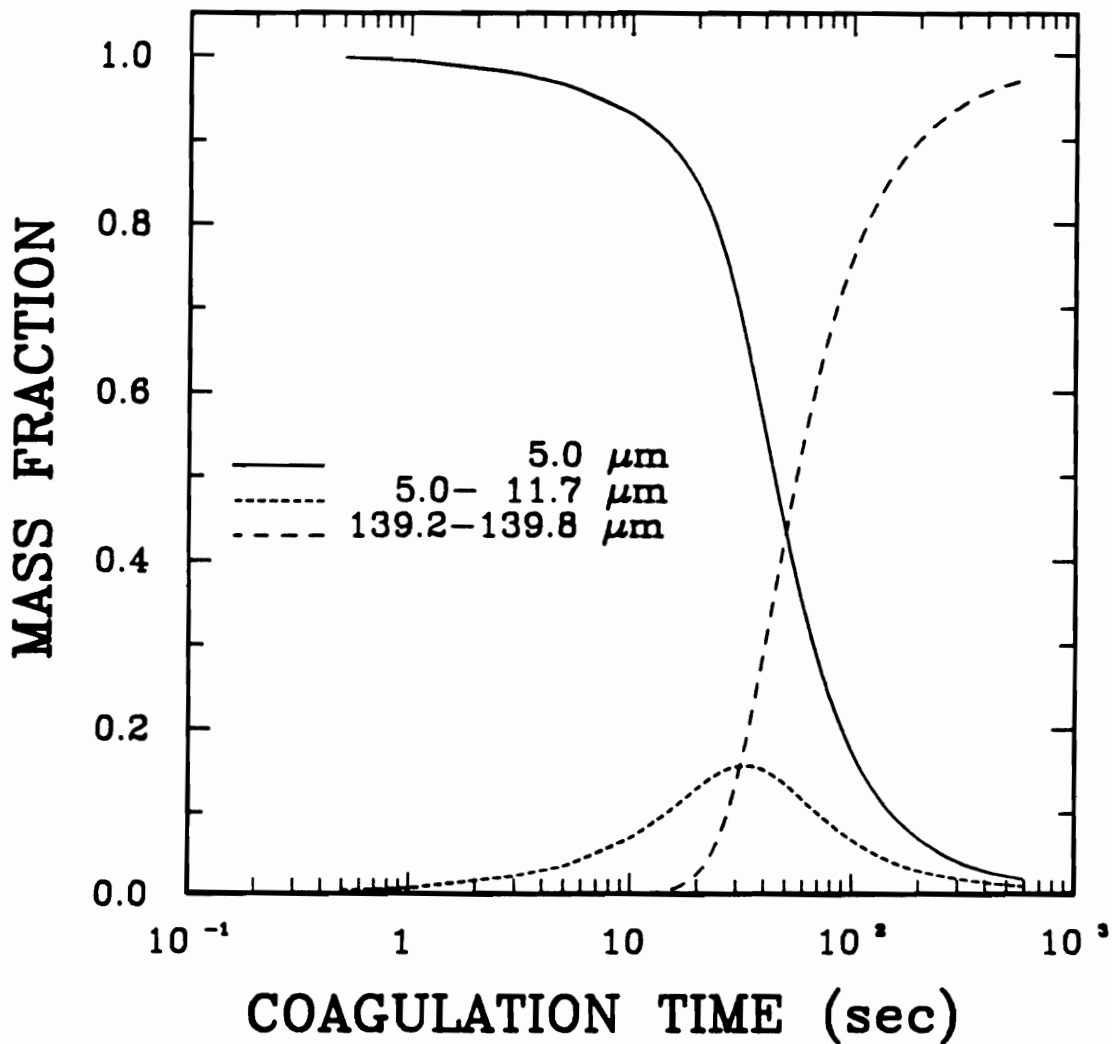


Figure 6.13. Evolution of Mass Fraction of Primary Particles and Aggregates in Different Size Ranges under Mixing Rate of 500 rpm

$$\begin{array}{lll}
 \beta = 0.138 (kT)^{-1}; & k_1 = 139.89; & k_3 = 507.38 \text{ dyne}^{-1}; \\
 A = 1.0 \times 10^5 \text{ sec}^{-1}; & \text{Mixing} = 500 \text{ rpm}; & \zeta = -43 \text{ mV}; \\
 A_{131} = 3.31 \times 10^{-21} \text{ J}; & C = -1.247 \text{ mJ/m}^2; & \gamma_{sw} = 26.72 \text{ dyne/cm}.
 \end{array}$$

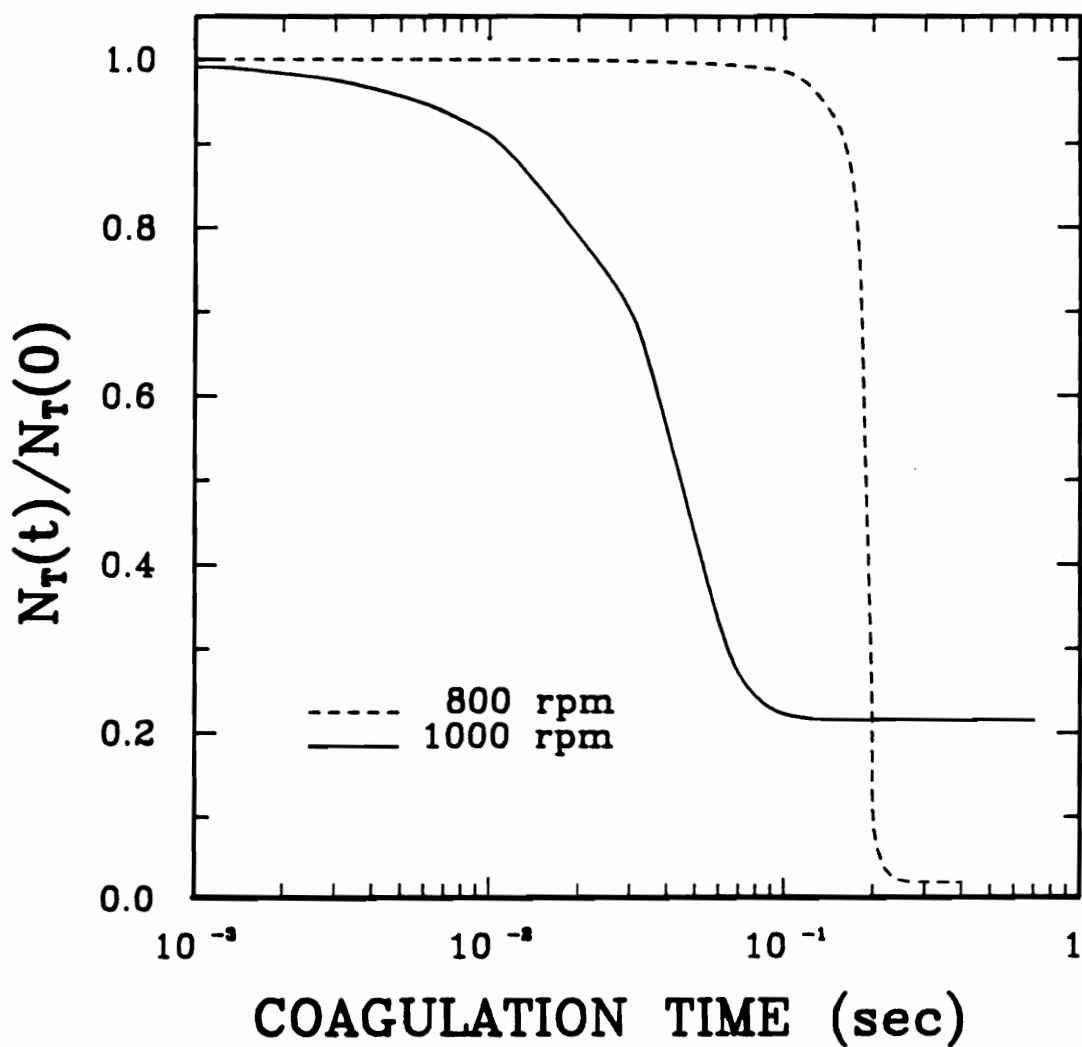


Figure 6.14. Changes of Dimensionless Number Concentration as a Function of Coagulation Time for Mixing Rates of 800 and 1000 rpm

$$\begin{array}{lll}
 \beta = 0.138 (kT)^{-1}; & k_1 = 139.89; & k_3 = 507.38 \text{ dyne}^{-1}; \\
 A = 1.0 \times 10^5 \text{ sec}^{-1}; & \zeta = -43 \text{ mV}; & A_{131} = 3.31 \times 10^{-21} \text{ J}; \\
 C = -1.247 \text{ mJ/m}^2; & \gamma_{sw} = 26.72 \text{ dyne/cm}. &
 \end{array}$$

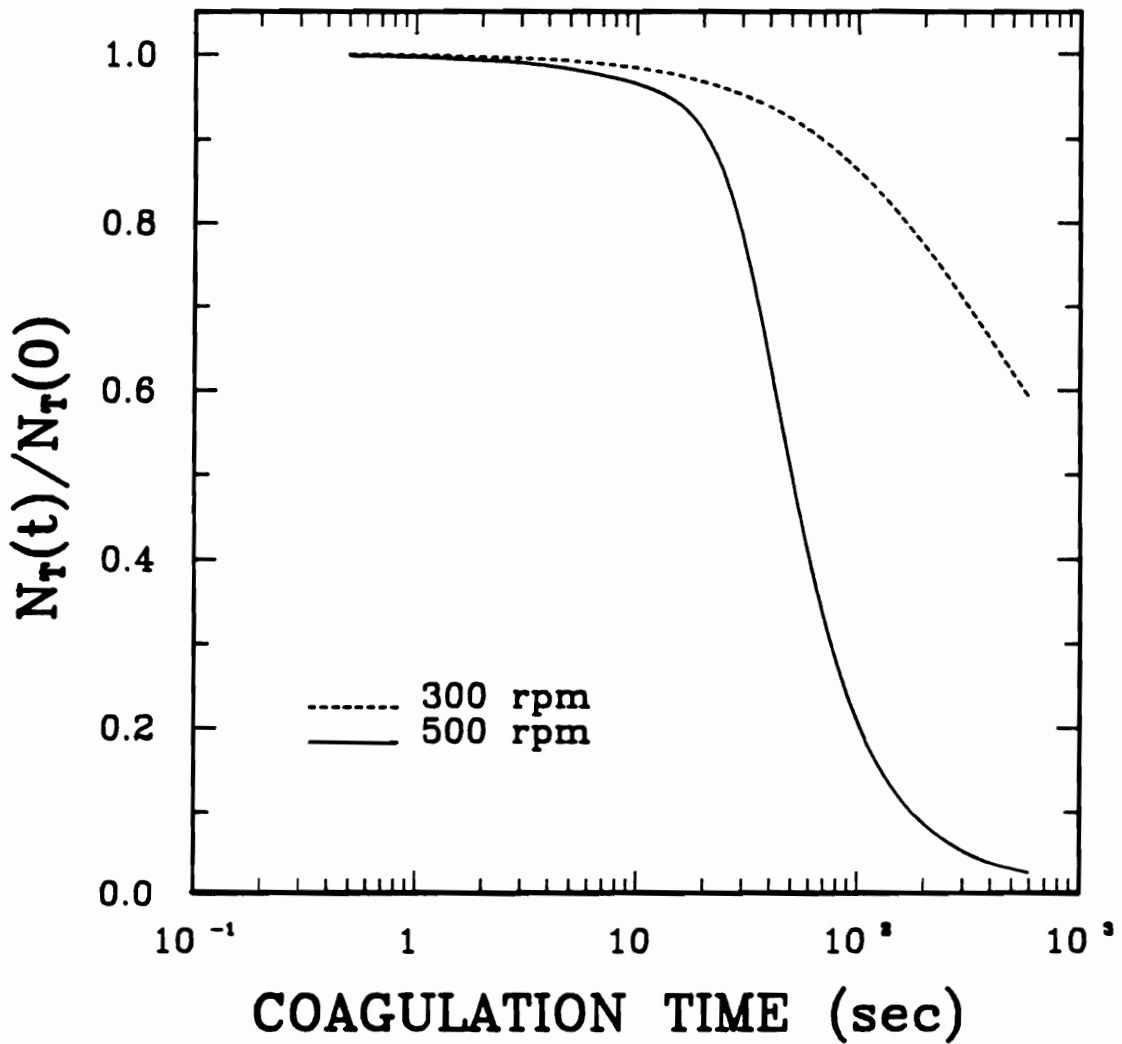


Figure 6.15. Changes of Dimensionless Number Concentration as a Function of Coagulation Time for Mixing Rates of 500 and 300 rpm

$$\begin{array}{lll}
 \beta = 0.138 \text{ (} kT \text{)}^{-1}; & k_1 = 139.89; & k_3 = 507.38 \text{ dyne/cm}^{-1}; \\
 A = 1.0 \times 10^5 \text{ sec}^{-1}; & \zeta = -43 \text{ mV}; & A_{131} = 3.31 \times 10^{-21} \text{ J}; \\
 C = -1.247 \text{ mJ/m}^2; & \gamma_{sw} = 26.72 \text{ dyne/cm}. &
 \end{array}$$

To understand the observed kinetic behavior, it is helpful to tabulate and plot some relevant constants calculated for each system. Taking binary association of primary particles as an example, the collision efficiency, collision frequency and the aggregation rate constants for each mixing condition have been calculated and the results are given in Table 6.1. Also included in Table 6.1 is d_b defined as the aggregate size at which aggregates start to break. The aggregation rate constants between primary particle and aggregates of any class are given in Figure 6.16.

Table 6.1. Calculated Values of V_k , α , $\omega(a_1, a_1)$, $k(1, 1)$ and d_b at Various Mixing Rates.

Mixing Rate	rpm	300	500	800	1000
V_k	kT	1.7	7.9	32.5	63.5
α		7.02×10^{-4}	7.02×10^{-4}	7.87×10^{-3}	5.66×10^{-1}
$\omega(a_1, a_1)$	sec^{-1}	4.46×10^{-8}	9.61×10^{-8}	1.94×10^{-7}	2.72×10^{-7}
$k(1, 1)$	sec^{-1}	1.57×10^{-11}	3.37×10^{-11}	7.65×10^{-10}	7.69×10^{-8}
d_b	μm	> 140.0	> 140.0	137.0	105.5

Figure 6.16 shows that when primary particles coagulate with the aggregates of increasing size, the coagulation rate constant increases significantly first, reaches a transition point at a certain aggregate size and, then, increases gradually, forming two distinct zones. The size at which the transition occurs is defined as d_t for the convenience of discussion. The transition may be considered to be from slow coagulation to rapid coagulation. It appears, from Figure 6.16, that d_t decreases as the mixing rate increases.

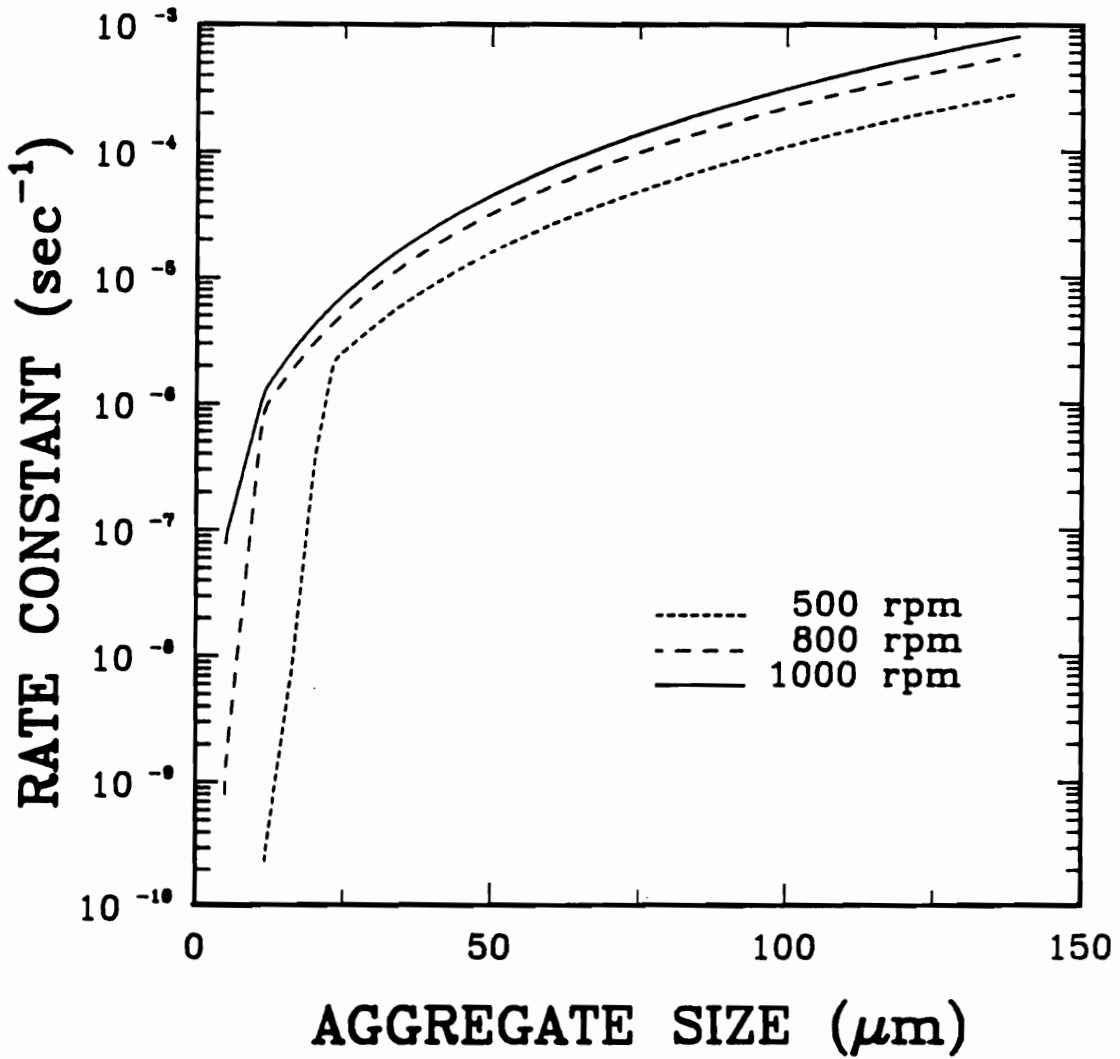


Figure 6.16. Comparison of Aggregation Rate Constants as a Function of Aggregate Size for Different Mixing Rates

$$\beta = 0.138 (kT)^{-1}; \quad \zeta = -43 \text{ mV}; \quad A_{131} = 3.31 \times 10^{-21} \text{ J};$$

$$C = -1.247 \text{ mJ/m}^2.$$

This suggests that with high mixing intensity, the relatively smaller aggregates can obtain sufficient kinetic energy to overcome the energy barrier, resulting in rapid coagulation. When a primary particle coagulates with the aggregates of the size smaller than d_c , Figure 6.16 shows a sharp increase in coagulation rate constant as aggregate size increases, which may be attributed merely to the sensitive dependence of collision efficiency on the increased kinetic energy of larger aggregates through the exponential function $e^{-E_p/kT}$. Figure 6.16 also shows that when primary particles coagulate with the aggregates of the same size but smaller than d_c , the coagulation rate constant increases about two orders in magnitude as the mixing rate increases due to the same reason. As shown in Table 6.1, the aggregation rate constant between primary particles will increase about 100 times if the mixing rate increases from 800 rpm to 1000 rpm.

However, when the aggregate size is larger than d_c , the coagulation rate constant between primary particles and aggregates increases gradually as illustrated in Figure 6.16. For the coagulation between the primary particles and the aggregates of given size greater than d_c , the aggregation rate constant increases only slightly with an increase in the mixing rate. In this aggregate size range, the collision efficiency equals unity since the kinetic energy of colliding particle/aggregate pair is equal to or greater than the potential energy barrier of the corresponding particle/aggregate pair. Therefore, the exponential dependence of aggregation rate constant on the mixing intensity disappears. The increase in aggregation rate constant in this case is due to the increase of collision frequency with increasing mixing rate. This finding suggests that the coagulation between the primary particles and the aggregates of size smaller than d_c controls the coagulation rate of the system, which explains the coagulation kinetic behavior as shown in Figure 6.14.

The equilibrium aggregate size distributions at various mixing rates are given in Figure 6.17. The mixing rate significantly affects the ultimate aggregate size distribution

as illustrated in Figure 6.17. At the mixing rate of 800 rpm, the three distinct size distribution zones observed at the mixing rate of 1000 rpm tend to disappear. Only a very small fraction, about 5%, of small aggregates can exist and about 80% of aggregates are larger than $125 \mu m$ in size. If the coagulation is conducted at a mixing rate of 500 rpm, only mono-size aggregates of top size are existing in the suspension.

In order to have a better understanding of the effects of mixing rate on equilibrium aggregate size distribution as uncovered in the above simulation, Table 6.1 is presented to show that if the suspension is mixed at 1000 rpm, the aggregates of size greater than $105.5 \mu m$ will be subjected to breakup, producing a spectrum of daughter aggregates of smaller size. Since there is a considerable number of classes above size $105.5 \mu m$, a substantial number of daughter aggregates due to the breakage of aggregates in these sizes is expected as shown in Figure 6.17. A decrease of mixing rate from 1000 rpm to 800 rpm increases d_b from $105.5 \mu m$ to $137.0 \mu m$ as shown in Table 6.1. Therefore, only the aggregates in a few classes of size greater than $130.0 \mu m$ are subjected to breakage. As a result, a negligible number of small aggregates is expected to exist under this mixing rate as illustrated in Figure 6.17.

Because of the difficulty of measuring true aggregate size distribution by using existing size analysis techniques as discussed in the literature (13-14), no experimental results have been obtained to testify quantitatively the above simulation results in the present work. However, the above simulation results are qualitatively in good agreement with the experimentally observed phenomena. As discussed, the system variables used in the above simulation have been determined experimentally at a mixing rate of 1000 rpm. It is interesting to note that good coagulation has been obtained experimentally at this mixing rate as shown in Figure 3.1, which is in good agreement with what has been predicted from the above simulation. However, a much clearer supernatant has been observed experimentally when the coagulation was conducted at

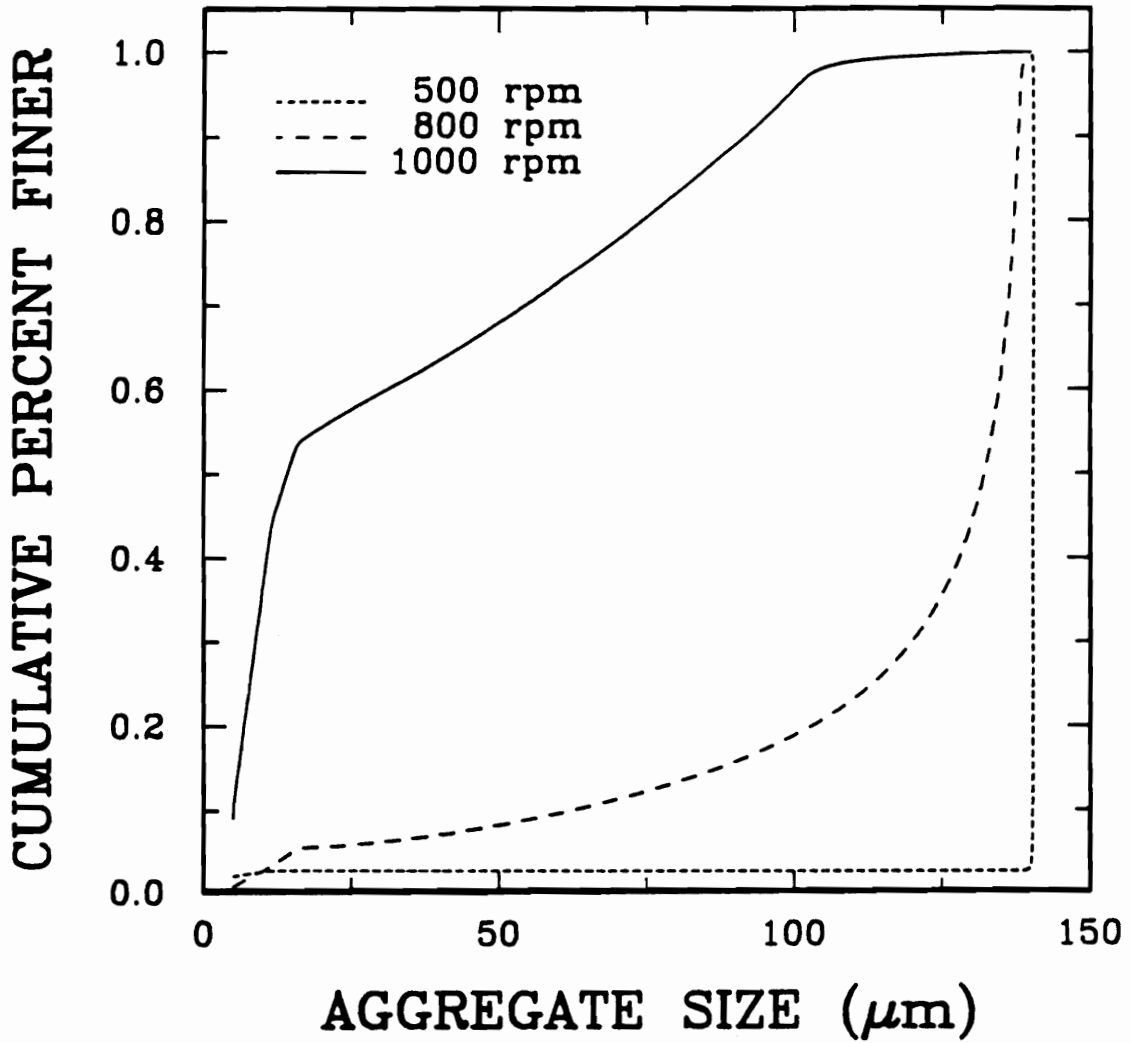


Figure 6.17. Equilibrium Cumulative Aggregate Size Distributions as a Function of Coagulation Time for Three Different Mixing Rates

$$\begin{array}{lll}
 \beta = 0.138 (kT)^{-1}; & k_1 = 139.89; & k_3 = 507.38 \text{ dyne}^{-1}; \\
 A = 1.0 \times 10^5 \text{ sec}^{-1}; & \zeta = -43 \text{ mV}; & A_{131} = 3.31 \times 10^{-21} \text{ J}; \\
 C = -1.247 \text{ mJ/m}^2; & \gamma_{sw} = 26.72 \text{ dyne/cm}. &
 \end{array}$$

a mixing rate of 800 rpm, which is consistent with what has been found in the above simulation as illustrated in Figure 6.17.

The above simulations show that the mixing is an important experimentally controllable variable in the coagulation performed under varying mixing conditions. From the simulation, it is possible to find an optimum mixing rate for obtaining the aggregates of conceivable settling rate within an acceptable coagulation time.

6.5.2 *Effect of Zeta Potential on Coagulation Kinetics*

The dimensionless number concentrations as a function of coagulation time obtained in the simulation using different values of zeta potential are given in Figure 6.18. Figure 6.18 shows that with a slight increase in the magnitude of zeta potential, the coagulation is delayed significantly. By changing the zeta potential value from -43 mV to -44 mV, the time at which coagulation starts increases from 0.001 seconds to 0.1 seconds. A further increase in the magnitude of zeta potential, from -44 mV to -45 mV, causes the coagulation to proceed at an inconceivable rate as shown in Figure 6.18. After allowing a two-hour coagulation in the simulation, 99.98% of primary particles are still existing as individual particles.

As contrasted to the effect of zeta potential values on the time at which coagulation initiates, Figure 6.18 shows that the coagulation does not delay reaching the steady state by a change of zeta potential value from -43 mV to -44 mV. To understand this behavior, the dimer formation rate constants at various values of zeta potential are given in Table 6.2. Also included in Table 6.2 are the values of corresponding interaction energy barrier and collision efficiency.

Table 6.2 shows that an increase in the magnitude of zeta potential increases substantially the interaction energy barrier, which causes the collision efficiency to de-

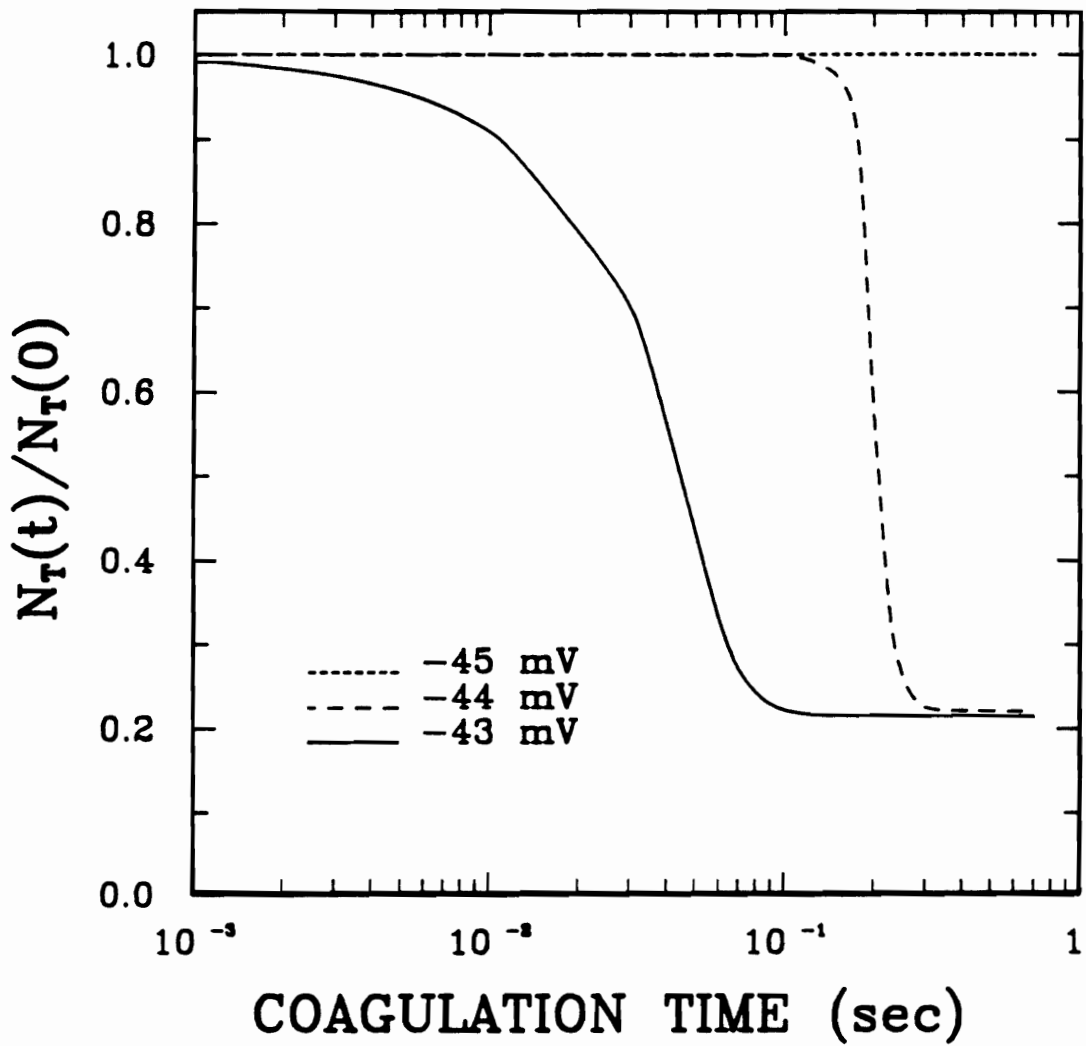


Figure 6.18. Changes of Dimensionless Number Concentration as a Function of Coagulation Time for Different Values of Zeta Potential

$$\begin{array}{lll}
 \beta = 0.138 (kT)^{-1}; & k_1 = 139.89; & k_3 = 507.38 \text{ dyne}^{-1}; \\
 A = 1.0 \times 10^5 \text{ sec}^{-1}; & \text{Mixing} = 1000 \text{ rpm}; & A_{131} = 3.31 \times 10^{-21} \text{ J}; \\
 C = -1.247 \text{ mJ/m}^2; & \gamma_{sw} = 26.72 \text{ dyne/cm}. &
 \end{array}$$

crease significantly through the exponential function. As a result, with the same collision mode, $\omega(a_i, a_j)$, the coagulation rate constant decreases dramatically, from 7.69×10^{-8} to 4.43×10^{-15} if zeta potential changes from -43 mV to -45 mV as shown in Table 6.2. Therefore, the observed effect of zeta potential on the coagulation kinetic behavior may be attributed to the significant effect of zeta potential on the dimer formation rate constant, which is a rate control step in the coagulation.

Table 6.2. Calculated Values of V_{\max} , α and $k(1, 1)$ for Three Different Values of Zeta Potential

Zeta Potential, mV		-43	-44	-45
V_{\max} , kT		67.6	121.6	188.7
α		5.66×10^{-1}	3.26×10^{-4}	3.06×10^{-8}
$k(1, 1)$, sec^{-1}		7.69×10^{-8}	4.43×10^{-11}	4.15×10^{-15}

However, as soon as a sufficient number of aggregates of low order is formed, the formation of high order aggregates dominates the consumption of primary particles and low order aggregates and, hence, determines the time at which coagulation reaches steady state and the equilibrium aggregate size distribution. Since the kinetic energy of collision increases significantly with increasing the size of aggregates, the increase of zeta potential by 1 mV in magnitude is unlikely to affect the collision efficiency of those aggregates whose kinetic energy level is sufficiently high. Therefore, the aggregation rate constant over the size spectrum of those aggregates remains unchanged. As a result, the time at which the system reaches dynamic equilibrium changes slightly in spite of the

significant change in the initial aggregation rate constant as observed in the simulation. This explanation conforms to what has been observed in carrier flotation, where coarse particles are added to initiate the coagulation.

The effect of zeta potential on the coagulation kinetic behavior uncovered in the simulation is in good agreement with what observed in the experiments as shown in Figure 3.1. Figure 3.1 shows that near the critical coagulation pH, the fine coal suspension changes from coagulation to dispersion within a narrow pH range over which the value of zeta potential changes only a few millivolts, while the simulation shows that a change of zeta potential value from -43 mV to -45 mV turns a system from coagulation to dispersion as illustrated in Figure 6.18.

The equilibrium aggregate size distribution obtained in the simulation using different values of zeta potential is given in Figure 6.19. As shown, the equilibrium aggregate size distribution does not change significantly as the value of zeta potential changes from -43 mV to -44 mV even though this change causes significant delay in the coagulation kinetics as shown previously in Figure 6.18. This is expected since the change in the value of zeta potential does not affect the breakage rate constants and the aggregation rate constants between the primary particle and the aggregate of size greater $11.6 \mu\text{m}$. The latter dominates the aggregation rate process, and combined with the breakage rate process, determines the equilibrium aggregate size distribution after the aggregation between the primary particles is initiated. Also shown in Figure 6.19 is the aggregate size distribution after the suspension is allowed to coagulate for 2 hours in the simulation using zeta potential value of -45 mV. In this case, the aggregate size distribution is essentially the same as that of mono size feed. This indicates that the coagulation is not practically possible if the present coal particles carry the electrical potential of -45 mV, which is in good agreement with the experimental observations as discussed previously.

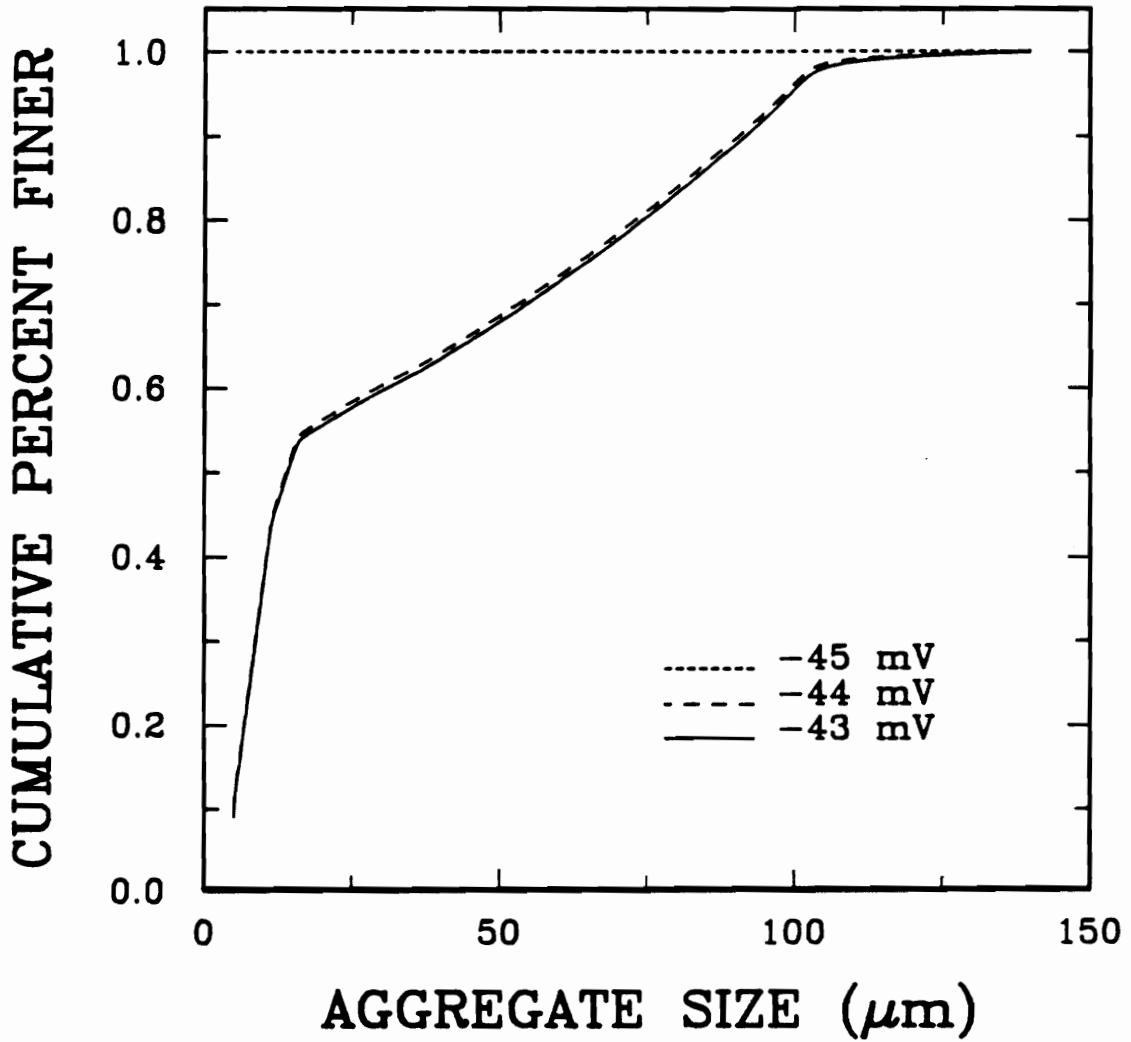


Figure 6.19. Equilibrium Cumulative Aggregate Size Distributions for Different Values of Zeta Potential

$$\beta = 0.138 (kT)^{-1}; \quad k_1 = 139.89; \quad k_3 = 507.38 \text{ dyne}^{-1};$$

$$A = 1.0 \times 10^5 \text{ sec}^{-1}; \text{ Mixing} = 1000 \text{ rpm}; A_{131} = 3.31 \times 10^{-21} \text{ J};$$

$$C = -1.247 \text{ mJ/m}^2; \quad \gamma_{sw} = 26.72 \text{ dyne/cm}.$$

6.5.3. Effect of Hamaker Constant on Coagulation Kinetics

The effects of Hamaker constant of solid on the coagulation kinetics have also been simulated by keeping other model parameters and system variables constant. The simulation results are given in Figures 6.20 and 6.21. Figure 6.20 shows that a 30% decrease in Hamaker constant of coal, from $6.07 \times 10^{-20} J$ to $4.07 \times 10^{-20} J$, shifts the kinetic curve to the longer coagulation time side. However, the influence of Hamaker constant on the coagulation kinetics is not as significant as that of surface electrical potential as discussed in Section 6.5.2. The dimensionless number concentration reaches almost the same value after the coagulation reaches a steady state at a time of 0.2 seconds. Figure 6.21 shows that the equilibrium aggregate size distributions obtained in simulation using two different values of Hamaker constant are almost identical.

It is not surprising to find that the coagulation kinetics is not as sensitive to the changes of Hamaker constant, as shown in Figure 6.20, as to the changes of surface electrical potential, as illustrated in Figure 6.18. In Chapter 4, it has been shown that, theoretically, the Hamaker constant is not as important as surface electrical potential in determining the stability of colloidal suspensions of very hydrophobic colloids suspended in water. The calculation has shown that the interaction energy barrier between primary particles increases from $67.6 kT$ to $78.9 kT$ as the Hamaker constant decreases from $6.07 \times 10^{-20} J$ to $4.07 \times 10^{-20} J$, which results in a reduction in collision efficiency of primary particles from 0.566 to 0.119. Thus, the dimer formation rate constant decreases from $7.69 \times 10^{-8} \text{ sec}^{-1}$ to $1.62 \times 10^{-8} \text{ sec}^{-1}$ at a given mixing rate of 1000 rpm, causing a slight delay in initiating the dimer formation which controls the starting time of coagulation as shown in Figure 6.21. As soon as dimer formation is initiated, forming sufficient number of dimers, the coagulation proceeds in the same way regardless of the changes of Hamaker constant over the studied range. This is because with an increase

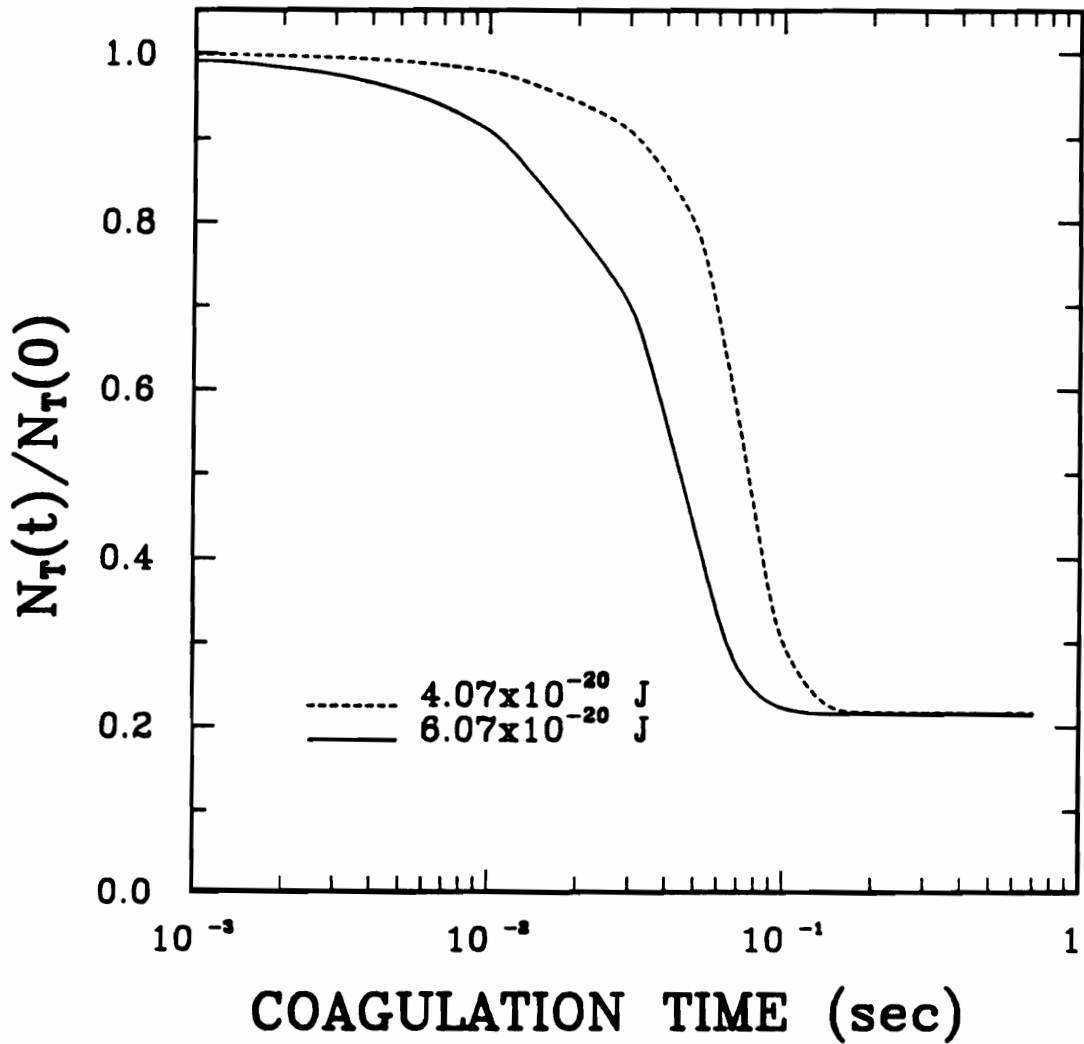


Figure 6.20. Changes of Dimensionless Number Concentration as a Function of Coagulation Time for Different Values of Hamaker Constant

$$\begin{array}{lll}
 \beta = 0.138 (kT)^{-1}; & k_1 = 139.89; & k_3 = 507.38 \text{ dyne}^{-1}; \\
 A = 1.0 \times 10^5 \text{ sec}^{-1}; & \text{Mixing} = 1000 \text{ rpm}; & \zeta = -43 \text{ mV}; \\
 C = -1.247 \text{ mJ/m}^2; & \gamma_{sw} = 26.72 \text{ dyne/cm}. &
 \end{array}$$

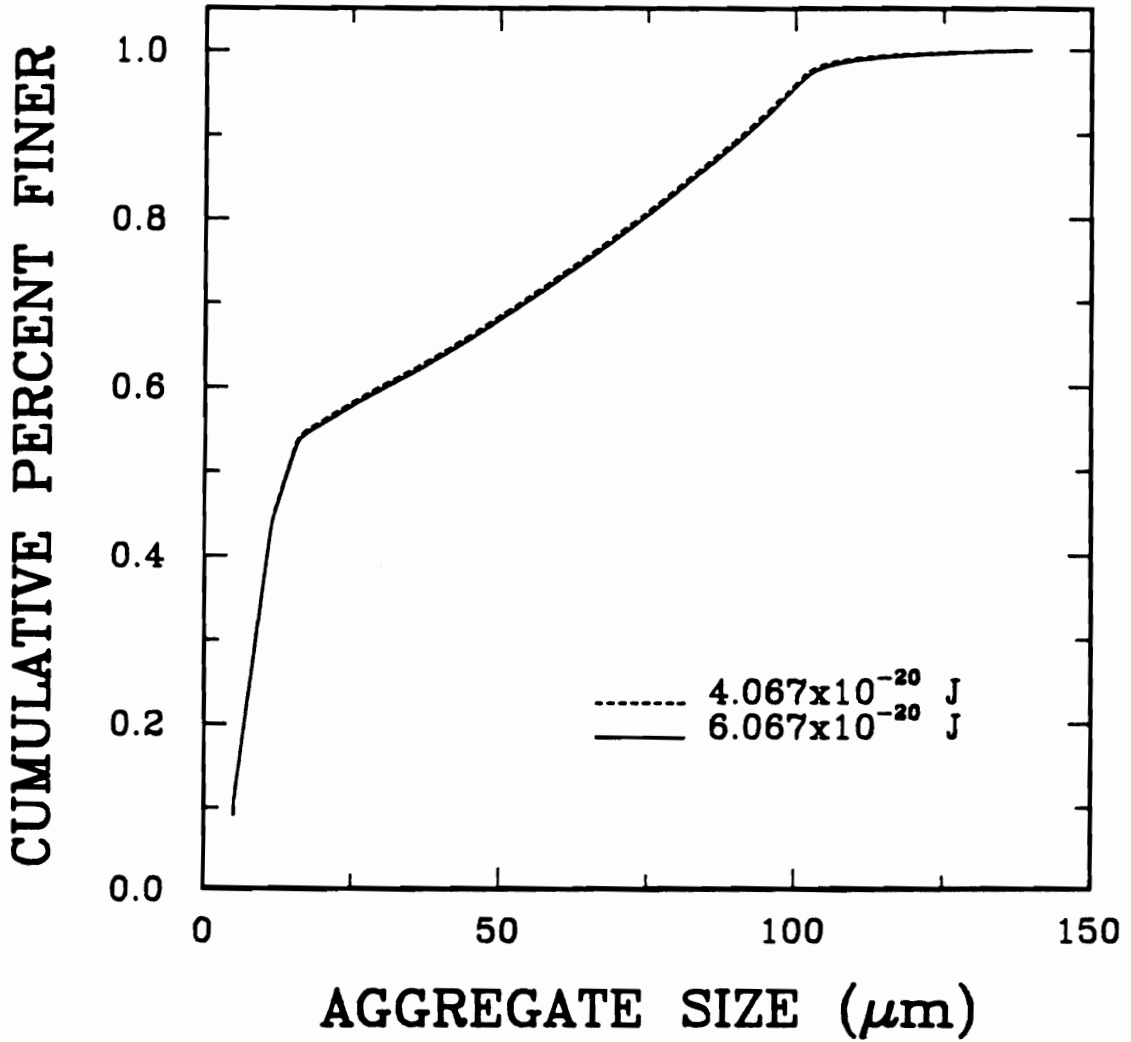


Figure 6.21. Equilibrium Cumulative Aggregate Size Distributions for Different Values of Hamaker Constant

$\beta = 0.138 (kT)^{-1}$;	$k_1 = 139.89$;	$k_3 = 507.38 \text{ dyne}^{-1}$;
$A = 1.0 \times 10^5 \text{ sec}^{-1}$;	Mixing = 1000 rpm;	$\zeta = -43 \text{ mV}$;
$C = -1.247 \text{ mJ/m}^2$;	$\gamma_{sw} = 26.72 \text{ dyne/cm}$.	

in the size of interacting particles, the kinetic energy increases significantly, which dominates the magnitude of collision efficiency. Therefore, the change of Hamaker constant shows a less pronounced effect on the collision efficiency of colliding particles of increasing size. As a consequence, the difference in the time at which the coagulation reaches a steady state is minor, and the equilibrium aggregate size distribution is almost identical.

6.5.4 *Effect of Hydrophobic Interaction on Coagulation Kinetics*

In order to understand the role of hydrophobic interaction in the coagulation kinetics under mixing condition, the simulations have been conducted by assigning different values to the hydrophobic interaction parameter C in Equation [4.10], keeping the other model parameters and system variables constant. The simulation results are given in Figures 6.22 and 6.23.

Figure 6.22 shows that if the magnitude of the hydrophobic interaction parameter C decreases from 1.247 mJ/m^2 to 1.147 mJ/m^2 , the time at which the coagulation proceeds with a conceivable rate increases significantly, from 0.001 seconds to 0.3 seconds. However, the time at which the coagulation reaches equilibrium increases only slightly, from 0.1 seconds to 0.4 seconds. This phenomenon is similar to what has been observed in the simulation of the effect of zeta potential on the coagulation kinetics as shown in Figure 6.18.

It is interesting to note that a further decrease in the magnitude of the hydrophobic interaction parameter to 1.407 mJ/m^2 causes the coagulation to proceed in an inconceivable rate as shown in Figure 6.22. After the coagulation is allowed to proceed for 2 hours in the simulation, the results show that 99.99% of the particles are still existing as individual primary particles.

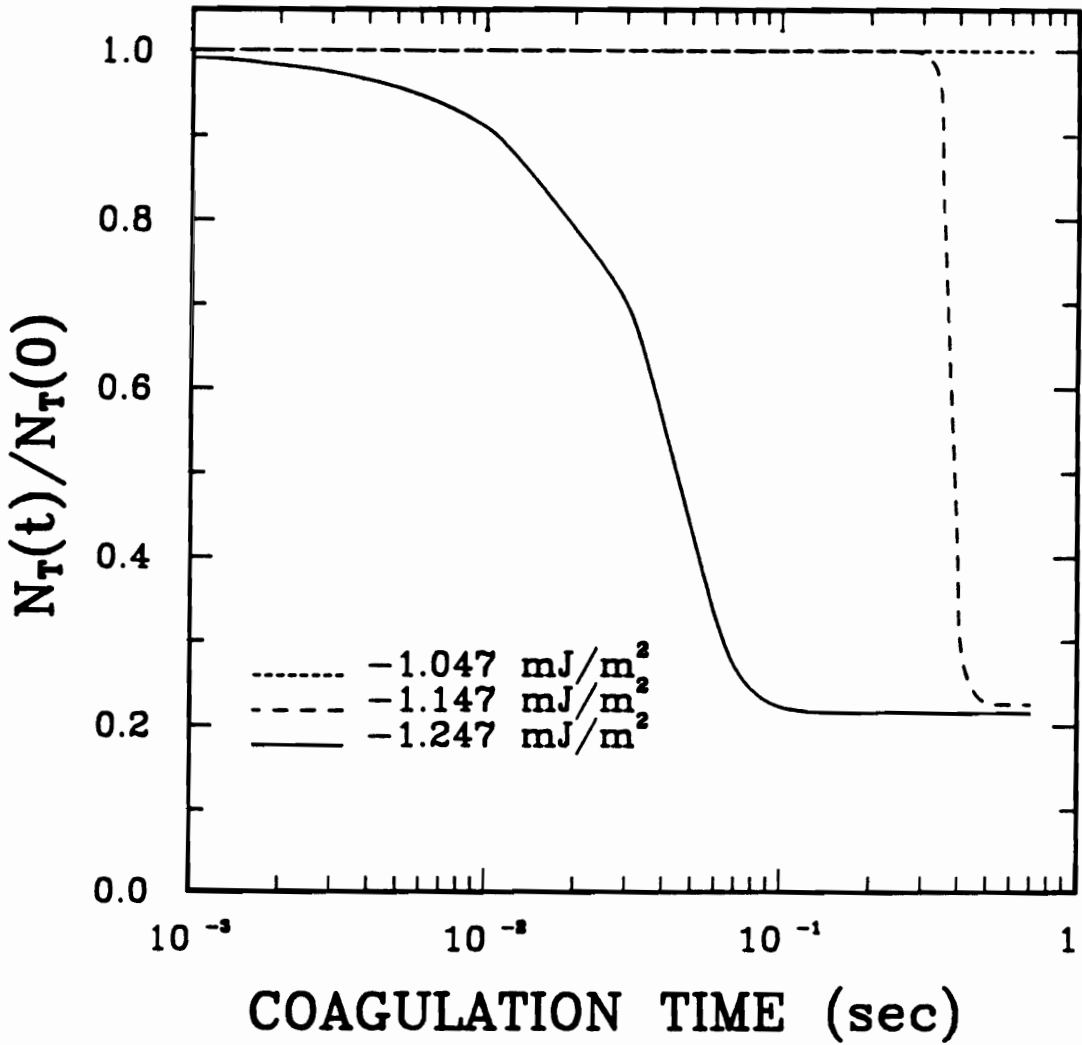


Figure 6.22. Changes of Dimensionless Number Concentration as a Function of Coagulation Time for Different Values of HI Parameter C

$\beta = 0.138 (kT)^{-1}$; $k_1 = 139.89$; $k_3 = 507.38 \text{ dyne}^{-1}$;
 $A = 1.0 \times 10^5 \text{ sec}^{-1}$; *Mixing* = 1000 rpm; $\zeta = -43 \text{ mV}$;
 $A_{131} = 3.31 \times 10^{-21} \text{ J}$; $\gamma_{sw} = 26.72 \text{ dyne/cm}$.

To understand the simulation results, it is helpful to examine the calculated values of V_{\max} , α , $\omega(a_1, a_1)$ and $k(1, 1)$ as tabulated in Table 6.3. Table 6.3 shows that as the value of hydrophobic interaction parameter C in Equation [4.10] decreases, the interaction energy barrier between the primary particles increases dramatically, giving a significantly decreased collision efficiency at the given mixing rate. As a result, the dimer formation rate constant decreases several orders of magnitude as shown in Table 6.3. Therefore, the initiation of dimer formation and hence the formation of high order aggregates are delayed significantly as found in the simulation.

Table 6.3. Calculated Values of V_{\max} , α and $k(1, 1)$ for Three Different Values of Hydrophobic Interaction Parameter C

C	mJ/m^2	-1.247	-1.147	-1.047
V_{\max}	kT	67.6	161.3	294.2
α		5.66×10^{-1}	1.35×10^{-6}	1.45×10^{-8}
$k(1, 1)$	sec^{-1}	7.69×10^{-8}	1.83×10^{-13}	1.96×10^{-21}

However, Figure 6.23 shows that the equilibrium aggregate size distribution does not change considerably as the value of hydrophobic interaction parameter C changes from $1.247 \text{ mJ}/m^2$ to $1.147 \text{ mJ}/m^2$. As has been discussed in Section 6.5.2, the less sensitivity of equilibrium aggregate size distribution to the changes of C values in the mentioned range may also be attributed to the fact that these changes do not affect the breakage rate constant and only slightly affect the values of the aggregation rate constants between the primary particles and the aggregates of increasing size. If a value of

-1.047 mJ/m^2 is used for the hydrophobic interaction parameter C in the simulation, it is not surprising to obtain a mono size distribution of the feed size as has been given in Figure 6.23. This is because the coagulation has not proceeded significantly after allowing for a two-hour coagulation in the simulation as illustrated in Figure 6.22.

The above simulation results suggest that the hydrophobic interaction is another important variable, along with the zeta potential, in controlling the coagulation kinetics of a hydrophobic colloidal suspension. It has been shown in Chapter 4 that the dispersion/coagulation of a hydrophobic colloidal suspension is determined mainly by the balance of repulsive electrostatic interaction and attractive hydrophobic interaction as illustrated in Figure 4.2. This statement has been proven qualitatively by the above simulation results.

In Chapter 3, it was found experimentally that as the surface hydrophobicity of coal samples decreases by oxidation with increasing temperatures, the pH range over which the coal sample coagulates decreases significantly as shown in Figures 3.1 and 3.2. This indicates that the maximum surface potential for effective coagulation decreases substantially as surface hydrophobicity decreases. These experimentally observed coagulation results of fine coal suspensions of different surface hydrophobicities are qualitatively in good agreement with what has been obtained from the simulation of coagulation kinetics.

6.5.5 Effect of Interfacial Tension on Coagulation Kinetics

It is believed that the solid/water interfacial tension plays an important role in determining the aggregate size distribution. Therefore, the effects of solid/water interfacial tension on the coagulation kinetics and equilibrium aggregate size distribution

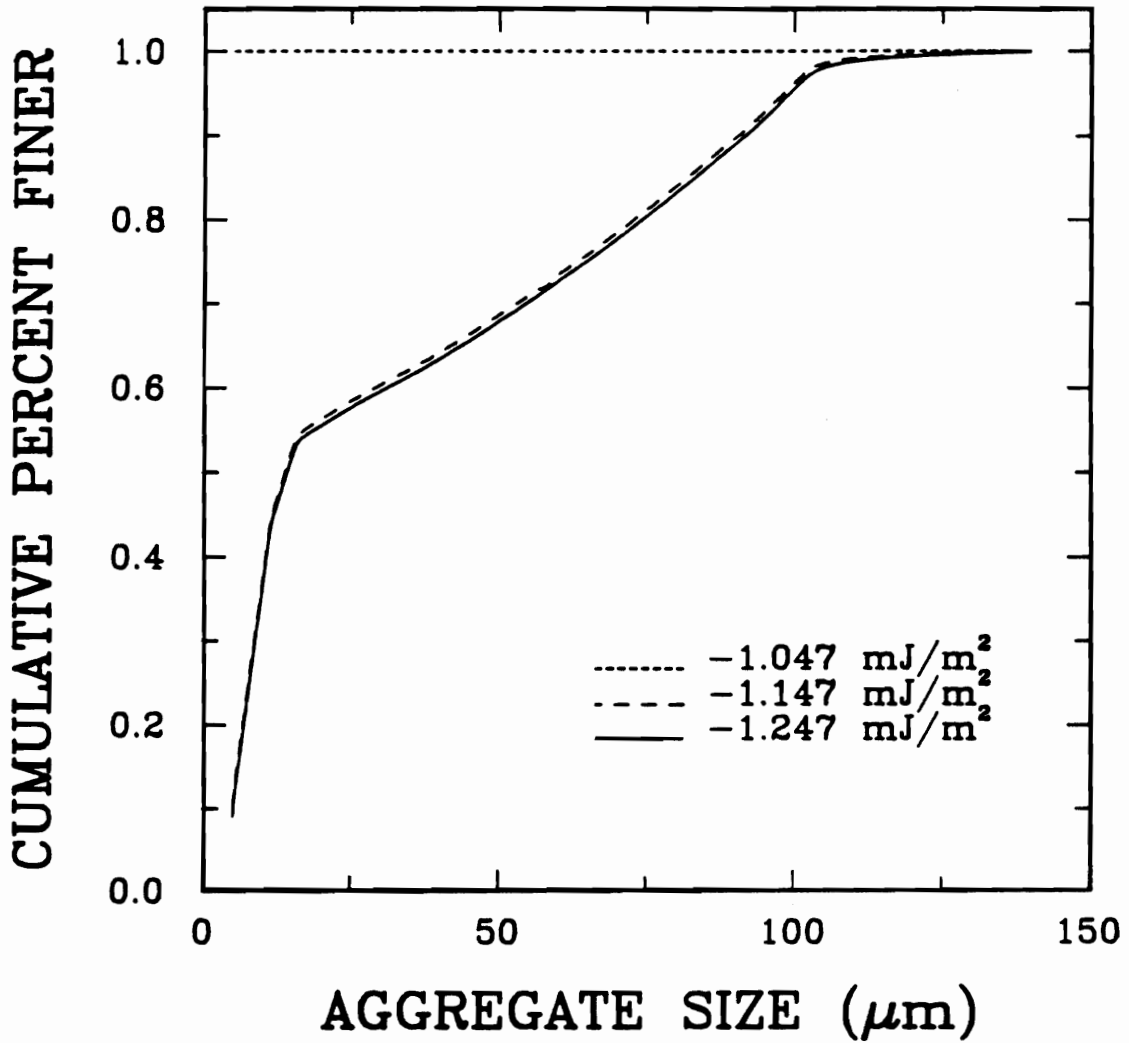


Figure 6.23. Equilibrium Cumulative Aggregate Size Distributions for Different Values of Hydrophobic Interaction Parameter C

$$\begin{array}{lll}
 \beta = 0.138 \text{ (} kT \text{)}^{-1}; & k_1 = 139.89; & k_3 = 507.38 \text{ dyne}^{-1}; \\
 A = 1.0 \times 10^5 \text{ sec}^{-1}; & \text{Mixing} = 1000 \text{ rpm}; & \zeta = -43 \text{ mV}; \\
 A_{131} = 3.31 \times 10^{-21} \text{ J}; & \gamma_{sw} = 26.72 \text{ dyne/cm}. &
 \end{array}$$

have also been studied by the simulation. The results are presented in Figures 6.24 and 6.25.

Figure 6.24 shows, as expected, that different values of solid/water interfacial tensions do not exhibit any significant impact on the coagulation kinetics. However, the dimensionless number concentration shows a noticeable difference after coagulation reaches a steady state as illustrated in Figure 6.24, indicating a significant influence of solid/water interfacial tension on the ultimate aggregate size distribution. Figure 6.25 shows that by increasing the solid/water interfacial tension, the equilibrium aggregate size distribution shifts in the direction of increasing aggregate size, preserving the shape of the distribution.

It is well known that with an increase in the solid/water interfacial tension, the energy associated with creating unit interface increases correspondingly. As a result, greater shear force is required to create new solid/water interface by breaking the aggregates of the same size but larger solid/water interfacial tension. To meet this requirement, only the aggregates of larger size can, at a given mixing intensity, possess sufficient shear force to cause them to be broken. Calculations have shown that with the increase in the solid/water interfacial tension from 27.72 *dyne/cm* to 30.72 *dyne/cm*, the d_b value changes from 105.51 μm to 111.8 μm , corresponding to a shift of top aggregate size. Since less number of classes of aggregates is subjected to the breakage in the higher solid/water interfacial tension of aggregates, only a small amount of daughter aggregates is produced from breakage, resulting in the equilibrium aggregate size distribution shifting in the increasing size direction.

In summary, the above simulations collectively show that the aggregation rate constant between primary particles is the most important factor in determining the coagulation kinetic behavior, while the equilibrium aggregate size distribution is most likely determined by the relative magnitude of the aggregation rate constants, forming the ag-

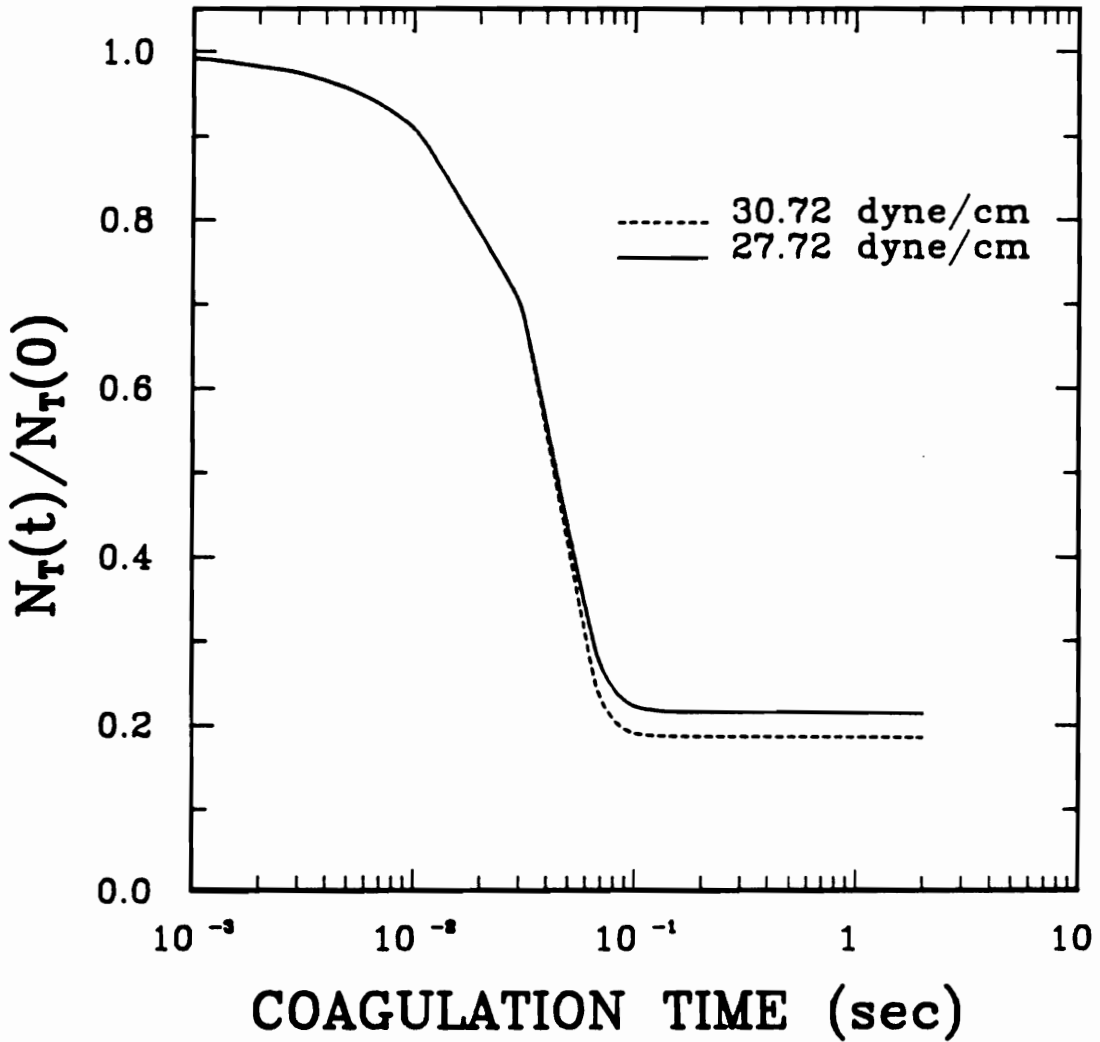


Figure 6.24. Changes of Dimensionless Number Concentration as a Function of Coagulation Time for Different Values of γ_{sw}

$\beta = 0.138 (kT)^{-1}$;	$k_1 = 139.89$;	$k_3 = 507.38 \text{ dyne}^{-1}$;
$A = 1.0 \times 10^5 \text{ sec}^{-1}$	Mixing = 1000 rpm;	$\zeta = -43 \text{ mV}$;
$A_{131} = 3.31 \times 10^{-21} \text{ J}$;	$C = -1.247 \text{ mJ/m}^2$.	

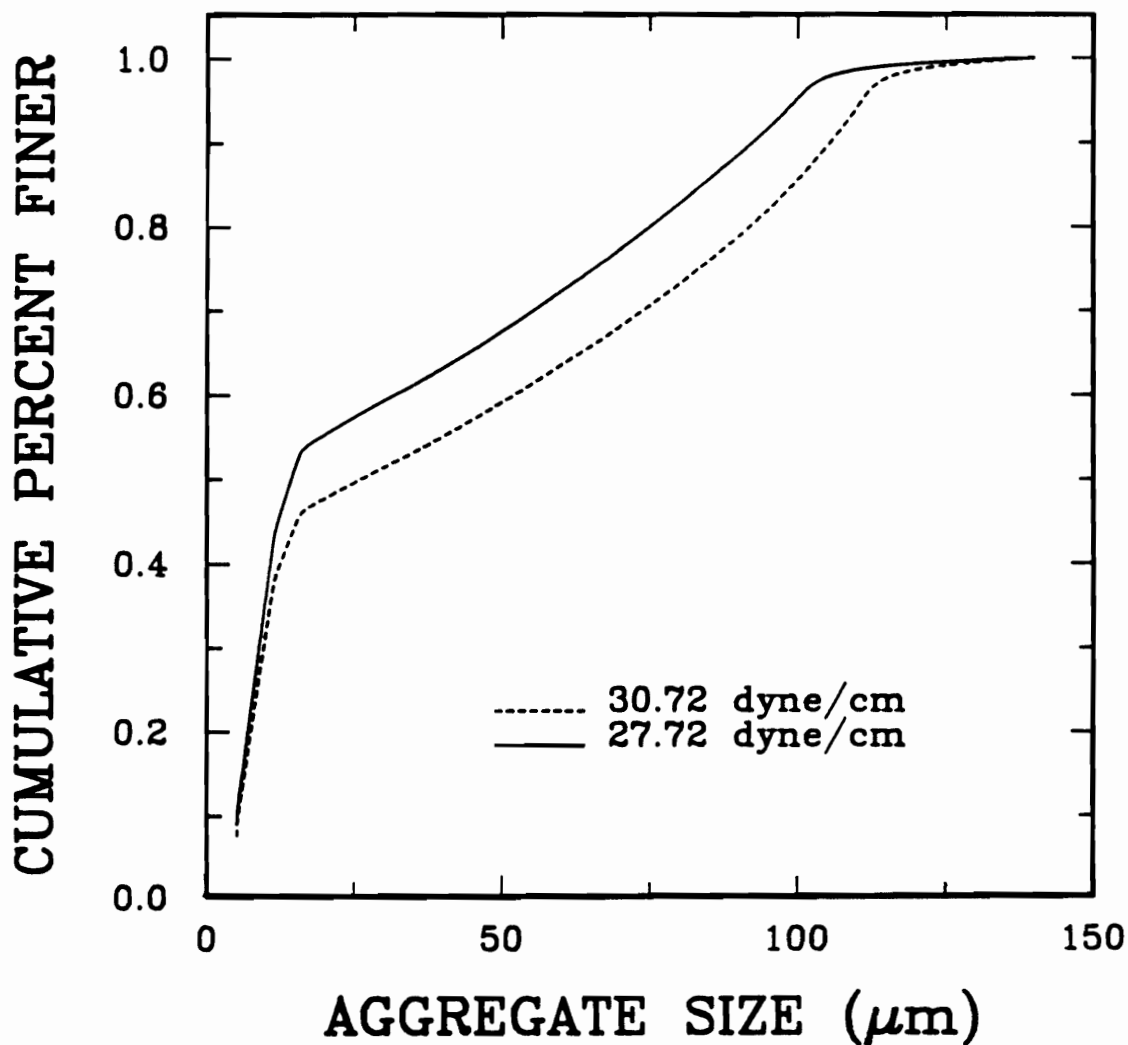


Figure 6.25. Equilibrium Cumulative Aggregate Size Distributions for Different Values of γ_{sw}

$$\begin{array}{lll}
 \beta = 0.138 (kT)^{-1}; & k_1 = 139.89; & k_3 = 507.38 \text{ dyne}^{-1}; \\
 A = 1.0 \times 10^5 \text{ sec}^{-1}; & \text{Mixing} = 1000 \text{ rpm}; & \zeta = -43 \text{ mV}; \\
 A_{131} = 3.31 \times 10^{-21} \text{ J}; & C = -1.247 \text{ mJ/m}^2. &
 \end{array}$$

gregates of larger size and the breakage rate constant of these aggregates. Therefore, any variable which affects one or more of the interaction energy barriers, kinetic energy, or collision frequency will change the coagulation kinetics more or less when it is subjected to changes in practice. These kinds of variables include surface potential, surface hydrophobicity, Hamaker constant, mixing rate and geometry of the mixing vessel. And any variable which affects the binding force or shear force will change the equilibrium aggregate size distribution and/or its functional form when this variable changes. Solid/water interfacial tension, mixing rate and geometry of mixing vessel are the examples.

6.6 Aggregate Size Distribution Measurement and Discussion

6.6.1 *Aggregate Size Distribution Measurement*

It has been proven that the accurate measurement of aggregate size and size distribution is a difficult, if not impossible, task (13-14). The available techniques for the study of aggregation give only global information for the overall degree of aggregation, but provide no unambiguous information about the size and size distribution. Although the techniques such as turbidity, light scattering and sedimentation have been used to determine the aggregate size distributions, none is an in-situ technology and, thus, only relative information is meaningful. To measure the aggregate size distribution for a coagulation system under severe mixing, these techniques may provide completely misleading information. Therefore, caution is called for when analyzing experimental data. In the present study, the classical Andreasen pipette technique (15) was used due to its simplicity. This technique is based on the principle of sedimentation.

Elkhorn No. 3 coal sample (3.5 %Ash) was used in this measurement. The sample was prepared by using the same procedures as those described in Chapter 3. The 450 ml suspension was made of 11 grams of minus 400 mesh coal sample in 10^{-3} M KCl solution of proper pH values. After mixed at 1000 rpm for 10 minutes using the mixer shown in Figure AI.1, the suspension was transferred into a graduated cylindrical flask and diluted to 550 ml corresponding to a suspension of 2% solid concentration. The suspension was then agitated by inverting the flask 20 times. Upon finishing the agitation, the solids in the suspension were allowed to settle and the timer was started. At the end of each given time interval, a 10 ml suspension at a fixed depth was taken by pipette and the settling distance was then determined by measuring the height between the free suspension surface and the sampling point. The solid in each 10 ml suspension was weighed after drying the sample in an oven set at 75 °C. The size of aggregate was calculated using the Stokes free settling law as given by:

$$d = 141 \left[\frac{h\eta}{t(\rho_s - \rho_l)} \right]^{1/2}, \quad [6.12]$$

in which h is the settling height in cm , η is the viscosity of the liquid in poises, t is the settling time in minutes, and ρ_s and ρ_l are the densities of solid and liquid, respectively. The diameter found thus is in μm . The solid percent finer than a corresponding size was calculated as $100 \times (W_t/W_0)$, where W_t and W_0 are the solid weights of 10 ml suspensions at time t and time 0, respectively.

To test the technique, a measurement of three different runs, each consisting of three different tests at identical conditions, was performed and the results are presented in Figure 6.26. The pH of the suspension for these measurements was adjusted to 8.4. Figure 2.26 shows a fairly good reproducibility between different runs. It was found

experimentally that the accurate data of size distribution for the aggregates of larger size is difficult to obtain using this technique because those aggregates settle very quickly.

The aggregate size distributions corresponding to different solution conditions are given in Figure 6.27 in which the data shown in Figure 6.26 are also included for the convenience of discussion. Figure 6.27 shows that the coal sample used in this study is of a fairly narrow size distribution as measured by dispersing coal in LOMAR-D, a coal dispersant. About 80% of the particles are less than $25 \mu\text{m}$. After the suspension is subjected to the coagulation at pH 8.4, the size distribution curve shifts significantly towards the larger size spectrum. The value of d_{50} , defined as the size of 50% finer, increases from $24 \mu\text{m}$ to $49 \mu\text{m}$, and the distribution becomes narrower. However, the aggregate size distribution of coal sample coagulating at pH 10.1 is almost identical to that of the initial particle size distribution, indicating that at this pH , coal particles are unable to coagulate. The results given in this figure are consistent with those presented in Figure 3.1 and agree qualitatively with the results predicted from the simulation as shown in Figure 6.19.

6.6.2 Discussion

The experimentally measured aggregate size distribution is compared with the distribution predicted in the simulation, as illustrated in Figure 6.28. The simulation has been conducted using the system parameters as found for Lower Cedar Grove coal samples at critical coagulation pH because of the similarities of these two coal samples. The d_{50} value of $16 \mu\text{m}$ as determined experimentally has been used as the primary particle size in this simulation. The values of $0.138 (kT)^{-1}$, 24.86, 1.07×10^5 , and 1.0×10^6 have been used for model parameters β , k_1 , k_3 , and A , respectively. Although the breakage function proposed by Broadbent and Callcott has been used in the simulations

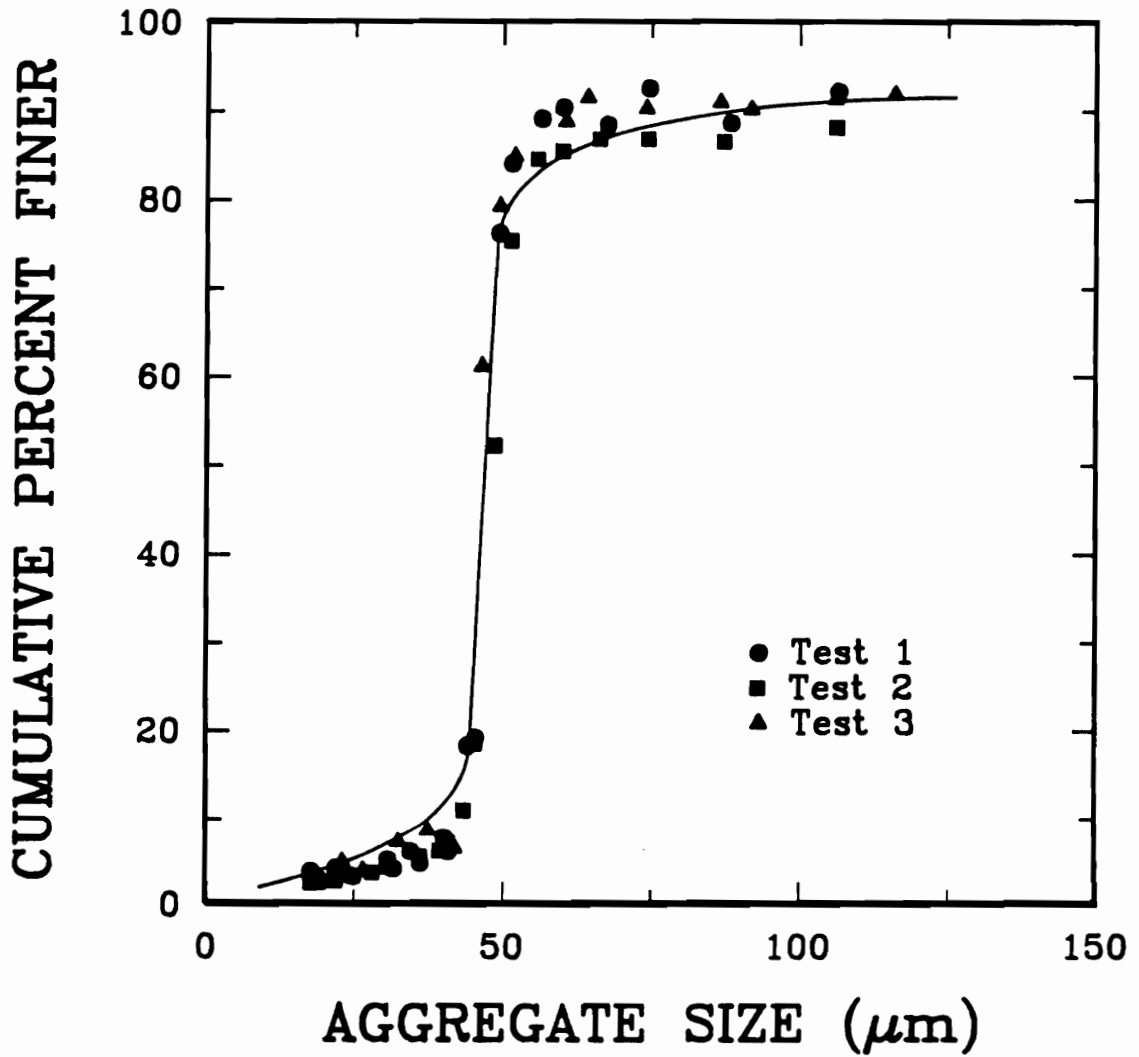


Figure 6.26. Aggregate Size Distribution Measured from Three Independent Runs Using the Andreasen Pipette Technique

Elkhorn No. 3 Coal Suspension of *pH* 8.4.

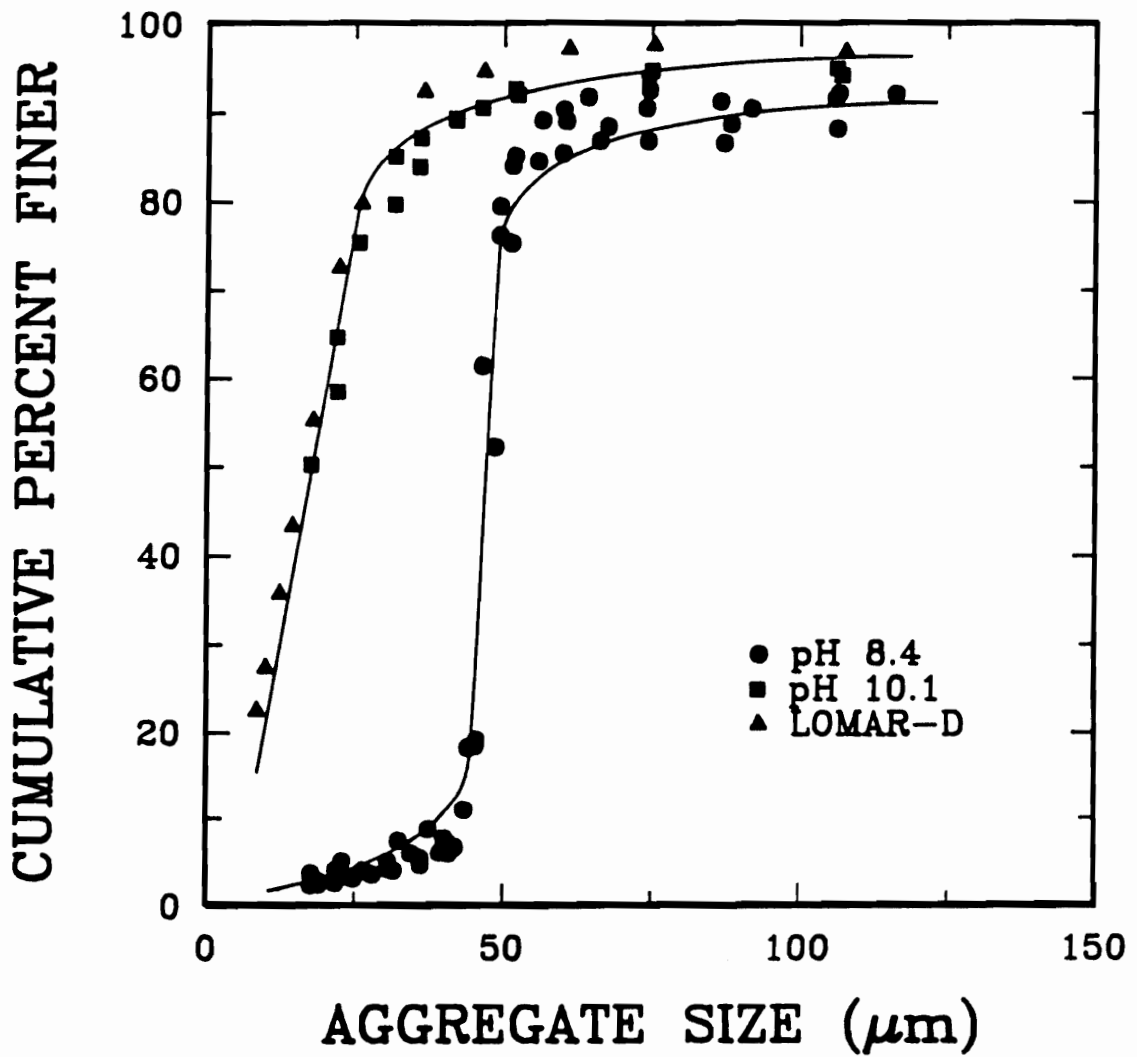


Figure 6.27. Aggregate Size Distribution of Elkhorn No. 3 Coal Formed in Three Different Suspension Conditions

as presented in the previous sections, a binary breakage function is used in this simulation in order to obtain a better agreement between experimental data and the simulation results. The daughter aggregate distribution in the binary breakage function is defined so that every aggregate consisting of an even number of primary particles will be broken into two fragments of equal size, or else into two fragments that fall in two successive classes. It has been found that the problem becomes even stiffer, and the convergence is rather slow when binary breakage function is used in the simulation.

A general agreement between aggregate size distributions, as measured experimentally and predicted from the simulation, is illustrated in Figure 6.28. The aggregate top size of approximately $50 \mu\text{m}$ as measured using Andreasen pipette technique is almost the same as that predicted from the simulation. The discrepancy found in the aggregate size range greater than $50 \mu\text{m}$ may be attributed to the inaccuracy of the aggregate size measurement using this technique as discussed previously. The simulation is also unable to predict a tail in the small size spectrum as experimentally measured due to the nature of the binary breakage function used in the simulation.

In spite of the general agreement between experimental data and simulation results, a few comments on the limitations of the experimental method and the theoretical models are worth mentioning. As is well known, the sedimentation method only gives the equivalent spherical particle size in which the porosity effect is completely ignored. Since the actual density of aggregates is smaller than that used in Equation [6.12], the top size of the aggregate obtained from the present measurement may underestimate the true value. However, the porosity correction can be made with the porosity model used in the population balance model. To do so, a calibration curve of settling rate as a function of aggregate size needs to be calculated by taking the apparent density of aggregate into account. The experimental aggregate size is evaluated from this calibration

curve based on the measured settling rate. In this case, the comparison may become more straightforward.

Primarily, the Andreasen pipette technique is an ex-situ technique which may create a completely different environment during the measurement, inducing further unintentional aggregation. The agitation by the inversion of the apparatus possibly initiates further aggregation between the aggregates of different sizes. Since it is unlikely that this type of agitation will generate a sufficiently strong shear force to break the aggregates significantly, the aggregation during this period may proceed without any aggregate breakage. Also, it is possible to induce further aggregation by differential sedimentation during the measurements. Even though the time elapsed by these two operations is fairly short, the simulation shows that it does not take very long to obtain effective coagulation as illustrated in Figure 6.14 for the suspension conditions used in this test. Therefore, the measured aggregate size distribution may be considered to be the same as that obtained in a coagulation process without any aggregate breakup being involved. Nevertheless, the measured size distribution can be predicted from the simulation if the binary breakage function is used as shown in Figure 6.28.

The value of 24.86 used in this simulation as the model parameter k_1 is determined by balancing the shear force and adhesion force exerting on the aggregate of top size as measured experimentally. A high value of 1×10^6 for the model parameter A has been used to ensure that all the aggregates of size greater than the top size will be broken upon the formation. Also a high value of 1.07×10^5 has been used for the model parameter k_3 to give an abrupt change in the breakage rate constant, which enables the simulation to predict a narrow aggregate size distribution as experimentally measured. Because of the expenses of computation time, no further simulation has been conducted that would give a best fit with the experimental result.

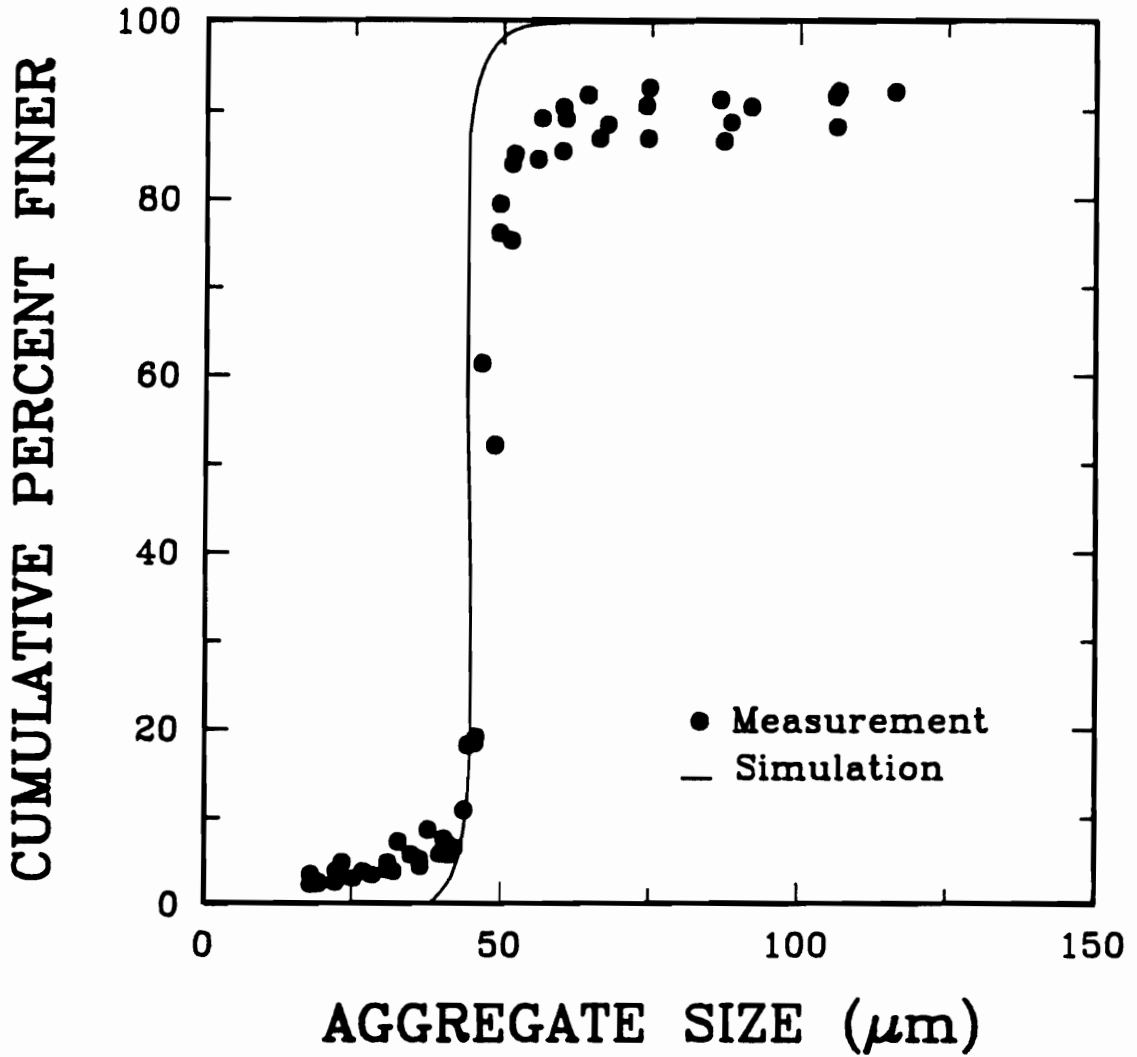


Figure 6.28. A Comparison of Aggregate Size Distributions Obtained from Computer Simulation and Experimental Measurements at *pH* 8.4

$\beta = 0.138 (kT)^{-1}$;	$k_1 = 24.86$	$k_3 = 1.07 \times 10^5 \text{ dyne}^{-1}$;
$A = 1.0 \times 10^6 \text{ sec}^{-1}$;	Mixing = 1000 rpm;	$\zeta = -43 \text{ mV}$;
$A_{131} = 3.31 \times 10^{-21} \text{ J}$;	$C = -1.247 \text{ mJ/m}^2$;	$\gamma_{sw} = 26.72 \text{ dyne/cm}$.

It is difficult at present to assess the validity of the model and to estimate the values of model parameters quantitatively because of the limitation of the techniques for the accurate in-situ determinations of aggregate size distributions. The limitation on the computer time due to the low stability of the problem (6) imposes additional difficulty on the study of the coagulation process using computer simulation. It is, therefore, necessary to develop a reliable in-situ technique for measuring the aggregate size distribution in order to have a better understanding of the details of the coagulation process and to improve the models and numerical procedures, such as the discreteness of the size classes.

6.7 Summary and Conclusions

Based on the population balance model developed in Chapter 5, a numerical scheme has been proposed to solve the coagulation kinetic equations. The standard Gear-method has been used in which the Jacobian Matrix is provided by the user.

The simulations have been conducted on the computer by changing one model parameter at a time to examine the feasibility of the coagulation kinetic model. The simulation results have shown that the model is fairly flexible for describing the coagulation process under different mixing conditions. The simulation results obtained by changing the system variables such as mixing condition, surface potential, and surface hydrophobicity are in reasonable agreement with what has been observed experimentally. The quantitative assessment of the model and the estimation of the values of the model parameters have proven difficult due to the lack of a reliable in-situ technique for determining aggregate size distribution.

6.8 References

1. Wang, C.S. and Friedlander, S.K., "The Self-Preserving Particle Size Distribution for Coagulation by Brownian Motion II. Small Particle Slip Correction and Simultaneous Shear Flow," *J. Colloid Interface Sci.*, 24, 170 (1967).
2. Lushnikov, A.A., "Evolution of Coagulation systems," *J. Colloid Interface Sci.*, 45, 549(1973).
3. Friedlander, S.K. and Wang, C.S., "The Self-Preserving Particle Size Distribution for Coagulation by Brownian Motion," *J. Colloid Interface Sci.*, 22, 126(1966).
4. Gelbard, F. and Seinfeld, J.H., "Numerical Solution of the Dynamic Equation for Particulate Systems," *J. Comp. Phys.*, 28, 357(1978).
5. Middleton, P. and Brock, J., "Simulation of Aerosol Kinetics," *J. Colloid Interface Sci.*, 54, 249(1976).
6. Vigil, R.D. and Ziff, R.M., "On the Stability of Coagulation-Fragmentation Population Balances," *J. Colloid Interface Sci.*, 133, 257 (1989).
7. Sastry, K.V.S. and Fuerstenau, D.W., "Size Distribution of Agglomerates in Coalescing Dispersed Phase Systems," *Ind. Eng. Chem. Fundam.*, 9, 145 (1970).
8. Lushnikov, A.A., "Evolution of Coagulating Systems II. Asymptotic Size Distributions and Analytical Properties of Generating Functions," *J. Colloid Interface Sci.*, 48, 400 (1974).
9. Peterson, T.W., Gelbard, F. and Seinfeld, J.N., "Dynamics of Source-Reinforced, Coagulating, and Condensing Aerosols," *J. Colloid Interface Sci.*, 63, 426 (1978).
10. Ramabhadran, T.E., Peterson, T.W. and Seinfeld, J.H., "Dynamics of Aerosol Coagulation and Condensation," *AIChE J.*, 22, 840 (1976).
11. Valioulis, I.A., "Coagulation in the Aquatic Environment: Theory and Practice," *Adv. Colloid Interface Sci.*, 24, 81 (1986).
12. Davis, M.E., *Numerical Methods & Modeling for Chemical Engineers*, John Wiley & Sons, New York, (1984).
13. Fuerstenau, D.W., Li, C., and Hanson, J.S., "Shear Flocculation and Carrier Flotation of fine Hematite," in *Production and Processing of fine Particles*, ed. by Plumpton, A.J., Can. IMM, 329 (1988).
14. Li, C. and Fuerstenau, D.W., "The Effect of the Adsorption of Sodium Dodecyl Sulfate on the Stability of Stirred Suspensions of Hematite Fines," in *Flocculation in Biotechnology and Separation Systems*, ed. by Attia, Y.A., Elsevier Science Publishers, B.V. Amsterdam, 695 (1987).
15. Taggart, A.F., *Handbook of Mineral Processing*, John Wiley Inc., 19:122 (1945).

CHAPTER 7 SUMMARY AND CONCLUSIONS

The major findings of the present investigation and their contributions to the understanding of hydrophobic interaction energy in coagulation processes may be summarized as follows:

1. Suspensions of weakly hydrophobic fine particles, such as oxidized coal, can only coagulate at suspension pH values near their *i.e.p.* where the electrical surface potential is minimal. This coagulation behavior can be satisfactorily explained in terms of the classical DLVO theory. However, suspensions of strongly hydrophobic fine particles, such as fresh coal and highly methylated silica, can still readily coagulate at high suspension pH values where the surface retains high electrical potential. A significant net repulsive interaction energy is then expected based on the classical DLVO theory. In order to explain the observed phenomenon, an additional attractive interaction energy, not accounted for in the classical DLVO theory, has to be assumed to overcome this repulsive energy to induce the coagulation. Using the back-calculation method proposed in this study, this additional attractive interaction energy, known as *hydrophobic interaction energy*, has been found to be on the order of $2900 kT$ for very hydrophobic particles in aqueous electrolyte solutions.

2. The surface hydrophobicity of the samples used in the coagulation experiments has been characterized by measuring the heat of wetting with heptane and the heat of heptane displacement with water, and by determining the contact angles of liquid methylene iodide and water on the solids from which the dispersion (W_a^d) and nondispersion (W_a^{nd}) components of the work of adhesion of water on the solid have been calculated. The results collectively show that W_a^{nd} is more sensitive to the changes in surface chemistry and is a good representation of the surface hydrophobicity. The hydrophobic interaction energy has been found to be important in the coagulation of very strongly hydrophobic particles of hydrophilic numbers less than 0.35.

3. On the basis of the mean-field gradient approach, an extension to the classical DLVO theory has been made by including a hydrophobic interaction energy term in the theory. The constants characterizing the hydrophobic interaction energy of each sample have been obtained by solving the equations corresponding to the coagulation boundary conditions. A three-parameter expression has been derived to generalize the hydrophobic interaction energy term as a function of W_a^{nd} and the distance between two interacting particles. The detailed calculations show that the hydrophobic interaction energy is the driving force for inducing the coagulation of very hydrophobic solids. In this case, van der Waals attractive interaction is less significant and the hydrophobic attraction coupled with the electrostatic repulsion determines the stability of the suspension. The theory developed in the present investigation allows elucidation of the mechanism behind the selective fine coal coagulation process.

4. The aggregation rate process has been analysed on the basis of thermodynamics and hydrodynamics. By considering a binary aggregation process, the aggregation rate constant has been formulated by including the role of kinetic energy in the classical stability theory. On the other hand, the aggregate breakage has been examined by considering the balance of the thermodynamic surface force and the hydrodynamic shear force. A functional form relating breakage rate constant to the relative magnitude of these two forces has been derived. A population balance model has been developed by incorporating both aggregate growth and breakage rate processes to describe coagulation kinetics behavior.

5. A simulation scheme has been proposed by solving coagulation kinetic equations numerically using the Gear method in which a Jacobian matrix needs to be provided by the user. The simulation has been conducted using different values for each model parameter to examine the feasibility of the model. The simulation results show that the model is flexible enough to cover a wide range of coagulation conditions. The simulations performed under various system conditions, such as mixing rate, suspension pH , Hamaker constant and surface hydrophobicity, show a reasonable agreement with what has been observed experimentally.

CHAPTER 8 RECOMMENDATIONS FOR FUTURE RESEARCH

On the basis of the present study, further research in the following areas is recommended:

1. Coagulation studies using other strongly hydrophobic materials, such as graphite and Teflon colloids, should be carried out to provide further evidence of the importance of the role of hydrophobic interaction in coagulation. Tests to study the effect of the temperature on the coagulation behavior of very hydrophobic particles would be helpful in understanding the mechanism of hydrophobic interaction. A detailed study of coagulation using both hydrophobic and hydrophilic materials in various types of liquids, organic and inorganic, could provide valuable information. From this information, it should be possible to delineate the nature of the structural force which has been proven to be an interesting but very difficult topic to study.
2. In order to have a better understanding of the nature of the hydrophobic interaction, the surface force between hydrophobic surfaces in various liquids or solutions should be measured directly as a function of surface hydrophobicity. A correlation between surface hydrophobicity and decay length of the hydrophobic interaction could be obtained from this measurement, which would make it pos-

sible to determine the validity of the mean-field gradient theory as applied to the study of structural forces and would provide a means to judge the assumption regarding constant decay length used in the present study. The direct force measurement would also provide values for the critical film thickness as a function of surface hydrophobicity, which could be used to check the expression derived in the present investigation. The measurement of the force between surfaces of different hydrophobicities, such as solid/droplet or solid/bubble, is of particular importance from a practical point of view.

3. It might also be instructive to use a more reliable technique than flow microcalorimetry, to characterize the surface hydrophobicity as a function of surface composition in order to have a more precise representation of surface hydrophobicity. These techniques might include the rate of wetting method for measuring contact angles and ellipsometry for determining the film thickness coupled with various surface analysis techniques such as IR and XPS. From these more representative and accurate measurements, one should be able to come up with a better correlation between surface hydrophobicity and hydrophobic interaction energy.
4. To understand the mechanism of hydrophobic interaction from the molecular theory, the statistical thermodynamics approach should be used to study the structure of the liquid thin layer adjacent to the solid surfaces. The information regarding liquid structure obtained from a Monte Carlo or a molecular dynamics simulation would be very helpful in deriving a theoretical force law using the mean-field gradient approach. This is particularly important for systems of two

different surfaces with varying surface hydrophobicities which are often encountered in practice.

5. It has been shown that the convergence of simulation is sometimes very slow due to the instability of the process. To reduce the computer running time, the simulation scheme needs to be improved, which would make it possible to study the coagulation kinetics more systematically and to examine and improve the models. More importantly, a reliable in-situ method for measuring aggregate size and size distribution should be used in order to determine the generality of the model and find the values of model parameters.

APPENDIX I CALCULATION OF KINETIC ENERGY

This appendix provides a step-by-step procedure for calculating kinetic energy of particles suspended in an aqueous medium. The structure and geometry of the mixer used in the coagulation tests is shown in Figure AI.1. The calculation of kinetic energy for a silica sample with an average particle size of $3.2 \mu m$ is also given as an example.

Calculation of Viscosity of Concentrated Suspension (Ref.1):

$$\frac{\eta}{\eta_l} = 1 + 2.5\bar{C} + 10\bar{C}^2 + 0.62 \exp\left(\frac{1.875\bar{C}}{1 - 1.595\bar{C}}\right), \quad [A - 1]$$

in which:

$$\bar{C} = \frac{(W_s/\rho_s)}{(W_s/\rho_s) + (W_l/\rho_l)}, \quad [A - 2]$$

where η and η_l are the viscosities of suspension and liquid, respectively, W_s and W_l are the weights of solid and liquid, respectively, and ρ_s and ρ_l are the densities of solid and liquid, respectively.

For silica suspension, we have:

$$\begin{aligned} W_s &= 5 \text{ g} \\ W_l &= 500 \text{ g} \end{aligned}$$

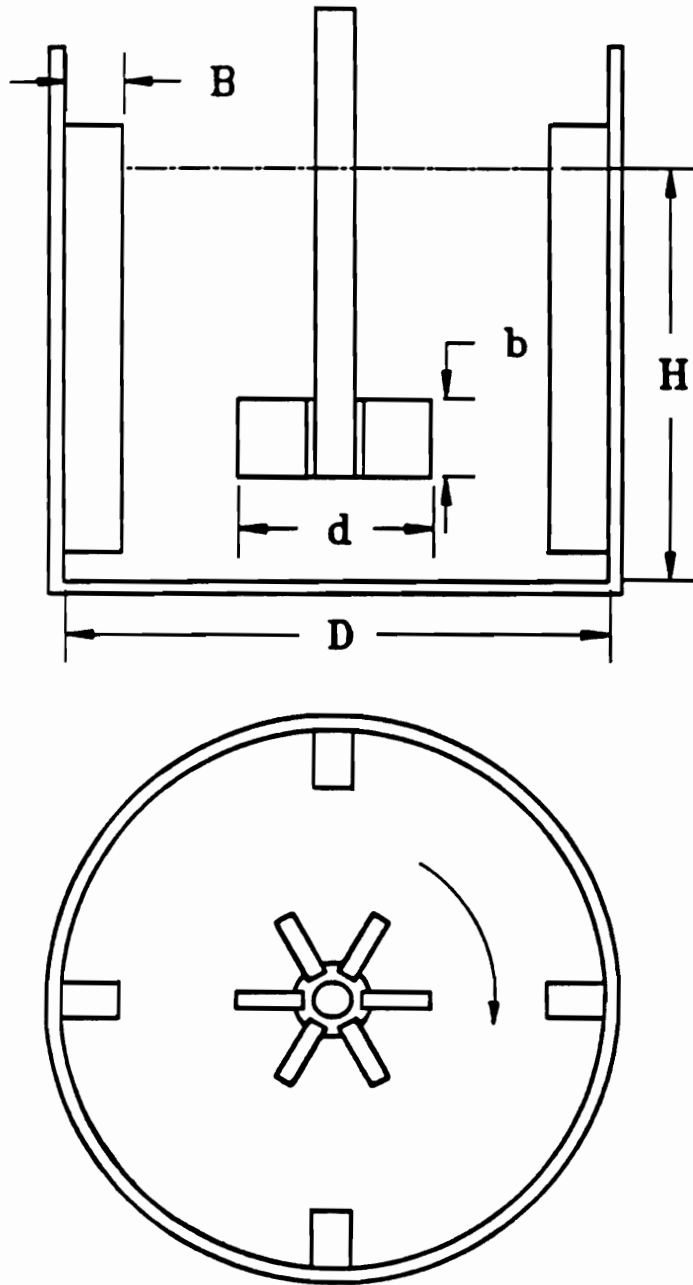


Figure AI.1. Structure and Geometry of the Mixer Used in Coagulation Tests

$$\begin{aligned}\rho_s &= 2.63 \text{ g/cm}^3 \\ \rho_l &= 1.00 \text{ g/cm}^3 \\ \eta_l &= 0.0089 \text{ poise(g/cms)} .\end{aligned}$$

The calculated \bar{C} is 0.00379 and the viscosity of suspension is 0.0145 poise.

Check Fully Baffled Condition (Ref. 2-Eq. 1.55a):

$$(B/D)^{1.2} \times n_B = 0.256 < 0.35 , \quad [A - 3]$$

where B is the width of the baffles (0.9 cm), D is the diameter of the container (8.9 cm) and n_B is the number of the baffles (4). Since calculated result of 0.26 is less than the fully baffled condition of 0.35, partially baffled condition should be used in calculating the power consumption.

Calculation of Critical Reynolds Number R_c (Ref.2-Eq. 1.57):

$$R_c = \frac{25}{(b/D)} \left(\frac{d}{D} - 0.4 \right)^2 + \left(\frac{b/D}{0.11(b/D) - 0.0048} \right), \quad [A - 4]$$

where b is the width of the impeller (3.2 cm) and d is the diameter of the impeller (3.9 cm). R_c was found to be 10.45 for the geometry of the mixer. The factor of Z , corresponding to R_c of 10.45, is found from Fig. 1.38 of Ref. 2 to be 0.991.

Calculation of Maximum Power Consumption (Ref. 1-Eq. 1.58):

$$N_{Pmax} = \frac{\bar{A}}{R_c} + \bar{B} Z^{\bar{P}} \left(\frac{H}{D} \right)^{(0.35+b/D)}, \quad [A - 5]$$

in which H is the height of suspension (8.5 mm), and:

$$\bar{A} = 14 + (b/D) [670(d/D - 0.6)^2 + 185] \quad [A - 6]$$

$$\bar{B} = 10^{[1.3-4(b/D-0.5)^2 - 1.14(d/D)]} \quad [A - 7]$$

$$\bar{p} = 1.1 + 4(b/D) - 2.5(d/D - 0.5)^2 - 7(b/D)^4 . \quad [A - 8]$$

For the mixer used in this study, it was found that $\bar{A} = 86.82$, $\bar{B} = 5.266$ and $\bar{p} = 2.412$. Therefore, the calculated $N_{Pmax} = 13.29$.

Calculation of Power Number

Power number N_{PB} with partially baffled condition is estimated by the following equation (Ref. 2-Eq. 1.60):

$$N_{PB} = N_{Pmax} - (N_{Pmax} - N_{P\infty}) [1 - 2.9(B/D)^{1.2} n_B]^2 , \quad [A - 9]$$

where $N_{P\infty}$ is the power number obtained at R , tending to infinity, i.e. (Ref. 2-Eq. 1.61):

$$N_{P\infty} = \bar{B}(0.6/1.6)^{\bar{p}} (H/D)^{(0.35+b/D)} . \quad [A - 10]$$

For the mixer used, $N_{P\infty}$ is calculated to be 0.479. N_{PB} is then found to be 12.46.

Calculation of the Rate of Energy Dissipation per Unit Mass

According to Nagata (Ref. 2-Eq. 1.52), power input, P , is related to the power number, N_{PB} , in the following manner:

$$P \cong N_{PB} \rho N^3 d^5 , \quad [A - 11]$$

where N is rotational speed and ρ is the density of suspension.

Based on the definition of the rate of turbulent energy dissipation per unit mass, it can be calculated in the following way:

$$\bar{\varepsilon} = \frac{P}{M} = \frac{N_{PB} N^3 d^5}{\bar{V}} \quad [A - 12]$$

where M is the mass of and \bar{V} is the volume of the suspension (502 cm^3). In the present case, $\bar{\varepsilon}$ is calculated to be $1.30 \times 10^4 \text{ cm}^2/\text{s}^3$ for $N = 500 \text{ rpm}$.

Calculation of Relative Particle Velocity (3)

From the Kolmogorov theory of isotropic turbulence, the relative velocity U_r depends on the turbulent scale λ , which is calculated as follows:

$$\lambda = (v^3/\varepsilon)^{1/2}, \quad [A - 13]$$

Under the conditions where the particle size is much smaller than the microscale of turbulence, the relative velocity at the moment of collision is given by (Ref. 3-Eq.4a):

$$U_r = (1/15)^{1/2} (\bar{\varepsilon}/v)^{1/2} (a_1 + a_2), \quad [A - 14]$$

where a_1 and a_2 are radius of approaching particles. However, if the particle size is larger than microscale of turbulence, the inertia mechanism is applicable and the relative velocity should be calculated by using the following equation (Ref. 2-Eq.4b):

$$U_r = 1.37 \bar{\varepsilon}^{1/3} (a_1 + a_2)^{1/3}, \quad [A - 15]$$

In our system, λ is calculated to be $39 \mu\text{m}$, which is much larger than the particle size of $3.6 \mu\text{m}$. Therefore, Eq. [A-14] is used and U_r is calculated to be 0.0884 cm/s .

Calculation of Kinetic Energy

From the obtained relative velocity of approaching particles, the kinetic energy provided by mixing can be calculated as:

$$V_k = 1/2\mu U_r^2 , \quad [A - 16]$$

where μ is the reduced mass of particles, which is defined by $1/\mu = 1/m_1 + 1/m_2$, in which m_1 and m_2 are the mass of approaching particles. In this example, V_k is calculated to be $1.26 \times 10^{-13} \text{erg}$ or $3.05 kT$.

The kinetic energy has been calculated using the procedures proposed in this appendix as a function of mixing rate for the coal samples of different particle sizes. The results are given in Figure AI.2. It is clearly shown in this figure that there exists a logarithmic linear relation between kinetic energy and mixing rate. The kinetic energy provided by mixing increases significantly as the mixing rate increases. At the same mixing rate, the kinetic energy increases with increasing particle size.

References

1. Chia, Y.H. and Somasundaran, P., "A Theoretical Approach to Flocculation in Carrier Flotation for Beneficiation of Clay," *Colloids Surfaces*, 8, 187 (1983).
2. Nagata, S., *Mixing: Principles and Applications*, Halsted Press, New York, (1975).
3. Delichatsios, M.A. and Probstein, R.F., "Coagulation in Turbulent Flow: Theory and Experiment," *J. Colloid Interface Sci.*, 51, 394 (1975).

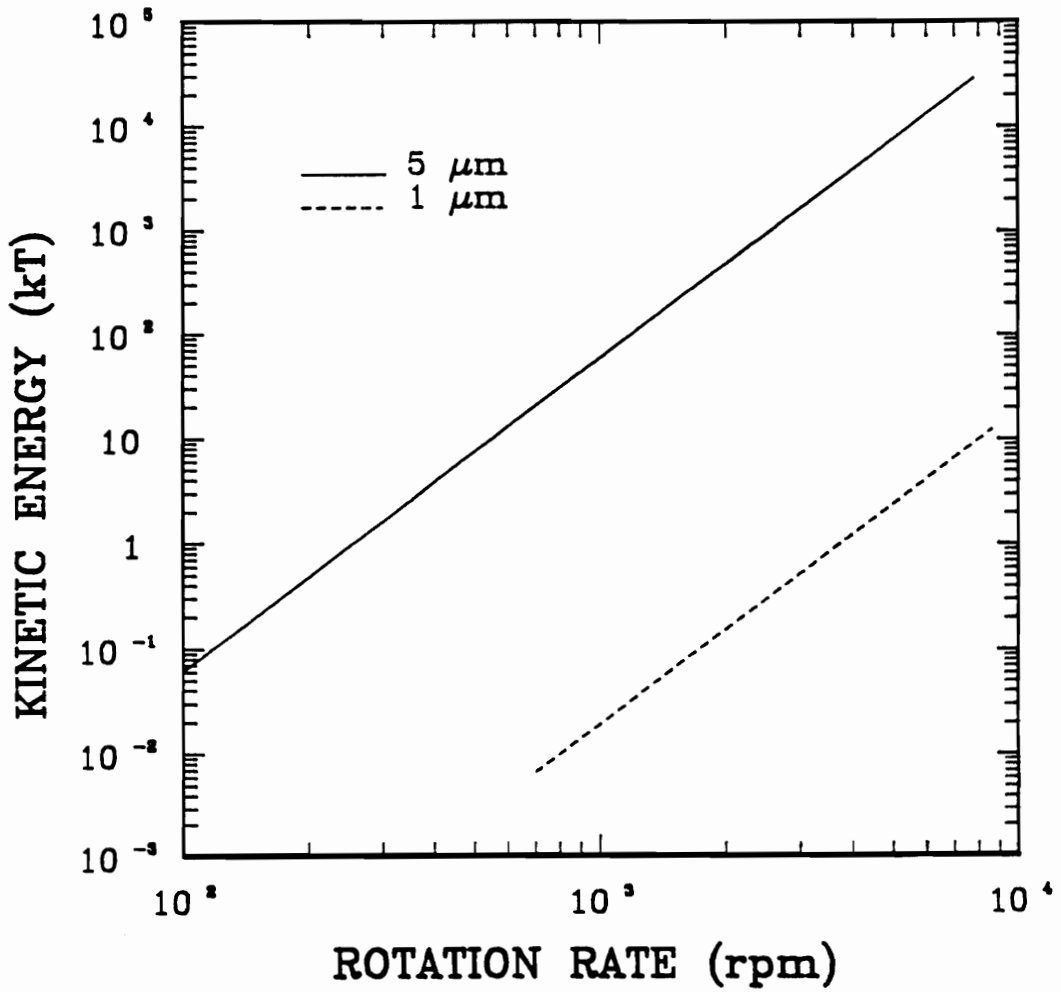


Figure A1.2. Kinetic Energy as a Function of Mixing Rate for Coal Samples of Two Different Particle Sizes

APPENDIX II PROGRAM FOR COAGULATION KINETIC SIMULATION

This appendix includes a program used in simulation of coagulation kinetics. This program can only be run on the mainframe since the numerical subroutine is called. The time of run varies depending on the input which determines the stiffness of the differential equations.

```

C *****
C * A FILE DESCRIBING THE PROGRAM "SIMUT FORTRAN". IT IS A PROGRAM *
C * FOR CALCULATING INTERACTION ENERGY BARRIER, KINETIC ENERGY, *
C * BINDING FORCE AND SHEAR FORCE, SIMULATING SHEAR COAGULATION WITH *
C * BREAKAGE AS A RATE PROCESS USING SUBROUTINE IVPAG WITH SINGLE *
C * PRECISION PROVIDED BY IMSL IN WHICH USER JACOBIAN MATRIX IS *
C * INCLUDED. FOLLOWED IS AN EXAMPLE OF THE DATA FILE: *
C * 8.85E-12 -43.0 2.5E-4 100.0 103 1.247E-3 5 1.0 5 2 *
C * 6.07E-20 3.7E-20 1.35 1.0 26.72 100.00 0.138 5.0738E2 4000 *
C * 8.5 8.9 3.2 3.9 1000.0 5.0 500.0 0.0089 0.9 4.0 *
C * 0.001 0.01 0.05 1 1 *
C * 10 10 40 30 300 *
C * 2 2 1 1 4 *
C * 1 1 2 3 34 *
C *****
C DATA FILE DESCRIPTION
C 1-1=PERM=PERMIBILITY OF VACUUM
C 1-2=ZET=ZETA POTENTIAL (MV)
C 1-3=R(1)=PRIMARY PARTICLE SIZE (CM)
C 1-4=G=RECIPICAL DOUBLE LAYER THICKNESS (ANGSTON)
C 1-5=DO=DECAY LENGTH OF HYDROPHOBIC INTERACTION (ANGSTON)
C 1-6=VC=STRENGTH OF HYDROPHOBIC INTERACTION (J/M**2)
C 1-7=NM=A NUMBER CONTROLLING OUTPUT INTERVAL (5=OUTPUT EVERY 5 SIZEES)
C 1-8=BSG=PREEXPONENTIAL CONSTANT OF BREAKAGE RATE FORMULA (SEC**-1)
C 1-9=IRUN=NUMBER OF DIFFERENT STEP SIZES USED IN ITERATION
C 1-10=NB=CONTROLLING THE BREAKAGE FUNCTION (:BINARY BREAKAGE)
C 2-1=A(1)=HAMAKER CONSTANT OF SOLID IN VACUUM (J)

```

```

C 2-2=A(2)=HAMAKER CONSTANT OF WATER IN VACUUM (J)
C 2-3=RU(1)=DENSITY OF SOLID (GRAM/CM**3)
C 2-4=RU(2)=DENSITY OF WATER (GRAM/CM**3)
C 2-5=DGAM=SOLID/WATER INTERFACIAL TENSION (DYNE/CM)
C 2-6=BET=ADJUSTABLE PARAMETER FOR CONTROLLING CONTACT SURFACE AREA,
C   CHANGING THIS WILL CHANGE THE SIZE AT WHICH BREAKAGE STARTS
C 2-7=ALPHA=ADJUSTABLE PARAMETER FOR CONTROLLING DECAY OF STABILITY
C   RATIO WITH KINETIC ENERGY AND ENERGY BARRIER
C 2-8=COEF=ADJUSTABLE PARAMETER CONTROLLING THE RATE OF CHANGE OF
C   BREAKAGE RATE WITH SHEAR FORCE
C 2-9=MXSTEP=MAXIMUM STEP SIZE FOR SUBROUTINE IVPAG
C 3-1=H=HEIGHT OF SUSPENSION IN MIXER (CM)
C 3-2=D=DIAMETER OF MIXER CONTAINER (CM)
C 3-3=B=WIDTH OF IMPELLAR (CM)
C 3-4=DP=DIAMETER OF IMPELLAR (CM)
C 3-5=AN=ROTATION RATE OF IMPELLAR (RPM)
C 3-6=WS=WEIGHT OF SOLID IN SUSPENSION (GRAM)
C 3-7=WL=WEIGHT OF LIQUID IN SUSPENSION (GRAM)
C 3-8=ETAL=VISCOSITY OF LIQUID (POISE)
C 3-9=BW=WIDTH OF BAFFLE (CM)
C 3-10=BN=NUMBER OF BAFFLES
C 4-I=RCON(I)=STEP SIZE OF EACH GROUP ITERATIONS
C 5-I=IECD(I)=END VALUE OF EACH GROUP ITERATIONS
C 6-I=ISTP(I)=INCREMENT OF EACH GROUP ITERATIONS
C 7-I=ISP(I)=START VALUE OF EACH GROUP ITERATIONS
C *****
C * DESCRIPTION OF VARIABLE AND CONSTANT SIZE *
C *****
PARAMETER (NEQ=500, NPARAM=50)
REAL PARAM(NPARAM),RWKSP(256520)
REAL R(NEQ),PORO(NEQ),HO(510),WT(NEQ),ADM(1,1)
REAL HM(NEQ,NEQ),VT(510),A(3),RU(2),RCON(5),IECD(5),ISTP(5),ISP(5)
REAL FS(NEQ),RN(NEQ),FB(500),VK(500,500),VM(500,500)
COMMON /RATE/VM/SELECT/FB/BREAK/VK
COMMON /WORKSP/RWKSP
EXTERNAL FCN,IVPAG,SSET,FCNJ
C *****
C * INPUT OF DATA *
C *****
READ(5,*)PERM,ZET,R(1),G,DO,VC,NM,BSG,IRUN,NB
READ(5,*)(A(I),I=1,2),RU,DGAM,BET,ALPHA,COEF,MXSTEP
READ(5,*)H,D,B,DP,AN,WS,WL,ETAL,BW,BN
READ(5,*)(RCON(I),I=1,IRUN),(IECD(I),I=1,IRUN),(ISTP(I),I=1,IRUN)
READ(5,*)(ISP(I),I=1,IRUN)
C *****
C * INITIATION OF VARIABLE FOR CHOOSING NUMERICAL METHOD AND THE *
C * ACCURACY OF SYSTEM *
C *****
HINIT=1.0E-3
MITER=1

```

```

INORM=2
IMETH=2
CALL SSET(NPARAM,0.0,PARAM,1)
PARAM(1)=HINIT
PARAM(4)=MXSTEP
PARAM(10)=INORM
PARAM(12)=IMETH
PARAM(13)=MITER
IDO=1
TOL=1.0E-6
C *****
C * CALCULATION OF COMBINED HAMAKER CONSTANT A(3) *
C *****
A(3)=(SQRT(A(1))-SQRT(A(2)))*(SQRT(A(1))-SQRT(A(2)))
A(3)=A(3)/(1.0-2.5E18*SQRT(A(1)*A(2)))
C *****
C * CALCULATION OF PARTICLE CLASS SIZE R(500) & POROSITY PORO(500) *
C *****
PORO(1)=0
PORO(2)=0.2
R(2)=R(1)/(1.0-PORO(2))**0.33333
DO 10 I=3,NEQ
Z1=FLOAT(I)
PZ=((1.0-PORO(I-1))/(Z1-1.0))**0.33333
EPZ=PZ*PZ*(1.0-PZ)/(1.0-PZ**5)
PORO(I)=1.0-Z1*(1.0-EPZ)*(1.0-PORO(I-1))/(Z1-EPZ)
10 CONTINUE
CT1=4.0*3.1416/3.0
WT(1)=CT1*R(1)**3*RU(1)
DO 20 I=2,NEQ
Z1=FLOAT(I)
R(I)=R(1)*(Z1/(1.0-PORO(I)))**0.33333
WT(I)=CT1*R(I)**3*((1.0-PORO(I))*RU(1)+PORO(I)*RU(2))
20 CONTINUE
DO 15 I=1,NEQ
FS(I)=R(I)*2.0
15 CONTINUE
WRITE(6,*)'SIZE SPECTRIUM'
WRITE(6,900)(FS(I),I=1,NEQ,NM),FS(NEQ)
C *****
C * CALCULATION OF INTERACTION ENERGY BARRIER VM(1000,1000) *
C *****
HO(1)=0.1
DO 100 I=2,10
HO(I)=HO(I-1)+0.1
100 CONTINUE
DO 110 I=11,510
HO(I)=HO(I-1)+1.0
110 CONTINUE
CT1=A(3)*4.0507E27

```

```

CT2=PERM*ZET*ZET*2.3988E15
CT3=VC*DO*2.4304E8
DO 120 I=1,NEQ
IF(I.GT.(NEQ-I))GOTO 121
DO 120 J=I,NEQ-I
RR=R(I)*R(J)/(R(I)+R(J))
DO 130 K=1,510
VT(K)=-CT1*RR/HO(K)+CT2*RR*ALOG(1.0+EXP(-HO(K)/G))
+-CT3*RR*EXP(-HO(K)/DO)
130 CONTINUE
VD=0
DO 140 K=1,510
IF((VT(K)-VD).LE.0)GOTO 140
VD=VT(K)
HM(I,J)=HO(K)
140 CONTINUE
VM(I,J)=VD
120 CONTINUE
C *****
C * CALCULATION OF MIXING ENERGY DISSIPATION *
C * CALCULATION OF SUSPENSION VISCOSITY *
C *****
121 VL=WS/RU(1)+WL/RU(2)
RN(1)=WS*3.0/(4.0*RU(1)*R(1)**3*3.1416*VL)
WRITE(6,*)'RN(1)=' ,RN(1)
DO 150 I=2,NEQ
RN(I)=0
150 CONTINUE
CT1=WS/(RU(1)*VL)
RUP=(WS+WL)/VL
CM=1.875*CT1/(1.0-1.595*CT1)
ETAS=ETAL*(1.0+2.5*CT1+10.0*CT1*CT1+0.62*EXP(CM))
ANU=ETAS/RUP
C *****
C * CALCULATION OF POWER NUMBER *
C *****
DD=DP/D
BD=B/D
HD=0.35+BD
HD=(H/D)**HD
AM=14.0+BD*(670.0*(DD-0.6)*(DD-0.6)+185.0)
P=1.1+4.0*BD-2.5*(DD-0.5)*(DD-0.5)-7.0*BD**4
BM=1.3-4.0*(BD-0.5)*(BD-0.5)-1.14*DD
BM=10.0**BM
C *****
C * CALCULATION OF CRITICAL REYNOLDS NUMBER *
C *****
RC=25.0/BD*(DD-0.4)*(DD-0.4)+BD/(0.11*BD-4.8E-3)
Z=9.91E-1
C *****

```

```

C * ESTIMATION OF FULLY BAFFLE CONDITION AND CALCULATION OF POWER *
C * NUMBER (ANP) *
C *****
  BWD=(BW/D)**1.2*BN
  IF((0.35-BWD).LT.0)GOTO 80
  YY=(1.0-2.9*BWD)*(1.0-2.9*BWD)
  ANPIFT=BM*(0.6/1.6)**P*HD
  ANP=AM/RC+BM*Z**P*HD
  ANP=ANP-(ANP-ANPIFT)*YY
  GOTO 95
80  ANP=AM/RC+BM*Z**P*HD
C *****
C * CALCULATION OF ENERGY DISSIPATION RATE PER UNIT MASS (EP) *
C *****
95  EP=ANP*AN**3*DP**5/VL/60.0**3
    ALMD=(ANU**3/EP)**0.25
C *****
C * CALCULATION OF KINETIC ENERGY AT CRITICAL SEPARATION HM *
C * VK(1000,1000) IN KT *
C *****
  CT1=SQRT(1.0/15.0)*SQRT(EP/ANU)
  CT2=1.37*EP**0.33333
  CT3=1.2152E13
  DO 200 I=1,NEQ
    IF(I.GT.(NEQ-I))GOTO 201
    DO 200 J=I,NEQ-I
      RR=R(I)*R(J)/(R(I)+R(J))
      WR=WT(I)*WT(J)/(WT(I)+WT(J))
      IF((ALMD-4*RR).GT.0)THEN
        VK(I,J)=CT1*(R(I)+R(J)+HM(I,J)*1.0E-8)
      ELSE
        VK(I,J)=CT2*(R(I)+R(J)+HM(I,J)*1.0E-8)**0.33333
      ENDIF
      VK(I,J)=CT3*VK(I,J)*VK(I,J)*WR
200  CONTINUE
201  WRITE(6,*)'ENERGY BARRIER ((VM(I,J),J=1,N),I=1,N)'
      WRITE(6,900)(VM(1,J),J=1,NEQ,NM)
      WRITE(6,*)'KINETIC ENERGY ((VK(I,J),J=1,N),I=1,N)'
      WRITE(6,900)(VK(1,J),J=1,NEQ,NM)
C *****
C * CALCULATION OF STABILITY RATIO EXP(-ALPHA*(VM-VK))=VM(I,J) *
C *****
  DO 210 I=1,NEQ
    IF(I.GT.(NEQ-I))GOTO 211
    DO 210 J=I,NEQ-I
      IF(VK(I,J).LT.15)VK(I,J)=15.0
      CT1=VM(I,J)-VK(I,J)
      IF(CT1.GT.0)THEN
        VM(I,J)=EXP(-ALPHA*CT1)
      ELSE

```

```

        VM(I,J)=1.0
        ENDIF
210  CONTINUE
C *****
C *  CALCULATION OF COLLISION RATE = VK(I,J) *
C *****
211  CT1=0.81116*SQRT(EP/ANU)
        CT2=4.304*EP**0.33333
        CT3=7/3
        DO 225 I=1,NEQ
        IF(I.GT.(NEQ-I))GOTO 226
        DO 225 J=I,NEQ-I
        RR=R(I)*R(J)/(R(I)+R(J))
        IF((ALMD-4*RR).GT.0)THEN
        VK(I,J)=CT1*(R(I)+R(J)+HM(I,J)*1.0E-8)**3
        ELSE
        VK(I,J)=CT2*(R(I)+R(J)+HM(I,J)*1.0E-8)**CT3
        ENDIF
225  CONTINUE
226  WRITE(6,*)'STABILITY RATIO ((W(I,J),J=1,N),I=1,N) '
        WRITE(6,900)(VM(1,J),J=1,NEQ,NM),VM(1,NEQ)
        WRITE(6,*)'COLLISION RATE ((J(I,J),J=1,N),I=1,N) '
        WRITE(6,900)(VK(1,J),J=1,NEQ,NM),VK(1,NEQ)
C *****
C *  CALCULATION OF RATE CONSTANTS K(I,J)=VM(I,J) *
C *****
        DO 235 I=1,NEQ
        IF(I.GT.(NEQ-I))GOTO 238
        DO 235 J=I,NEQ-I
        VM(I,J)=VK(I,J)*VM(I,J)
235  CONTINUE
238  DO 236 I=1,NEQ-1
        DO 236 J=NEQ-I,NEQ
        VM(I,J)=0
236  CONTINUE
        VM(NEQ,NEQ)=0
        DO 237 I=1,NEQ
        DO 237 J=I+1,NEQ
        VM(J,I)=VM(I,J)
237  CONTINUE
        DO 239 I=1,NEQ
        VM(I,I)=0.5*VM(I,I)
239  CONTINUE
        WRITE(6,*)'RATE CONSTANTS ((RK(I,J),J=1,N,NM),I=1,N,NM) '
        WRITE(6,900)(VM(1,J),J=1,NEQ,NM)
C *****
C *  CALCULATION OF SHEAR FORCE FS(500) *
C *****
        CT1=RU(2)*EP/ANU*0.5/15.0
        CT2=0.5*1.37*1.37*EP**0.6667*RU(2)

```

```

DO 220 I=1,NEQ
IF((2.0*R(I)-ALMD).GT.0)THEN
FS(I)=CT2*(2.0*R(I))**2.66667
ELSE
FS(I)=CT1*(2.0*R(I))**4
ENDIF
220 CONTINUE
C *****
C * CALCULATION OF ADHESION FORCES FB(40) *
C *****
DO 240 I=1,NEQ
FB(I)=R(I)*R(I)*(1.0-PORO(I))**0.66667*DGAM*BET
240 CONTINUE
WRITE(6,*)'FS(N)'
WRITE(6,900)(FS(I),I=1,NEQ,NM),FS(NEQ)
WRITE(6,*)'FB(N)'
WRITE(6,900)(FB(I),I=1,NEQ,NM),FB(NEQ)
C *****
C * CALCULATION OF SELECTION FUNCTION S(500)=FB(500) *
C *****
DO 250 I=1,NEQ
IF((FB(I)-FS(I)).GT.0)THEN
FB(I)=0
ELSE
FB(I)=BSG*(1.0-EXP(COEF*(FB(I)-FS(I))))
ENDIF
250 CONTINUE
WRITE(6,*)'SELECTIVE FUNCTION (S(I),I=1,N,NM)'
WRITE(6,900)(FB(I),I=1,NEQ,NM),FB(NEQ)
C *****
C * CALCULATION OF BREAKAGE FUNCTION BF(500,500)=VK(I,J) *
C *****
DO 255 I=1,NEQ
DO 255 J=1,NEQ
VK(I,J)=0
255 CONTINUE
CT1=0.63212
DO 260 I=2,NEQ
CT2=FLOAT(I)
VK(1,I)=(1.0-EXP(-1.0/(CT2-1.0)))/CT1*CT2
260 CONTINUE
DO 270 I=3,NEQ
CT3=FLOAT(I)-1.0
DO 270 J=2,I-1
CT4=FLOAT(J)
VK(J,I)=(EXP(-(CT4-1.0)/CT3)-EXP(-CT4/CT3))/CT1*(CT3+1.0)/CT4
270 CONTINUE
WRITE(6,*)'BREAKAGE FUNCTION ((B(I,J),J=1,NEQ,NP),I=1,NEQ,NP)'
WRITE(6,900)(VK(1,J),J=1,NEQ,NM)
C *****

```

```

C * NUMERICAL SOLUTION OF POPULATION BALANCE EQUATION USING A *
C * SUBROUTINE PROVIDED BY MAINFRAME *
C *****
WRITE(6,*)'OUTPUT OF SIMULATION AS MASS DISTRIBUTION'
CALL IWKIN(256520)
SMF=1
T=0
DO 600 K=1, IRUN
DO 500 IEND=ISP(K), IECD(K), ISTD(K)
TEND=IEND*RCON(K)
CALL IVPAG(IDO,NEQ,FCN,FCNJ,ADM,T,TEND,TOL,PARAM,RN)
SM1=RN(1)
DO 310 I=2,NEQ
SM1=SM1+RN(I)*FLOAT(I)
310 CONTINUE
FS(1)=RN(1)
SM2=RN(1)
DO 355 I=2,NEQ
FS(I)=FS(I-1)+RN(I)*FLOAT(I)
SM2=SM2+RN(I)
355 CONTINUE
DO 345 I=1,NEQ
FS(I)=FS(I)/FS(NEQ)
345 CONTINUE
WRITE(6,901)T,SM1,SM2
WRITE(6,900)(FS(I),I=1,NEQ,NM),FS(NEQ)
IF((FS(1)-0.5).GT.0)GOTO 500
CJUG=ABS(SMF-SM2/SM1)
IF((CJUG-0.00001).LT.0)GOTO 700
SMF=SM2/SM1
500 CONTINUE
600 CONTINUE
700 IDO=3
CALL IVPAG(IDO,NEQ,FCN,FCNJ,ADM,T,TEND,TOL,PARAM,RN)
900 FORMAT(1X,5(E11.5,1X))
901 FORMAT(1X,'TIME=',E10.5,2X,'SM1=',E10.5,2X,'SM2=',E10.5)
STOP
END
C *****
C * THE FOLLOWING IS A SUBROUTINE PROVIDING ORDINARY DIFFERENTIAL *
C * EQUATIONS FOR NUMERICAL ROUTINE FROM MAINFRAM *
C *****
SUBROUTINE FCN (NEQ,T,RN,YPRIME)
C RN(NEQ)=PREVIOUS NUMBER CONCENTRATION OF PARTICLES OF EACH CLASS
C YPRIME(NEQ)=PRESENT NUMBER CONCENTRATION (OUTPUT)
C RK(NEQ,NEQ)=RATE CONSTANTS OF COAGULATION
C NEQ=NUMBER OF CLASS TO BE CONSIDERED IN SIMULATION
C T=INCREMENT OF TIME FOR SIMULATION
C B(NEQ,NEQ)=BREAKAGE FUNCTION OF FLOCS
C S(NEQ)=SELECTION FUNCTION

```

```

REAL RN(NEQ),VM(500,500),FB(500),VK(500,500),YPRIME(NEQ)
REAL RWKSP(256520)
COMMON /RATE/VM/SELECT/FB/BREAK/VK
COMMON /WORKSP/RWKSP
DO 10 K=1,NEQ
YPRIME(K)=0
10 CONTINUE
DO 20 K=1,NEQ
YPRIME(1)=YPRIME(1)-VM(1,K)*RN(1)*RN(K)
20 CONTINUE
DO 30 K=2,NEQ
YPRIME(1)=YPRIME(1)+VK(1,K)*FB(K)*RN(K)
30 CONTINUE
YPRIME(2)=YPRIME(2)+VM(1,1)*RN(1)*RN(1)-FB(2)*RN(2)
DO 40 K=1,NEQ
YPRIME(2)=YPRIME(2)-VM(2,K)*RN(2)*RN(K)
40 CONTINUE
DO 50 K=3,NEQ
YPRIME(2)=YPRIME(2)+VK(2,K)*FB(K)*RN(K)
50 CONTINUE
DO 90 I=3,NEQ-1
YPRIME(I)=YPRIME(I)-FB(I)*RN(I)
DO 60 K=1,I-1
YPRIME(I)=YPRIME(I)+0.5*VM(K,I-K)*RN(K)*RN(I-K)
60 CONTINUE
DO 70 K=1,NEQ
YPRIME(I)=YPRIME(I)-VM(I,K)*RN(I)*RN(K)
70 CONTINUE
DO 80 K=I+1,NEQ
YPRIME(I)=YPRIME(I)+VK(I,K)*FB(K)*RN(K)
80 CONTINUE
90 CONTINUE
YPRIME(NEQ)=YPRIME(NEQ)-FB(NEQ)*RN(NEQ)
DO 85 K=1,NEQ-1
YPRIME(NEQ)=YPRIME(NEQ)+0.5*VM(K,NEQ-K)*RN(K)*RN(NEQ-K)
85 CONTINUE
DO 95 K=1,NEQ
YPRIME(NEQ)=YPRIME(NEQ)-VM(NEQ,K)*RN(NEQ)*RN(K)
95 CONTINUE
RETURN
END
C *****
C * THIS IS A SUBROUTINE REQUIRED FOR CALLING THE NUMERICAL *
C * TECHNIQUE ROUTINE WITH JACOBIAN BEING PROVIDED BY USER *
C *****
SUBROUTINE FCNJ(NEQ,T,RN,DYPDY)
REAL DYPDY(NEQ,NEQ),RN(NEQ)
REAL VM(500,500),FB(500),VK(500,500)
REAL RWKSP(256520)
COMMON /WORKSP/RWKSP

```

```

COMMON /RATE/VM/SELECT/FB/BREAK/VK
DO 10 I=1,NEQ
DO 10 J=1,NEQ
DYPDY(I,J)=0
10 CONTINUE
DYPDY(1,1)=-2.0*VM(1,1)*RN(1)
DO 20 I=2,NEQ
DYPDY(1,1)=DYPDY(1,1)-VM(1,I)*RN(I)
20 CONTINUE
DO 30 I=2,NEQ
DYPDY(1,I)=-VM(1,I)*RN(1)+VK(1,I)*FB(I)
30 CONTINUE
DYPDY(2,1)=2.0*VM(1,1)*RN(1)-VM(2,1)*RN(2)
DYPDY(2,2)=-VM(2,1)*RN(1)-2.0*VM(2,2)*RN(2)-FB(2)
DO 40 I=3,NEQ
DYPDY(2,2)=DYPDY(2,2)-VM(2,I)*RN(I)
40 CONTINUE
DO 50 I=3,NEQ
DYPDY(2,I)=-VM(2,I)*RN(2)+VK(2,I)*FB(I)
50 CONTINUE
DO 100 J=3,NEQ-1
DO 60 I=1,J-1
DYPDY(J,I)=VM(I,J-I)*RN(J-I)-VM(J,I)*RN(J)
60 CONTINUE
DYPDY(J,J)=-2.0*VM(J,J)*RN(J)-FB(J)
DO 70 I=1,J-1
DYPDY(J,J)=DYPDY(J,J)-VM(J,I)*RN(I)
70 CONTINUE
DO 80 I=J+1,NEQ
DYPDY(J,J)=DYPDY(J,J)-VM(J,I)*RN(I)
80 CONTINUE
DO 90 I=J+1,NEQ
DYPDY(J,I)=-VM(J,I)*RN(I)+VK(J,I)*FB(I)
90 CONTINUE
100 CONTINUE
DO 110 I=1,NEQ-1
DYPDY(NEQ,I)=VM(I,NEQ-I)*RN(NEQ-I)-VM(NEQ,I)*RN(NEQ)
110 CONTINUE
DYPDY(NEQ,NEQ)=-2.0*VM(NEQ,NEQ)*RN(NEQ)-FB(NEQ)
DO 120 I=1,NEQ-1
DYPDY(NEQ,NEQ)=DYPDY(NEQ,NEQ)-VM(NEQ,I)*RN(I)
120 CONTINUE
RETURN
END
C *****

```

VITA

Zhenghe Xu was born on September 2, 1956, in Jiangying County, Jiangshu Province, China, where he lived until graduation from the Nanqing High School of Jiangshu Province in 1974. He then worked as a farmer in Shaguan community of Jiangying County until he enrolled at Central-South Institute of Mining and Metallurgy, Changsha, Hunan Province, China in March, 1978. He received his B.S. degree in January, 1982 and his M.S. in October 1984 from the Institute.

After teaching at the Institute for one year, he traveled to the US in January 1986, to continue his graduate study in the Department of Mining and Minerals Engineering, Virginia Polytechnic Institute and State University, Blacksburg, Va to pursue a Ph.D. degree. He transferred to the Department of Materials Engineering Science in August 1987.

He has eight publications and two presentations on professional meetings to his credit. He has accepted a research associate position in the Department of Mining and Minerals Engineering at Virginia Polytechnic Institute and State University.

A handwritten signature in black ink, appearing to read 'Zhenghe Xu', is centered on the page. The signature is written in a cursive, flowing style.